Stony Brook University

The dynamics of the seismogenic layer within the plate boundary zone of Western North America

A Dissertation Presented

by

Elliot Charles Klein

to

The Graduate School

in Partial fulfillment of the

Requirements

for the Degree of

Doctor of Philosophy

in

Geosciences

Stony Brook University

August 2008

Stony Brook University

The Graduate School

Elliot Charles Klein

We, the dissertation committee for the above candidate for the
Doctor of Philosophy degree,
hereby recommend acceptance of this dissertation.

William E. Holt, Dissertation Advisor, Professor
Department of Geosciences

Troy Rasbury, Associate Professor
Department of Geosciences
[Chairperson of Defense]

Lianxing Wen, Associate Professor
Department of Geosciences

Donald J. Weidner, Professor
Department of Geosciences

Wayne Thatcher, Research Geophysicist
Earthquake Hazards Program, United States Geological Survey

This dissertation is accepted by the Graduate School

Lawrence Martin
Dean of the Graduate School

Abstract of the Dissertation

The dynamics of the seismogenic layer within the plate boundary zone of Western North America

by

Elliot Charles Klein

Doctor of Philosophy

in

Geosciences

Stony Brook University

2008

I utilized inverse and forward dynamic modeling methods to investigate the forces responsible for driving the long-term deformation of the seismogenic crust of western North America. I have quantified depth integrated deviatoric stresses arising from internal buoyancy forces and the accommodation of relative plate motions for the upper crust of the diffuse plate boundary zone. The deviatoric stress field generated with the inverse method delineates nearly equal contributions from these driving forces. The deviatoric stress field generated with the forward dynamic method identifies the need for internal buoyancy forces that dominate over plate boundary forces for upper crust within regions east of the San Andreas system. For the inverse models, I quantified depth-integrated deviatoric stresses associated with differences in gravitational potential energy per unit area (GPE) for the upper crust using densities defined by seismic velocity data. I then accounted for sources of stress outside the model space by solving for a deviatoric stress field boundary condition that provides a best-fit to the tensor styles of the principal axes of the kinematic strain rates. The magnitudes of total deviatoric stress in the long-term seismogenic crust, from the surface to 20 km

below the sea level, range between 0.05 – 0.75 x 10^{12} N $\cdot$ m^{-1}. The depth integrated total stress differences are used as a proxy for depth integrals of fault strength in moderate-to-high strain rate regions. I calculated low long-term fault friction coefficients ($\overline{\mu} = 0.02$ – 0.20), under hydrostatic pore pressure conditions, associated with these deforming regions. I assimilated a large set of highly detailed Quaternary fault observations into an existing data set in order to generate an updated long-term kinematic strain rate tensor field and model velocity field for western North America. I constructed forward dynamic models of the upper crust where the body force distributions, inferred lateral variations in effective viscosity, and the known far-field velocity boundary conditions are defined. The depth-integrated viscosities are proportional to the assumed long-term friction on faults and inversely proportional to the long-term strain rates. The velocity boundary conditions are defined using plate motion estimates. Self-consistent dynamic strain rate tensor solutions to the force-balance equations were solved and tested for best-fit match with the updated long-term kinematic strain rate and velocity fields of western North America. Models constructed with low fault friction coefficients ($\mu < 0.20$) achieve a better fit to Quaternary fault observations than models with intermediate or high fault friction coefficients. I also delineate block model geometries for the crust of western North America. These block model geometries consist of weak shear zones and strong block-like interiors. The dynamic strain rate tensor styles associated with the forward dynamic models possessing block geometries yielded a poor match to the updated long-term kinematic strain rate and velocity fields of western North America. The scoring of self-consistent dynamic model output with detailed kinematic output show that models with a distributed fault fabric, defined with low uniform fault friction, provide a far better match to patterns of finite strain observed within the diffuse plate boundary zone of western North America than is achieved with the block model geometries explored to date.

Contents

List of Figures

List of Tables

Acknowledgements

Many individuals have provided me support while I undertook the work needed to present the studies included in this dissertation. None more than my wife, Yi-Ju Chen. The collective emotional support provided by each of our family members, alive or deceased, at times, overwhelmed me. I can not thank our family members enough.

My sincere gratitude goes to my doctoral advisor William Holt for believing in me and for sticking with me during many trying moments. This work would not be without his guidance, intelligence, and creativity. I am indebted to John Haines of Cambridge University for his insight and encouragement. His codes and mathematics define a large part of the results the reader will find here. I owe a tremendous debt to Lucy Flesch of Purdue University, as she has shared her data, codes, and insights with me throughout my years as a Stony Brook University student. I also benefitted greatly, and will always appreciate one on one discussions about aspects of life and science with Dan Davis.

Over the years, all the faculty have treated me well and have been open to my questions or concerns. I especially thank in no particular order, Lianxing Wen, Tengfong Wong, Gilbert Hanson, Don Lindsley, Troy Rasbury, Bob Liebermann, Donald Weidner, John Parise, Bill Meyers, Brian Phillips and Scott McLennan. My life as a student was made easier and was more fun through the departmental staff efforts of Owen Evans, Loretta Budd, and Aline Radu. Intellectual exchanges with current or former students (in no particular order) Corné Kreemer, Saad Haq, Andy Winslow, Brian Hann, Wen-che Yu, Daniel Hernandez, Attreyee Ghosh, Lada Dimitrova, Yi Wang (female), Yi Wang (male), Tony Yu, Natalie, Sheryl Tembe, Stacey Cochiara, Andrea Harrington, Alex Smirnov, Francis McCubbin, Richard Laffers, Lauren Beavon, Nick Tosca, Harris Mason, Marc Michel, and Wei Zhu contributed to my development as a scientist.

I greatly appreciate and thank Wayne Thatcher for being on my dissertation committee. I thank Sinan Ozeren, Eric Hetland, Gail Schaefer, and Richard Harrington for providing me with perspective in aspects of science and academic life beyond that of a student. Occasional cries of "Wrap it up" from my friend Ed Hilbrich along with our near daily conversations will be with me for a long, long time to come. Lengthy discussions and shared humor with another close friend, Rob Finkenthal helped me to always keep my sanity in check.

Chapter 1

Introduction

Introduction

Continental deformation zones do not fit into a simple plate tectonics model because deformation associated with some of the Earths continental margins are not restricted to narrow zones between rigid plates. Instead broad, diffuse zones of continental lithosphere may deform far into the interior of a continent. A classic example of a diffuse plate boundary zone is found in western North America. The North America plate accommodates the right-lateral stike-slip motion of Pacific plate along the well known San Andreas Fault system, yet deformation well into the plate interior is predominately extensional. Deformation in North America gradually ends hundreds of kilometers to the east of the transform boundary [e.g. *Thatcher*, 1995; *Thatcher et al.*, 1999; *Thatcher*, 2003; *Bennett et al.*, 1999; *Sonder and Jones*, 1999; *Humphreys and Coblentz*, 2007; *Flesch et al.*, 2007]. How continental lithosphere deforms and where it holds strength is still controversial [see e.g., *Jackson*, 2002; *Burov and Watts*, 2006]. Reasonable bounds for the absolute magnitudes of the long-term strength of the continental lithosphere and how such strength is distributed laterally and with depth need to be resolved. Such bounds hold important implications for the long-term strength of faults and are of wide interest to geologists, geodesists, geophysicists, and seismologists.

Constraints on long-term frictional resistance to sliding on active faults holds information on processes that affect earthquake rupture and the seismic cycle in general. Knowledge of the limits of frictional strength on faults could potentially shed light on the relative roles weakening mechanisms play in deforming seismogenic crust. High friction coefficients have been found in rock mechanic experiments in dry conditions for most upper crustal rock types [e.g. *Byerlee*, 1978]. Laboratory derived friction coefficients were used by *Brace and Kohlstedt* [1980] to estimate the strength of the brittle crust of the continental lithosphere. However much lower fault friction coefficients were found by *Bird and Kong* [1994] for the faults of California using a

thin-plate finite element model constrained to match geologic, geodetic, and stress data. Similar fault friction results for regions in California were obtained using related finite element modeling techniques and updated geophysical data sets [*Geist and Andrews*, 2000; *Parsons*, 2002]. More recently *Fay and Humphreys* [2006] predicted low effective fault friction coefficients using models that balanced the forces and torques associated with GPE variations, tectonic loading, and basal tractions acting on the Salton block. *d'Alessio et al.* [2006] used models of heat flow to constrain low apparent coefficients of fault friction along the creeping section of the San Andreas fault.

Low friction coefficients may arise from dynamic weakening mechanisms capable of lowering shear resistance on faults during the earthquake rupture process and the seismic cycle in general [e.g. *Di Toro et al.*, 2004]. Some potentially active dynamic weakening mechanisms that occur within the fault zone during periods of rapid coseismic slip include reduction of fault normal stress due to acoustic fluidization [*Melosh*, 1979, 1996; *Sornette and Sornette*, 2000], mechanical lubrication by a viscous fluid [*Brodsky and Kanamori*, 2001; *Ma et al.*, 2003; *Spray*, 2005], formation of silica gel at slip velocities that approach seismic rates [*Di Toro et al.*, 2004], thermal decomposition of calcite as a result of frictional heating during seismic slip [*Han et al.*, 2007], reduction of fault normal stress through strain energy minimization as a consequence of interacting faults [*Parsons*, 2002], and remote triggering of seismicity on faults by seismic waves shortly after very large earthquake events [e.g. *Gomberg et al.*, 2004; *West et al.*, 2005; *Brodsky and Prejean*, 2005; *Johnson and Jia*, 2005].

Low friction may also arise from intrinsic weakening mechanisms. Ancient exposures of mid-crustal fault cores in geologic studies and results from deformation experiments on material that closely match fault rocks suggest the presence of a broad frictional-viscous regime in the upper crust [*Handy and Brun*, 2004; *Holdsworth*, 2004; *Jefferies et al.*, 2006]. Fault reactivation may result in the long-term weakening of

the fault zone [*Holdsworth et al.*, 2001; *Holdsworth*, 2004; *Edwards and Ratschbacher*, 2005]. An abundance of quartz-mica phyllonites in the middle to upper crust of continental fault zones may indicate activation of fluid assisted deformation mechanisms at lower differential stress than that predicted by Byerlee's law [*Janecke and Evans*, 1988; *Stewart et al.*, 2000; *Imber et al.*, 2001; *Jefferies et al.*, 2006]. Numerous experiments on water saturated clay minerals, which are often present in fault gouge, have intrinsically low friction coefficients and their presence in the internal structures of fault zones could explain fault weakness [e.g. *Byerlee*, 1978; *Morrow et al.*, 1992; *Streit*, 1997; *Moore and Lockner*, 2004]. Results of compression experiments on natural samples containing high mica content indicate that the weakening inferred from field studies of phyllosilicate-rich fault zones could be due to pressure-insensitve, brittle-plastic deformation of micas [*Shea and Kronenberg*, 1992; *Wintsch et al.*, 1995]. Ring shear experiments on halite-muscovite mixtures led to microphysical models that estimate differential strength reduction in the upper crust [*Bos and Spiers*, 2001, 2002; *Niemeijer and Spiers*, 2005]. *Tembe et al.* [2006] ascertained low friction from drill core and cuttings extracted from the San Andreas Fault Observatory at Depth (SAFOD) scientific borehole. These authors indicate that the presence of two weak shear zones at depth is consistent with, and may partially explain, the apparent weakness of the San Andreas Fault

The role of fluids within fault zones also must be considered. Impermeable fault gouge within the internal structure of a fault zone may promote sliding at low shear stress through overpressure of fault sealed fluids [e.g. *Sibson*, 1990a; *Byerlee*, 1990; *Blanpied et al.*, 1992; *Rice*, 1992; *Sleep and Blanpied*, 1992; *Byerlee*, 1993; *Faulkner and Rutter*, 2001]. How faults might seal and possibly over pressure the fault zone has required most models to include a minimum of some interaction among fault zone fluids, crustal structure, fault materials, and the stress field [*Chester et al.*, 1993; *Sleep and Blanpied*, 1994; *Miller et al.*, 1996; *Streit*, 1997; *Miller and Nur*, 2000; *Miller*,

2002; *Parsons*, 2002; *Fitzenz and Miller*, 2003; *Wilson et al.*, 2005]. Fault zone fluids may include CO_2 derived from the upper mantle [*Kennedy et al.*, 1997], the deep crust[*Miller et al.*, 2004], or meteoric water infiltration from surrounding country rocks [*Sleep and Blanpied*, 1992; *Byerlee*, 1993]. Fluids may circulate in the lower crust and eventually supply the seismogenic zone during the seismic cycle [e.g. *McCaig*, 1988; *Cox*, 2002; *Connolly and Podladchikov*, 2004]. Fluid movements associated with naturally occurring meteoric fluids or purposefully injected anthropogenic fluids within the seismogenic crust can directly enhance deformation rates and lead to the triggering of seismicity [*Raleigh et al.*, 1976; *Hill et al.*, 1993; *Brodsky et al.*, 2000; *Bawden et al.*, 2001; *Watson et al.*, 2002; *Brodsky et al.*, 2003].

The incorporation of geodetic measurement into kinematic models has led to insight regarding how interseismic strain is accommodated within diffuse plate boundary settings [*Haines and Holt*, 1993; *Shen-Tu et al.*, 1999; *Holt et al.*, 2000; *Beavan and Haines*, 2001; *Pollitz*, 2003; *Pollitz and Vergnolle*, 2006; *Pollitz et al.*, 2008; *Hammond and Thatcher*, 2004, 2005, 2007; *McCaffrey*, 2005; *McCaffrey et al.*, 2007; *Flesch et al.*, 2007; *Bürgmann and Dresen*, 2008]. Recently, the United States Geologic Survey updated its Quaternary fault and fold data base of the United States (QFBD). This updated data base provides unprecedented spatial and temporal resolution for the fault networks of the western United States. Kinematic constraints defined by the QFBD provide an opportunity for hypothesis testing. Some unresolved and important questions for the diffuse plate boundary zone of western North America include: (1) What are the bounds on deviatoric stress magnitudes for the continental margins? (2) What are the relative influences of the forces that drive continental deformation and how might they change over the long-term? (3) Is a greater portion of the continental strength in the crust or in the upper mantle? (4) What controls rupture history in damaged volumes of crust? (5) Do off-fault earthquakes in block-like regions imply that strain may be taken up on distributed sets of faults? (6) What are the precise

levels of fault strength in the seismogenic crust and how might they vary across the plate boundary zone? (7) Which weakening mechanisms most likely facilitate slip on faults within the diffuse plate boundary zone?

In this dissertation, I addressed some of these questions as I investigated the dynamics of the continental lithosphere of western North America. This work uses numerical models to shed light on the long-term physics of the seismogenic crust within the diffuse plate boundary zone. The data-driven inverse and forward models presented here are built upon seismic, geodetic, and Quaternary fault observations. I solve the force balance equations to quantify the level and origin of deviatoric stresses responsible for driving seismic deformation within the crust over the past 750,000 years. Calibrating the styles and magnitudes of deviatoric stress for the upper crust allowed for the first time quantification of the long-term frictional strength of faults throughout the diffuse plate boundary zone of western North America. I define lateral variation in effective viscosity using an assumed fault friction to define the theoretical value for depth-integrated stress difference for an expected fault style, along with use of strain rates from the long-term kinematic modeling. I then use a forward modeling method to solve the force-balance equations. Self-consistent dynamic stress tensor, velocity, and strain rate tensor fields of the seismogenic layer are scored to determine a best-fit match with long-term stress field indicators and kinematic indicators within western North America. Forward dynamic solutions that closely match deformation indicators and patterns of finite strain in western North America allowed, for the first time, quantification of the Argand Number (Ar) for western North America. I found that a more distributed fault fabric, with long-term friction coefficients of 0.10–0.20 under hydrostatic conditions, rather than block model geometries, is required to explain the patterns of finite strain observed within the diffuse plate boundary zone of western North America. On the basis scoring self-consistent dynamic model output with detailed kinematic output I solved the outstanding controversy of whether block-

like or distributed faulting can explain the long-term deformation field in western North America.

In addition to this introductory chapter (Chapter 1), this dissertation consists of three main chapters and a conclusion. Chapter 2 is recommended for publication, pending minor revision. Chapters 3 and 4 are in preparation for publication. A summary and the main conclusions of this dissertation are found in Chapter 5.

In Chapter 2, I address the strength of the faults within the seismogenic crust using the inverse method. Within this chapter I define the modeling method that allowed for the quantification of depth integrals of stress difference. These depth integrals then provide a proxy for depth integrals of fault strength in moderate-to-high strain rate regions. This in turn, allowed calculation of fault friction coefficients for the long-term seismogenic crust of western North America. In chapter 3, I introduce the updated suite of kinematic models defined with Quaternary fault observations. Rather than infer fault strength from stress magnitudes, in Chapter 3 I assume a fault strength, and then explore the dynamic response using the forward modeling approach. I test models of crust defined with lateral variation in effective viscosity and show that the forward dynamic solutions are sensitive to the level of friction on the faults and the distribution of the fault fabric. These two factors primarily control the relative influence that internal crustal buoyancies and plate boundary forces have on the deformation field. In Chapter 4, I defined and scored block model geometries with same long-term kinematic solutions determined in Chapter 3 to compare block model geometries with the more distributed faulting defined by the uniform fault friction models. Block model geometries explored to date yield dynamic strain rate tensor styles that are a poor match with the kinematic strain rate tensor styles associated with Quaternary deformation indicators.

Chapter 2

Evidence of long-term weakness on seismogenic faults in western North America from dynamic modeling

Evidence of long-term weakness on seismogenic faults in western North America from dynamic modeling

Elliot C. Klein, Lucy M. Flesch, William E. Holt, and A. John Haines

(Recommend for publication, pending minor revision in *Journal of Geophysical Research Solid Earth*, 113, B, doi:10.1029/xxxxx, 2008)

Abstract

We investigate the long-term strength of faults within the plate boundary zone of Western North America by quantifying the absolute magnitudes and styles of the depth integrated deviatoric stresses acting within the seismogenic portion of the crust. We solve the depth integrated 3-D force-balance equations for the deviatoric stress field acting within the seismogenic layer of the plate boundary zone. Forcings are the horizontal gradients in gravitational potential energy per unit area (GPE). Seismic velocity data defines the densities we use to define GPE. We also solve for stress field boundary conditions that when added to the contribution from GPE differences, provides a best-fit to stress indicators. The absolute magnitude of the long-term deviatoric stress field is calibrated by the absolute magnitude of deviatoric stresses associated with GPE differences within the seismogenic layer. We estimate that the long-term depth integrated deviatoric stress magnitudes range between 0.05 – 0.75 x 10^{12} N $\cdot$ m^{-1} for the case where depth integration is performed down to a maximum depth of 20 km below sea level in western North America. Long-term depth integrated total stress differences within the approximately 20 km thick seismogenic layer are of the order of 0.05 – 1.4 x 10^{12} N $\cdot$ m^{-1}. Using these stress differences as a proxy for depth integrals of fault strength within the actively deforming regions, we infer that the long-term values of coefficients of friction on faults within the Basin and Range of Nevada and Utah, and most of California, are 0.02 – 0.30 under long-term hydrostatic to wet conditions. We test the sensitivity of these results by considering a range of

maximum depths of integration. We show that for depths of integration in excess of 20 km below sea level, there is diminishing contribution to the depth integrated stress differences, and by proxy depth integrated fault strength. This is consistent with a brittle-ductile transition in the plate boundary zone at depths less than 20 km below sea level, and with a weak lower crust.

2.1 Introduction

A more precise understanding of the fundamental physics that control the long-term failure of frictionally sliding continental upper crust in diffuse plate boundary zones requires linking tectonic fault regimes with geodynamic estimates of upper crustal strength. For instance, a major question unresolved in the fault mechanics community is whether or not the San Andreas Fault is a weak or strong fault [e.g., *Brune et al.*, 1969; *Mount and Suppe*, 1987; *Zoback et al.*, 1987; *Lachenbruch and Sass*, 1992; *Zoback and Beroza*, 1993; *Scholz*, 2000; *Saffer et al.*, 2003; *Scholz and Hanks*, 2004; *Townend and Zoback*, 2004; *Horsman and Tikoff*, 2005; *d'Alessio et al.*, 2006]. Ambiguity about the relative degree of friction on this well- studied major transform fault suggests that frictional strength on faults of all fault types in plate boundary settings needs reexamination. Most estimates of the long-term strength of the seismogenic upper crust and the frictional properties on faults within that layer have come from extrapolation of experimental data obtained through rock mechanics experiments [e.g., *Byerlee*, 1978; *Brace and Kohlstedt*, 1980; *Carter and Tsenn*, 1987; *Kohlstedt et al.*, 1995] or from deep drilling into the crust [e.g., *McGarr*, 1980; *Zoback and Healy*, 1992; *Sibson*, 1994; *Brudy et al.*, 1997; *Townend and Zoback*, 2000; *Hickman and Zoback*, 2004]. Others have constructed numerical models to ascertain the level of friction on faults [e.g., *Bird and Piper*, 1980; *Reasenberg and Simpson*, 1992; *Bird and Kong*, 1994; *Geist and Andrews*, 2000; *Chéry et al.*, 2001; *Parsons*,

2002; *Zoback and Townend*, 2001; *Chéry et al.*, 2004; *Fialko et al.*, 2005; *Fay and Humphreys*, 2006].

Rather than determine the fault strength of the seismogenic crust by assigning friction coefficients obtained from deep drilling, modeling results, or from the laboratory to crustal rocks, we infer the long-term depth integrated strength of the faults using a dynamic method. The approach we take enables us to directly estimate the long-term depth integrated deviatoric stresses acting within the seismogenic layer using: (1) density variations isolated within the seismogenic crust and (2) constraints provided by stress field indicators, which enable us to solve for stress field boundary conditions. Solutions associated with (1) and (2) are added together to provide magnitudes of total depth integrated deviatoric stresses acting within the seismogenic layer. We are then able to independently estimate long-term friction on faults in regions that are actively deforming over geologic time scales. The advantage of the approach we take is that it enables us to estimate the magnitudes and directions of depth integrated deviatoric stresses directly from sources of stress found within the uppermost crust.

The depth integrated deviatoric stresses that we obtain provide constraints on the long-term coefficient of friction magnitudes expected for seismogenic crust under long-term hydrostatic and wet conditions. These fault friction coefficient results are most robust within the diffuse plate boundary zone of the North American plate where the long-term state of stress is inferred to be close to failure and thus where long-term depth integrated stress differences can be interpreted to represent long-term depth integrated fault strength.

2.2 Long-term Kinematics of the Seismogenic Layer

Seismically generated strain within the upper crust is relieved mainly by frictional failure occurring on pre-existing fractures. The shaping of the deformed crust results mainly from rare but large earthquakes within the seismogenic crust causing the largest crustal strains [*Sibson*, 1984]. Figure 2.1 provides a comparison of the distribution of faults with historic rupture with the distribution of faults that have been reported to have last slipped as recently as 750,000 years ago. The Quaternary fault and fold database (see Figure 2.1) identifies the relative timing and locations involved in the long-term deformation of the crust [see *Thatcher*, 2003]. Inference of long-term principal axes of strain rate and the strain rate tensor style from kinematic models [e.g., *Holt et al.*, 2000; *Kreemer et al.*, 2003] are useful for constraining the long-term directions of principal axes and style of deviatoric stress responsible for the frictional slip of faults embedded within the seismogenic crust (e.g., Figure 2.1).

In order to quantify the long-term kinematics we define a curvilinear gird over the uppermost crust that encompasses the zone of diffuse PA-NA plate boundary deformation (Figure 2.2). We also solve each of our geodynamic thin sheet models using this grid. *Hetland and Hager* [2004] argue that transient behavior recorded by GPS measurements may cause appreciable error in estimates of magnitude and spatial distribution of the long-term strain rate field. Therefore, we use a first order long-term kinematic strain rate and velocity field model based on interpolation of Quaternary strain rates, long-term spreading estimates of mid-ocean ridges, and to a lesser extent, in areas where fault slip data are sparse, GPS velocity vectors (Figures 2.3 and 2.4) [see *Flesch et al.*, 2007].

To date, we do not include the faults of the Quaternary fault and fold database for the United States into our kinematic modeling. Instead, we use the Quaternary fault data presented in the second, revised long-term kinematic model of *Flesch et al.* [2007].

As was done in that model, we remove GPS observations in Oregon and Washington in order to avoid possible elastic effects due to the locked Juan de Fuca, Gorda, and Explorer plates [e.g., *McCaffrey et al.*, 2007]. Moreover, we also define the Cascadia forearc and Sierra Nevada block to be more rigid than neighboring regions. As such, the model yields concentrated strain rates in the Juan de Fuca Trench, and almost no strain in the Cascadia Forearc, consistent with inference that the subduction thrust there involves a weak fault [*Hyndman and Wang*, 1993] (Figure 2.4). Because this is a long-term model it is reflective of the interaction of long-term applied stress and accommodation of steady-state and associated long-term steady-state slip rates of faults within the seismogenic layer. Although our modeled strain rate magnitudes generally increase from east to west across western North America, it is only the directions and tensor styles of the horizontal components of the principal strain rates that constrain our modeled principal deviatoric stress directions.

2.3 Estimating Depth Integrals of Deviatoric Stress Differences Within the Long-Term Seismogenic Crust

In our approach, we perform depth integrals of the full three dimensional force-balance equations (spherical form) from the surface of variable topography down to depths in the vicinity of the base of the seismogenic layer or brittle-ductile transition within actively deforming regions. The brittle-ductile transition divides the continental crust into two distinct rheologies [*Bird*, 1978; *Sibson*, 1982, 1984; *Ranalli and Murphy*, 1987; *Scholz*, 1988]. The top rheological layer, is a mechanically strong brittle upper crust, which overlies a mechanically weak plastic middle or lower crust [*Brace and Kohlstedt*, 1980; *Sibson*, 1983; *Ranalli and Murphy*, 1987; *Jackson*, 2002].

The base of the seismogenic portion of the crust, marked by the "cut-out" depth of shallow earthquakes, effectively delineates the present depth at which there is a transition from a brittle, seismically active elastic upper crust to a plastic, aseismic lower crustal layer [*Macelwane*, 1936; *Sibson*, 1982; *Chen and Molnar*, 1983; *Sibson*, 1984; *Jackson and White*, 1989; *Bonner et al.*, 2003].

Seismic observations suggest that the present-day transition depth from brittle to ductile rheology is highly variable, but in general ranges from 5 to 40 km. The actual depth of the present-day brittle-ductile transition for a given location is a consequence of the local fault regime, strain rate, and temperature gradient [*Chen and Molnar*, 1983; *Wong and Chapman*, 1990; *Paterson*, 2001; *Bonner et al.*, 2003] and could be modeled using the depth of the isotherm at 300° C. On the other hand, the depth to the deepest anticipated crustal earthquake marks the location of the expected long-term brittle-ductile transition within the crust [*Sibson*, 1984]. In spite of the significant vertical variation in the depth to the present-day brittle-ductile transition, we show in the following section that if horizontal shear stresses are small then our solutions should reflect accurate depth integrals of deviatoric stress, regardless of the location of the brittle-ductile transition.

For simplicity we provide the force balance equations in Cartesian form:

$$\frac{\partial \sigma_{ij}}{\partial x_j} + \rho g_i = 0 \tag{2.1}$$

where g is acceleration of gravity, ρ is density, and σ_{ij} is the total stress tensor. If horizontal gradients in shear tractions τ_{xz} and τ_{yz} are small compared with ρg, then we can relate the depth integral of density in a gravitational field, $\int \rho(z) g dz$, to vertical stress, $\sigma_{zz}(z)$ with depth, z. The depth integrated force-balance equation can be written as

$$-\frac{\partial \overline{\sigma}_{zz}}{\partial x_\alpha} = \frac{\partial}{\partial x_\beta}(\overline{\tau}_{\alpha\beta} + \delta_{\alpha\beta}\overline{\tau}_{\gamma\gamma}), \tag{2.2}$$

where $\overline{\tau}_{\alpha\beta}$ is the depth integrated horizontal deviatoric stress tensor, $\overline{\sigma}_{zz}$ is the depth integrated vertical stress, and a 2-D summation notation with $\overline{\tau}_{\gamma\gamma} = \overline{\tau}_{xx} + \overline{\tau}_{yy} = -\overline{\tau}_{zz}$ is implied.

We express depth integrated vertical stress, $\overline{\sigma}_{zz}$, or equivalently gravitational potential energy per unit area (herein referred to as GPE), as

$$\overline{\sigma}_{zz} = -g \int_{-h}^{L} \left[\int_{-h}^{z} \rho(\acute{z}) d\acute{z} \right] dz, \tag{2.3}$$

where $\acute{z}$ is a variable of integration, h is elevation with respect to sea level, and L is the depth to the approximate base of the seismogenic layer. The depth L, in equation (2.3) also defines the reference level for the depth integrals of vertical stress.

2.3.1 Validity of approximation

On a global scale, tractions associated with coupling between density-buoyancy driven mantle circulation and the lithosphere are important for explaining both plate motions and the deviatoric stress field within the lithosphere [*Steinberger et al.*, 2001; *Becker and O'Connell*, 2001; *Lithgow-Bertelloni and Guynn*, 2004; *Ghosh et al.*, 2008b]. These driving tractions integrate over long wavelengths and are particularly important for providing compressional deviatoric stress contributions across the Andes and Tibet, where lithospheric gravitational potential energy differences are large [*Ghosh et al.*, 2008b]. The boundary conditions that we solve for include the influence of such driving tractions outside of the plate boundary zone. However, even in the presence of a weak middle crust, the question arises as to the influence of tractions associated with density buoyancy driven mantle flow directly below the plate boundary zone within western North America [*Sonder and Jones*, 1999]. We have assumed that these tractions have a small enough effect such that (1) horizontal gradients of the horizontal tractions are small relative to ρg and (2) despite the presence

of horizontal tractions at depth, one of the principal axes of stress will nevertheless be near-vertical. In terms of the approximation in (1), what is important is that the horizontal variations in the depth integral of horizontal shear stress need to be small in comparison with the depth integrals of ρg:

$$\frac{\partial}{\partial x}\int_{-h}^{z}\tau_{xz}(z)dz \ll \int_{-h}^{z}\rho(z)gdz. \tag{2.4}$$

For the purpose of this argument let us assume $\tau_{xz}(z)$ is linear function varying from zero at the surface to $\tau_{xz}(L)$ at the base of lithosphere:

$$\tau_{xz}(z) = \frac{\tau_{xz}(L)}{L}\cdot z \tag{2.5}$$

Assuming a depth of integration of 20 km and a crustal density of 2800 kg $\cdot$ m^3 in (2.4), horizontal gradients in shear stress have to be as high as 2.8 MPa $\cdot$ km^{-1} acting at the base of the lithosphere in order for the the integral on the left of (2.4) to be 1% of the integral on the right of (2.4). Large-scale density buoyancy driven flow calculations associated with long-wavelength mantle circulation suggest that horizontal gradients of horizontal shear tractions acting at the base of the lithosphere are $\sim$ 2–3 orders of magnitude smaller than this [*Steinberger et al.*, 2001; *Becker and O'Connell*, 2001; *Lithgow-Bertelloni and Guynn*, 2004; *Humphreys and Coblentz*, 2007; *Ghosh et al.*, 2008b], thus showing the appropriateness of our approximation here.

In order for one of the principal axes to be vertical, the depth integral of the horizontal shear tractions must be much smaller than the depth integrals of the horizontal deviatoric stresses.

$$\int_{-h}^{z}\tau_{xz}(z)dz \ll \int_{-h}^{z}\tau_{xx}(z)dz. \tag{2.6}$$

In order to evaluate the integral expressions above we assume $z = 20$ km for the base of the seismogenic layer and $\tau_{xz}(L) = 5\ MPa$ for the horizontal shear tractions

acting at the base of the lithosphere at $L = 100$ km depth [*Becker and O'Connell*, 2001; *Humphreys and Coblentz*, 2007], and $\rho = 2800$ kg $\cdot$ m^{-3}. We find values of order 1 x 10^{10} N $\cdot$ m^{-1} for the depth integral of shear traction. We will show later that this magnitude is at most 20% of the magnitude of the depth integrals of horizontal deviatoric stresses that we calculate within the seismogenic layer, and in most places is of order 2-5% of the horizontal values. This result is consistent with the observation that large normal fault earthquakes within the Basin and Range have moment tensors reflecting near vertical compression axes [*Jackson and White*, 1989]. Therefore, despite the likely existence of moderate-sized horizontal basal tractions beneath the plate boundary zone of western North America, their influence is still small enough on the regional scale such that assumptions in (1) and (2) above appear valid for the seismogenic layer. That is, because the depth-integrals of τ_{xz} are small, our solutions should contain accurate stress magnitudes within the seismogenic layer. This conclusion holds true regardless of whether the maximum depth of integration is above or below the brittle-ductile transition zone.

2.3.2 Estimation of depth integrated vertical stress within the seismogenic layer

Our first step is to estimate depth integrated vertical stress distributions (GPE) in the upper crust of western North America. Spatial variations of these quantify the magnitude of the depth integrated horizontal deviatoric stress (equation 2.2). This requires $\rho(z)$, which we assign empirically from scaling density to seismic velocity data. The seismic velocities we use were collected from a large seismic data set presented by *Chulick and Mooney* [2002] who reported estimates of crustal thickness for regions within the North American plate and surrounding ocean basins. The seismic records used herein contain P-wave velocity measurements that define velocity

structure profiles beneath survey areas down to the Moho. We assigned density within the crust at every kilometer below sea level throughout the entire thickness of the seismogenic zone at grid locations where velocity structure profiles exist.

We quantify our seismically defined densities at depth by applying a simple velocity to density conversion to the P-wave velocity, depth, and density data presented in *Lowry and Smith* [1995]. We construct a 5^{th} order polynomial curve to interpolate *Lowry and Smith*'s seismically defined data set, which was obtained by grouping and averaging their P-wave velocity and associated density data for each of ten provinces defined within the western U.S. Cordillera. The densities produced by our method (Figure 2.5) are consistent with expected densities at depth within western U.S. Cordillera [*Lowry and Smith*, 1995; *Kaban and Mooney*, 2001] and the earth's crust in general [*Ludwig et al.*, 1970; *Brocher*, 2005].

We seek to establish both vertical and lateral density distributions beneath our grid areas but do not have sufficient seismic velocity data coverage to do so. In order to overcome the lack of adequate areal data coverage in our data set we smooth the existing vertical density distributions laterally throughout the entire grid space. We perform lateral smoothing on available seismically inferred density data for each layer of 1 km thickness, one layer at time. If more than one density estimate exists at a particular grid location depth, we compute the mean density there before smoothing. We assign a grid area a density value, which corresponds to the weighted average of the densities of its immediate neighboring grid areas. The weights assigned to the density values reflect the surface area of each grid location. The smoothing procedure is repeated until each grid area is assigned a non-zero density value. We specify uniform density values to crustal rock in grid areas above sea level. Such density values are defined to be equal to the density values found in the topmost seismically defined layer below sea-level. We assign a uniform density of *1030* $\text{kg} \cdot \text{m}^{-3}$ for sea water.

The vertical stress, expressed in terms of the overburden pressure at each layer is

$$\sigma_{zz}(z_i) = -P(z_i) = -P(z_{i-1}) - g\int_{z_{i-1}}^{z_i} \rho(z_i)dz_i, \tag{2.7}$$

where the subscript i denotes individual layers of seismically determined density at depth. Depth integrated vertical stress for grid areas that are coincident with land mass above sea level are calculated using

$$\overline{\sigma}_{zz} = -\sum_{i=1}^{n} \frac{1}{2}\Big[P(z_i) + P(z_{i-1})\Big](z_i - z_{i-1}). \tag{2.8}$$

Since sea water only contributes pressure to the depth integrated vertical stresses, we calculate the depth integration of the vertical stresses for grid areas overlying ocean floor with

$$\overline{\sigma}_{zz} = -\sum_{i=2}^{n} \frac{1}{2}\Big[P(z_i) + P(z_{i-1})\Big](z_i - z_{i-1}), \tag{2.9}$$

taking $i = 1$ to correspond to the water layer.

Maggi et al. [2000] argue that variations in the effective elastic thickness of the continental crust reveal and correlate to variations in seismogenic zone thickness. They show that elastic thicknesses rarely exceed 15 kilometers and found that the bulk of continental seismicity occurs within the upper continental crust. Therefore, in Figure 2.6 we quantify GPE magnitudes for western North American seismogenic crust with seismically defined densities down to a uniform base 20 kilometers below sea level. These GPE magnitudes range from 4.6 – 7.0 x 10^{12} N $\cdot$ m^{-1} (Figure 2.6) throughout western North America. In general, the seismically defined densities produce the highest magnitudes of GPE for areas with highest topography and lowest magnitudes of GPE for areas beneath sea water.

2.3.3 Deviatoric stress field associated with horizontal variations in depth integrated vertical stress

Deformation due to frictional sliding within seismogenic crust is expected to be driven in part by horizontal variations in the GPE field. We follow the method of *Flesch et al.* [2000, 2001, 2007] to determine the horizontal components of the depth integrated deviatoric stress field associated with GPE differences, where depth of integration is performed to a uniform base 20 kilometers below sea level (see Figure 2.6). The depth integrated force-balance equations are solved under the constraint of minimization of the second invariant of depth integrated deviatoric stress [*Flesch et al.*, 2001]. Solutions like that in Figure 2.7 are important inputs as they calibrate the magnitude of the total depth integrated deviatoric stress field within the seismogenic layer of western North America (see Appendix 2.8 for details). The depth integrated deviatoric stress field associated with GPE differences within the bulk of the seismogenic layer are within the range of 0.05 – 0.7 x 10^{12} N $\cdot$ m^{-1} (Figure 2.7) throughout the western United States. Compressional deviatoric stresses associated with the lower elevations of the PA-NA plate margin are oriented NE-SW. Areas of high topography are in deviatoric tension. N-S tension dominates the Basin and Range. The styles of deviatoric stress inferred from GPE variations are, by themselves, inconsistent with the styles of strain depicted by the principal axes of strain rate shown in Figure 2.4. Sources of stress in addition to GPE differences are needed. We incorporate all additional sources into a stress field boundary condition solution that we solve for next.

2.3.4 Stress field boundary condition solution

To incorporate the stress field boundary condition we again solve equation (2.2) using the method of *Flesch et al.* [2001, 2007]. In our implementation of this method

we form a continuous boundary condition along the entire grid boundary by dividing the boundary into fifty six linked segments. We also use two additional "ring" boundaries each comprised of seven linked boundary segments within the interior of the grid to define the Rivera and Juan de Fuca plate boundaries [*Flesch et al.*, 2007]. In total there are 70 boundary segments and in general the shortest boundary segments are proximal to areas of the grid with highest GPS coverage (Figure 2.2). At every boundary segment we calculate a deviatoric stress field response that minimizes the second invariant of deviatoric stress while satisfying the depth integrated 3-D force-balance equations (see equation 2.2), while all other boundary segments are held fixed. In the boundary condition solution, $\overline{\sigma}_{zz}$ is set equal to zero, and forcing is applied at one node point at the boundary only. This procedure yields a total of 210 stress field basis functions. The complete stress field boundary condition is arrived at by summation of these stress field basis functions. This boundary condition is added to the deviatoric stress field associated with horizontal variations in depth integrated vertical stress such that

$$\tau = \tau_o + \sum_{j=1}^{n} \sum_{i=1}^{3} a_{ij} \tau_{ij} \tag{2.10}$$

where τ_o is the deviatoric stress field associated with depth integrated vertical stress variations within the seismogenic crust (Figure 2.7), n is the total number of boundary segments, a_{ij} are the scaling factors for the stress field basis functions (3 for each boundary segment), and τ_{ij} are the stress field basis functions. We use an iterative least-squares inversion to determine the 210 scaling factors. In the inversion process we minimize the objective function

$$\sum_{areas} \left\{ T - \frac{e \cdot \tau}{E} \right\} \Delta S, \tag{2.11}$$

where

$$
\begin{aligned}
E &= \sqrt{\dot{\epsilon}_{xx}^2 + \dot{\epsilon}_{yy}^2 + \dot{\epsilon}_{zz}^2 + \dot{\epsilon}_{xy}^2 + \dot{\epsilon}_{yx}^2} \\
&= \sqrt{2\dot{\epsilon}_{xx}^2 + 2\dot{\epsilon}_{xx}\dot{\epsilon}_{yy} + 2\dot{\epsilon}_{yy}^2 + 2\dot{\epsilon}_{xy}^2}
\end{aligned}
$$

$$
\begin{aligned}
T &= \sqrt{\tau_{xx}^2 + \tau_{yy}^2 + \tau_{zz}^2 + \tau_{xy}^2 + \tau_{yx}^2} \\
&= \sqrt{2\tau_{xx}^2 + 2\tau_{xx}\tau_{yy} + 2\tau_{yy}^2 + 2\tau_{xy}^2}
\end{aligned}
$$

$$
\begin{aligned}
e \cdot \tau &= \dot{\epsilon}_{xx}\tau_{xx} + \dot{\epsilon}_{yy}\tau_{yy} + \dot{\epsilon}_{zz}\tau_{zz} + \dot{\epsilon}_{xy}\tau_{xy} + \dot{\epsilon}_{yx}\tau_{yx} \\
&= 2\dot{\epsilon}_{xx}\tau_{xx} + \dot{\epsilon}_{xx}\tau_{yy} + \dot{\epsilon}_{yy}\tau_{xx} + 2\dot{\epsilon}_{yy}\tau_{yy} + 2\dot{\epsilon}_{xy}\tau_{xy}
\end{aligned}
$$

$\dot{\epsilon}_{ij}$ is the strain rate from our kinematic modeling (Figure 2.4), τ_{ij} is the total deviatoric stress tensor, and ΔS is the grid area [*Flesch et al.*, 2007]. The objective function is minimized when the directions and styles of deformation predicted by the stress field and the directions and styles of strain rate inferred from the kinematic modeling align and when the tensor styles of the total depth integrated deviatoric stresses are matched to the tensor styles of the observed strain rate [*Flesch et al.*, 2001, 2007]. Like *Flesch et al.* [2000, 2007] we dded the constraint of a rigid Cascadia forearc and have removed the San Andreas shear zone and from the data set to be fitted, since there is unlikely to be an isotropic relation between the deviatoric stress and strain rate tensors within that zone [*Provost and Houston*, 2001; *Chéry et al.*, 2004; *Hickman and Zoback*, 2004; *Townend and Zoback*, 2004].

As shown in Figure 2.8, the vast majority of long-term depth integrated stress magnitudes in the boundary condition solution range between 0.05 – 0.65 x 10^{12} N $\cdot$ m^{-1}, which is similar in magnitude to the depth integrated stress field associated with GPE differences (Figure 2.7). Overall the style of deviatoric stresses obtained from

this solution agree well with the results of *Flesch et al.* [2007], which solves for the applied stress field boundary conditions over the entire lithosphere thickness, rather than for the upper crust alone, as we have done here.

Approximately 50% of the total depth integrated deviatoric stress field solution results from GPE variations (Figure 2.7). The remaining contribution to the total depth integrated deviatoric stress field solution arises from boundary condition stresses (Figure 2.8). The minimum total depth integrated deviatoric stresses depicted in Figure 2.9, obtained with the base of the seismogenic crust defined at a uniform depth 20 kilometers below sea level, yields long-term deviatoric stress magnitudes between 0.05 – 0.75 x 10^{12} N $\cdot$ m^{-1}. Overall, this solution is very similar to those obtained in previous studies by *Flesch et al.* [2000, 2007] see Table 2.1 of this study and Table 1 of *Flesch et al.* [2007]).

As expected, we observe tensor styles of stress (thrust, normal, strike-slip, oblique slip) that are consistent with stress field indicators for much of western North America. For example, the roughly NE-SW orientation of the directions of deviatoric compression along the NA-PA plate margin in southern California correlate with maximum horizontal crustal stress orientations obtained from focal mechanism inversions, borehole breakout data, and hydraulic fracture data [*Townend and Zoback*, 2004]. In general, we find good agreement between model deviatoric stresses and the stress field indicators throughout the Basin and Range and California (note regions of interest 7–9 in Table 2.1).

2.4 Long-Term Frictional Strength

Deformation of the uppermost brittle crust is accommodated most readily by rapid frictional slip failure of rock material along preexisting fault planes. This frictional failure mode generally requires significantly less differential stress to activate when

compared with the amount of differential stress required to cause rock failure through the breaking of new fault surfaces in otherwise equivalent conditions [e.g., *Brace and Byerlee*, 1966; *Byerlee*, 1978; *Sibson*, 1985; *Scholz*, 1998; *Ruff*, 2004]. Mechanical failure by frictional sliding has been estimated by laboratory controlled deformation experiments for most upper crustal rock types. These studies show that the majority of rock types of the uppermost crust frictionally fail in a predictable manner described by the empirical relationship known as 'Byerlee's law' [*Byerlee*, 1968, 1978; *Brace and Kohlstedt*, 1980]. Byerlee's law also predicts differential stress and shear stress magnitudes that vary as a function of tectonic regime when measured at the same crustal depths and pore pressure conditions [*Brace and Kohlstedt*, 1980; *Carter and Tsenn*, 1987; *Kohlstedt et al.*, 1995]. For these reasons we use our depth integrated total deviatoric stresses for the seismogenic layer to provide estimates on the long-term frictional behavior of fault zones.

For areas undergoing active deformation, long-term depth integrated deviatoric stresses within the seismogenic crust allow us to infer lateral variations of long-term depth integrated fault strength. Within these regions we also investigate sensitivity of the coefficients of friction to variations in long-term crustal pore pressure. We assume: (1) one of the three principal stress directions is vertical (2) the crust fails by frictional sliding on preexisting optimally oriented faults satisfying the Coulomb frictional-failure criterion (3) effective stress only depends on the difference between applied stress and pore pressure (4) randomly oriented fractures of all lengths permeate the crust and (5) the long-term state of stress on the faults is close to the long-term frictional yield strength of faults within deforming volumes of seismogenic crust within the diffuse plate boundary zone of the North American plate.

Frictional failure on faults within the seismogenic crust is controlled by the Coulomb frictional-failure criterion [*Sonder and England*, 1986], which can be written as

$$|\tau_s| = c - \mu\sigma_n, \tag{2.12}$$

where $|\tau_s|$ is the shear stress at failure on a fault, c is a constant, μ is the coefficient of friction that supports the stresses in the upper crust, and σ_n is the total normal stress with sign convention such that positive σ_n indicates tension. Since the simplest expression for the effective normal stress, σ_n' , is written as $\sigma_n' = \sigma_n - \sigma_p$, we then define λ as the ratio of pore pressure, σ_p, to lithostatic stress, σ_n, in the crust [*Hubbert and Rubey*, 1959; *Sibson*, 1974; *Sonder and England*, 1986]. Cohesion is thought to be small on faults [*Sibson*, 1974; *Bird and Kong*, 1994] so c is set to zero. Thus the Coulomb frictional-failure criterion reduces to

$$|\tau_s| = -\mu\sigma_n' = -\mu\sigma_n(1 - \lambda), \tag{2.13}$$

which adequately approximates Byerlee's [1978] curve for frictional strength associated with rocks of the brittle crust if $\mu \approx 0.75$ [*Sibson*, 1982, 1984]. In addition, for actively deforming regions we define the depth integrated strength on the faults within seismogenic crust down to the brittle-ductile transition, F_{BC}, as

$$F_{BC} = \int_{-h}^{L} (\sigma_1 - \sigma_3) dz, \tag{2.14}$$

where BC is the thickness of the brittle crust above the brittle-plastic transition and σ_1 and σ_3 are the maximum and minimum principal total stresses for the brittle crust. In order to make use of equation (2.14) we need to identify fault styles associated with our long-term depth integrated deviatoric stress field solution, since Byerlee's law predicts differential stress and shear stress magnitudes that vary as a function of tectonic regime [*Brace and Kohlstedt*, 1980].

2.4.1 Accounting for fault styles

Anderson [1951] showed how styles of faulting in the upper crust relate to relative principal stress magnitudes and principal stress directions, concluding it reasonable to assume one principal stress direction is nearly vertical with depth allowing for the three major geologic fault types to be related to tectonic regimes. The assumption *Anderson* [1951] made regarding the expected orientation of the principal stress directions is reasonable since earth's surface is a free surface, and thus one principal stress direction must be in the direction normal to that free surface at the free surface itself [*Jaeger and Cook*, 1976]. Furthermore, τ_{xz} and τ_{yz} are generally so much smaller than σ_{zz} that one principal axis of deviatoric stress is effectively zero and therefore one principal axis is effectively vertical throughout the seismogenic layer. Our thin sheet modeling approach regards depth integrated principal stress directions within the seismogenic layer as vertical and horizontal, allowing us to equate principal deviatoric stress styles with pure fault styles. However, in such cases we do not impose a plane-strain or plane-stress constraint, but instead define $\overline{\tau}_{xx} + \overline{\tau}_{yy} = -\overline{\tau}_{zz}$. Consequently, the long-term total depth integrated deviatoric stress field solution shown in Figure 2.9 contains tensor styles that in some places do not represent either pure dip-slip or pure strike-slip deformation. Instead, in such areas all principal axes may be non-zero and of unequal length. One possible parameterization is to explicitly partition the deformation for these cases into a combination of pure dip-slip and pure strike-slip. We feel, however, that such a treatment of mixed styles may make the model overly complicated in terms of defining fault strength or fault friction in a given area. Therefore, we simplify the approach and make an approximation by grouping fault styles associated with the long-term vertically integrated deviatoric stress field into one of three pure tectonic fault regimes (i.e., normal, strike-slip, or thrust). The delineation of discrete styles is obtained through normalization of the horizontal principal axes, $\overline{\tau}_{xx}$ and $\overline{\tau}_{yy}$, of the long-term depth integrated deviatoric

stresses using

$$\mathcal{A}_o = \frac{\overline{\tau}_{xx} + \overline{\tau}_{yy}}{\sqrt{\overline{\tau}_{xx}^2 + \overline{\tau}_{yy}^2}}. \tag{2.15}$$

Values possible for $\mathcal{A}_o$ (see second column of Table 2.2) must fall between pure compression, $-\sqrt{2}$, and pure extension, $+\sqrt{2}$. The actual value of $\mathcal{A}_o$ allows us to infer the relative magnitudes and signs of the three long-term principal deviatoric stresses and to assign each grid area a pure fault style. It is important to note that the fault styles inferred here refer to the expected style of deformation associated with faults that are close to failure or that have failed within the seismogenic crust over the long term, such as those regions shown in Figure 2.4). In contrast, for regions of very low strain rate, fault styles are poorly constrained because such zones are not expected to fail, and may not have failed over the longer-term.

The long-term fault styles determined for the case of a seismogenic crust extending from the surface to a uniform depth 20 km below sea level are shown in Figure 2.10. Normal faulting dominates the seismogenic crust of the Basin and Range in Nevada, western Utah, southern Idaho, and southeastern Oregon. The strike-slip fault styles that govern the deformation within areas of southern and eastern California indicate small components of both crustal extension and contraction during seismogenic failure. The seismogenic crust within and to the west of California's Central Valley is defined by thrust styles of faulting, mixed with strike-slip styles of faulting, indicating that the crust accommodates modest amounts of compression there during failure. This region of coastal California contains the San Andreas system, which is likely anisotropic in behavior. That is, the mixed thrust and strike-slip style of faulting predicted there (Figures 2.9, 2.10), with long-term principal axes of compression at a high angle to the strike of the San Andreas fault, is not necessarily a poor prediction. Rather, the fault is likely weak in the direction of slip [*Mount and Suppe*, 1987; *Zoback et al.*, 1987]. Fault styles associated with thrust faulting are found in a

distinct band to the west of western North America's plate margin running parallel with the Northern Mexican coast through the Mendocino Triple Junction.

2.4.2 Equating long-term depth integrated stress differences with depth integrated fault strength

The value of $\mathcal{A}_o$ allows us to determine which of the three vertically integrated principal stress directions is vertical, enabling us to equate the long-term depth integrated stress differences with fault strength. The principal assumption here is that volumes of seismogenic crust that are actively deforming have long-term depth integrated stress differences that are equal to the long-term depth integrated strength of the faults within the seismogenic crust. Therefore, to quantify the depth integrated fault strength of the seismogenic crust we depth integrate equation (2.13). The solution to the integrated form of equation (2.13) is equated to equation (2.14) and is solved on the basis of the assigned pure fault style determined from (2.15). We also employ the relations $\overline{\sigma}_{ij} = \overline{\tau}_{ij} + (\overline{\sigma}_{zz} - \overline{\tau}_{zz})\delta_{ij}$ and $\overline{\tau}_{zz} = -(\overline{\tau}_{xx} + \overline{\tau}_{yy})$, such that we define the depth integrated strength of the faults within the seismogenic crust associated with normal faulting by,

$$\begin{aligned} \int_{-h}^{L}(\sigma_1 - \sigma_3)dz &= (\overline{\sigma}_{xx} - \overline{\sigma}_{zz}) \\ &= \int_{-h}^{L}\Big[\frac{-2\mu\sigma_{zz}(1-\lambda)}{\sqrt{\mu^2+1}+\mu}\Big]dz \\ &= 2\overline{\tau}_{xx} + \overline{\tau}_{yy}, \end{aligned} \tag{2.16}$$

thrust faulting by,

$$\begin{aligned} \int_{-h}^{L}(\sigma_1 - \sigma_3)dz &= (\overline{\sigma}_{zz} - \overline{\sigma}_{xx}) \\ &= \int_{-h}^{L}\Big[\frac{-2\mu\sigma_{zz}(1-\lambda)}{\sqrt{\mu^2+1}-\mu}\Big]dz \end{aligned}$$

$$= -2\overline{\tau}_{xx} - \overline{\tau}_{yy}, \tag{2.17}$$

and strike-slip faulting by,

$$\begin{aligned} \int_{-h}^{L}(\sigma_1 - \sigma_3)dz &= |\overline{\sigma}_{xx} - \overline{\sigma}_{yy}| \\ &= \int_{-h}^{L}\Big[\frac{-2\mu\sigma_{zz}(1-\lambda)}{\sqrt{\mu^2+1}}\Big]dz \\ &= \overline{\tau}_{xx} - \overline{\tau}_{yy}, \end{aligned} \tag{2.18}$$

where $\overline{\sigma}_{xx}$, $\overline{\sigma}_{yy}$, and $\overline{\sigma}_{zz}$ are the long-term depth integrated principal stresses, known from our dynamic solution (see Table 2.2). Long-term depth integrated fault strength magnitudes, defined from the surface down to a depth of 20 kilometers below sea level, range from $0.05 - 1.4\ x\ 10^{12}\ \mathrm{N \cdot m^{-1}}$ (Figure 2.11). Discretization of the long-term principal horizontal deviatoric stresses through use of equation (2.15) into single pure faulting styles dictates that the depth integrated strength magnitudes associated with non-pure dip-slip or non-pure strike-slip cases (constrained by tensor styles of principal strain rate) are themselves first-order approximations of the true long-term depth integrals of strength. However, as mentioned above the bulk of the regions fall into styles of deviatoric stress that correspond to styles of faulting very close to the pure end-member cases of strike-slip, normal, and thrust (Figure 2.9). Errors in predicted fault strength may also occur within regions where anisotropic behavior between stress and strain are predominant, such as along the San Andreas fault system. Our dynamic model predicts thrust faulting styles along the San Andreas fault from northern California to the Big Bend portion of fault in southern California (see Figures 2.9 and 2.10). Therefore, in those locations we may over estimate the long-term depth integrated fault strength and the long-term level of friction on the faults within that volume of seismogenic crust.

2.4.3 Long-term depth integrated friction coefficients

Direct estimates of pore pressures and friction coefficients from deep boreholes within the uppermost crust are scarce in location and rarely are made below five kilometers depth [*Hubbert and Rubey*, 1959; *Townend and Zoback*, 2000; *Zoback and Townend*, 2001]. However, the widespread occurrence of hydrostatic and suprahydrostatic pore pressure within the deforming crust is expected [*Sibson*, 1990b; *Zoback and Townend*, 2001]. The most direct way of establishing the long-term coefficients of friction from our dynamically constrained depth integrated strength magnitudes of the faults is to assume that the vertically integrated long-term ratio of pore pressure to lithostatic stress, $\overline{\lambda}$, does not vary along fault planes throughout the entire seismogenic layer considered. Using equations (2.16), (2.17), and (2.18) the long-term depth integrated coefficient of friction is for normal faulting,

$$\overline{\mu} = \sqrt{\frac{(2\overline{\tau}_{xx} + \overline{\tau}_{yy})^2}{4[\overline{\sigma}_{zz}^2(1-\overline{\lambda})^2 + (2\overline{\tau}_{xx} + \overline{\tau}_{yy})\overline{\sigma}_{zz}(1-\overline{\lambda})]}}, \tag{2.19}$$

for thrust faulting,

$$\overline{\mu} = \sqrt{\frac{(-2\overline{\tau}_{xx} - \overline{\tau}_{yy})^2}{4[\overline{\sigma}_{zz}^2(1-\overline{\lambda})^2 + (2\overline{\tau}_{xx} + \overline{\tau}_{yy})\overline{\sigma}_{zz}(1-\overline{\lambda})]}}, \tag{2.20}$$

and for strike-slip faulting,

$$\overline{\mu} = \sqrt{\frac{(\overline{\tau}_{xx} - \overline{\tau}_{yy})^2}{4\overline{\sigma}_{zz}^2(1-\overline{\lambda})^2 - (\overline{\tau}_{xx} - \overline{\tau}_{yy})^2}}. \tag{2.21}$$

The long-term friction coefficients, $\overline{\mu}$, do not exceed values of 0.14 for long-term dry conditions ($\overline{\lambda} = 0.0$). If the pore pressure level is approximated as long-term 'hydrostatic' ($\overline{\lambda} = 0.4$) within the 20 km thick seismogenic layer (Figure 2.12a), then the long-term coefficients of friction are all generally less than 0.20. Long-term friction coefficients are significantly lower ($\overline{\mu} < 0.12$) throughout the Basin and Range and much

of California. These long-term friction coefficient estimates are meaningful where active faults since 750,000 years are concentrated (Figure 2.1b). Within such regions, long-term friction coefficients of ~ 0.1 are found within the San Andreas fault system in California, central Nevada, and the Wasatch fault system from Southern Utah into Yellowstone and eastern Idaho. Relatively low long-term friction coefficients are found within the Lake Meade region of northwestern Arizona, northwestern Nevada, and southern Oregon. Overall, these long-term friction coefficients are much lower than the friction coefficients measured by Byerlee [1978] in the laboratory for rocks typical of the brittle upper crust. The long-term coefficients of friction obtained for long-term 'wet' ($\overline{\lambda} = 0.7$) 20 km thick seismogenic crust (Figure 2.12b) rarely exceed values of 0.30 on land and remain far below accepted 'Byerlee-like' friction coefficient values found for typical upper crustal rocks. Only when long-term pore pressures within the seismogenic crust reach levels approaching lithostatic stress magnitudes do long-term friction coefficients become reconcilable with laboratory results for most upper crustal rock types.

2.5 Sensitivity

We have limited our depth integration of the 3-D force-balance equations to a uniform base of 20 km below sea level. We now test the sensitivity of our long-term friction estimates to cases of deeper depth integration. We determine eight different solutions for depth integrated deviatoric stress where the maximum depth of integration is increased in steps of 5 km. All eight solutions gave good matches to the deformation indicators, similar to the solution for the 20 km thick layer (see Table 2.3).

The results of our sensitivity tests are shown as a function of maximum depth of integration along three vertical cross-sections. Each of the three cross-sections tran-

sect through the diffuse plate boundary zone of deformation (see Figure 2.2). Figure 2.13 shows the long-term depth integrated fault strength for all eight layers tested along the three transect lines. We find that long-term depth integrated fault strength magnitudes within the Basin and Range do not steadily increase with each increase in depth below 20 km. Instead there is a diminishing increase in depth integrated strength for depths greater than 20 km. Long-term depth averages of fault strength within the Basin and Range (Figure 2.14) clearly decline with increasing depth of integration. This is consistent with sharply reduced long-term depth integrated fault strength with increasing depth in those regions of the Basin and Range. However, long-term depth averages of crustal strength remain nearly constant just outside of the plate boundary zone, in areas where strain rates are much lower (Figure 2.4). Figures 2.15a,b,c show that when the maximum depth of integration is at or below 20 kilometers below sea level, the decrease in long-term depth integrated friction coefficient values becomes less sensitive to increases in maximum depth of integration. This result, suggests that most of the long-term strength for faults of the crust within the diffuse plate boundary zone of western North America is located in the upper 20 km of the seismogenic crust.

2.6 Discussion

Our most reliable long-term depth integrated fault strength and friction coefficient estimates are in areas well-covered by Quaternary fault slip-rate observations (Figure 2.1b). Such areas correspond to most of the Basin and Range and California (Figure 2.4). We find that within the Basin and Range depth averages of fault strength decline with increasing depth of integration. The largest drops in long-term depth averaged strength occurs when maximum depth of integration extends only as deep as 10 km below sea level (see Figure 2.13). This may imply that peak long-term differential

stresses occur in the shallow upper crust ($\leq$ 15 km) within the Basin and Range, consistent with thicknesses found in models of effective elastic thickness for the region [e.g., *Lowry and Smith*, 1995; *Lowry et al.*, 2000; *Puskas et al.*, 2007].

Observations of strain within the Great Basin region of western U.S. show that deformation since 750,000 years ago has been relatively distributed across the Great Basin region (Figure 2.1b). However, present-day strain rates, constrained by GPS observations, are concentrated in western Great Basin and along eastern edge of Basin and Range along the Wasatch Fault zone [*Thatcher et al.*, 1999; *Bennett et al.*, 2003; *Hammond and Thatcher*, 2004, 2005; *McCaffrey*, 2005]. Central and eastern Nevada and westernmost Utah are characterized by much lower strain rates (see Figure 2.4). The disparity between present-day Great Basin strain rate distributions and the more distributed distribution of ruptures since 750,000 years suggests that deformation must migrate spatially over time [e.g., *Wallace*, 1984].

Relatively concentrated strain rates in parts of the Basin and Range may be enhanced by transient strain rate phenomenon. Viscoelastic studies indicate that transient behavior constitutes a viscous coupling between elastic upper crust and straining visous lower crust and upper mantle that causes concentrations of strains in regions of past crustal earthquakes [e.g., *Dixon et al.*, 2000, 2003; *Hetland and Hager*, 2004]. Concentrations of strain rates in regions such as western Nevada [*Hetland and Hager*, 2004] are thus not an artifact of strong lateral strength heterogeneity within the crust. Instead, these concentrations must come from transient stress heterogeneity that is associated with the transient viscous coupling between crustal seismogenic layer and viscoelastic lower layer [e.g., *Pollitz and Vergnolle*, 2006]. Given that stress transients might govern where failure occurs, our steady state deviatoric stress field estimates, and the long-term friction coefficients obtained from them, may represent a minimum estimate. Estimates of such stress transients can be obtained by integrating the transient surface displacements in the vicinity of fault rupture during an entire

seismic cycle. Maximum time integrated transient surface displacements, based on calculations by *Hetland and Hager* [2004], are of the order of one half of the fault displacement in the previous rupture. This would imply a maximum transient stress accumulation during one seismic cycle of one half the stress drop. For a stress drop of 3 MPa the depth integrated stress transient would be about 3 x 10^{10} N $\cdot$ m^{-1} within a 20 km thick seismogenic layer. This is about 10% of the depth integrated long-term deviatoric stress magnitudes that we have calculated for the seismogenic portion of the crust. Therefore, our estimates of long-term friction from the steady-state deviatoric stress magnitudes may not be grossly underestimated.

In our models we do not evaluate the long-term frictional strength of the country rock of the crust. At a minimum, the country rock may be only slightly frictionally stronger than the faults within the crust. However, we place no upper bound on the frictional strength of the country rock and speculate that the frictional properties outside shear zones may be Byerlee-like. We obtain long-term depth integrated friction coefficients that are far less than those reported in rock mechanics studies under dry conditions for most upper crustal rock types [e.g., *Byerlee*, 1978]. Low long-term friction coefficients with respect to those cited by *Byerlee* [1978] are thought to arise from intrinsic and/or dynamic weakening mechanisms capable of lowering shear resistance on faults during the earthquake rupture process and the seismic cycle in general [e.g., *Di Toro et al.*, 2004]. For instance, results from ring shear experiments on halite-muscovite mixtures led to microphysical models that predict differential strength reduction in the upper crust by as much as 50 – 70% [*Bos and Spiers*, 2001, 2002; *Niemeijer and Spiers*, 2005]. Experiments by *Numelin et al.* [2007] on natural fault gouge samples from a low-angle normal fault in southeastern California discriminate between weak fault gouge found for samples with greater than 50 wt% clay content versus samples consistent with Byerlee's law that contained less than 50 wt% clay content. *Tembe et al.* [2006] measured the frictional properties of drill cuttings and

core extracted from the San Andreas Fault Observatory at Depth (SAFOD) scientific borehole and found low friction coefficients ($\mu = 0.4 – 0.55$) on alteration minerals at approximately 2.5 and 3.0 km depth. The presence of these two weak shear zones at depth is consistent with and may partially explain the apparent weakness of the San Andreas Fault [*Tembe et al.*, 2006]. More recently, slightly lower friction coefficients ($\mu = 0.3 – 0.5$) on hand selected clay-rich drill cutting separates from the SAFOD scientific borehole were measured by *Morrow et al.* [2007].

Examination of ancient exposures of mid-crustal fault cores in geologic studies and results from deformation experiments on material with qualities that closely match fault rocks suggest the existence of a broad frictional-viscous regime in the upper crust [*Handy and Brun*, 2004; *Holdsworth*, 2004; *Jefferies et al.*, 2006]. For instance, the rich presence of quartz-mica phyllonites in the middle to upper crust of continental faults zones may indicate activation of fluid assisted deformation mechanisms at lower differential stress than that predicted by Byerlee's law [*Janecke and Evans*, 1988; *Stewart et al.*, 2000; *Imber et al.*, 2001; *Jefferies et al.*, 2006]. Long-term weakening of the fault zone itself may be the result of fault reactivation [*Holdsworth et al.*, 2001; *Holdsworth*, 2004; *Edwards and Ratschbacher*, 2005] or thermomechanical feedback effects [*Regenauer-Lieb et al.*, 2006].

Our models indicate that long-term friction on faults is very low even if long-term fault zone pore pressures are elevated well above hydrostatic conditions. These results corroborate other thin-plate dynamic modeling efforts. For instance, *Bird and Kong* [1994] computed fault friction coefficients of 0.17 for a best-fit thin-plate finite element model of major faults within California. This low friction result was obtained with a model constrained to match geologic, geodetic, and stress data with no shear tractions at the base of the crust. *Bird and Kong* [1994] also included mantle shear tractions in their models. They found values of μ ranged between 0.17 and 0.25 and concluded that all faults in their model region are weak. Slightly lower friction results ($\mu <$

0.15) were found on faults within the San Francisco Bay area by *Geist and Andrews* [2000]. These authors used the modeling technique developed by *Bird and Kong* [1994] and more recently obtained geophysical data sets to look at the San Francisco Bay fault network in greater detail. *Parsons* [2002] used long-term fault slip behavior and finite element modeling of a three layer lithosphere to obtain friction coefficients comparable to those obtained by *Geist and Andrews* [2000]. These authors used the modeling technique developed by *Bird and Kong* [1994] and more recently obtained geophysical data sets to look at the San Francisco Bay fault network in greater detail. *Parsons* [2002] used long-term fault slip behavior and finite element modeling of a three layer lithosphere to obtain friction coefficients comparable to those obtained by *Geist and Andrews* [2000].

Average differential stress in the upper crust, as quantified by *Fialko et al.* [2005] using topographic and strike variations along the San Andreas fault, produced estimates of effective fault strength that are a factor of two lower than frictional strength estimates predicted by Byerlee's law under hydrostatic pore pressure conditions. *Fay and Humphreys* [2006] predict effective friction coefficients between 0.10 – 0.21 given a brittle-ductile transition at depths from 15 to 30 km below sea level based on balance of forces and torques associated with GPE variations, tectonic loading, and basal tractions acting on the Salton block. *d'Alessio et al.* [2006] use models of heat flow to constrain the apparent coefficients of friction to be about 0.1 along the creeping section of the San Andreas fault. These models combine slip rates, displacement histories, and asperity sizes to a depth of 15 km to compare modeled surface heat flow patterns with existing measurements. We predict long-term depth integrated friction coefficients on faults ranging from 0.10 – 0.15 for the Salton Block area, from 0.13 – 0.19 for the San Francisco Bay area, and from 0.12 – 0.16 for the creeping section of the San Andreas fault using depth integration extending from the surface to 15 km below sea level under long-term hydrostatic pore pressure conditions.

2.7 Conclusions

We have used a geodynamic approach to quantify the long-term absolute magnitudes of depth integrated deviatoric stress for the seismogenic layer in western North America. We exploited seismic velocity profiles to define density structure throughout the seismogenic layer. The absolute magnitude of depth integrated deviatoric stresses associated with gravitational potential energy differences calibrate the total depth integrated deviatoric stress magnitudes acting within the seismogenic layer. Inferences on long-term deformation patterns provide constraints on the needed depth integrated boundary condition solution; together, the boundary condition solution and the GPE differences solution provide robust estimates of the magnitude of the long-term depth integrated deviatoric stresses acting within the seismogenic layer. We have used these absolute magnitudes of depth integrated deviatoric stress to infer the long-term depth integrated fault strength of the seismogenic crust.

Our dynamic models estimate long-term depth integrated friction coefficients on faults within the diffuse plate boundary zone of western North America that are far less than those obtained for most upper crustal rock types sampled in the laboratory. Dynamic weakening during large slip and/or intrinsic weakening of fault core material due to repeated fault reactivation may be fundamental processes that promote the progress of finite strain within the brittle seismogenic layer in the presence of the relatively low values of long-term vertically integrated stress differences present in the crust.

2.8 Appendix A:

Recall that we argue that the absolute magnitude of deviatoric stresses associated with GPE differences calibrates the absolute magnitude of the long-term deviatoric stress field. This is particularly true for cases where contributions to deviatoric stress

related to GPE differences are comparable to contributions from stress boundary conditions. We will investigate whether our inversion methodology can retrieve the absolute magnitudes of deviatoric stress, as well as the stress tensor style, using synthetic dynamic solutions generated in forward dynamic models. We investigate two cases: one where the faults within the crust are low friction of $\overline{\mu} = 0.1$, and one where faults have higher, Byerlee-type, friction of $\overline{\mu} = 0.75$. We show that for weak fault case the effects of GPE differences are approximately equal to effects of boundary conditions and that we recover stress magnitudes and tensor styles exactly. For the strong fault case, however, we show that the boundary conditions dominate over the influence of GPE differences. For this case we recover the tensor field almost exactly, but manage to recover only 70% of the absolute magnitudes of stress. Nevertheless, the recovered stress magnitudes are significantly larger than in the weak fault case.

We use the forward model methodology of *Flesch et al.* [2001], and apply it to the thickness of the long-term seismogenic crust. We define the internal body force distributions (GPE per unit area), velocity boundary conditions, and lateral variations in depth integrated effective viscosity, from the surface to 20 km below sea level. The depth integrated effective viscosities are defined by the friction on the faults, not the strength of the regions between the faults. As in *Flesch et al.* [2001] we minimize the functional,

$$\Theta(v) = \int\int_s [D - v_\alpha f_\alpha]\, dxdy, \tag{2.22}$$

where f_α, is the body force term associated with gradients in gravitational potential energy per unit area, v_α is the velocity, and D is the dissipation potential, which provides a solution to the force balance equations. *Flesch et al.* [2001] show that the dissipation potential depends on the strain rates, on the value of the rheological parameter B, and the power law exponent n,

$$D = \frac{n}{n+1} B(\dot{\epsilon}_{\alpha\beta}\dot{\epsilon}_{\alpha\beta} + \dot{\epsilon}_{\gamma\gamma}\dot{\epsilon}_{\gamma\gamma})^{\frac{n+1}{2n}}), \tag{2.23}$$

where $\dot{\epsilon}_{\gamma\gamma} = (\dot{\epsilon}_{xx} + \dot{\epsilon}_{yy}) = -\dot{\epsilon}_{zz}$.

We estimate values of the depth integrated effective viscosity, B, for the seismogenic crust, [*England and McKenzie*, 1982; *Sonder and England*, 1986] for a given element by

$$B = \frac{T}{E^{\frac{1}{n}}}, \tag{2.24}$$

where E, and T, the second invariants of strain rate and stress respectively, are defined in equation 2.11 of the main text. T and therefore B is defined by the fault strength, F_{BC} by equations (2.16), (2.17), and (2.18) in the main text. We simplify the B value distribution by allowing variations in T that are only a function of fault style, friction, and pore pressure. The discretization of the fault types per grid area into one of three pure fault styles (i.e., thrust, normal, or strike-slip) per grid area, as inferred from the long-term kinematic model shown in figure (2.4), yields the T value distribution we use to define B values. For all three cases of pure fault style:

$$T = \frac{F_{BC}}{\sqrt{2}}. \tag{2.25}$$

We define both a frictionally weak and a frictionally strong long-term hydrostatic (λ = 0.4) seismogenic crust. For the weak crust, the frictional strength on the faults embedded within the layer are uniformly low ($\overline{\mu} = 0.1$), whereas for the strong crust the frictional strength is Byerlee-like ($\overline{\mu} = 0.75$) on the same set of faults.

We test the two forward models with the B values thus defined using power law exponent, n=1, input depth integrals of vertical stress, $\overline{\sigma}_{zz}$ from the surface to 20 km below sea level (GPE), velocity boundary conditions, and a starting guess for strain rate from our long-term kinematic model. The depth integrals of vertical stress, $\overline{\sigma}_{zz}$, the gradients of which define the body forces, are defined with the seismic data and methods described in section (2.3.2). It is therefore the same data set of GPE used to define our actual stress field estimate for western North America.

The velocity boundary conditions are the known relative plate motions. For the forward models in this appendix, we define our velocity boundary conditions using the Pacific-North America (PA-NA) plate motion estimate of *McCaffrey* [2005], the Cocos-North America (CO-NA) and Juan de Fuca-North America (JF-NA) plate motion estimates of *DeMets et al.* [1994], and the Rivera-North America (RI-NA) plate motion estimate of *DeMets and Wilson* [1997]. For slow strain rate regions the B values are capped at a maximum value, as those low strain rate areas are unlikely to possess faults that are yielding. In addition, we spatially smooth the input B value distribution. Both of these procedures combine to dampen large order magnitude variations in B values over short lateral wavelengths. For the weak fault synthetic crust (Figure 2.16), the maximum B value is 3.05 x 10^{27} N/m $\cdot$ s. For the weak fault model, the internal buoyancies forces play an approximately equal role as the boundary conditions (Figure 2.17). Tensional deviatoric stress styles are prevalent in the central and eastern portion of the diffuse plate boundary zone, consistent with the dominant extensional faulting found there (Figure 2.17).

For the strong fault synthetic crust (Figure 2.18) the maximum B value is 6.10 x 10^{27} N/m $\cdot$ s. In the diffuse plate boundary zone, where strain rates are moderate to high, the B values for the faults of the strong crust are five to seven times larger than the B values for the same network of faults for the weak crust. For the strong fault model, the velocity boundary conditions dominate the deviatoric stress field, and the internal buoyancies play a minor role (Figure 2.19). For the strong fault model, the deviatoric stress styles are consistent with strike-slip faulting (Figure 2.19). There is also a dramatic difference east of the Juan de Fuca subduction zone for the strong fault case (Figure 2.19) in comparison with the weak fault case [*Hyndman and Wang*, 1993]. The deviatoric stress magnitudes of the strong fault model are generally five to seven times larger than those of the weak fault model, consistent with the differences in B values.

We use the strain rate output from the dynamic solution to constrain our boundary condition solution in the inverse method. Recall that we seek a stress field boundary solution that, when added to the deviatoric stresses associated with GPE differences, provides a best fit to the tensor styles embedded in the strain rate tensor solution. The deviatoric stresses associated with GPE differences for both the strong and weak models are nearly identical to one another. Therefore, differences in the tensor fields for both the strong and weak crust models arise from the different responses to boundary conditions of velocity in the two forward dynamic models. The dynamic strain rate tensor field associated with the weak fault model is dominated by pure extension in the central and western Basin and Range (Figure 2.20). On the other hand, pure extension is absent in the dynamic strain rate tensor field associated with the strong crust model (Figure 2.21).

For the case of the weak fault model, the deviatoric stress field obtained with the inverse method (Figure 2.22) and the deviatoric stress field associated with the forward dynamic solution (Figure 2.17) are near exact matches with one another in terms of magnitude, style and direction. For the case of the strong fault model, the deviatoric stress field obtained with the inverse method (Figure 2.23) provide a nearly exact match with the tensor styles from the forward dynamic model (Figure 2.21). For the strong fault model, the inverse method recovers on average, roughly 70% of the magnitude of the forward dynamic deviatoric stress field solution (Figure 2.19).

We have shown that the inversion method that we employ can distinguish between the weak fault and the strong fault cases, even though we are unable to recover the full stress magnitudes in the strong fault model. The inability to recover the full stress magnitudes for the strong fault model arises because the solution is dominated by boundary condition effects, with internal buoyancies playing a minor role in the total deviatoric stress field. That is, our inverse method optimizes the fit to the tensor styles. Because the boundary condition effects dominate, an increase in the

magnitudes of deviatoric stresses associated with the boundary conditions will not yield a significant improvement in the fit to the tensor field. Therefore, for such cases where boundary conditions dominate over the influence of internal crustal buoyancies, there is a limit in ability to recover the full deviatoric stress magnitudes. The plate boundary zone in western North America appears to be more consistent with the scenario where boundary condition effects are at parity with internal buoyancy effects. That is, for the weak fault case internal buoyancies and boundary conditions contribute approximately equally, and it yielded deformation patterns in accord with observation in the western United States (Figure 2.20). Moreover, our inverse method was able to recover the exact deviatoric stress tensor magnitudes for the weak fault case. Based on these tests, we are confident that our inverse approach is recovering the long-term magnitudes of depth integrated deviatoric stresses in the seismogenic layer of the plate boundary zone of western North America.

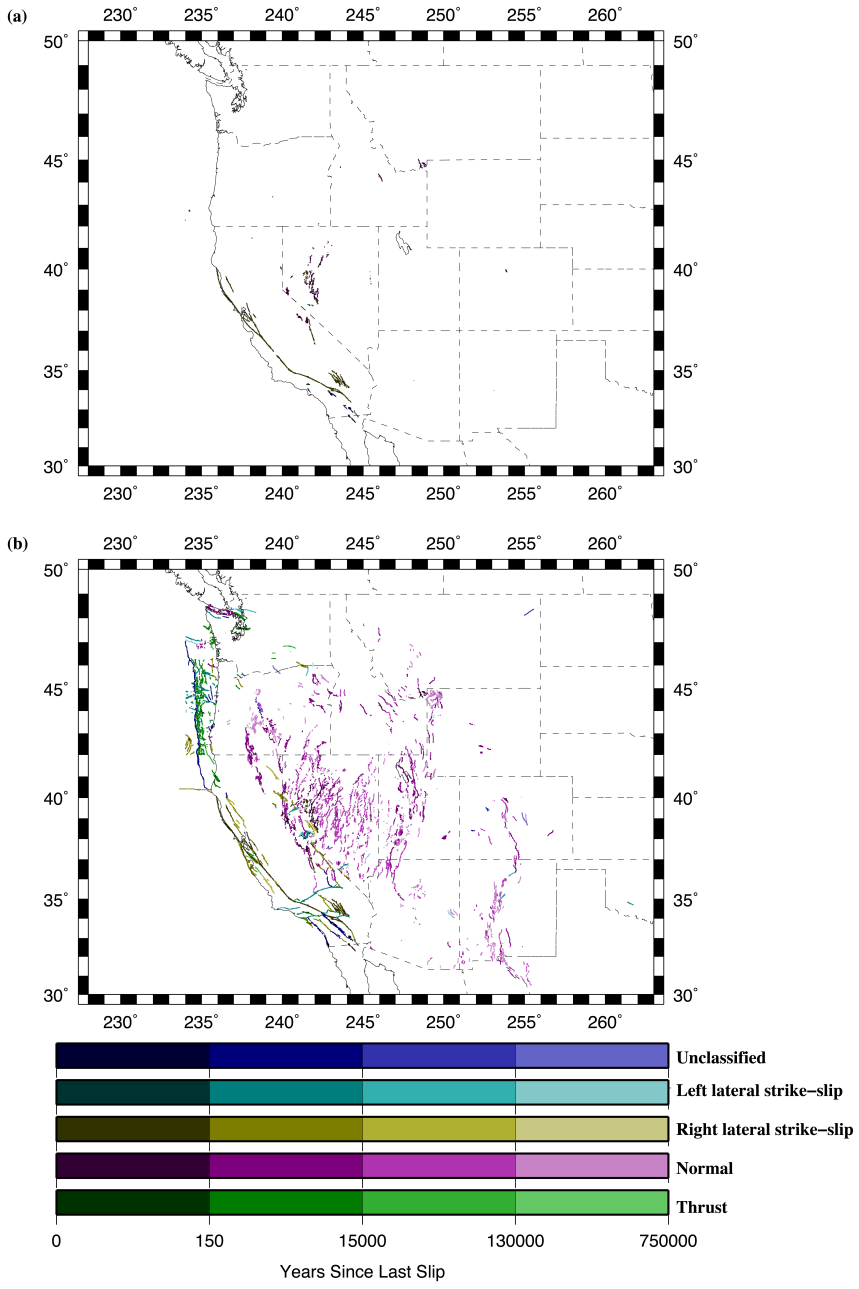

Figure 2.1: Western North America Quaternary fault data drawn as a function of fault trace, fault type, and last slip event in years before present. Fault characteristics obtained from the Quaternary fault and fold database for the United States, 2006, maintained by the United States Geological Survey (web site: http//earthquakes.usgs.gov/regional/qfaults/). (a) Distribution of historic faults to present day (b) Distribution of faults from 750,000 years ago to present day.

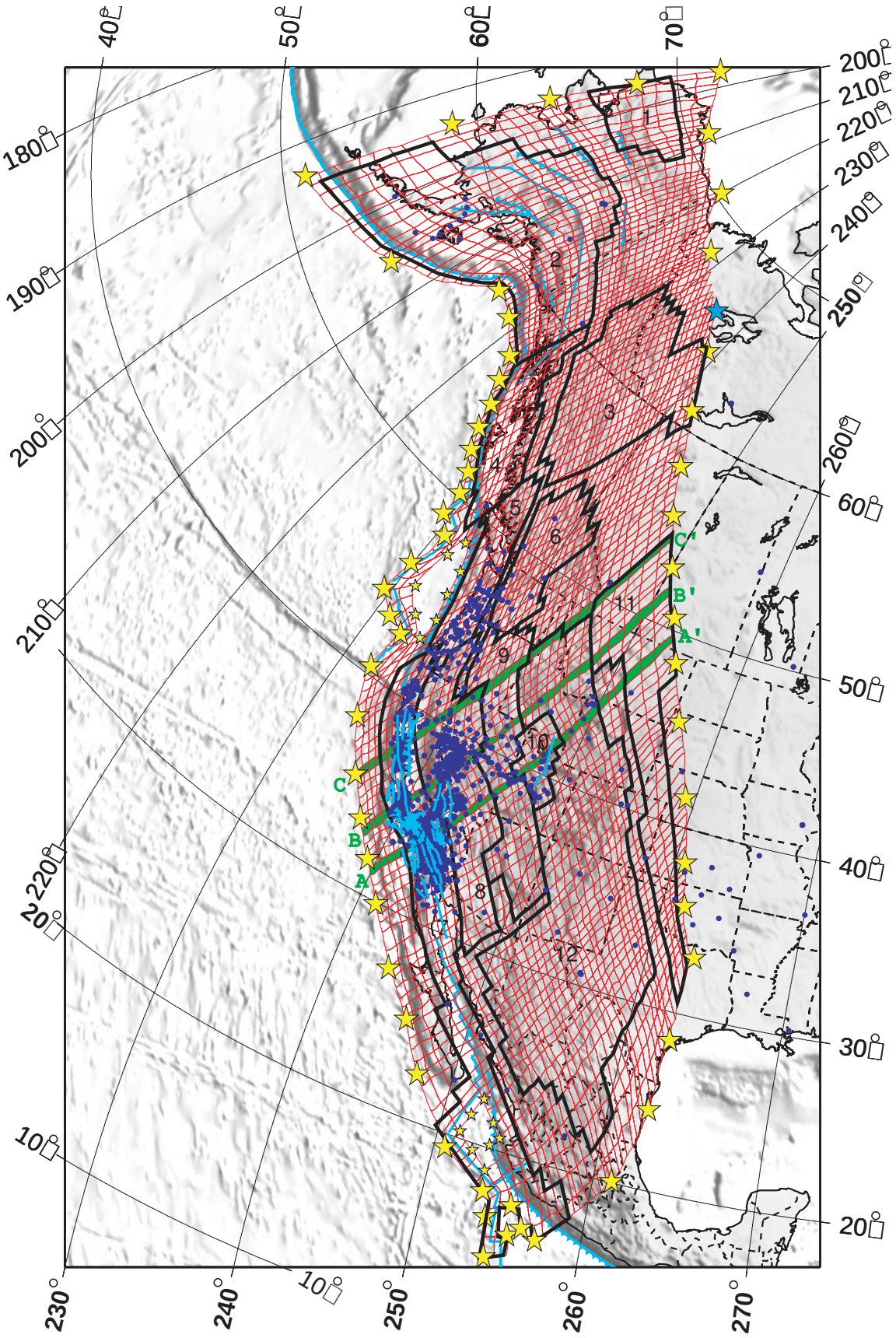
40°
50°
60°
70°
180°
190°
200°
210°
220°
200°
210°
220°
230°
240°
250°
260°
60°
50°
40°
30°
20°
10°
230°
240°
250°
260°
270°
1
2
3
4
5
6
7
8
9
10
11
12
A
B
C
A'
B'
C'

Figure 2.2: The grid (red mesh) from *Flesch et al.* [2007] used in the kinematic and dynamic modeling. In this study we have defined the Pacific, Rivera, Cocos, Juan de Fuca, and North American plates as rigid blocks. Dark blue dots represent the GPS and VLBI data [IGS; USGS; SCEC; *Sauber et al.*, 1997; *Ma and Ryan*, 1998; *Antonelis et al.*, 1999; *Bennett et al.*, 1999, 2002, 2003; *Freymueller et al.*, 1999; *Khazaradze et al.*, 1999; *Dixon et al.*, 2000; *Gan et al.*, 2000; *Lavallee et al.*, 2001; *McCaffrey et al.*, 2000; *McClusky et al.*, 2001; *Miller et al.*, 2001b, a; *Prescott et al.*, 2001; *Svarc et al.*, 2002a, b; *Oldow*, 2003; *Savage et al.*, 2004]. Quaternary fault slip rate data [*DeMets and Stein*, 1990; *Wilson*, 1993; *DeMets et al.*, 1994; *Jennings*, 1994; *Petersen and Wesnousky*, 1994; *Plafker and Berg*, 1994; *DeMets*, 1995; *Bird*, 1996; *DeMets and Dixon*, 1999; *Shen-Tu et al.*, 1999] ridge spreading rates, and long term estimates of plate motions from NUVEL-1A [*DeMets et al.*, 1994] are represented as light blue lines. Large yellow stars denote the boundary condition segments used to determine the stress field boundary conditions (see section 2.3.4 and Figure 2.8), small yellow stars denote the internal ring segments. Boundary segments are calculated relative to the fixed reference point denoted by the blue star. Numbered areas correspond to Table 2.8. Green transect lines A-A', B-B', and C-C' indicate locations of the three vertical cross sections shown in Figures 2.13 – 2.15.

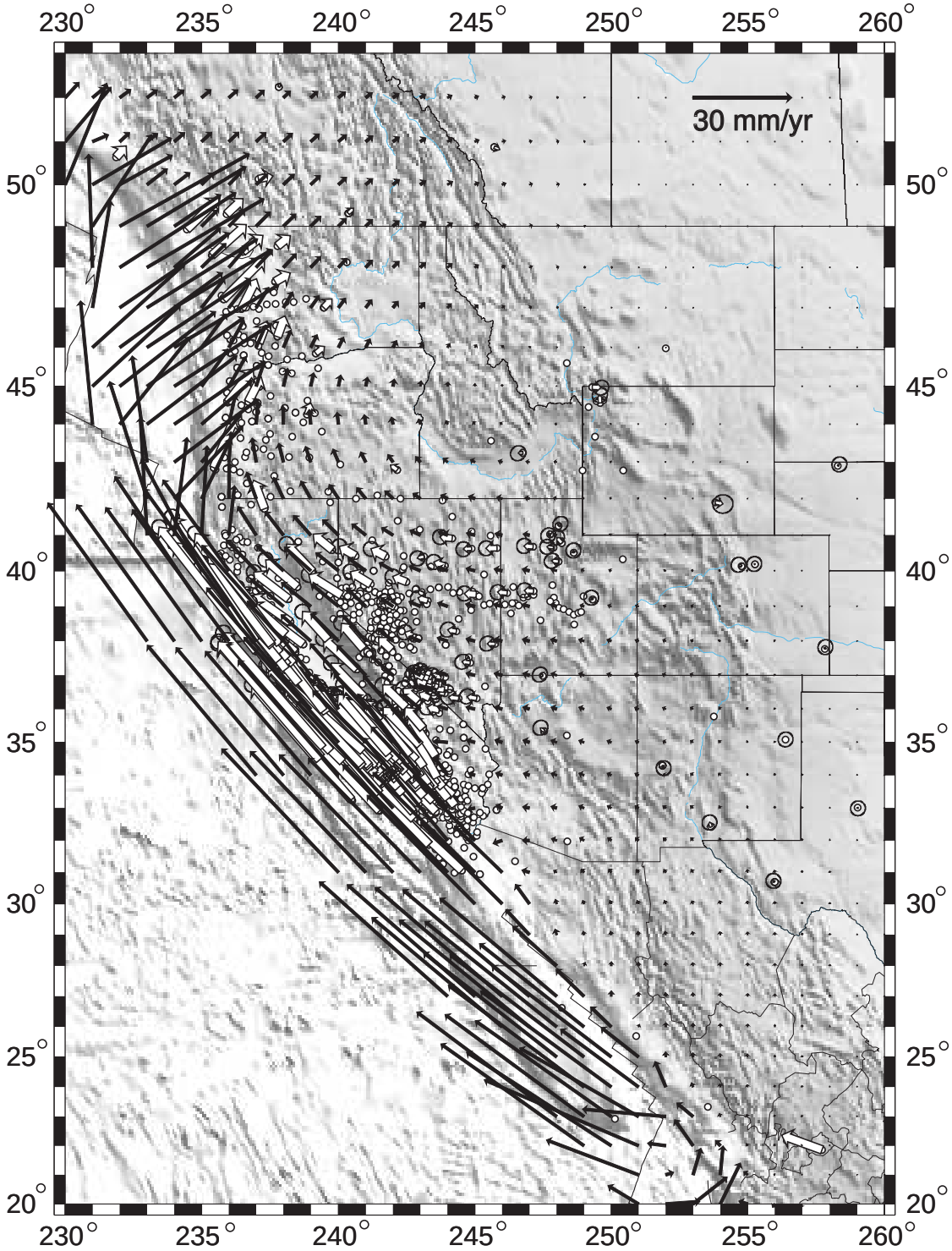

Figure 2.3: Estimate for the continuous long-term model velocity field (black vectors), along with GPS data (white vectors) from *Bennett et al.* [1999] plotted relative to a North American frame of reference. The remaining GPS and VLBI data used in this model are plotted as white dots for clarity. Error ellipses represent the 95% confidence limits.

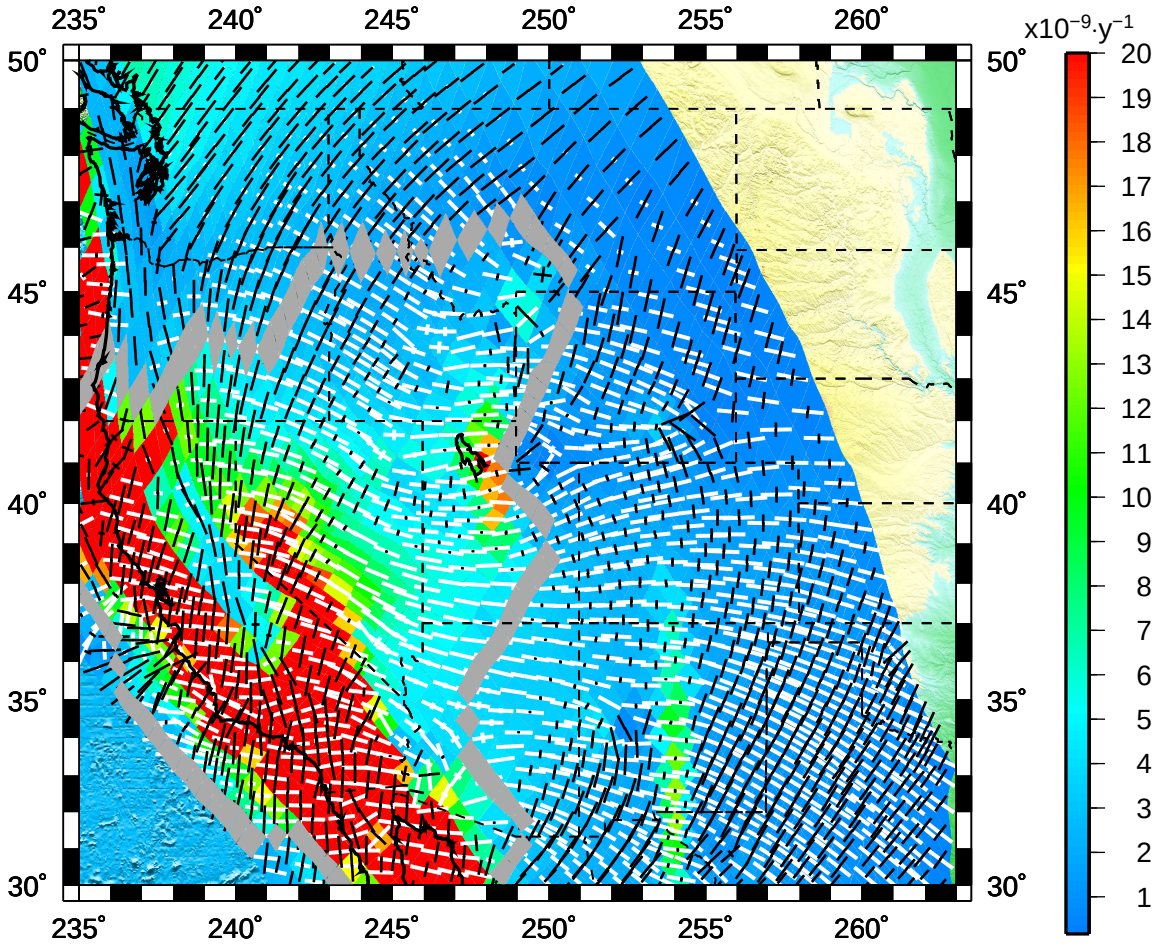

Figure 2.4: The continuous model strain rate field associated with the model velocity field in figure 2.3. Principal axes of the strain rates are plotted as unit tensors with the second invariant of strain rate plotted in the background grid. Values of 20 x 10^{-9} $\cdot$ yr^{-1} or greater are plotted in red. Areas contained within the interior of the grey boundary are locations where seismic events return over time periods of at most tens of thousands of years. White vectors represent principal axes of extensional strain rate, black vectors represent principal axes of compressional strain rate.

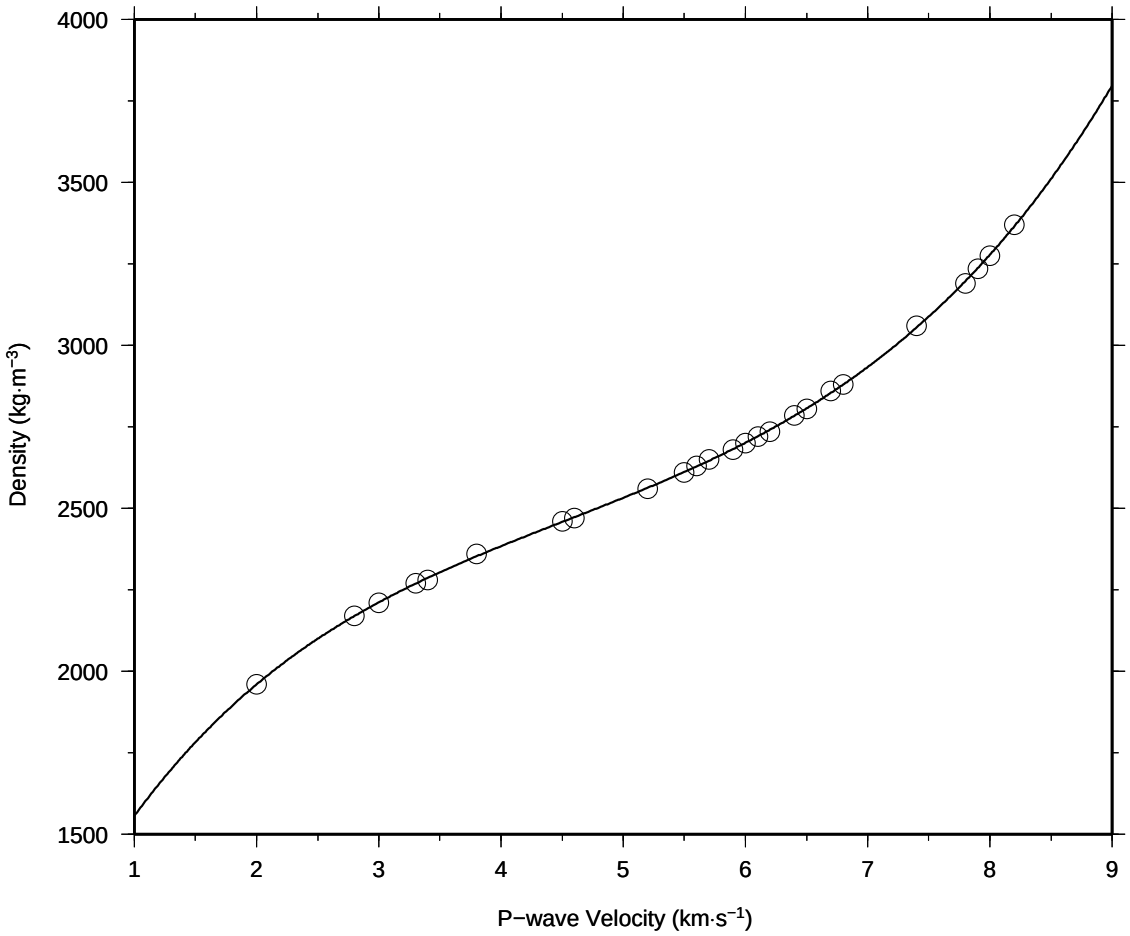

Figure 2.5: Density as a function of P-wave velocity for western North America. Open circles indicate grouped and averaged P-wave velocity and density data defined within the western U.S. Cordillera. The solid black line represents the 5^{th} order polynomial curve used to interpolate and extrapolate the seismically defined data set.

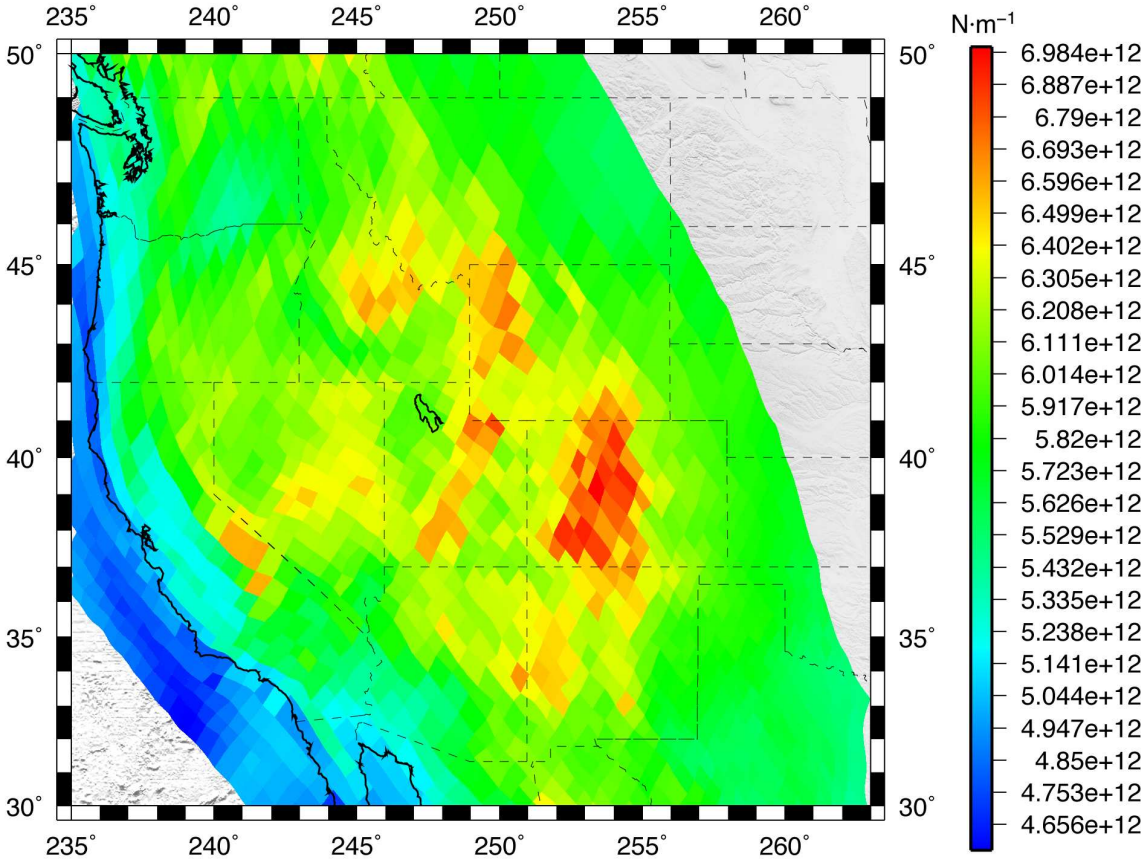

Figure 2.6: The absolute magnitudes of the depth integrated vertical stress (see equations (2.3), (2.8), and (2.9)) associated with seismically defined densities in the upper crust of western North America. Depths of integration are from the surface to a uniform depth of 20 km below sea level.

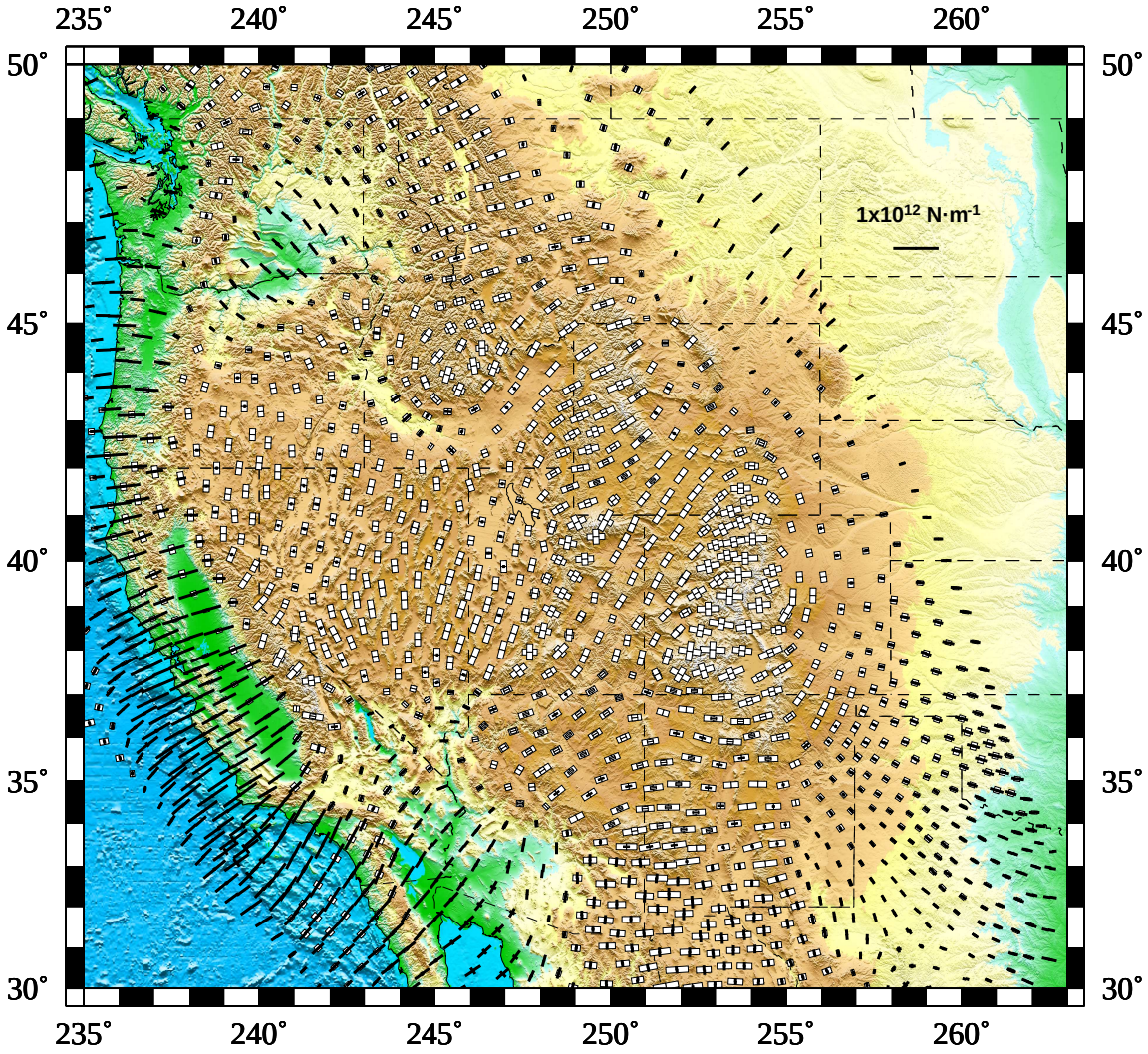

Figure 2.7: The depth integrated deviatoric stress field associated with gravitational potential energy variations in Figure 2.6. White vectors represent tensional principal axes of deviatoric stresses, black vectors represent compressional principal axes of deviatoric stresses.

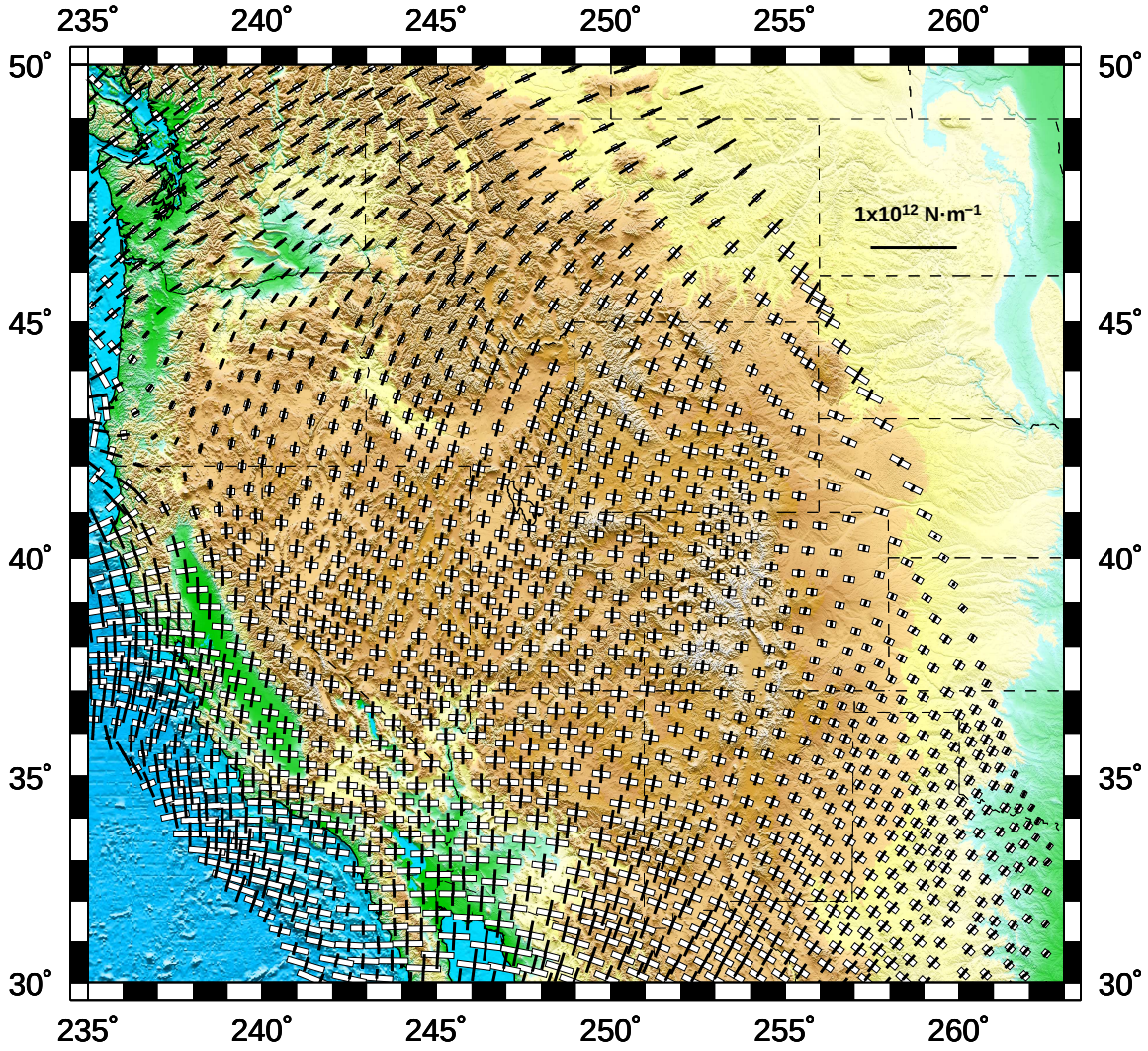

Figure 2.8: The best-fit deviatoric stress field boundary condition. This boundary condition solution is obtained through minimization of (2.11). The linear combination of basis functions, when added to the deviatoric stress field associated with GPE variations in the seismogenic crust (Figure 2.7), provides a best-fit with the long-term stress field indicators in Figure 2.4. White vectors represent principal axes of tensional deviatoric stresses, and black vectors represent principal axes of compressional deviatoric stresses.

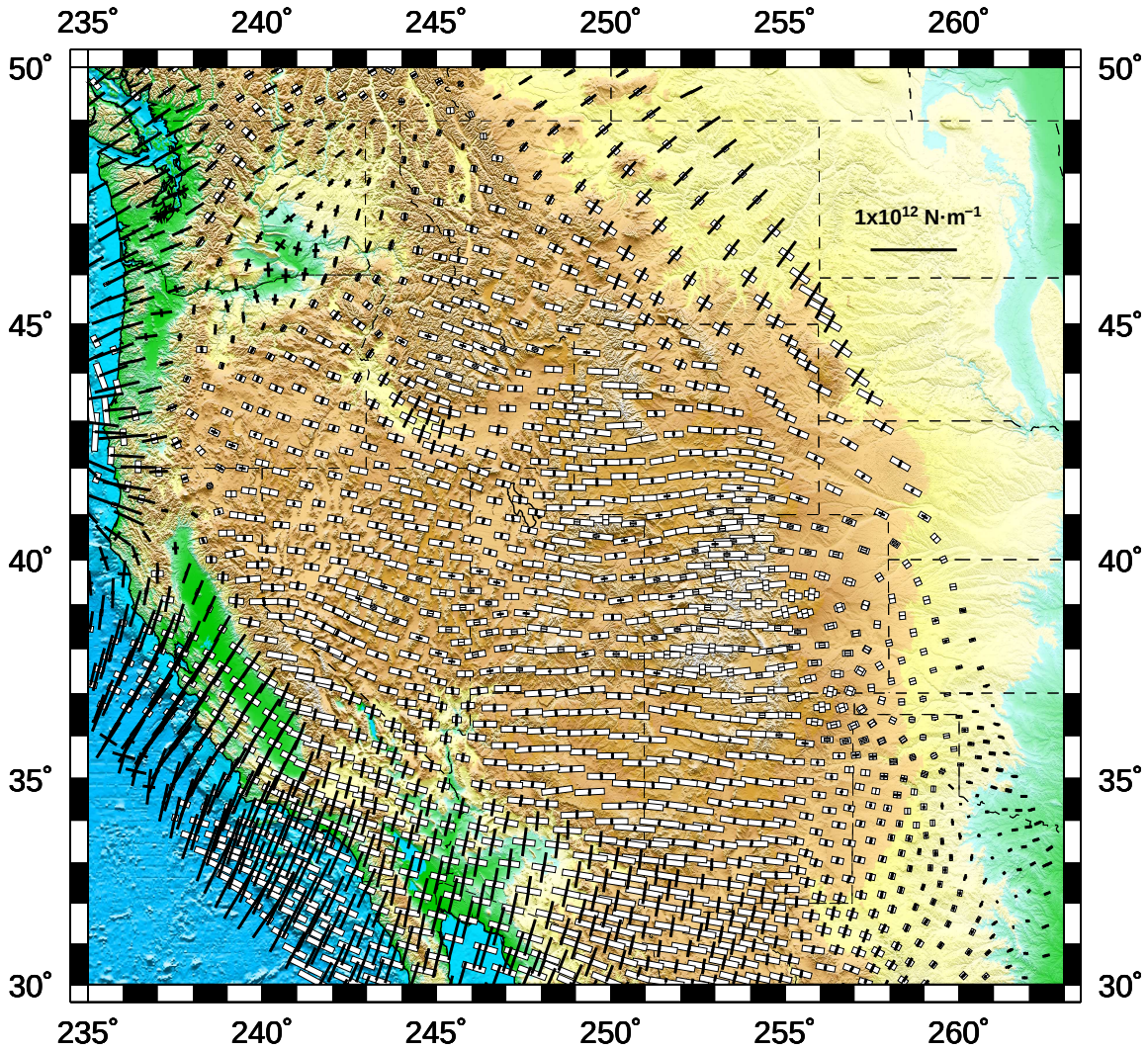

Figure 2.9: The best-fit long-term total depth integrated deviatoric stress field within a seismogenic layer extending from the surface to a uniform depth of 20 km below sea level for western North America. White vectors represent principal axes of tensional deviatoric stresses, and black vectors represent principal axes of compressional deviatoric stresses.

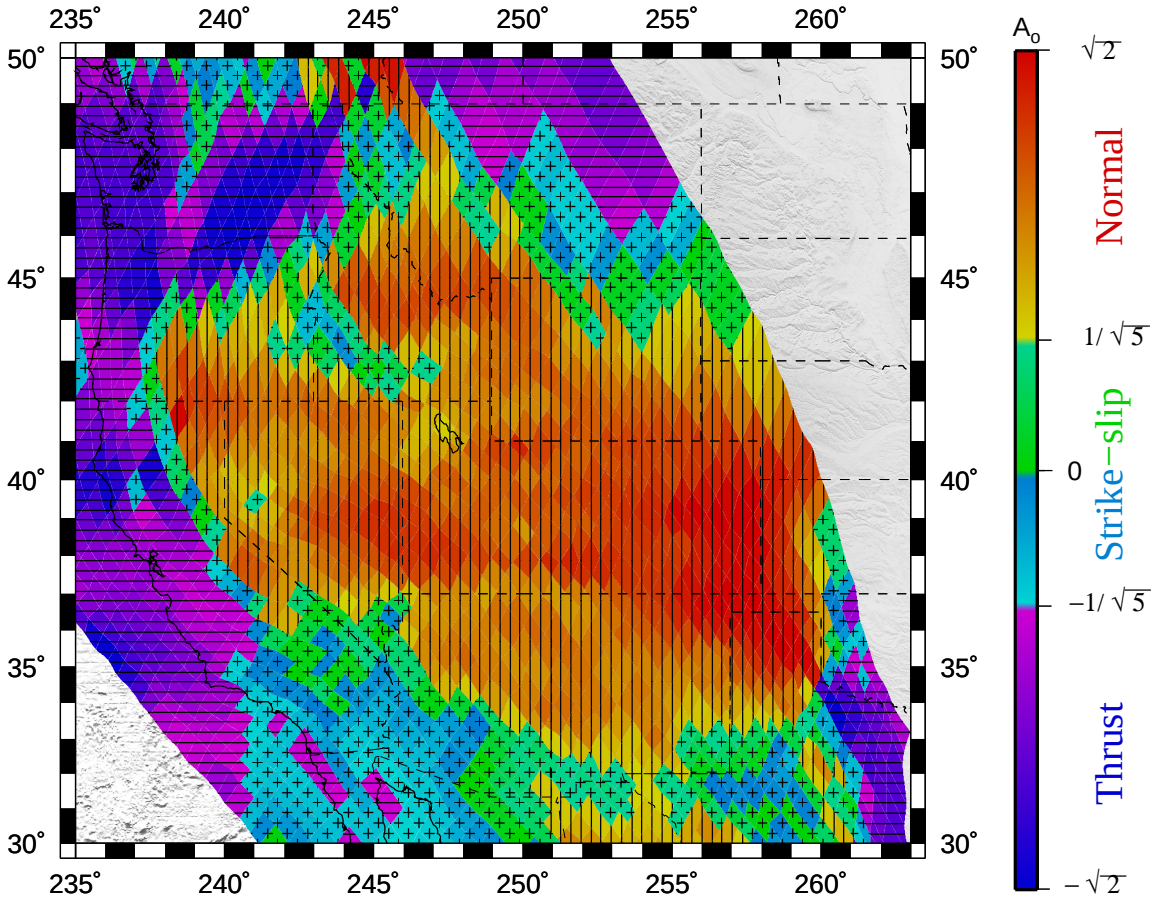

Figure 2.10: The style of faulting associated with the best-fit long-term total depth in tegrated deviatoric stress field of western North America to a depth of 20 km below sea level (see Figure 2.9). The value of the normalization parameter, $\mathcal{A}_o$, denoted by color, defines the fault style for a given grid area (equation (2.15)). Values ranging from $-\sqrt{2} \leq \mathcal{A}_o < -\frac{1}{\sqrt{5}}$ indicate thrust style faulting regimes. Values ranging from $-\frac{1}{\sqrt{5}} \leq \mathcal{A}_o \leq +\frac{1}{\sqrt{5}}$ indicate strike-slip style faulting regimes and values ranging from $+\frac{1}{\sqrt{5}} < \mathcal{A}_o \leq +\sqrt{2}$ indicate normal style faulting regimes. All fault styles are divided into one of three pure tectonic fault regimes. Grid areas regarded as pure thrust regimes are striped with black horizontal lines. Grid areas regarded as pure strike-slip fault regimes are marked with black crosses and grid areas regarded as pure normal fault regimes are striped with black vertical lines.

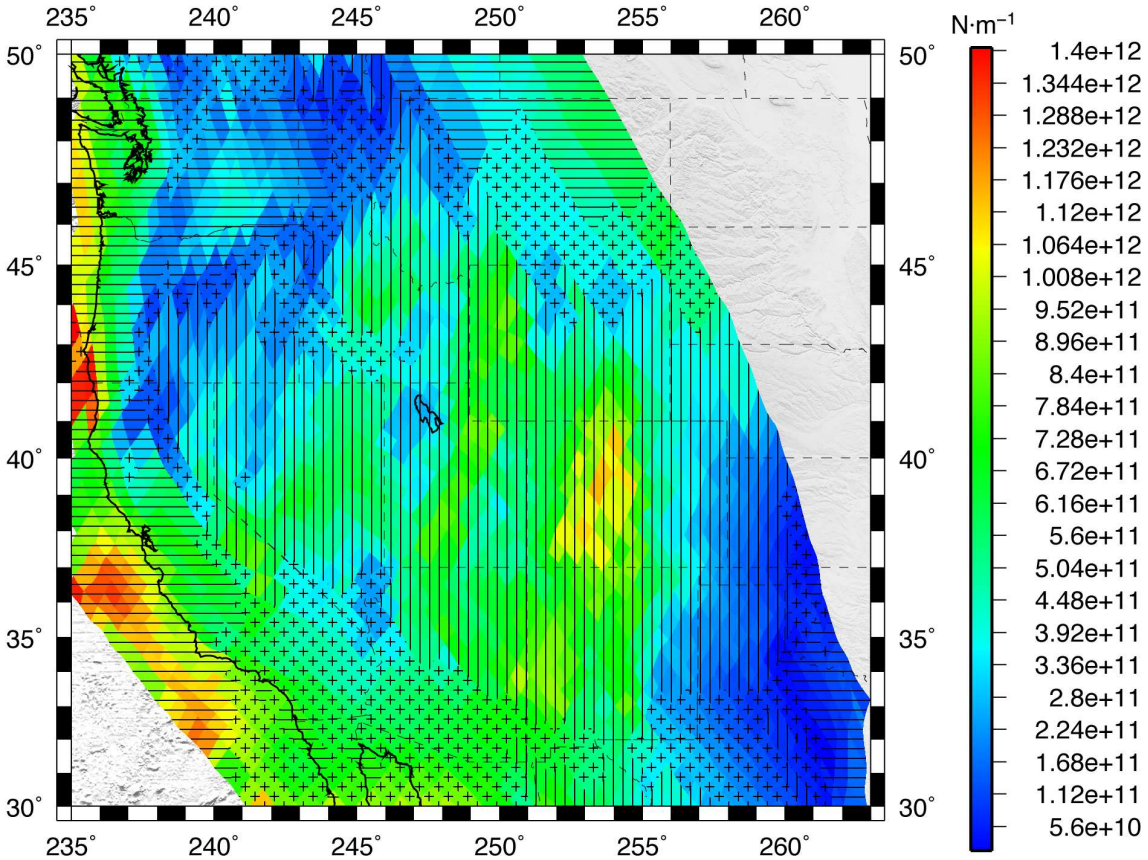

Figure 2.11: The magnitudes of long-term vertically integrated fault strength (equation (2.15) and equations (2.16–2.18)) for western North America. Limits on integration are from the surface of variable topography to a depth of 20 km below sea level. As shown in Figure 2.10, fault styles designated as pure thrust regimes are striped with black horizontal lines, pure strike-slip fault regimes are marked with black crosses, and pure normal fault regimes are striped with black vertical lines.

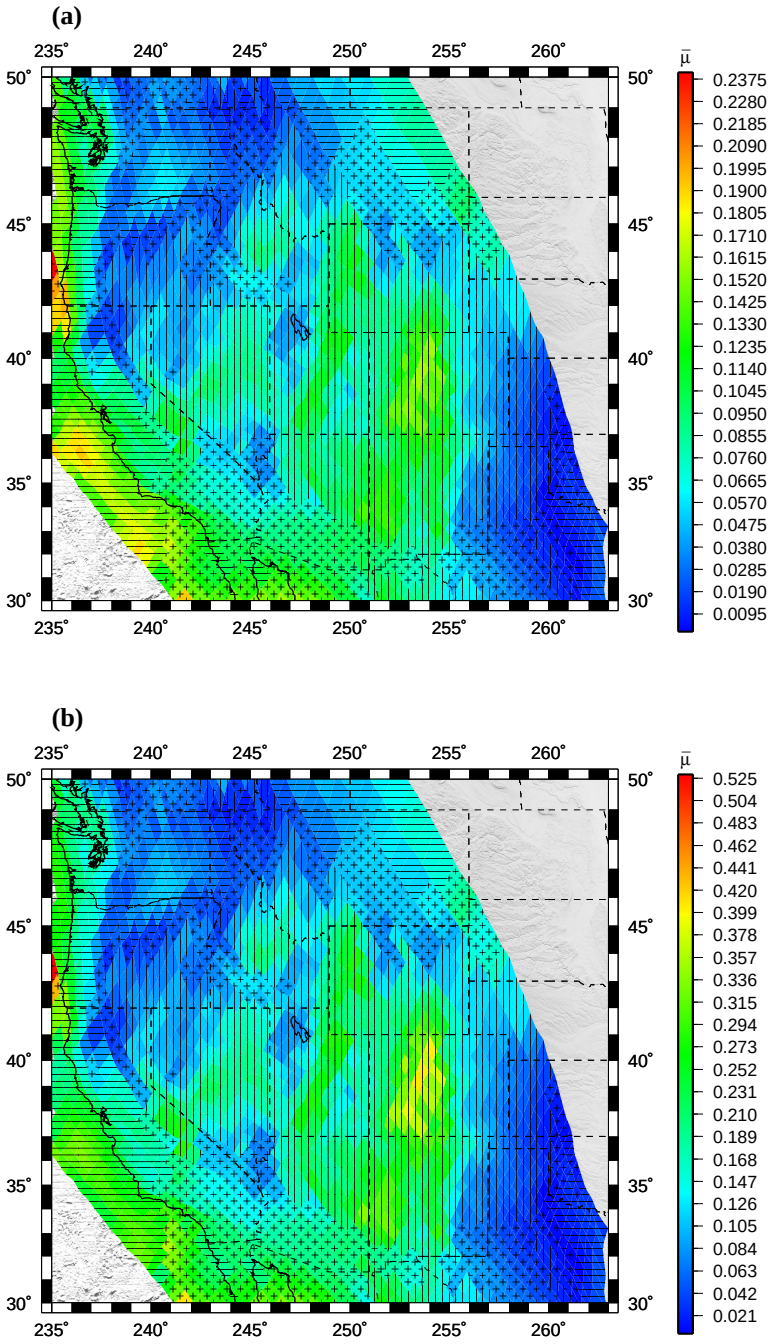

Figure 2.12: (The long-term coefficients of friction, $\overline{\mu}$, resolved on faults for the seismogenic crustal layer, obtained from depth integrals of stress differences in Figure (2.11). As shown in Figure 2.10, fault styles designated as pure thrust regimes are striped with black horizontal lines, pure strike-slip fault regimes are marked with black crosses, and pure normal fault regimes are striped with black vertical lines. (a) Assuming a long-term hydrostatic crust ($\overline{\lambda} = 0.4$). (b) Assuming a long-term wet crust ($\overline{\lambda} = 0.7$).

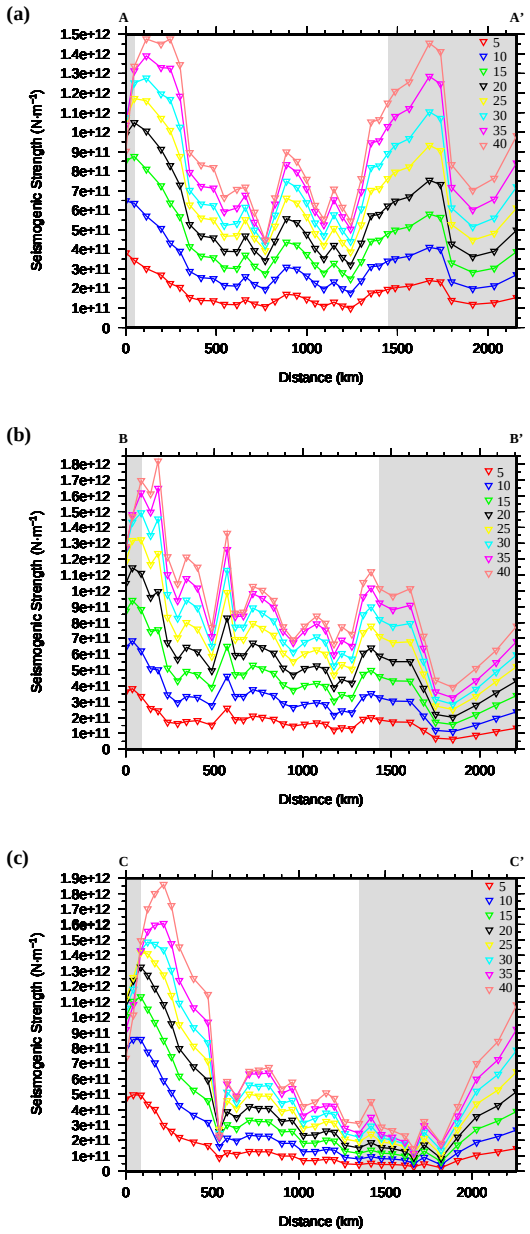

Figure 2.13: Long-term depth integrated fault strength as a function of position and modeled layer thickness along three vertical cross-sections (see Figure 2.2). Colored triangles indicate the uniform depth in kilometers to the base of the modeled layer. The long-term vertically integrated fault strength magnitudes increase as layer thickness increases. Note that there is a diminishing contribution to depth integrated strength within the Basin and Range (between 500 – 1000 km) for depth integrals in excess of 20 km. (a) Long-term vertically integrated fault strength variations along transect A-A'. (b) same as (a) expect across transect B-B'. (c) same as (a) expect across transect C-C'. Areas within the diffuse PA-NA plate boundary zone, as delineated in Figure 2.4, plot in the unshaded region of each panel.

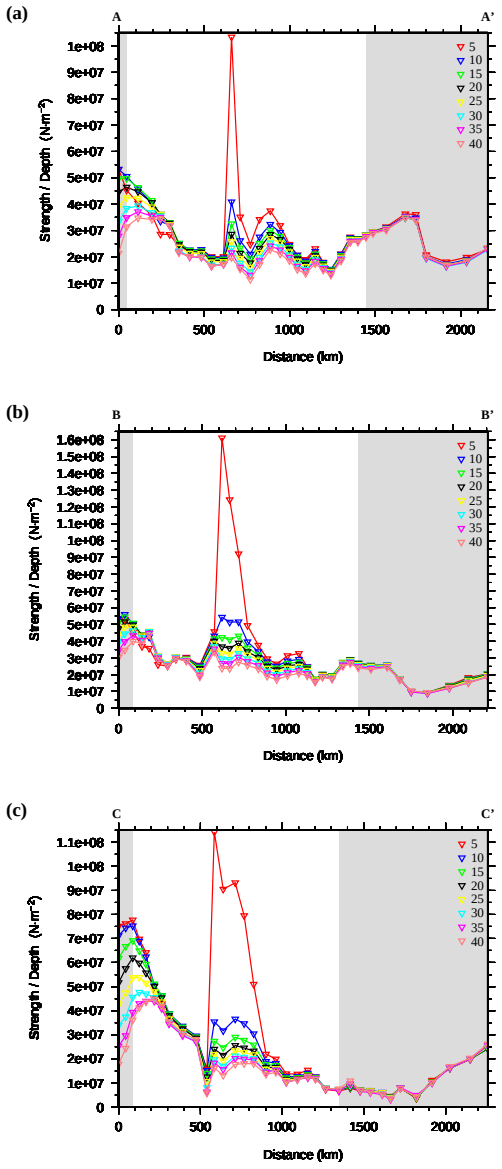

Figure 2.14: Long-term depth averaged crustal strength as a function of position and modeled layer thickness along the same three vertical cross-sections as Figure 2.13. Colored triangles indicate the uniform depth in kilometers to the base of the modeled layer. The long-term depth averaged crustal strength declines with increase in modeled layer thickness within the the Basin and Range province (between 500 – 1000 km). The declines are sharpest for cases in which the uniform base of the modeled layer remains at or above the depth of 20 km below sea level. Outside the Basin and Range province there is little to no dependence of long-term depth averaged crustal strength with layer thickness. (a) Long-term depth averaged crustal strength variations along transect A-A'. (b) same as (a) expect across transect B-B'. (c) same as (a) expect across transect C-C'. Areas within the diffuse PA-NA plate boundary zone, as delineated in Figure 2.4, plot in the unshaded region of each panel.

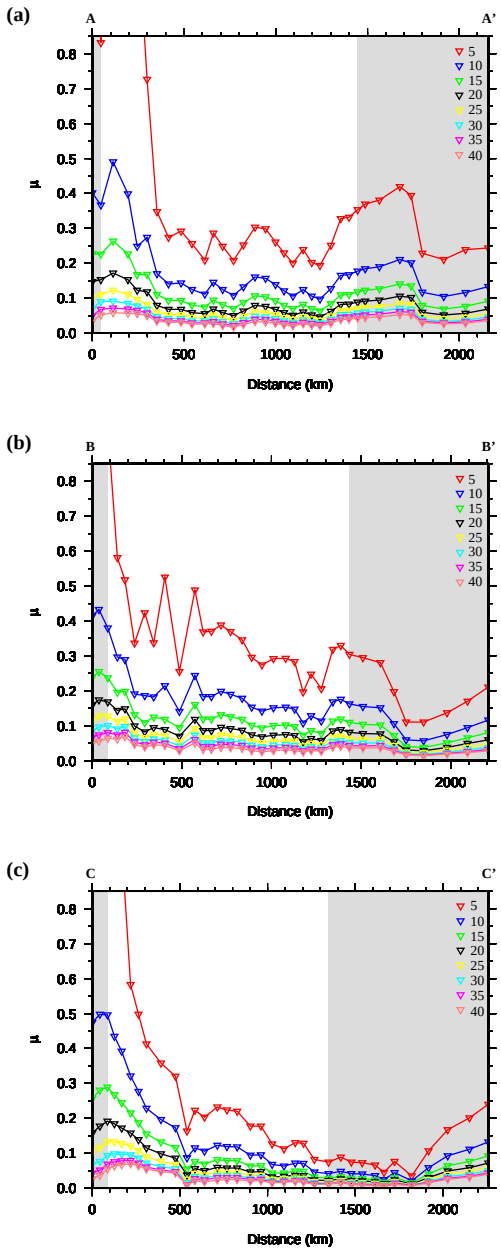

Figure 2.15: Long-term depth integrated coefficients of friction, $\overline{\mu}$, as a function of position and modeled layer thickness under long-term hydrostatic conditions ($\overline{\lambda} = 0.4$) along the same three vertical cross-sections as Figure 2.13. Colored triangles indicate the uniform depth in kilometers to the base of the modeled layer. Long-term friction coefficients associated with areas within the diffuse PA-NA plate boundary zone, as delineated in Figure 2.4, plot in the unshaded region of each panel. Long-term friction coefficients within the diffuse plate boundary zone diminish with increase in modeled layer thickness. (a) Predicted long-term coefficients of friction along transect A-A'. (b) same as (a) expect across transect B-B'. (c) same as (a) expect across transect C-C'.

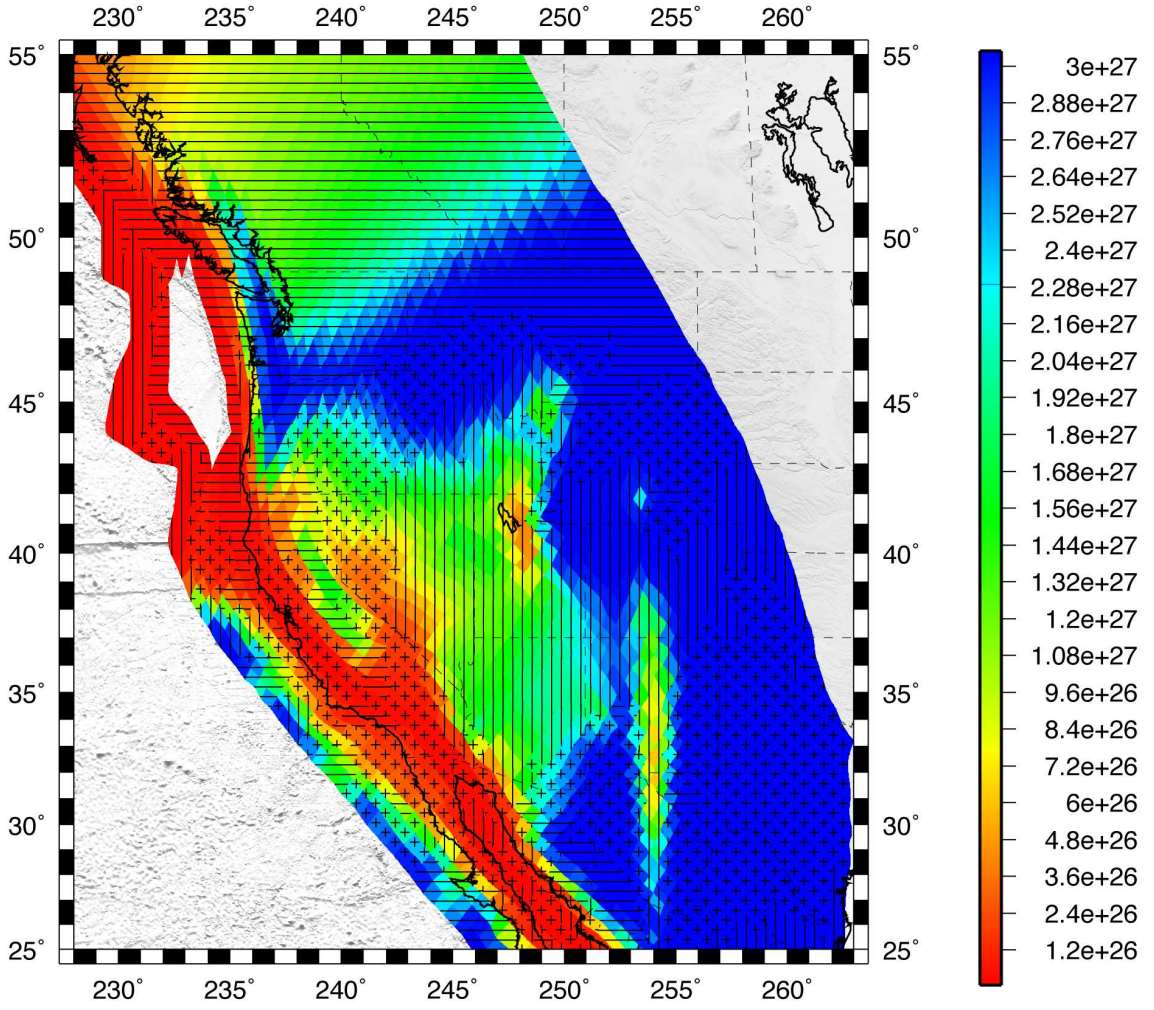

Figure 2.16: The distribution of B values associated with the weak fault model a. The B values are defined with $\overline{\mu} = 0.1$, $\overline{\lambda} = 0.4$, n=1, velocity boundary conditions, $\overline{\sigma}_{zz}$ to 20 km below sea level, and a starting guess for strain rate from our long-term strain rate tensor field. The B values are capped a maximum value of 3.05 x 10^{27} N/m $\cdot$ s. All fault styles are divided into one of three pure tectonic fault regimes. Grid areas regarded as pure thrust regimes are striped with black horizontal lines. Grid areas regarded as pure strike-slip fault regimes are marked with black crosses and grid areas regarded as pure normal fault regimes are striped with black vertical lines.

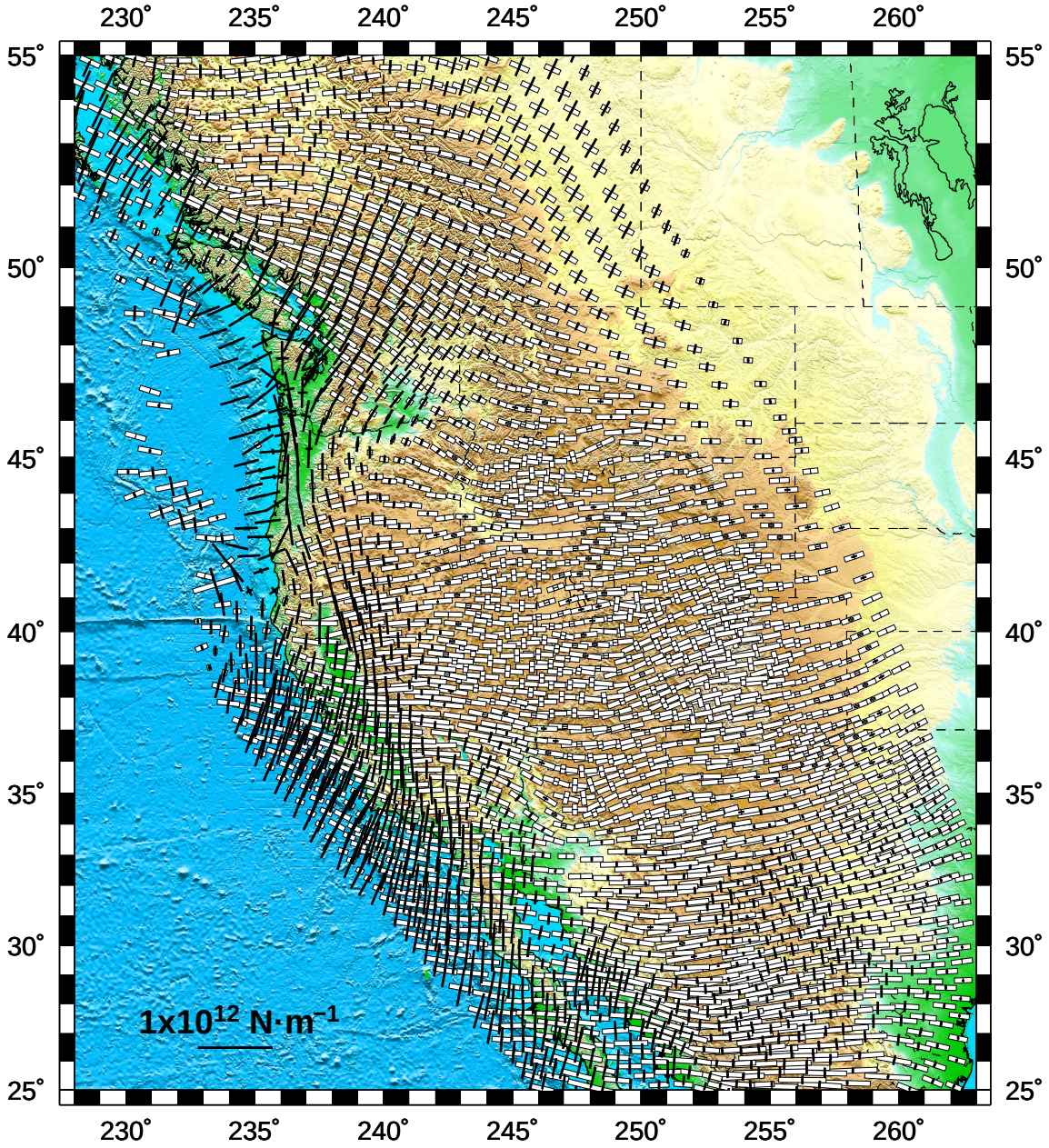

Figure 2.17: The forward dynamic solution for the weak fault model associated with the B value distribution shown in Figure 2.16. The internal buoyancies forces and the velocity boundary conditions contribute nearly equally to this solution. White vectors represent principal axes of tensional deviatoric stresses, and black vectors represent principal axes of compressional deviatoric stresses.

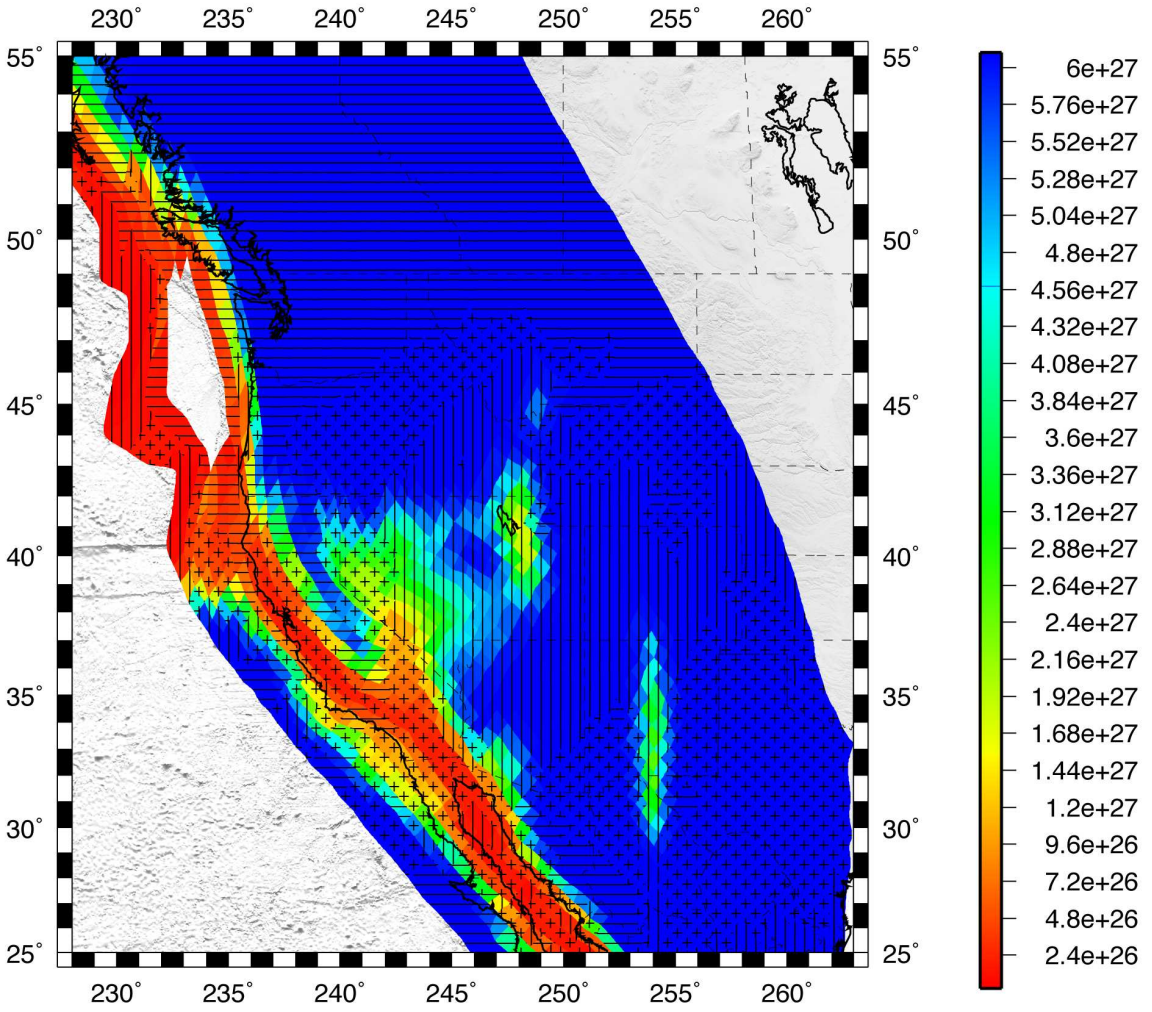

Figure 2.18: The distribution of B values associated with the strong fault model. The B values are defined with $\overline{\mu} = 0.1$, $\overline{\lambda} = 0.4$, n=1, velocity boundary conditions, $\overline{\sigma}_{zz}$ to 20 km below sea level, and a starting guess for strain rate from our long-term strain rate tensor field. The B values are capped a maximum value of 3.05 x 10^{27} N/m $\cdot$ s. All fault styles are divided into one of three pure tectonic fault regimes. Grid areas regarded as pure thrust regimes are striped with black horizontal lines. Grid areas regarded as pure strike-slip fault regimes are marked with black crosses and grid areas regarded as pure normal fault regimes are striped with black vertical lines.

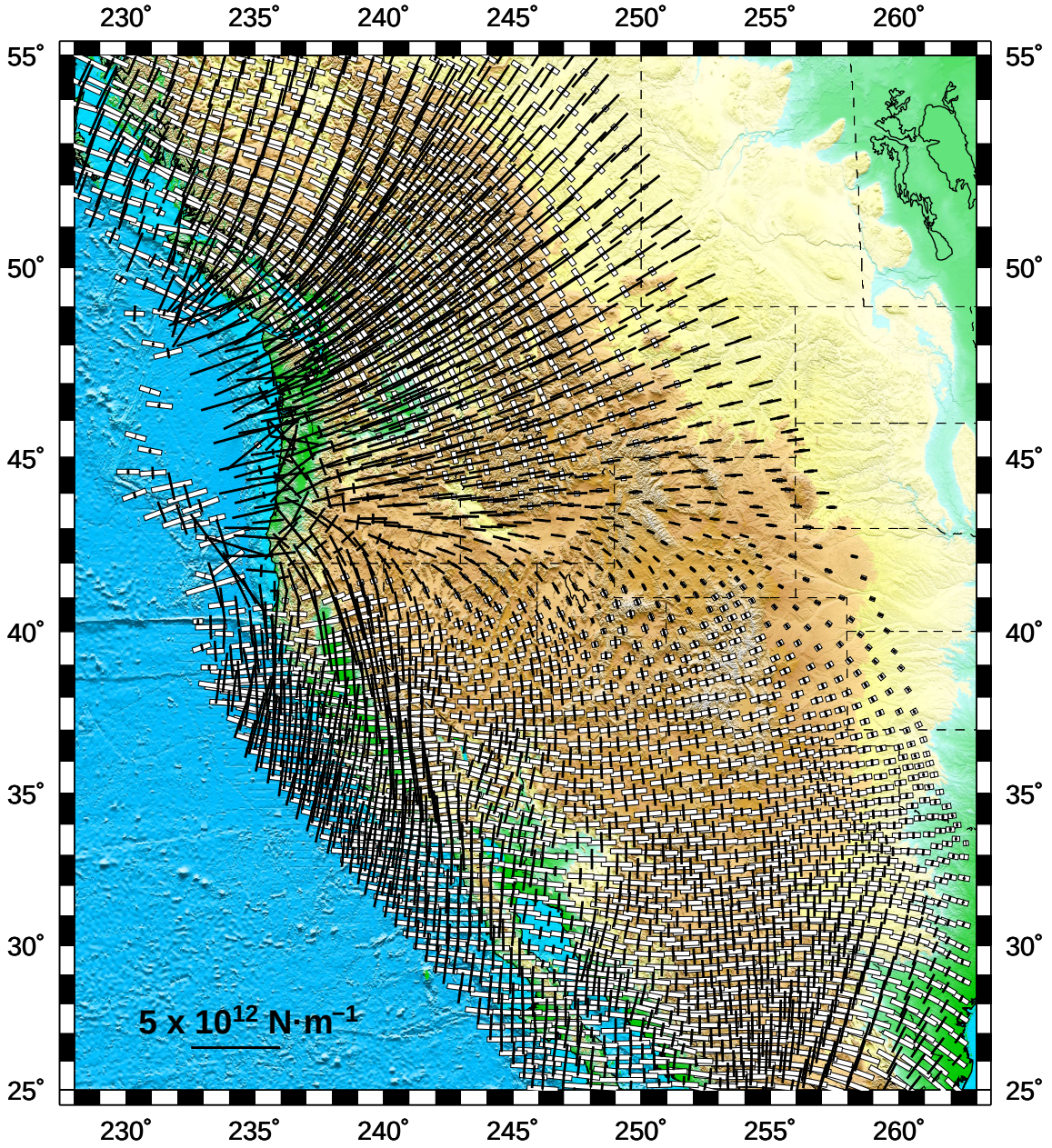

Figure 2.19: The forward dynamic solution for the strong fault model associated with the B value distribution shown in Figure 2.18. The velocity boundary conditions dominate the deviatoric stress field, overwhelming the contribution of the internal buoyancies. White vectors represent principal axes of tensional deviatoric stresses, and black vectors represent principal axes of compressional deviatoric stresses.

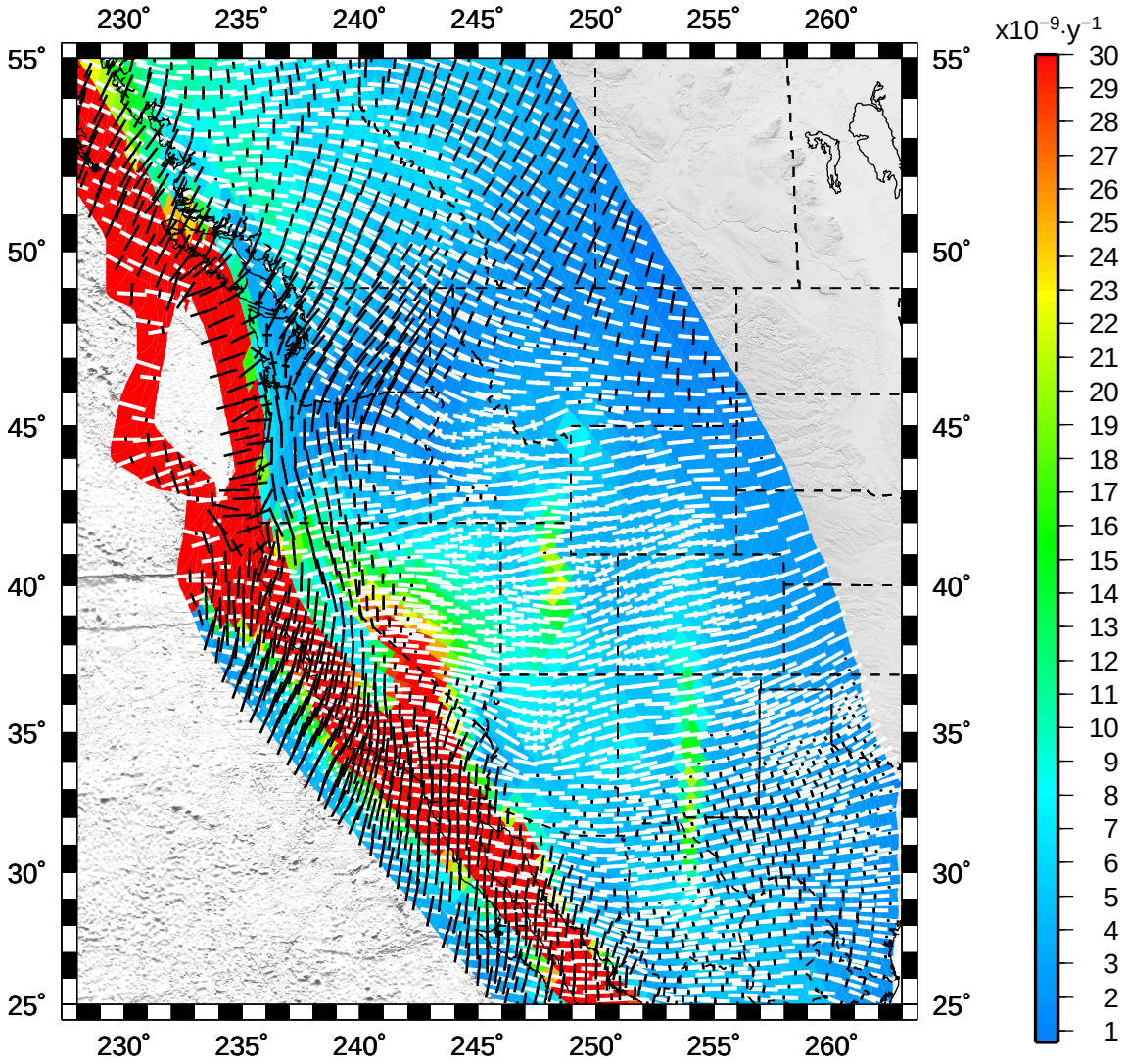

Figure 2.20: The continuous model strain rate field associated with the weak fault model. Principal axes of the strain rates are plotted as unit tensors with the second invariant of strain rate plotted in the background grid. Values of 30 x $10^{-9} \cdot \mathrm{yr}^{-1}$ or greater are plotted in red.

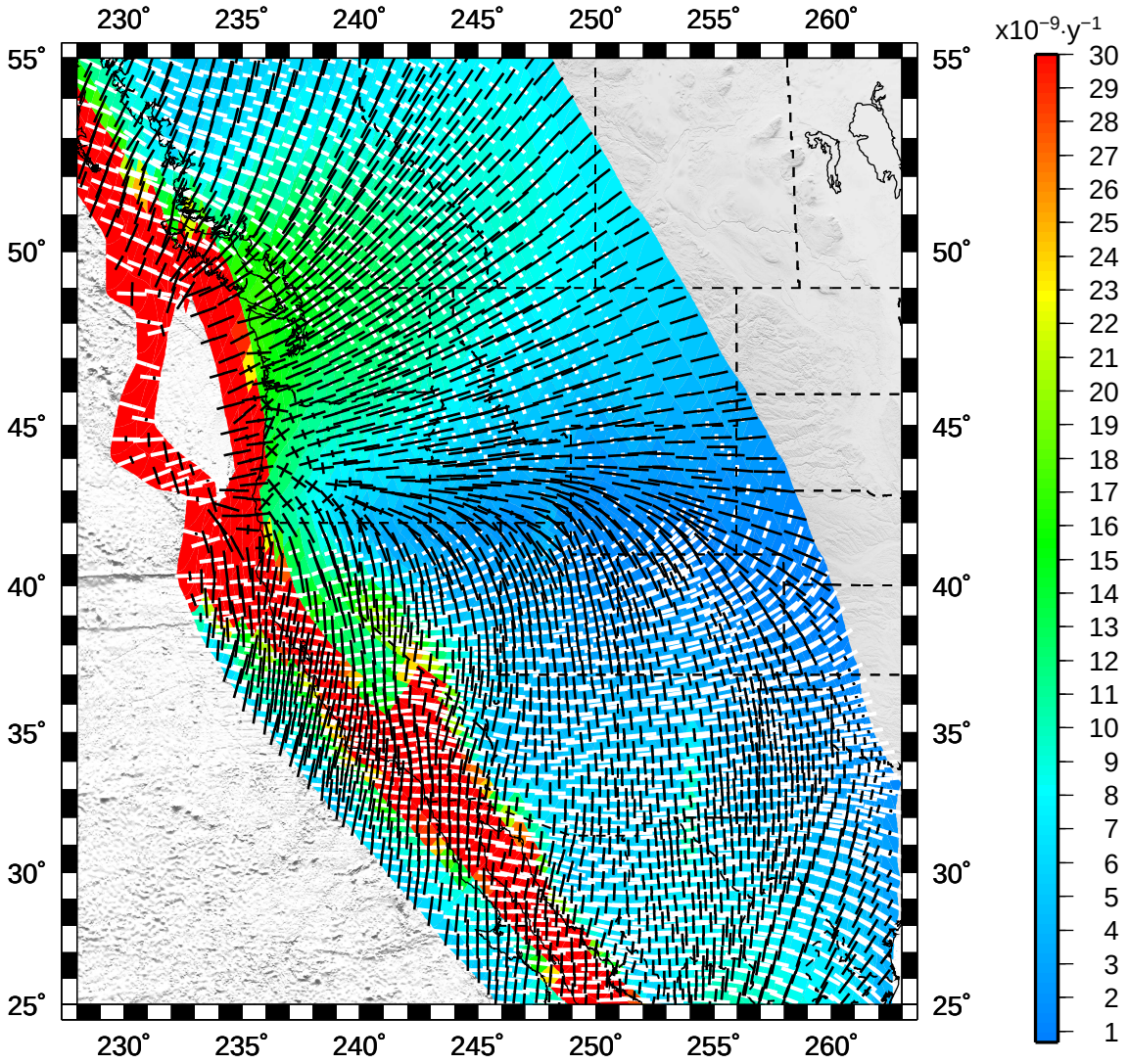

Figure 2.21: The continuous model strain rate field associated with the strong fault model. Principal axes of the strain rates are plotted as unit tensors with the second invariant of strain rate plotted in the background grid. Values of 30 x $10^{-9} \cdot \mathrm{yr}^{-1}$ or greater are plotted in red.

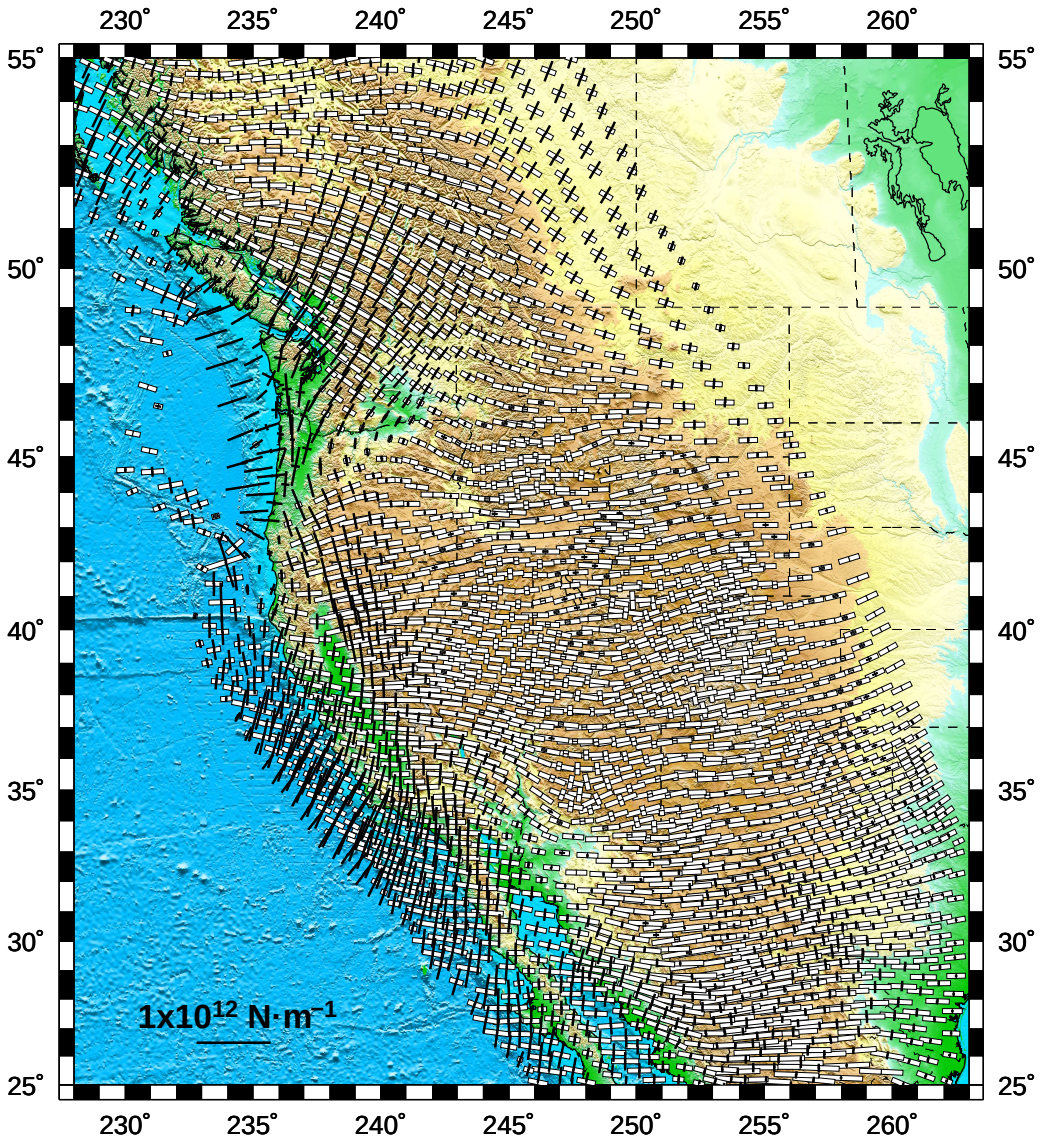

Figure 2.22: The best-fit total depth integrated deviatoric stress field extending from the surface to a uniform depth of 20 km below sea level for the weak fault model. This deviatoric stress field solution is arrived at through minimization of (2.11) such that the linear combination of basis functions, when added to the deviatoric stress field associated with GPE variations, provides a best-fit with the dynamic stress field indicators shown in Figure 2.20 (see Section 2.8). Note the near exact match between the deviatoric stress field solution obtained using the inverse method and the deviatoric stress field solution (Figure 2.17) obtained in the forward modeling approach. White vectors represent principal axes of tensional deviatoric stresses, and black vectors represent principal axes of compressional deviatoric stresses.

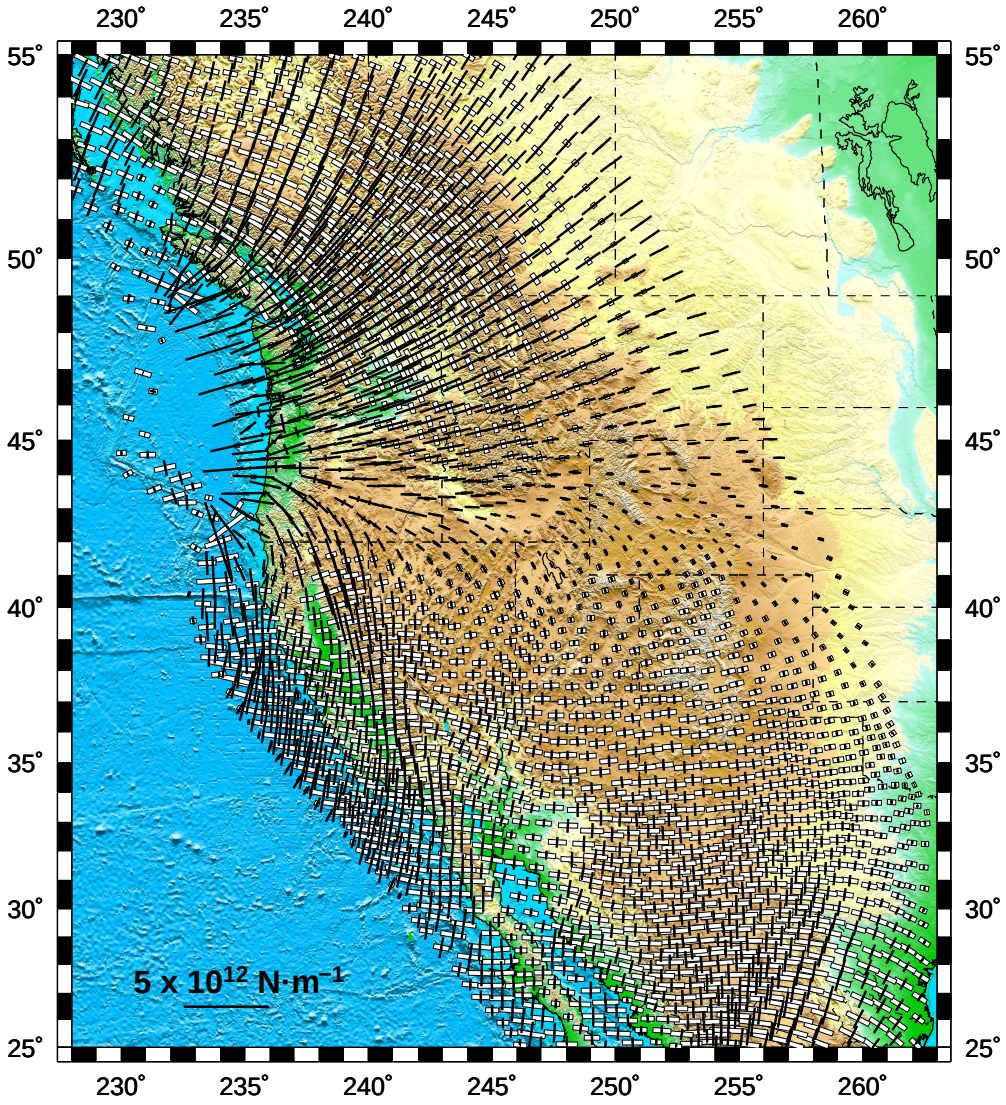

Figure 2.23: The best-fit total depth integrated deviatoric stress field extending from the surface to a uniform depth of 20 km below sea level for the strong fault model. This deviatoric stress field solution is arrived at through minimization of (2.11) such that the linear combination of basis functions, when added to the deviatoric stress field associated with GPE variations, provides a best-fit with the dynamic stress field indicators shown in Figure 2.21 (see Section 2.8). Note the near exact matches in styles of deviatoric stress field obtained with the inverse method and the forward dynamic solution (Figure 2.19). The inverse method recovers, on average, approximately 70% of the magnitude of the forward dynamic deviatoric stress field solution. White vectors represent principal axes of tensional deviatoric stresses, and black vectors represent principal axes of compressional deviatoric stresses.

Table 2.1: Model fit with stress field indicators for the case of a seismogenic layer with a uniform base 20 kilometers below sea level for each region of interest as delineated in Figure 1.

region of interest	number of areas	total regional area[a]	average strain magnitude[b]	total misfit[c]	average misfit[d]	average correlation between unit tensors[e]	average misfit between unit tensors[f]
All	3574	2.868e-01	54.5	4.634e+10	1.616e+11	0.56	0.22
1	66	6.494e-03	2.3	5.435e+08	8.370e+10	0.74	0.13
2	365	3.337e-02	111.7	6.714e+09	2.012e+11	0.50	0.25
3	325	1.695e-02	6.6	1.351e+09	7.968e+10	0.51	0.25
4	118	7.259e-03	111.6	2.010e+09	2.768e+11	0.59	0.20
5	71	6.417e-03	55.5	1.478e+09	2.303e+11	0.52	0.24
6	116	7.669e-03	5.0	5.214e+08	6.799e+10	0.58	0.21
7	257	2.817e-02	217.2	8.143e+09	2.890e+11	0.47	0.26
8	141	1.226e-02	11.6	1.865e+09	1.522e+11	0.50	0.25
9	146	1.155e-02	4.0	3.737e+08	3.236e+10	0.87	0.06
10	30	2.049e-03	8.5	4.159e+07	2.030e+10	0.93	0.04
11	162	1.964e-02	41.8	1.147e+09	5.841e+10	0.66	0.17
12	511	4.051e-02	1.8	5.074e+09	1.252e+11	0.66	0.17

Table notes:

a. Area normalized by the square of the radius of the Earth.

b. The average strain rate magnitude is defined as

$$\frac{\sqrt{\sum_{areas}\{E^2\}\Delta S}}{\sum_{areas}\Delta S}.$$

Strain rate magnitudes are in units of $10^{-9}\cdot$ yr^{-1}

c. The total misfit to the objective functional defined in eq. (2.11),

$$\sum_{areas}\left\{T-\frac{e\cdot\tau}{E}\right\}\Delta S.$$

Depth integrated stress units are N $\cdot$ m^{-1}.

d. The average misfit to the functional is defined as

$$\frac{\sum_{areas}\left\{T-\frac{e\cdot\tau}{E}\right\}\Delta S}{\sum_{areas}\Delta S}.$$

e. The average correlation between the unit tensors is defined as

$$\frac{\sum_{areas}\left\{\frac{e\cdot\tau}{ET}\right\}\Delta S}{\sum_{areas}\Delta S}.$$

f. The average misfit between the unit tensors is defined as

$$\frac{\sum_{areas}0.5*\left\{1-\frac{e\cdot\tau}{ET}\right\}\Delta S}{\sum_{areas}\Delta S}.$$

Table 2.2: Pure fault styles for seismogenic crust determined using $\mathcal{A}_o$. Also indicated are the principal stress orientations and the vertically integrated vertical strength formulations for each fault style.

Fault Style	Normalization Parmeter	σ_1	σ_3	F_{BC}
Thrust	$-\sqrt{2} \leq \mathcal{A}_o < -\frac{1}{\sqrt{5}}$	$\overline{\sigma}_{zz}$	$\overline{\sigma}_{xx}$	$-2\overline{\tau}_{xx} - \overline{\tau}_{yy}$
Strike-slip	$-\frac{1}{\sqrt{5}} \leq \mathcal{A}_o \leq +\frac{1}{\sqrt{5}}$	$\overline{\sigma}_{yy}$	$\overline{\sigma}_{xx}$	$\overline{\tau}_{xx} - \overline{\tau}_{yy}$
Normal	$+\frac{1}{\sqrt{5}} < \mathcal{A}_o \leq +\sqrt{2}$	$\overline{\sigma}_{xx}$	$\overline{\sigma}_{zz}$	$2\overline{\tau}_{xx} + \overline{\tau}_{yy}$

Table 2.3: Model fit with stress field indicators for each of the layer thicknesses modeled.

depth to base of layer (km)	average correlation between unit tensors	average misfit between unit tensors
5	0.57	0.21
10	0.57	0.22
15	0.57	0.22
20	0.56	0.22
25	0.56	0.22
30	0.55	0.22
35	0.56	0.22
40	0.56	0.22

Chapter 3

The long-term dynamics of the seismogenic layer in Western North America

The long-term dynamics of the seismogenic layer in Western North America

Elliot C. Klein, Lucy M. Flesch, William E. Holt, and A. John Haines

(In preparation for submission to the *Journal of Geophysical Research Solid Earth*)

Abstract We investigate the dynamics of the seismogenic layer within the plate boundary zone of western North America. Because the depth integrals of horizontal tractions are expected to be small in comparison with depth integrals of horizontal deviatoric stress, it is only necessary to integrate from the surface down to a common depth reference level in order to infer accurate depth-integrated stress magnitudes within the seismogenic layer under investigation. We use a forward dynamic modeling approach, where the body force distributions, inferred lateral variations in effective viscosity, and the known far-field velocity boundary conditions are defined. Body forces are the differences in gravity potential energy per unit area (GPE), obtained by performing depth integration of vertical stress from the surface down to a uniform depth of 20 km below sea level. In our treatment of the long-term seismogenic layer, the effective viscosity of a given crustal volume is proportional to the long-term friction coefficients of the faults within that volume. We investigate models by assigning a uniform friction coefficient to the fault planes of western North America using a range of long-term fault friction coefficients from 0.02–1.0 under hydrostatic pore pressure conditions. We score our dynamic model velocity and strain rate fields with estimates of the long-term deformation field built from Quaternary fault observations. Models where faults are given a long-term friction coefficient of 0.10 yield a best-fit to deformation indicators. Models where faults are given a long-term friction coefficient of 0.20 achieve a minimum reduced chi-square misfit between the long-term velocity field and the forward dynamic model velocity field. The precise long-term friction on the faults, along with the distribution of fault fabric, control the relative influence that internal crustal buoyancies and plate boundary forces have on the deformation

field. Solutions determined for models constructed from lower fault friction ($\mu < 0.20$) require stress contributions from differences in GPE that are at a minimum equal to stress contributions from boundary conditions. However, for higher fault friction ($\mu > 0.50$), stresses arising from boundary conditions dominate over stresses arising from GPE differences. These solutions with higher fault friction yield poor fits to deformation indicators. Our modeling shows that GPE differences must dominate over velocity boundary condition effects within regions east of the San Andreas fault system in order to accurately predict deformation in western North America. Moreover, GPE related effects cannot dominate over velocity boundary condition effects unless the crust contains a relatively dense network of faults with low long-term friction of 0.10 – 0.20.

3.1 Introduction

Geodetic data provide an ideal constraint for defining the interseismic kinematic fields associated with the contemporary deformation of the diffuse plate boundary zone [*Thatcher*, 2003; *Hammond and Thatcher*, 2004, 2005, 2007]. Kinematic block models defined with geodetic data, combined with some geologic data, successfully delineate western North American interseismic deformation [*McCaffrey*, 2005; *McCaffrey et al.*, 2007]. In many regions of western North America there are discrepancies between geodetic and geologic slips rates [*Dixon et al.*, 2003; *Meade and Hager*, 2005; *Becker et al.*, 2005; *Pollitz and Vergnolle*, 2006; *Oskin et al.*, 2007]. Kinematic velocity models defined with geodetic data may be significantly influenced by coseismic, postseismic, and interseismic transient deformation [*Pollitz*, 2003; *Hetland and Hager*, 2004, 2006; *Freed et al.*, 2007]. Such transients need to be well-quantified in order to produce accurate kinematic models of present-day deformation [*Pollitz and Vergnolle*, 2006; *Smith and Sandwell*, 2006; *Pollitz et al.*, 2008].

There is a link between longer-term deformation, in which the influence of many seismic cycles are considered, and the interseismic deformation field described above. Ultimately, however, this link cannot be bridged without an understanding of the dyanmics responsible for longer-term deformation. The key to understanding long-term deformation in western North America depends on our ability to link active deformation with the relative driving influences of plate motion accommodation, internal crustal buoyancies, and horizontal tractions coming from below the crust. We thus seek to quantify the long-term dynamics of the seismogenic crust in western North America that can explain deformation mechanisms and kinematic motions over time periods encompassing many seismic cycles. Such a dynamic description then holds promise for understanding and interpreting dynamics responsible for the interseismic deformation field, and ultimately whether block models or a more dense network of active faults are most appropriate for a description of western North American kinematics and dynamics.

Our aim is to accurately quantify the levels and combinations of deviatoric stress and strain rate for the long-term seismogenic layer that provide the best-fit to long-term crustal deformation indicators. We take the long-term crustal deformation indicators to be the styles of the strain rate tensor field that are associated with observations of Quaternary faulting. The self-consistent dynamic models have internal body force distributions, lateral variations in depth-integrated effective viscosity, and applied velocity boundary conditions equal to present-day plate motions. The depth-integrated effective viscosities are controlled by the input fault friction coefficients and expected long-term strain rate magnitudes. A first step is to therefore estimate the long-term kinematic strain rates of the region using Quaternary fault slip rate observations. We show in this paper that the input fault friction controls the relative ratio of stresses associated with internal buoyancy forces to stresses associated with the accommodation of plate motion. Furthermore, we show that only low long-term

friction on faults within the plate boundary zone interior can explain the long-term dynamics of western North America.

3.2 Quaternary Fault Observations and a Long-Term Kinematic Solution for Western North America

It is necessary to have an estimate of the long-term kinematics of western North America before undertaking the dynamic analysis. First, magnitudes of strain rate provide constraints on initial estimates of depth-integrated effective viscosity. Second, the forward dynamic models output a model strain rate tensor field and model deviatoric stress tensor field, which will be scored with the strain rate tensor field associated with the Quaternary fault slip rate data. Finally, the forward dynamic model velocity field will be compared with the long-term estimate of the velocity field in western North America.

In this study of the diffuse plate boundary zone of western North America, we combine known relative plate motions, ridge spreading rates, and wide-spread Quaternary fault slip rates to define a set of long-term kinematic observations. We define the Cocos, Juan de Fuca, North America, Rivera, and Pacific plates as rigid blocks. We use the Pacific-North America (PA-NA) plate motion estimate of *McCaffrey* [2005]; *McCaffrey et al.* [2007], the Cocos-North America (CO-NA) and the Rivera-North America (RI-NA) plate motion estimate of *DeMets and Wilson* [1997], and the Juan de Fuca-North America (JF-NA) plate motion estimates of *McCaffrey et al.* [2007]. We use ridge spreading rate estimates [*DeMets and Stein*, 1990; *Wilson*, 1993; *DeMets et al.*, 1994; *DeMets*, 1995; *DeMets and Dixon*, 1999] and Quaternary fault slip rate data estimates for Alaska, northwestern Canada, and much of Califor-

nia [*Jennings*, 1994; *Petersen and Wesnousky*, 1994; *Plafker and Berg*, 1994; *Bird*, 1996; *Shen-Tu et al.*, 1999] from previous long-term kinematic models of *Flesch et al.* [2007] and *Klein et al.* [2008]. Additional Quaternary fault slip rate estimates were culled from the U.S. Geological Survey, 2006, Quaternary fault and fold database for the United States (herein referred to as QFDB), accessed March 23, 2006, from USGS web site: http://earthquake.usgs.gov/regional/qfaults. We utilize QFDB fault characteristics for grid areas with no other data sources. Moreover, we select from the QFDB only those faults with established slip-sense and recorded slip rate during the last 750 ka (see Figure 3.1).

We follow the method of *Shen-Tu et al.* [1999] to estimate the long-term average horizontal strain rate tensor field for grid areas containing geologic rate data. The procedure uses a variant of *Kostrov's* 1974 formula,

$$\bar{\dot{\epsilon}}_{ij} = 1/2 \sum_{k=1}^{n} \frac{L_k \dot{u}_k}{\Delta S \sin \delta_k} m_{ij}^k, \tag{3.1}$$

where the cell area ΔS contains n number of fault segments. Each fault segment has a length L_k, a dip angle δ_k, and slip rate $\dot{u}_k$. The fault orientation and unit slip vector define the unit moment tensor m_{ij}^k [*Shen-Tu et al.*, 1999; *Holt et al.*, 2000].

The long-term average horizontal strain rate tensor field associated with Quaternary fault observations is shown in Figure (3.2). Regions well-covered with long-term strain rate observations include much of California, the Pacific Northwest coast, Oregon, the Basin and Range, Yellowstone region, and the Rio Grande rift. Regions without recorded strain rate observations include the Colorado Plateau, the Snake River Plain, and the Sierra Nevada Block. In general, pure styles of deformation (e.g., normal, thrust, and strike-slip) are associated with the majority of the long-term strain rate observations. Extensional strain rates are ubiquitous in the normal fault dominated Basin and Range. Compressional strain rates are found offshore

coastal Oregon and northern California, consistent with thrust faulting along the Cascadia subduction zone. A mix of principal extensional and compressional strain rate axes are present throughout southern and western California, compatible with the multitude of right lateral strike-slip faults found within the San Andreas and eastern California fault networks. Figure 3.2 shows Quaternary rates of strain for western North America. High strain rates are found in California, western Nevada, offshore Oregon, and central Utah along the Wasatch. Low strain rates are concentrated in the Pacific Northwest, Colorado, Arizona, and western Utah.

In order to establish a reliable estimate of a continuous long-term kinematic velocity and strain rate field within western North America, we build on the methodology of previous workers [e.g., *Haines and Holt*, 1993; *Shen-Tu et al.*, 1999; *Holt et al.*, 2000; *Beavan and Haines*, 2001; *Kreemer et al.*, 2003] who model a continuous horizontal deformation field on the Earths surface, described by

$$\mathbf{u}(\hat{\mathbf{x}}) = r\mathbf{W}(\hat{\mathbf{x}}) \times \hat{\mathbf{x}} \tag{3.2}$$

where $\mathbf{W}(\hat{\mathbf{x}})$ is a vector rotation function, $\hat{\mathbf{x}}$ is the position vector, and r is the Earth radius. In a least-squares fitting procedure we minimize the objective function

$$\chi = \sum_{cells} \sum_{ij,kl} (\bar{\dot{e}}_{ij} - \bar{\dot{e}}_{ij}^{obs})^T \mathbf{V}_{ij,kl}^{-1} (\bar{\dot{e}}_{kl} - \bar{\dot{e}}_{kl}^{obs}) \tag{3.3}$$

where $\dot{e}_{ij}$ are the model strain rates predicted by the continuous model horizontal velocity field, $\dot{e}_{ij}^{obs}$ are the observed rates of strain provided by the Quaternary rates of slip, and $\mathbf{V}_{ij,kl}$ is the variance-covariance matrix of the Quaternary rates of strain. The variance-covariance matrix contains terms that are defined by fault slip rate uncertainties, as well as an isotropic incompleteness factor that represents uncertainty in strain rate associated with slip on unknown faults within grid areas [*Shen-Tu et al.*, 1999]. We chose an isotropic component equivalent to a slip rate on an unknown fault

that spans the dimension of any given grid region having a slip rate of 0.25 mm/yr. We have tried a range of isotropic incompleteness factors of between 0.1 – 1 mm/yr and have found only minor sensitivity of the solution to this value. Since the QFDB is extensive, it is unlikely that an incompleteness factor much higher than 0.25 mm/yr is justified.

Model velocities from the inversion of the Quaternary Fault strain rates are plotted with respect to a North America frame of reference (Figure 3.3). Velocities predicted by the long-term kinematic model in the easternmost portion of our grid are typically less than 2 mm/yr. Velocities gradually increase in magnitude (up to 7 mm/yr) from east to west throughout the Basin and Range, reflecting the dominant extension across the region. However, extension rates are heterogeneous in space (Figure 3.4). The direction of motion within these regions is to the west-northwest with respect to North America. There is a broad pattern of clockwise rotation in the long-term kinematic velocity field through Oregon and Washington, but the rotation is not as pronounced as in the interseismic velocity field [*McCaffrey et al.*, 2007].

Our long-term model continuous strain rate tensor solution (Figure 3.4) provides an estimate of area-averaged strain rates for each grid cell, which arises from the best-fit match to the Quaternary strain rates (see Figure 3.2). The long-term kinematic model strain rate tensor solution is more smoothed than the Quaternary strain rate distribution. The strain rate tensor solution yields a mix of principal extensional and compressional strain rate axes within western Utah, just west of the Wasatch fault zone. This is in contrast to the observed pure axes of extensional strain rate found for these areas. Note, however, that model rates of strain here are low, less than 3 x $10^{-9} \cdot \mathrm{yr}^{-1}$, consistent with low interseismic rates there [*McCaffrey*, 2005; *Hammond and Thatcher*, 2004, 2005, 2007]. Overall the fit to the Quaternary strain rates is excellent, with a sum of squares divided by number of degrees of freedom of 0.579 (equation 3.3).

3.3 Parameterization of Forward Models

We seek a solution to the depth-integrated three-dimensional force balance equations, where depth integrals involve most of the seismogenic layer for most regions. Force balance equations are solved through the optimization of the functional:

$$\Theta(v) = \int\int_s [D - v_\alpha f_\alpha]\, dxdy, \tag{3.4}$$

where f_α is the body force term associated with gradients in gravitational potential energy per unit area (GPE), v_α is the velocity, and D is the dissipation potential [*Flesch et al.*, 2001]. The dissipation potential depends on the components of strain rate, on the value of the rheological parameter B, and the power law exponent n,

$$D = \frac{n}{n+1} B(\dot{\epsilon}_{\alpha\beta}\dot{\epsilon}_{\alpha\beta} + \dot{\epsilon}_{\gamma\gamma}\dot{\epsilon}_{\gamma\gamma})^{\frac{n+1}{2n}}), \tag{3.5}$$

where $\dot{\epsilon}_{\gamma\gamma} = (\dot{\epsilon}_{xx} + \dot{\epsilon}_{yy}) = -\dot{\epsilon}_{zz}$.

Flesch et al. [2001] have shown that optimization of equation 3.4 provides a solution to the depth-integrated three-dimensional force balance equations. Optimization involves finding the optimal strain rate distribution (continuous velocity field) embedded in the dissipation potential, D, where velocity boundary conditions of PA-NA, JF-NA, CO-NA, and RV-NA are imposed (see section 3.2), and the internal body forces are defined by gradients in vertically integrated vertical stresses (GPE). The GPE distribution is the same as that defined by *Klein et al.* [2008]. Critical for defining these forward model solutions is the distribution of B for the seismogenic layer, which we will show depends on the long-term friction on the faults, as well as the expected strain rates for the volumes containing the faults.

The depth-integrated B-value for the seismogenic crust, [*England and McKenzie*,

1982; *Sonder and England*, 1986; *Klein et al.*, 2008] for a given grid element is

$$B = \frac{\int_{-h}^{L} (\sigma_1 - \sigma_3) dz}{\sqrt{2}\dot{E}^{\frac{1}{n}}}, \tag{3.6}$$

where $\dot{E}$ is the second invariant of strain rate, and n is the power law exponent. The numerator is the depth-integrated strength for the seismogenic layer containing faults with long-term frictional resistance to sliding, where σ_1 and σ_3 are the maximum and minimum, respectively, principal total stress at frictional failure. Since the strain rates within areas are linked to the fault slip rates, and since the long-term friction applies to the faults as well, the inferred B-value distribution is proportional to the depth-integrated long-term friction on the faults, and is inversely proportional to the long-term slip rates on the faults; the B-values do not represent the depth-integrated influence of strength or strain rates of the country rock surrounding the faults.

Equation 3.6 can be written:

$$B = \frac{\int_{-h}^{L} \left[\frac{-2\mu\sigma_{zz}(1-\lambda)}{\sqrt{\mu^2+1}+c\mu} \right] dz}{\sqrt{2}\dot{E}^{\frac{1}{n}}}, \tag{3.7}$$

where μ is the coefficient of fault friction that supports the stresses in the upper crust, σ_{zz} is the vertical stress or lithostatic stress, λ is the ratio of pore pressure to lithostatic stress, and c is a constant that is 1 for normal faulting, -1 for thrust faulting, and 0 for strike-slip faulting domains [*Klein et al.*, 2008]. Equation 3.7 has $\sqrt{2}$ in the denominator in order to equate depth-integrated fault strength estimates with the expected second invariant of deviatoric stress, T, at fault failure. Note that these formulae apply to pure end-member fault cases. To build a B-value distribution, we need to identify the expected fault style to define the c-coefficient in 3.7. The principal axes of strain rate from our long term kinematic strain rate tensor solution (see Figure 3.4) constrain the styles of faulting for the seismogenic crust of western

North America [*Klein et al.*, 2008]. Once the expected fault style is identified, we then use the second invariant of the strain rate from the long-term estimates within areas to fully define the B-value distribution using a power law exponent of n=1 (equation 3.7).

We present the depth-integrated fault strength (scaled by $1/\sqrt{2}$) associated with the weak ($\mu = 0.10$), intermediate ($\mu = 0.30$), and strong ($\mu = 0.7$) values for long-term friction in Figure (3.5). Volumes of crust associated with thrust faulting hold the largest depth integrals of fault strength, whereas volumes of crust associated with normal faulting hold the smallest. The maximum depth integrals of strength (scaled by $1/\sqrt{2}$) for the strong fault case are 6.26 x 10^{12} N $\cdot$ m^{-1} and the maximum depth integrals for the weak fault case are 0.51 x 10^{12} N $\cdot$ m^{-1}. In contrast, the minimum depth integrals of strength (scaled by $1/\sqrt{2}$) for the strong fault case are 1.70 x 10^{12} N $\cdot$ m^{-1} and the minimum depth integrals for the weak fault case are 0.42 x 10^{12} N $\cdot$ m^{-1} (Figure 3.5).

Figure 3.6 shows the depth integrals of effective viscosity, B, associated for seismogenic crust with weak ($\mu = 0.10$), intermediate ($\mu = 0.30$), and strong ($\mu = 0.70$) faults (equation 3.7). Regions associated with very low long-term strain rate define the largest depth integrals of effective viscosity within western North America. Such regions exhibit little lateral variation in stiffness. On the other hand, areas such as the Basin and Range and the Rio Grande rift regions contain significant lateral variations in depth-integrated effective viscosity. The smallest depth integrals of effective viscosity are associated with the high to very high strain rates found in much of California and coastal Washington and Oregon (see Figure 3.6). In the diffuse plate boundary zone, where strain rates are moderate to high, the B-values for the faults of the strong crust are five to seven times larger than the B-values for the same network of faults for the weak crust. Overall, the maximum B-values for the strong crust are 5.73 x 10^{29} N/m $\cdot$ s and the maximum values for the weak crust are 7.60 x 10^{28} N/m

$\cdot$ s. In contrast, the minimum B-values for the strong crust are 9.75 x 10^{25} N/m $\cdot$ s and the minimum values for the weak crust are 1.20 x 10^{25} N/m $\cdot$ s.

3.4 Dynamic Modeling Results

We systematically test forward dynamic models using B-values generated using a range of friction coefficients between $\mu = 0.02$–1.0, with increment, μ=0.02 (see equation 3.7). Optimization of 3.4 yields a continuous strain rate and velocity field solution that satisfies force-balance equations, given imposed velocity boundary conditions, internal body force distributions, and effective viscosity variations. The dynamic strain rates are then used to calculate deviatoric stress, given the constitutive relation

$$\tau_{ij} = BE^{\frac{1}{n}-1}\dot{\epsilon}_{ij}, \tag{3.8}$$

The forward dynamic stress field solutions associated with the weak and strong fault models are dramatically different from each other. The weak crust model yields tensional deviatoric stresses throughout most of the Basin and Range (Figure 3.7). On the other hand, the strong crust model yields a mix of tensional and compressional deviatoric stress in the southern and western portion of the Basin and Range and pure compressional deviatoric stress in the northern portion of the Basin and Range (Figure 3.8). The weak crust model produces relatively heterogeneous tensor styles of stress throughout the Pacific Northwest: East-West compression in the trench and North-South oriented compressive deviatoric stress in Oregon and Washington, which is in agreement with *Wang and He* [1999] and World Stress Map observations (available online at www.world-stress-map.org). For the strong fault model, however, there is a relatively homogeneous, northeast-southwest dominated compressional style of stress over the same region; these orientations are significantly different from observation. The strong fault model is dominated by a strike-slip style of deformation along the

San Andreas fault and within much of the Basin and Range. By contrast, the weak fault model shows thrust style on the westernmost edge of the plate boundary zone, strike-slip style throughout much of the San Andreas system and eastern California shear zone, and normal style throughout the Basin and Range, Rio Grande Rift, Yellowstone, and central Idaho. In general, the depth-integrated deviatoric stress magnitudes associated with forward dynamic solution for the strong crust are roughly five times greater than the depth-integrated deviatoric stress magnitudes of the weak crust (see Figure 3.7).

3.4.1 Model misfit

Using the method of *Flesch et al.* [2007] we assess the misfit of each of the forward model strain rate tensor fields with the Quaternary strain rate tensor observations (Figure 3.2) using

$$M = \frac{1}{2}\left(1 - \frac{e^{obs} \cdot e^{dyn}}{E^{obs} E^{dyn}}\right), \tag{3.9}$$

where the second invariant of strain rate, E^{obs} and E^{dyn} are computed from Quaternary strain rate observations and forward dynamic strain rate solutions, respectively, and

$$\begin{aligned} e^{obs} \cdot e^{dyn} &= \dot{\epsilon}_{xx}^{obs}\dot{\epsilon}_{xx}^{dyn} + \dot{\epsilon}_{yy}^{obs}\dot{\epsilon}_{yy}^{dyn} + \dot{\epsilon}_{zz}^{obs}\dot{\epsilon}_{zz}^{dyn} + \dot{\epsilon}_{xy}^{obs}\dot{\epsilon}_{xy}^{dyn} + \dot{\epsilon}_{yx}^{obs}\dot{\epsilon}_{yx}^{dyn} \\ &= 2\dot{\epsilon}_{xx}^{obs}\dot{\epsilon}_{xx}^{dyn} + \dot{\epsilon}_{xx}^{obs}\dot{\epsilon}_{yy}^{dyn} + \dot{\epsilon}_{yy}^{obs}\dot{\epsilon}_{xx}^{dyn} + 2\dot{\epsilon}_{yy}^{obs}\dot{\epsilon}_{yy}^{dyn} + 2\dot{\epsilon}_{xy}^{obs}\dot{\epsilon}_{xy}^{dyn}. \end{aligned}$$

Our best-fit model ($\mu = 0.10$), shown in Figure 3.9a, matches Quaternary stress field indicators ($M < 0.15$) throughout the Basin and Range, Rio Grande rift, and N-S compression orientations in Washington State. The poor correlation between predicted stress tensor (Figure 3.7) and observed strain tensor (Figure 3.2) within parts of coastal Pacific Northwest occurs where there are normal faults within the QFDB. Our solutions do not predict this style of deformation there. Figure 3.9b

shows the spatial distribution of model misfit values for $\mu = 0.20$. This model fits all regions nearly the same as the model with $\mu = 0.10$, with the exception of a degraded fit within northern Oregon and Central Washington. That is, this model no longer generates N-S oriented compression axes in Washington State; compression axes are instead oriented NE-SW. Higher friction of $\mu = 0.30$ yields a worse match (Figure 3.9c), with an expanded misfit within Oregon, Washington and Idaho. The spatial distribution of model misfit values for strong uniform fault friction ($\mu = 0.70$) show significant misfit north of 40°N, and degraded fit within the Basin and Range. Note that the Yellowstone region is an area where deformation indicators are matched when modeled with intermediate fault friction ($\mu = 0.30$), but when modeled with strong fault friction ($\mu = 0.70$), deformation indicators are poorly fit.

The best-fit model for the aggregate of all (3,574) model grid cells is achieved with a weak long-term fault friction coefficient of $\mu = 0.10$, consistent with the results of inverse and forward models of *Klein et al.* [2008]. Area 6 (delineated in Figure 3.1) has a well-defined minimum at $\mu = 0.10$, which corresponds to the prediction of N-S oriented compression in Washington State that is in agreement with E-W striking thrust faults there. This region is misfit as soon as friction coefficients reach $\mu = 0.20$.

3.4.2 Comparison of Dynamic Predictions with the Long-Term Kinematics

The dynamic strain rate tensor and velocity fields (Figures 3.11 – 3.20) can be compared with our long-term kinematic estimates (Figures 3.4 and 3.3). Lower fault friction has the influence of bringing out the extensional component within regions of higher GPE. The most extreme example is the case where fault friction coefficients are set to a uniform value of μ=0.02, where the velocity and strain rate tensor fields show excessive extension rates for all regions east of the San Andreas (Figures 3.11

and 3.12). The model strain rate tensor solution that provides a best match with the Quaternary fault data base (Figure 3.13) shows dominant extension east of the Sierra Nevada. The westward directed velocities (Figure 3.14) within the Great Basin for this model are significantly reduced from the case where μ is set to 0.02 (Figure 3.12), but are still in excess of our long-term estimate. With friction coefficients set to 0.20, the Eastern California Shear Zone and the Walker Lane regions are characterized with a greater component of strike-slip faulting than the case where μ is set to 0.10 (compare Figures 3.15 and 3.13). East and northeast of Walker Lane, the solution for μ=0.20 is dominated by pure normal faulting (Figure 3.15). As mentioned, this solution misfits the observations of north-south compression within northern Oregon and Central Washington. However, the velocity field throughout the Great Basin and the motion of the Sierra Nevada block (Figure 3.16) appears to be in accord with the long-term (Figure 3.3). The influence of higher friction is to increase the component of strike-slip deformation within the Great Basin, as evidenced by velocity vectors becoming subparallel to parallel to Pacific-North America relative motion directions (Figures 3.17 – 3.20). The other characteristic of higher friction is the influence of stronger coupling with the subducting Juan de Fuca plate (pervasive northeast-southwest compressional strain-rate).

We output the dynamic model velocity fields on a 0.5° x 0.5° grid and compare these predictions with the model velocity field inferred from our long-term kinematic solution at the same points. The minimum reduced chi-square difference between the long-term velocity field and the model dynamic velocity field occurs for the case of μ of 0.20 (Figure 3.16, 3.21, 3.22). The difference between the best-fit to the Quaternary Fault Strain Rates (μ=0.10) and the best fit to the velocity field (μ=0.20) can be explained by the failure of the higher friction model to match areas within the Pacific Northwest. Otherwise, the higher friction model (μ=0.20) tends to produce a better quality of solution within the Basin and Range region for both velocity and strain

rates. One possible explanation is that long-term friction on faults may vary spatially, with lower values favored in the Pacific Northwest (μ=0.10) and higher values in the Basin and Range region (μ=0.20).

It is important to note that different regions are more sensitive than others to changes in long-term friction coefficient on faults. The region that contains the San Andreas fault system is not sensitive to changes in friction coefficient on faults (area 7 of Figure 3.10). The Rio Grande Rift and Wasatch Fault regions are also relatively insensitive to changes in long-term friction coefficients, where they are matched nearly as well with higher friction (μ=0.70) as with low friction (μ=0.10) (Figure 3.9). On the other hand, the Pacific Northwest region, as well as the northern Basin and Range region are sensitive to increases in long-term friction coefficient. In general, as friction coefficients are increased, strike-slip deformation within the Basin and Range becomes more dominant and the influences of the Juan de Fuca subduction becomes more dominant.

3.4.3 Argand number distribution for western North America

It is clear from the previous section that the relative contribution of GPE differences and the contribution from the accommodation of plate motions changes as a function of friction coefficient. In order to quantify this, we next compute the following ratio, which we denote the Argand numbe, Ar:

$$Ar = \frac{T_{GPE}}{T_{flat}}, \tag{3.10}$$

where T_{GPE} represents the second invariant of the deviatoric stress associated with GPE differences and T_{flat} represents the second invariant of deviatoric stress related to the accommodation of plate motions, in the absence of internal body forces or

GPE differences. This definition of the Argand number differs from the Argand number described by *England and McKenzie* [1982]. They designate the numerator for the Argand number as the pressure difference associated with the crustal thickness contrast, and not the stress magnitude associated with GPE differences. For this reason their Argand numbers cannot be specifically equated with ours. We compute the stresses associated with GPE differences using the method described in *Flesch et al.* [2001], but with variable depth-integrated B values, for cases with μ=0.10 and μ=0.70. The same B values are used in the computation of the GPE related stresses as were used in the computation of the forward dynamic models. Secondly, we compute the deviatoric stresses associated with the accomodation of velocity boundary conditions through the minimization of the dissipation potential (equation 3.5), but with no internal body forces.

The deviatoric stress distributions for GPE differences for cases with μ=0.1 and μ=0.7 are similar to one another in both style and magnitude (Figures 3.23, 3.24). It is clear that the GPE differences are not sensitive to the magnitude of the depth-integrated B values. The patterns of deviatoric stress associated with accommodation of plate motions are similar to one another, but show an increase in magnitude for the higher friction coefficient of μ=0.70 (Figures 3.25, 3.26). Figures 3.27 and 3.28 show the Argand number distribution for the weak and strong long-term fault friction models for western North America, respectively. The Argand number distribution associated with our best-fit model (μ=0.10) corresponds well with broad tectonic features of the diffuse plate boundary zone and the Pacific Northwest. For example, along the San Andreas Fault zone and the Juan de Fuca subduction zone the Ar is less than 1.0, indicating that plate boundary forces are more important there than GPE differences. For the Basin and Range and the Rio Grande rift regions, however, Ar ranges from 1–10 , and for the Wasatch and Colorado Rocky mountain ranges, Ar is greater than 10 (Figure 3.27, indicating that GPE differences are dominant in

these regions.

The Argand number distribution for the strong fault friction model ($\mu = 0.70$) also can be associated with broad tectonic features of the diffuse plate boundary zone and the Pacific Northwest. For instance, along the San Andreas and Juan de Fuca subduction zone, Ar is less than 0.10; for the Basin and Range and the Rio Grande rift regions, Ar is generally less than 1, and for the Wasatch and Colorado Rocky mountain ranges, Ar is greater than 1 (Figure 3.28). Overall, the Argand number distribution associated with our strong fault model shows that in most regions the forces associated with the accommodation of plate motion dominate over forces associated with GPE differences, a feature that leads to a poor match with deformation indicators.

We present area-averaged Argand numbers as a function of uniform fault friction coefficients in Figure 3.29. Argand distributions obtained with low fault friction coefficients yield higher area-averaged Argand numbers than models built with intermediate to strong fault friction coefficients. Argand distributions generated with low long-term friction coefficients $\mu \approx 0.1$ are favored over those generated with intermediate to strong fault friction coefficients because low friction models provide a better fit to Quaternary deformation indicators. For lower fault friction cases, the contribution to the total deviatoric stress field from differences in GPE is at minimum equal to the contribution from the accommodation of plate motions (see Figure 3.29). Hence, stresses arising from GPE differences (E and NE of Sierra Nevada) have a greater role in driving the long-term deformation of the diffuse plate boundary zone of western North America than boundary conditions stresses.

3.5 Discussion

We have refined the forward dynamic method of *Flesch et al.* [2001] to quantify the absolute magnitudes of depth-integrated deviatoric stresses acting within the long-term seismogenic layer by explicitly addressing the role of long-term friction on faults. *Klein et al.* [2008] have shown that reliable depth integrals of deviatoric stress magnitudes can be obtained for the seismogenic layer alone by integrating from the surface down to a fixed-depth reference level. This is true if depth integrals of horizontal shear stress terms are small in comparison with depth integrals of horizontal deviatoric stress. *Klein et al.* [2008] demonstrate that depth integrals of horiozntal tractions can be estimated from mantle-circulation-generated basal traction applied at the base of the lithosphere (1-5MPa) [*Becker and O'Connell*, 2001; *Humphreys and Coblentz*, 2007; *Ghosh et al.*, 2008a, c] and that they are indeed small in comparison with depth integrals of horizontal deviatoric stress. Furthermore, *Klein et al.* [2008] infer that the horizontal gradients in shear stress acting at the base of the lithosphere are a negligible percentage of depth integrals of ρg, validating the thin sheet approach. Furthermore, [*Klein et al.*, 2008] showed that with greater depths of integration there is diminishing contribution to the depth-integrated stress differences, and by proxy depth-integrated fault strength. This result was consistent with a brittle-ductile transition in the plate boundary zone at depths less than 20 km below sea level, and with a weak lower crust [*Klein et al.*, 2008]. We are thus confident that we have isolated the dynamics of the seismogenic layer alone.

The Quaternary fault observations allow us to test and evaluate our set of forward dynamic models in unprecedented detail. Our modeling results suggest that the long-term patterns of finite strain in the western North America can be explained well with a distributed fabric of uniformly weak faults embedded within the seismogenic layer of the upper crust. Forward dynamic models built with such low long-term fault

friction coefficients fit the kinematic strain rate field associated with Quaternary fault observations far better than models constructed with high long-term fault friction coefficients (see Figure 3.10). Again, this result is compatible with low long-term fault friction results obtained by *Klein et al.* [2008] using inverse modeling methods. Other numerical studies of fault networks in California predict low fault friction for the Californian faults [e.g., *Bird and Kong*, 1994; *Geist and Andrews*, 2000; *Fay and Humphreys*, 2006]. Such results are in general agreement with our prediction for low uniform long-term fault friction for the faults of western North America.

Although our simple forward dynamic models fit the kinematic strain rate and velocity fields associated with Quaternary fault observations quite well in western North America, they collectively fail to produce a good agreement with long-term geologic fault data to the west of the Puget Sound region of Washington state. Quaternary deformation indicators show the prevalence extensional strain styles to the west of Puget Sound (see Figure 3.2). Yet our dynamic models do not produce the required extension in this region (see Figure 3.13).

The minimum reduced chi-square misfit between the dynamic model velocity field and the long-term velocity field estimate is achieved with a long-term fault friction coefficient of 0.20. On the other hand, the minimum misfit for the forward dynamic strain rate tensor field solution is achieved with a long-term fault friction coefficient of 0.10. This discrepancy stems from the fact that the forward dynamic strain rate solutions generated with friction coefficients of 0.2 fail to match the N-S oriented compression within Washington State. The discrepancy may indicate that friction coefficients are laterally variable, with a best-fit in the Basin and Range region of μ=0.20 and a best-fit in the Pacific Northwest of μ=0.10.

Our forward modeling method allows us to solve directly for the Argand number distribution. The input of low uniform long-term fault friction on the fault networks of western North America provides meaningful Argand number distributions.

This Argand number distribution reflects the delicate balance of forces that, over the longer-term are responsible for driving the deformation of the seismogenic crust into the spatially diverse patterns of finite strain observed in western North America.

3.6 Conclusions

We have constructed forward dynamic models of the seismogenic layer within the plate boundary zone of western North America. In our method, forward dynamic models of the crust are defined by the known internal buoyancy distributions, inferred lateral variations in effective viscosity, and the known far-field velocity boundary conditions. Our models extend from the surface to a uniform depth of 20 km below sea level. Body forces are generated from differences in gravity potential energy per unit area for the model layer. Uniform fault friction coefficients and fault styles predicted from our long-term kinematic strain rate model define lateral variation in effective viscosity. Solutions to the force-balance equations define self-consistent dynamic stress tensor, velocity, and strain rate tensor fields of the seismogenic layer.

We built our models using a range of uniform long-term fault friction coefficients under hydrostatic pore pressure conditions. Our forward dynamic solutions are sensitive primarily to the level of friction on the faults and the distribution of the fault fabric. These two factors control the relative influence that internal crustal buoyancies and plate boundary forces have on the deformation field. We evaluate dynamic solutions resulting from our fault friction models using two different measures of fitness. In one fitness measure, the forward dynamic strain rate solutions are scored with the kinematic strain rate field associated with Quaternary fault observations. In another fitness measure, the dynamic model velocity fields are scored with the long-term kinematic model velocity field. The long-term kinematic velocity field is defined using estimates of long-term deformation built from Quaternary fault observations.

We determined that a uniform long-term fault friction coefficient of 0.10 applied to the faults of western North America achieves a best-fit with tensor styles of strain rate defined by Quaternary fault observations. We also found that the same network of faults, given a uniform long-term fault friction coefficient of 0.20, achieves a minimum reduced chi-square misfit with the long-term forward dynamic model velocity field. Forward dynamic solutions require at least equal to or greater contributions of stress from differences in GPE than from boundary conditions in order to closely match deformation indicators and patterns of finite strain in western North America. Such results are obtained for models of the seismogenic crust built with low ($\mu < 0.20$) fault friction coefficients.

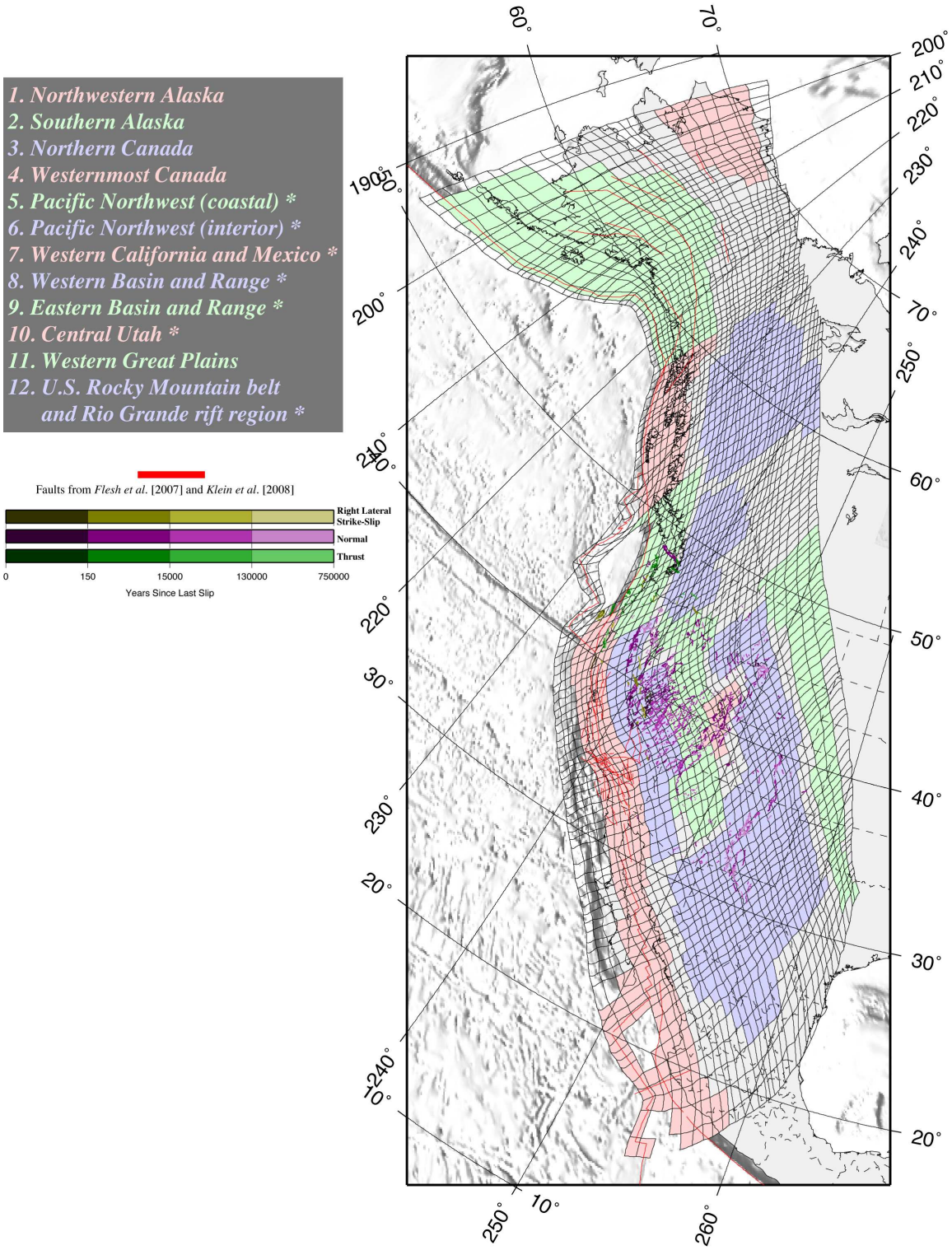
1. Northwestern Alaska
2. Southern Alaska
3. Northern Canada
4. Westernmost Canada
5. Pacific Northwest (coastal) *
6. Pacific Northwest (interior) *
7. Western California and Mexico *
8. Western Basin and Range *
9. Eastern Basin and Range *
10. Central Utah *
11. Western Great Plains
12. U.S. Rocky Mountain belt and Rio Grande rift region *
Faults from Flesh et al. [2007] and Klein et al. [2008]
Right Lateral Strike-Slip
Normal
Thrust
0
150
15000
130000
750000
Years Since Last Slip
60°
70°
200°
210°
220°
230°
240°
70°
250°
60°
50°
40°
30°
20°
260°
10°
250°
240°
230°
220°
210°
200°
190°

Figure 3.1: The finite element grid (black) used in the kinematic and dynamic modeling. We combine the Quaternary fault observations (red traces) of *Flesch et al.* [2007] and *Klein et al.* [2008] with Quaternary fault data obtained from the Quaternary Fault and Fold Database (QFDB). We depict the fault characteristics of the QFDB as function of fault trace, fault type, and last slip event in years before present. Results for all highlighted regions are quantified. Regions well constrained by geologic data (asterisked entries in the legend) are particularly important to this study.

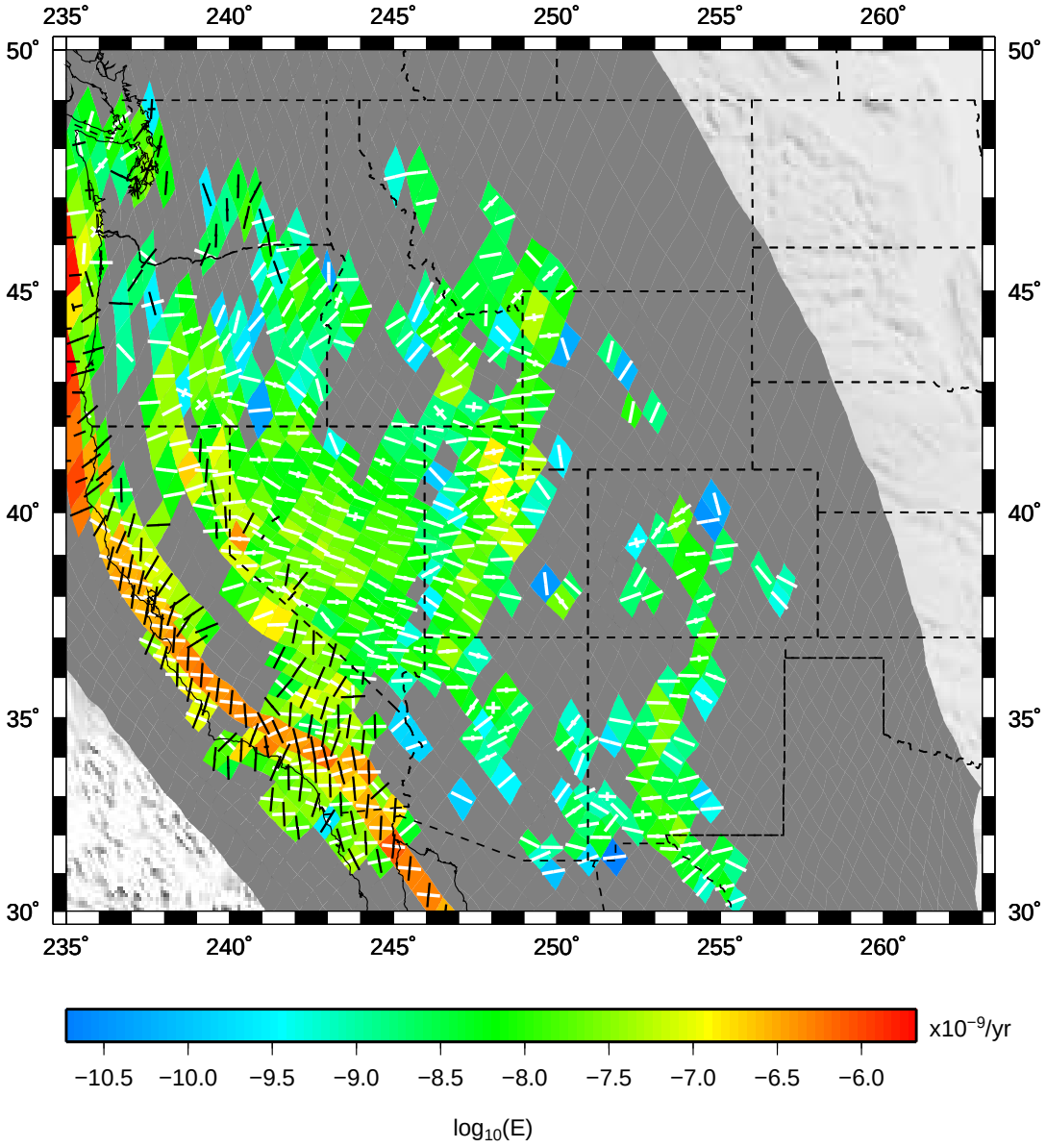

Figure 3.2: The long-term estimate of the horizontal strain rate tensor field for grid areas containing geologic rate data obtained from moment rate tensor summation from QFDB. Principal axes of strain rates (area averages) have been normalized by the maximum value of the principal axis strain rate within each grid area (bold = compressional, white = extensional). Color background is the log of the second invariant of strain rate (area averages). Grid areas without data plot in gray.

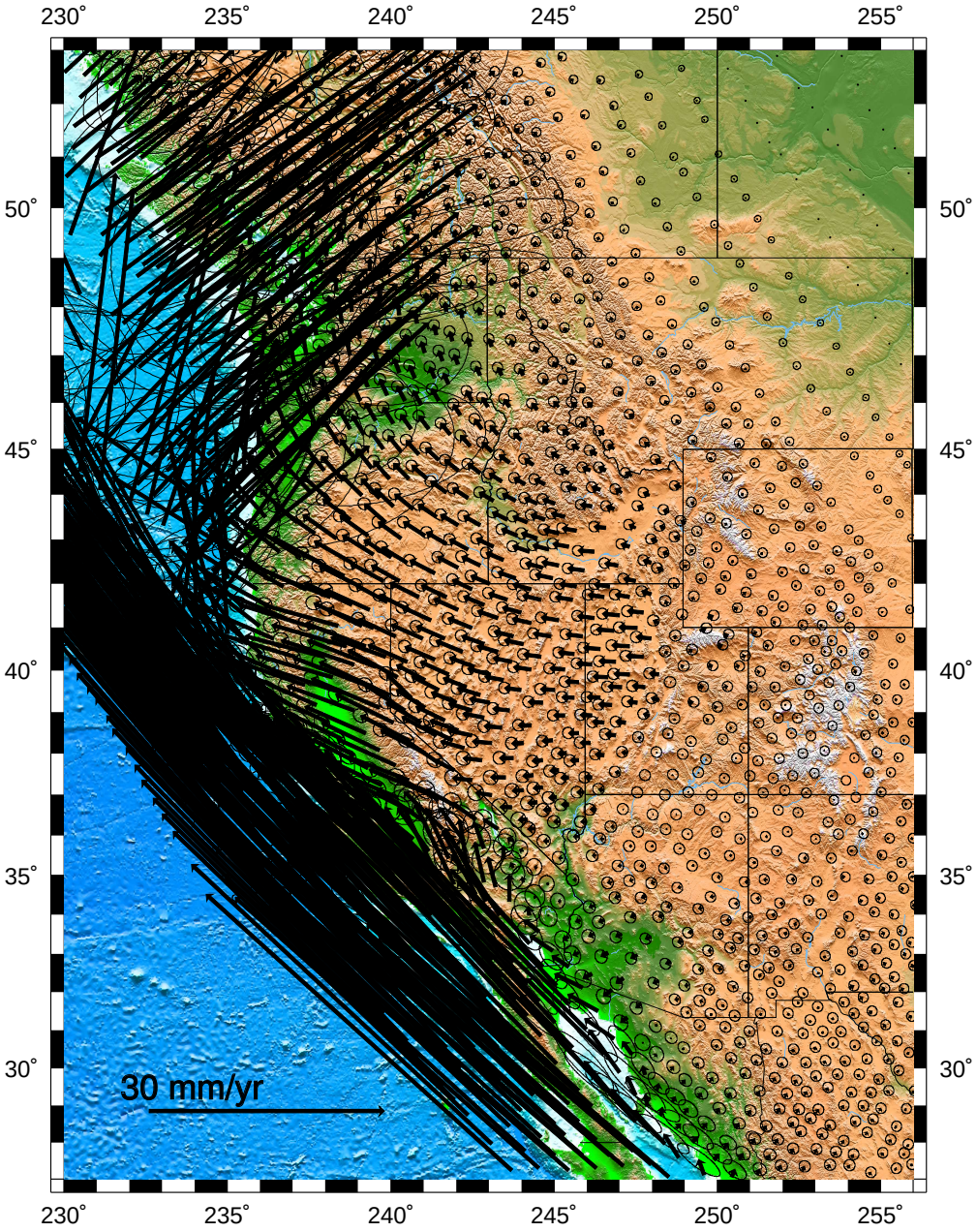

Figure 3.3: Kinematic solution estimate for the long-term velocity field obtained through fitting of Quaternary fault strain rate in Figure 3.2 observations with imposed velocity boundary conditions for western North America. Model velocity vectors are 95% confidence.

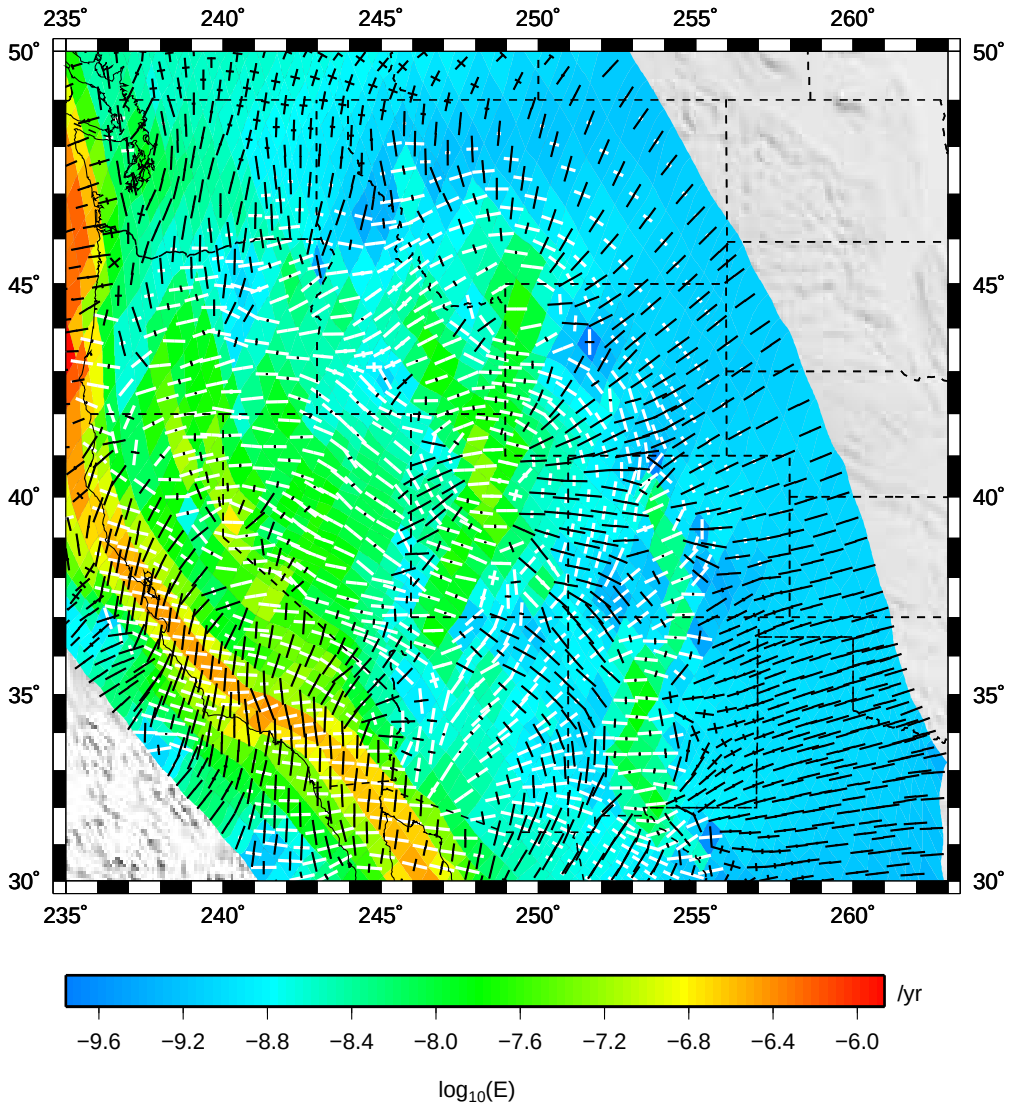

Figure 3.4: The long-term kinematic model solution for the horizontal strain rate tensor field associated with Quaternary fault observations obtained through fitting of QFDB observations in Figure 3.2, with imposed velocity boundary conditions. Principal axes of strain rates (area averages) have been normalized by the maximum value of the principal axis strain rate within each grid area (bold = compressional, white = extensional). Color background is the log of the second invariant of strain rate (area averages).

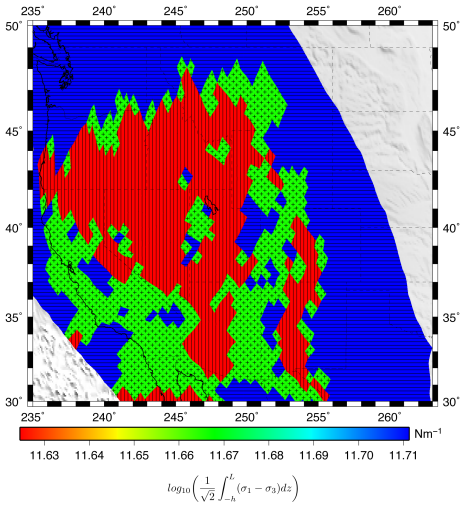
235° 240° 245° 250° 255° 260°
50° 45° 40° 35° 30°
Nm⁻¹
11.63 11.64 11.65 11.66 11.67 11.68 11.69 11.70 11.71
$log_{10}\left(\frac{1}{\sqrt{2}}\int_{-h}^{L}(\sigma_1-\sigma_3)dz\right)$

(a)

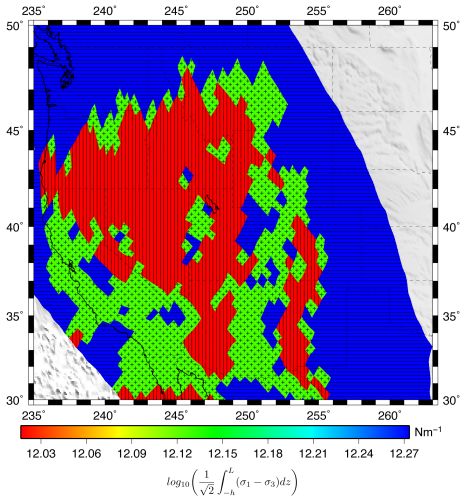
235° 240° 245° 250° 255° 260°
50° 45° 40° 35° 30°
Nm⁻¹
12.03 12.06 12.09 12.12 12.15 12.18 12.21 12.24 12.27
$log_{10}\left(\frac{1}{\sqrt{2}}\int_{-h}^{L}(\sigma_1-\sigma_3)dz\right)$

(b)

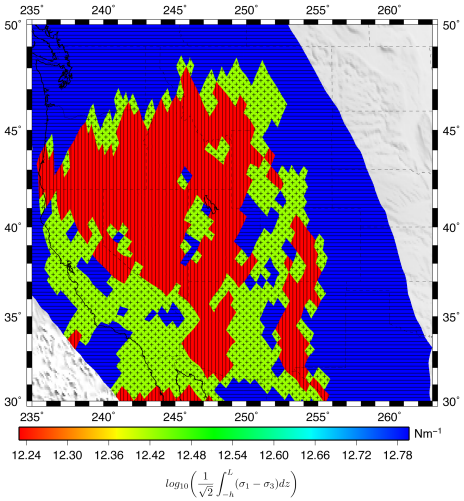
235° 240° 245° 250° 255° 260°
50° 45° 40° 35° 30°
Nm⁻¹
12.24 12.30 12.36 12.42 12.48 12.54 12.60 12.66 12.72 12.78
$log_{10}\left(\frac{1}{\sqrt{2}}\int_{-h}^{L}(\sigma_1-\sigma_3)dz\right)$

(c)

Figure 3.5: The distribution of the log of depth-integrated fault strength scaled by $1/\sqrt{2}$ for the weak, intermediate, and strong fault friction models. Depth integration is from the surface of variable elevation to 20 km below sea level. All fault styles are grouped into one of three pure tectonic regimes defined by the long-term kinematic strain rate tensor field solution. Vertical rule indicates normal faulting style, horizontal is thrust, and cross is strike-slip. (a) weak fault friction model ($\mu = 0.10$). (b) intermediate fault friction model ($\mu = 0.30$). (c) strong fault friction model ($\mu = 0.70$).

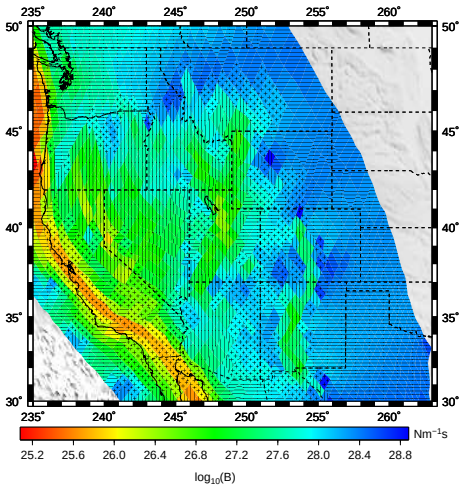
235° 240° 245° 250° 255° 260°
50° 45° 40° 35° 30°
Nm⁻¹s
25.2 25.6 26.0 26.4 26.8 27.2 27.6 28.0 28.4 28.8
log10(B)

(a)

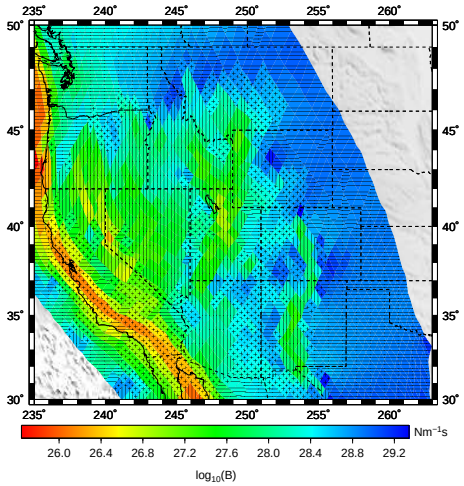
235° 240° 245° 250° 255° 260°
50° 45° 40° 35° 30°
Nm⁻¹s
26.0 26.4 26.8 27.2 27.6 28.0 28.4 28.8 29.2
log10(B)

(b)

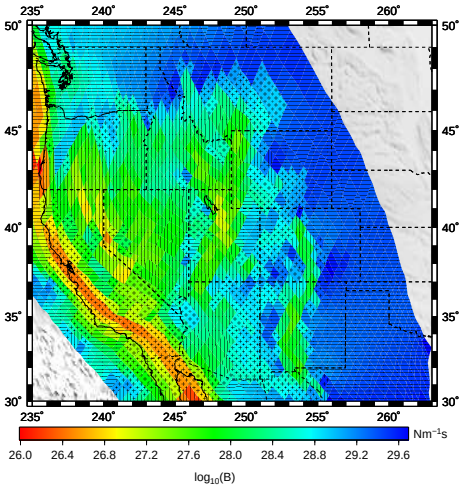
235° 240° 245° 250° 255° 260°
50° 45° 40° 35° 30°
Nm⁻¹s
26.0 26.4 26.8 27.2 27.6 28.0 28.4 28.8 29.2 29.6
log10(B)

(c)

Figure 3.6: The distribution of the log of the depth-integrated B-values for the weak, intermediate, and strong fault friction models, assuming depth integrals of the fault strength, a power law exponent of $n = 1$, and strain rate from our long-term model strain rate tensor field. All fault styles are grouped into one of three pure tectonic regimes defined by the long-term strain rate tensor field solution. Vertical rule indicates normal faulting style, horizontal is thrust, and cross is strike-slip. (a) B-values for the weak fault friction model ($\mu = 0.10$). (b) B-values for the intermediate fault friction model ($\mu = 0.30$). (c) B-values for the strong fault friction model ($\mu = 0.70$).

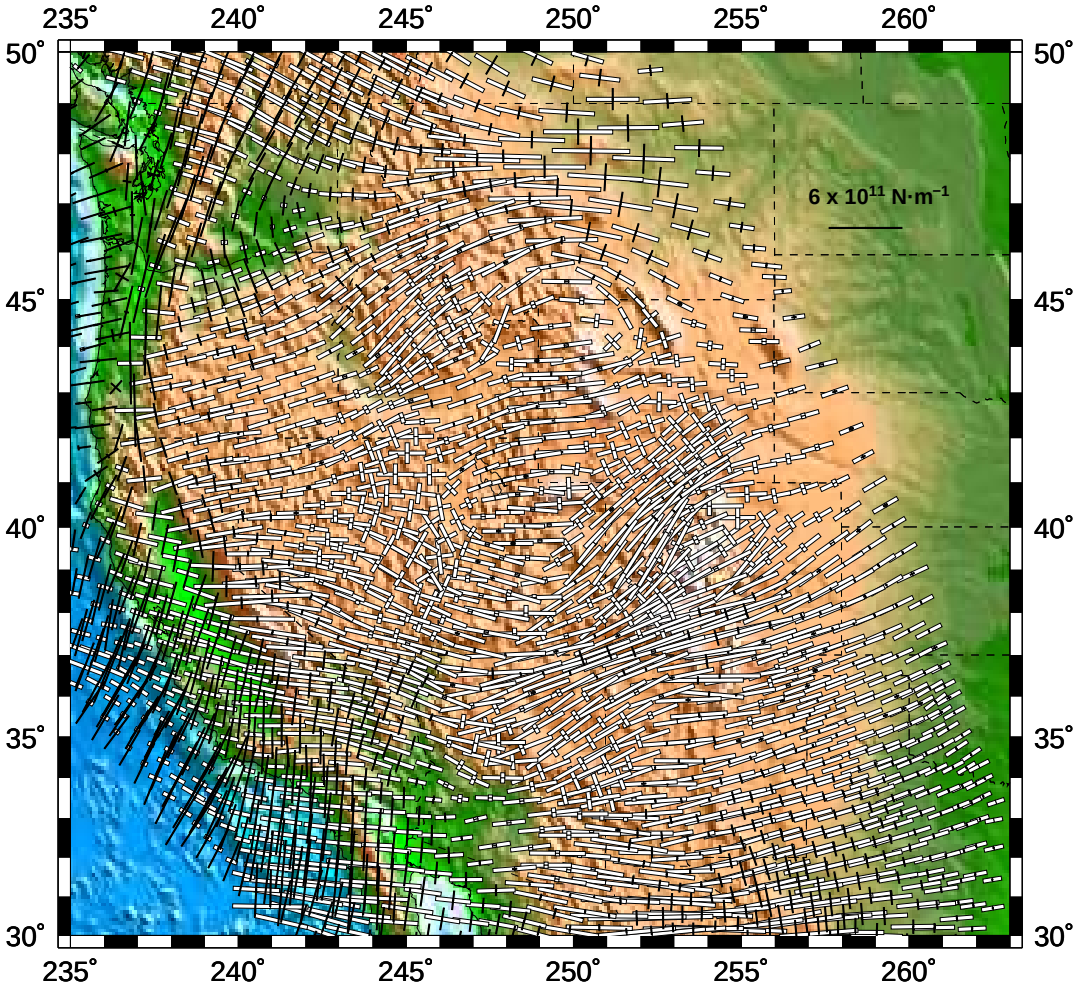

Figure 3.7: The forward dynamic depth-integrated deviatoric stress field solution associated with the weak fault friction model ($\mu = 0.10$). White vectors represent tensional principal axes of deviatoric stress. Bold vectors represent compressional principal axes of compressional stress.

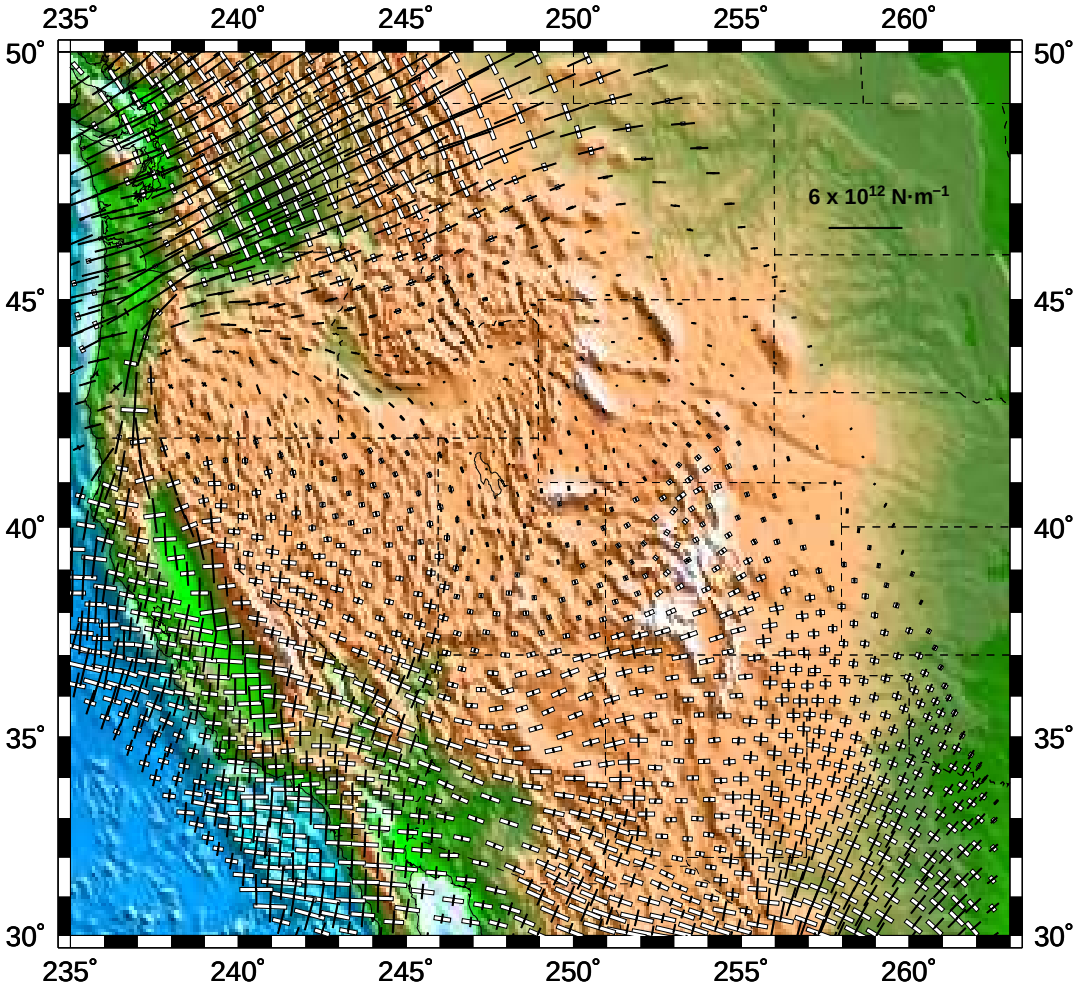

Figure 3.8: The forward dynamic depth-integrated deviatoric stress field solution associated with the strong fault friction model ($\mu = 0.70$). White vectors represent tensional principal axes of deviatoric stress. Bold vectors represent compressional principal axes of compressional stress.

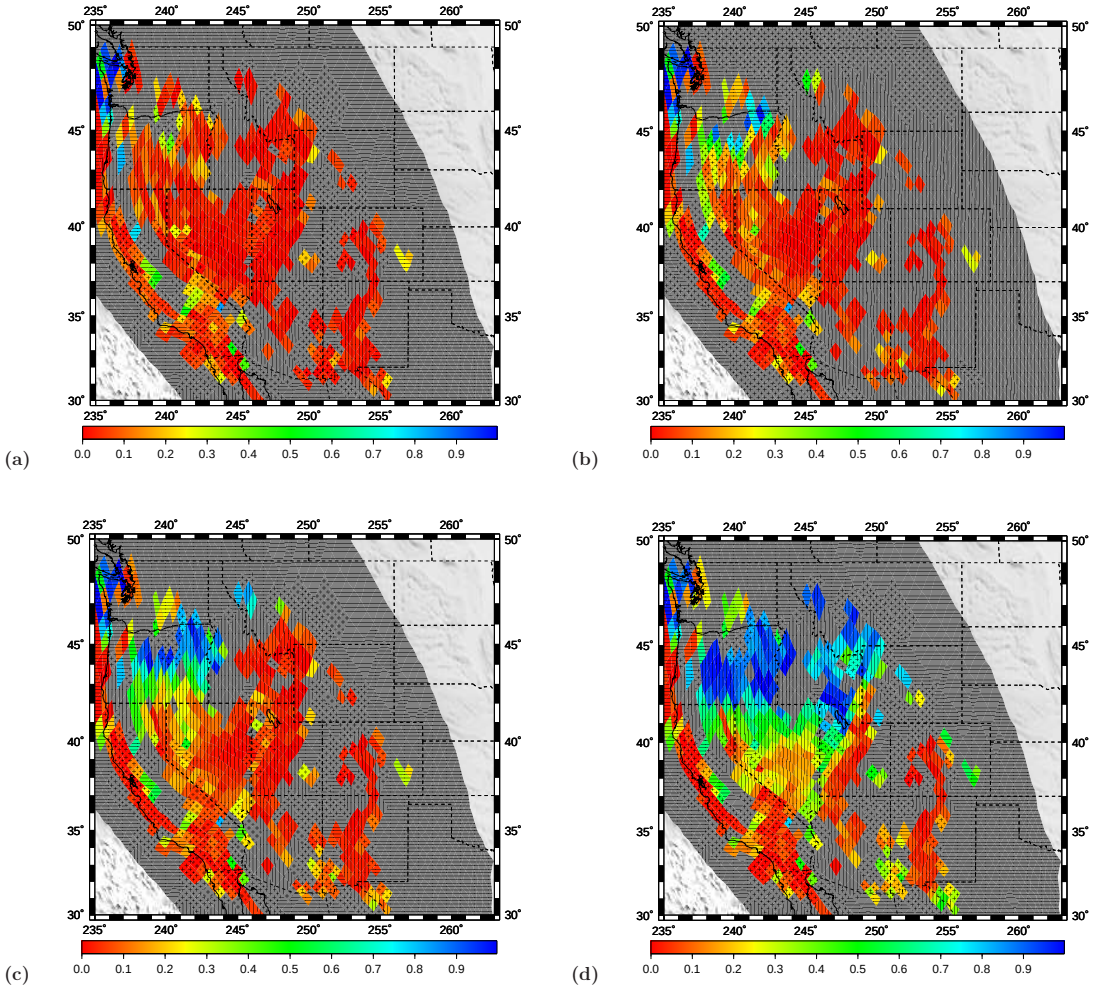

Figure 3.9: The distribution of misfit (defined in equation 3.9) for weak, intermediate, and strong fault friction models. The misfit function quantifies the agreement between the unit tensors from the depth-integrated deviatoric stress fields obtained from forward modeling with the long-term strain rate field inferred from Kostrov summation of faults (see in Figure 3.2). The forward model with effective depth-integrated viscosities defined with low friction on faults ($\mu = 0.10$) provides a best-fit to long-term observations of styles of strain rate. The misfit function values are plotted on top of pure tectonic regimes defined by the long-term strain rate tensor field solution (Figure 3.4). Vertical rule indicates normal faulting style, horizontal is thrust, and cross is strike-slip. (a) Misfit values with $\mu = 0.10$ on the faults. (b) Misfit values with $\mu = 0.20$ on the faults. (c) Misfit values with $\mu = 0.30$ on the faults. (d)Misfit values with $\mu = 0.70$ on the faults.

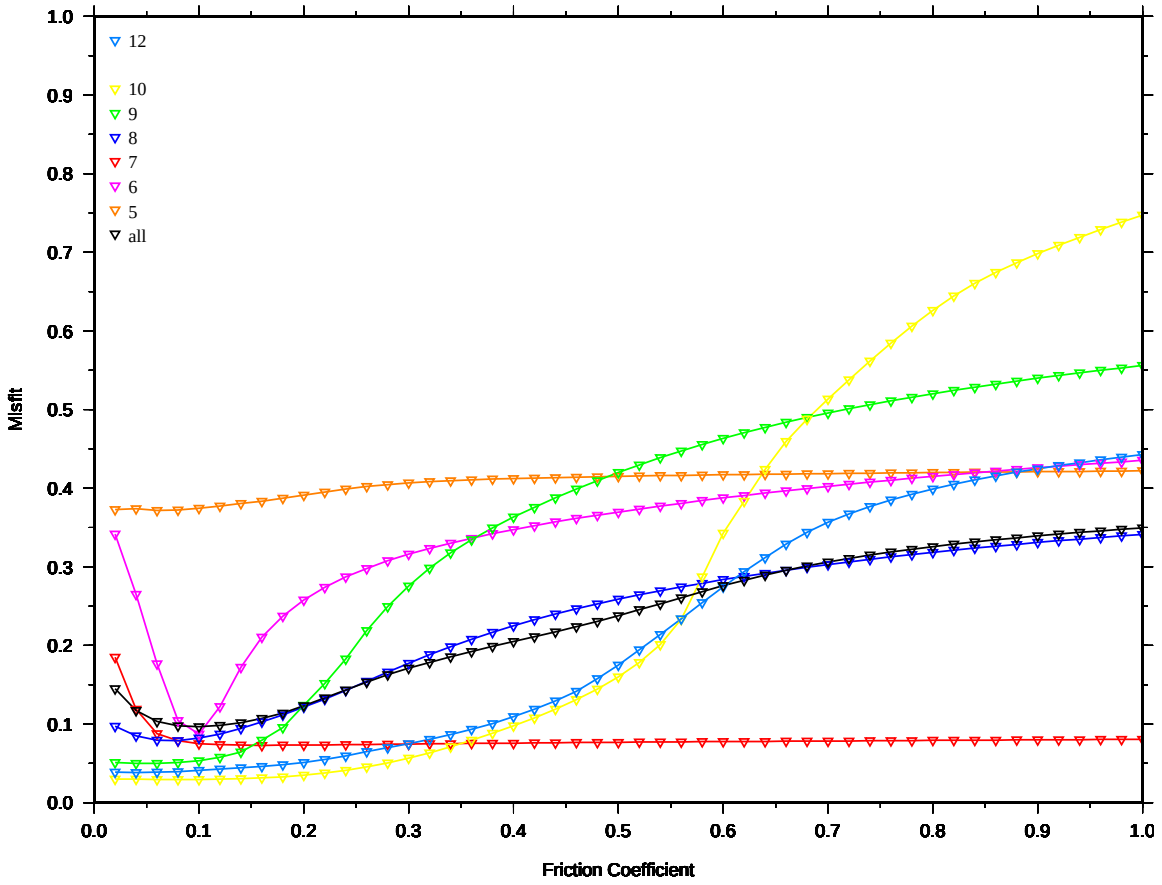

Figure 3.10: Misfit as a function of long-term friction coefficient used in the forward dynamic models for all grid elements as well as for regions well constrained by geologic fault data (asterisked entries in the legend of Figure 3.1). The misfit quantifies the agreement between the unit tensors from the depth-integrated deviatoric stress field obtained from forward modeling, and the long-term strain rate field inferred from Kostrov summation of the faults from Quaternary observations. Minimum misfit occurs for most regions where long-term friction coefficients on the faults are low, close to $\mu = 0.10$.

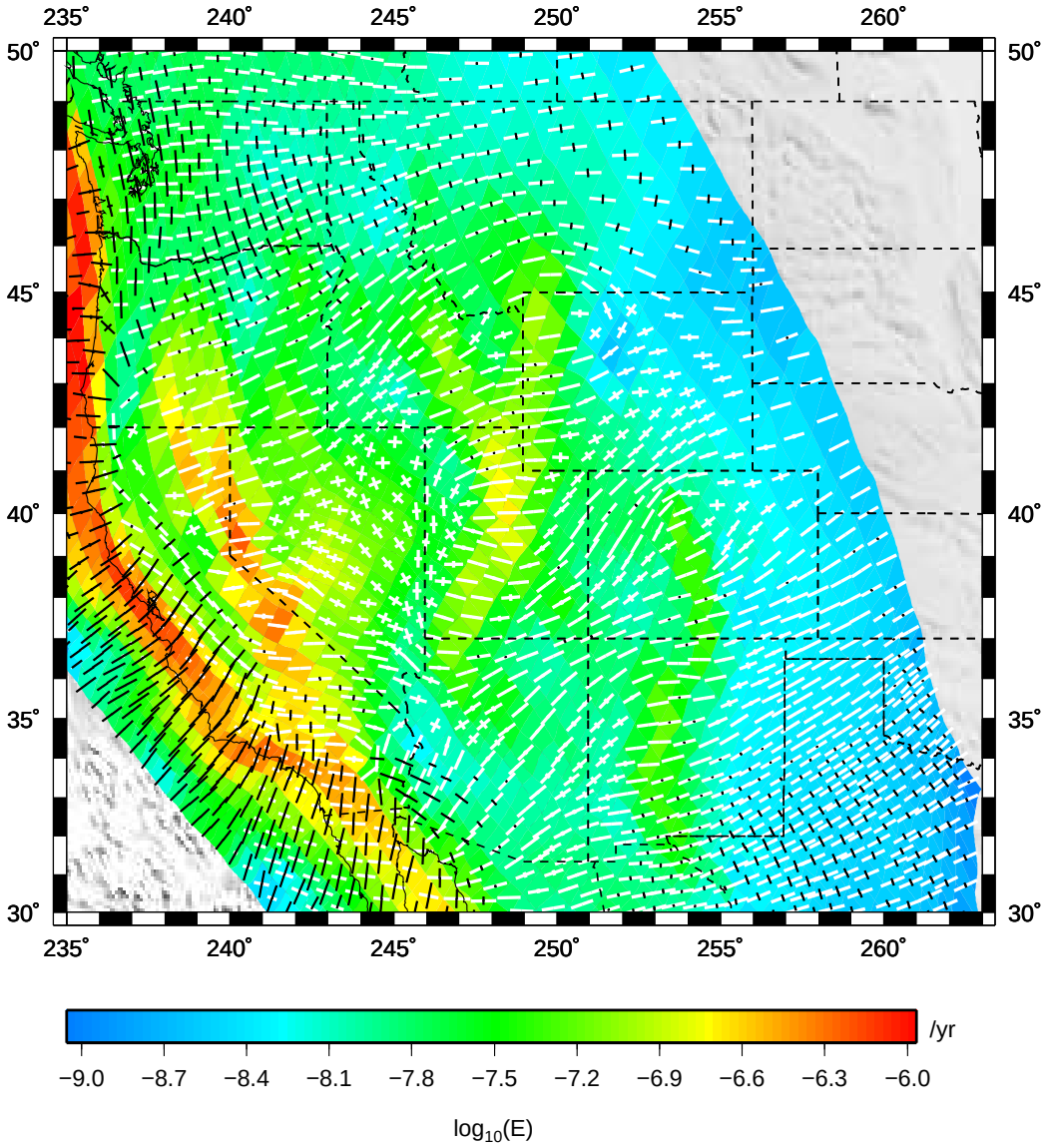

Figure 3.11: The forward dynamic strain rate tensor field for the case of a seismogenic crust defined with $\mu = 0.02$ on the faults. Principal axes of strain rates (area averages) have been normalized by the maximum value of the principal axis strain rate within each grid area (bold = compressional, white = extensional). Color background is the log of the second invariant of strain rate (area averages).

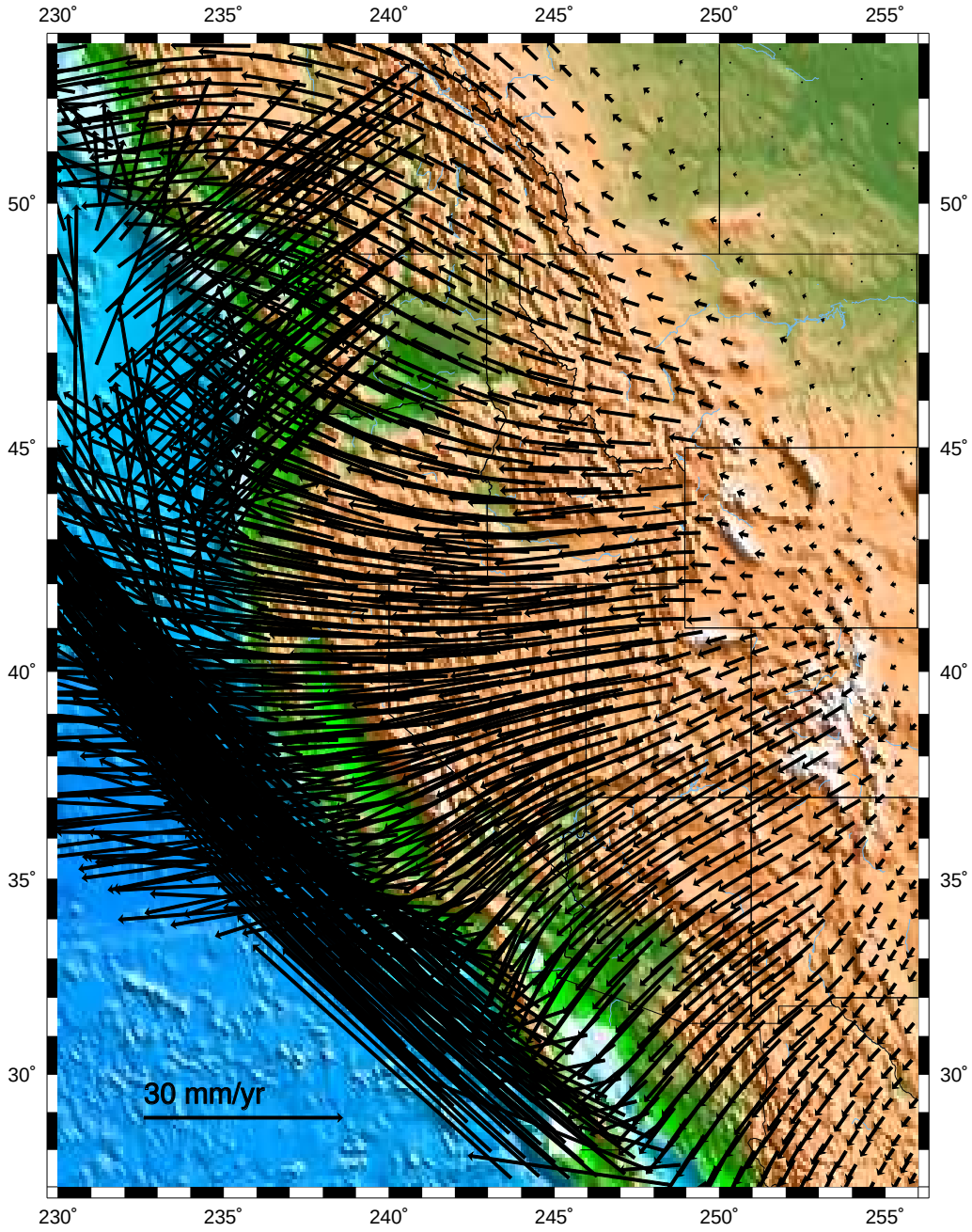

Figure 3.12: The forward dynamic velocity field for the case of a seismogenic crust defined with $\mu = 0.02$ on the faults.

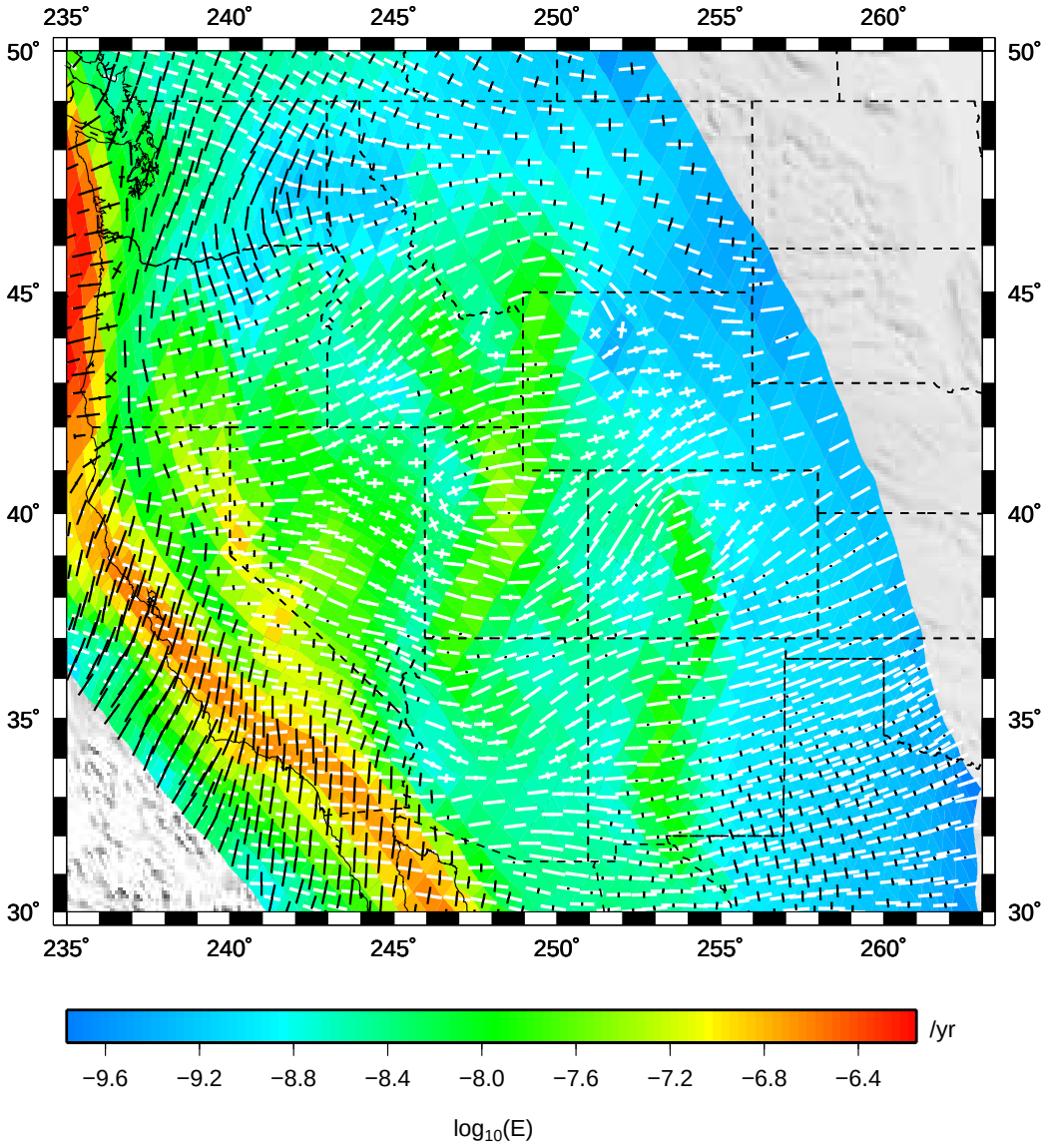

Figure 3.13: The forward dynamic strain rate tensor field for the case of a seismogenic crust defined with $\mu = 0.10$ on the faults. Principal axes of strain rates (area averages) have been normalized by the maximum value of the principal axis strain rate within each grid area (bold = compressional, white = extensional). Color background is the log of the second invariant of strain rate (area averages). This forward dynamic strain rate tensor field achieves a best-fit to the long-term strain rate field inferred from Kostrov summation of the faults from Quaternary observations (see Figure 3.9).

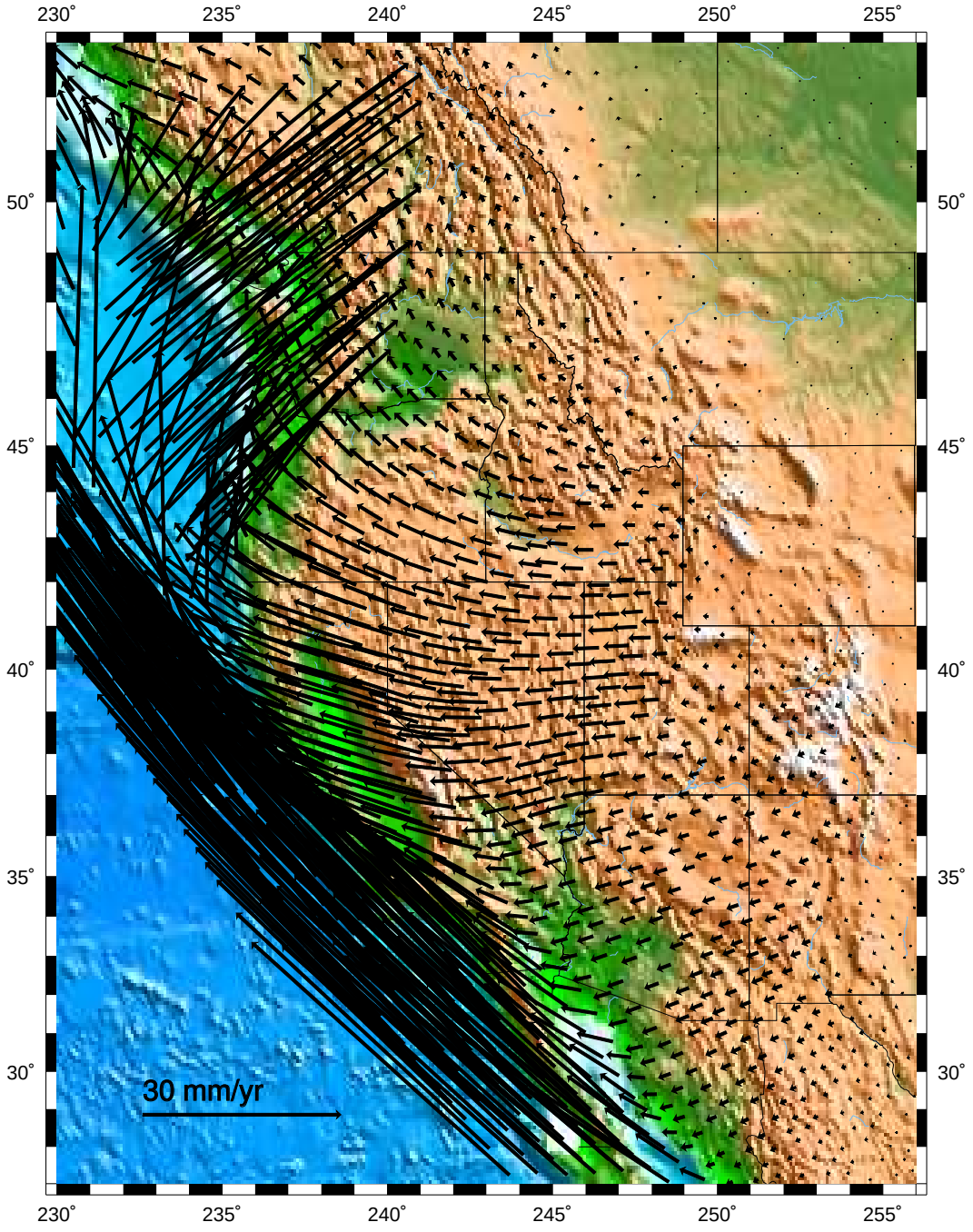

Figure 3.14: The forward dynamic velocity field for the case of a seismogenic crust defined with $\mu = 0.10$ on the faults.

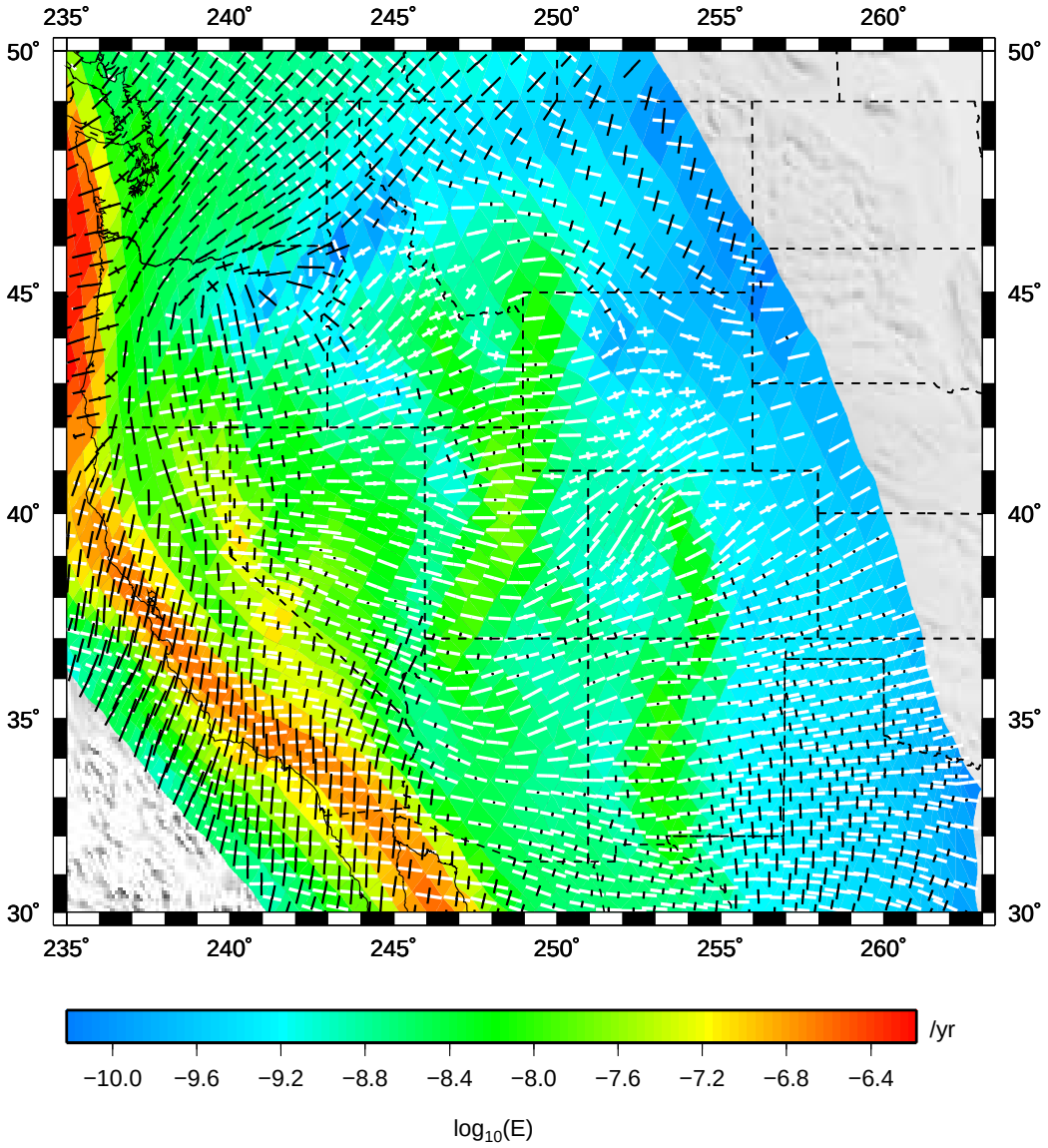

Figure 3.15: The forward dynamic strain rate tensor field for the case of a seismogenic crust defined with $\mu = 0.20$ on the faults. Principal axes of strain rates (area averages) have been normalized by the maximum value of the principal axis strain rate within each grid area (bold = compressional, white = extensional). Color background is the log of the second invariant of strain rate (area averages).

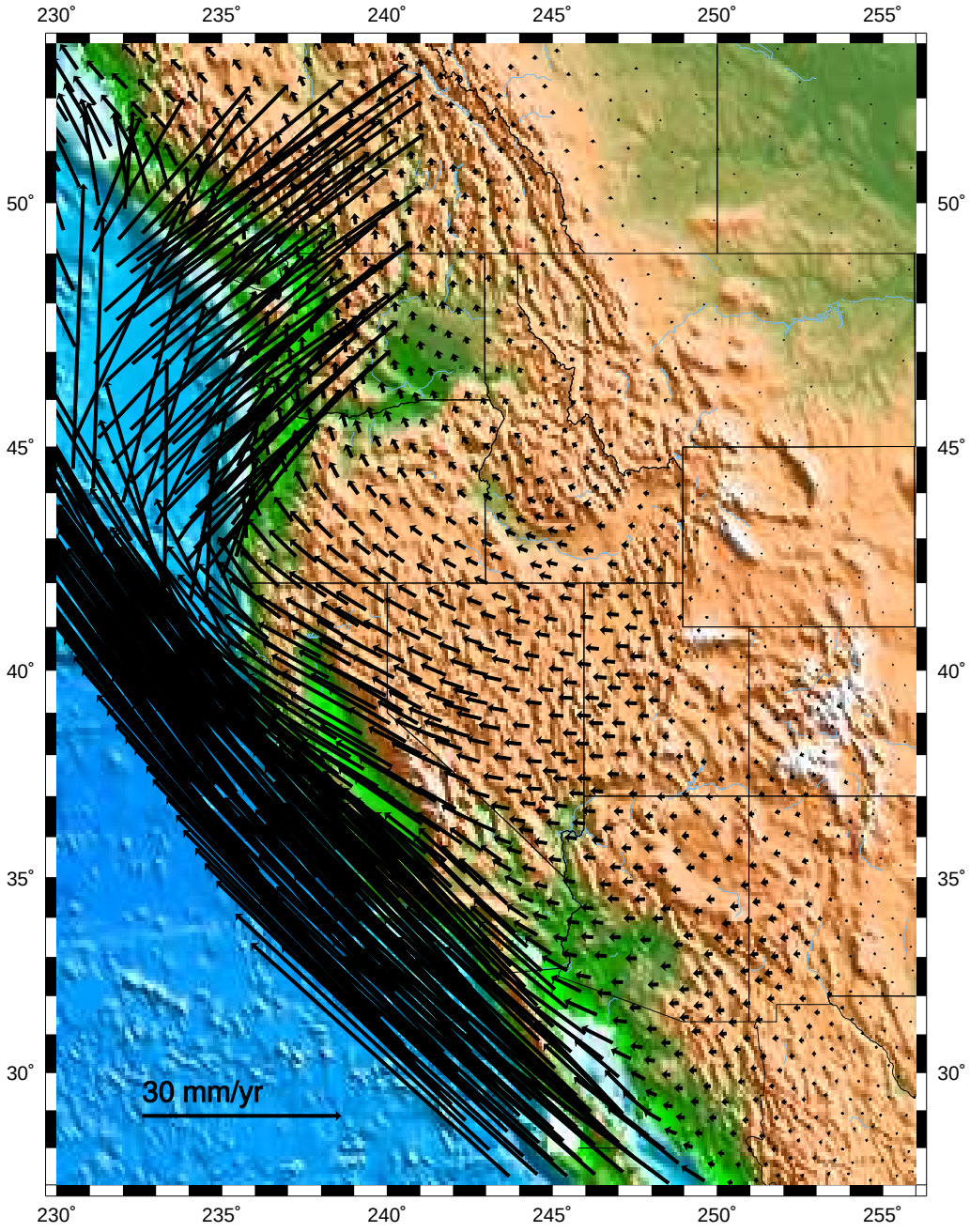

Figure 3.16: The forward dynamic velocity field for the case of a seismogenic crust defined with $\mu = 0.20$ on the faults. The dynamic velocities obtained with this fault friction model achieve the minimum reduced chi-square misfit with the long-term kinematic velocities shown in Figure 3.4.

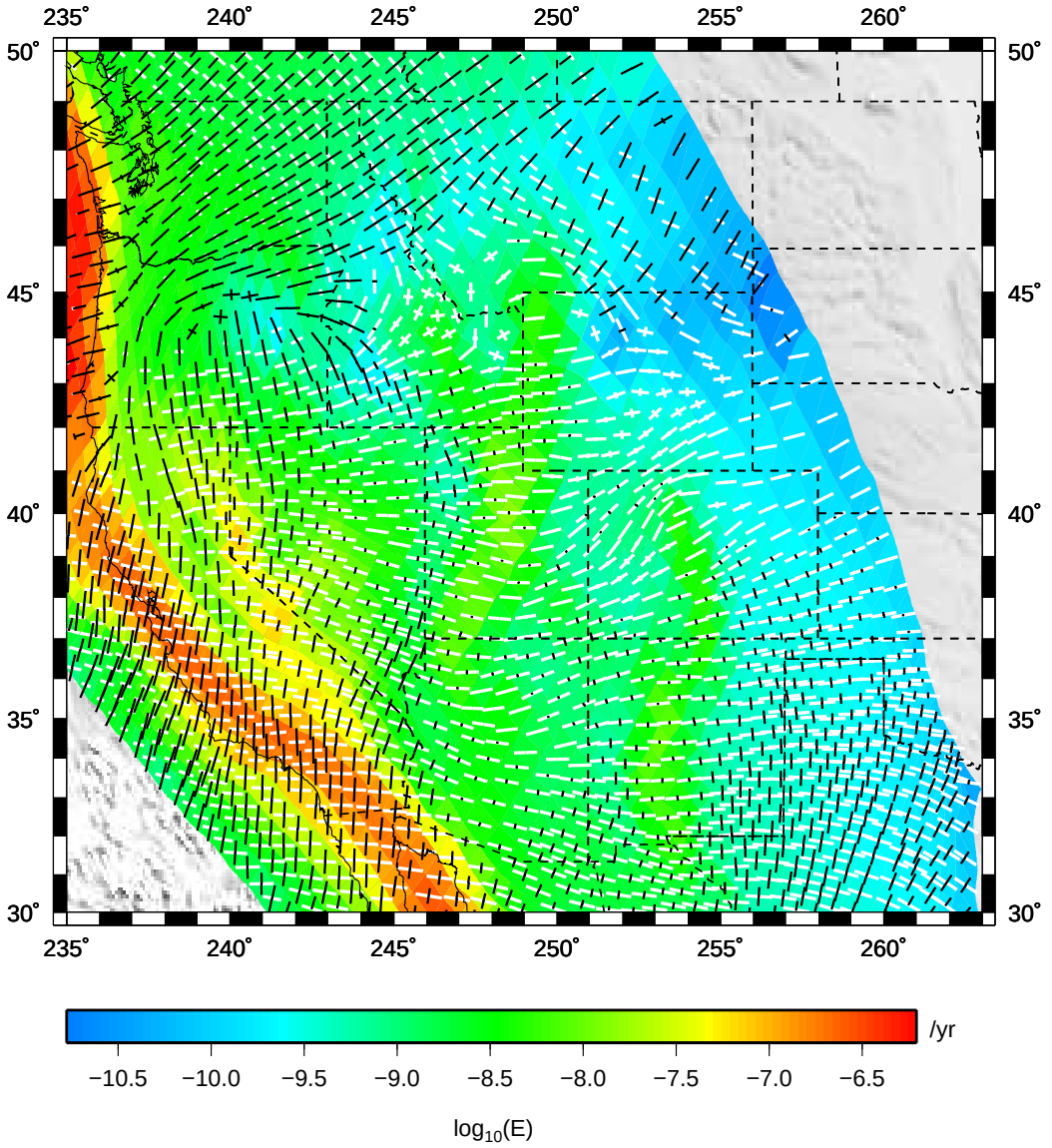

Figure 3.17: The forward dynamic strain rate tensor field for the case of a seismogenic crust defined with $\mu = 0.30$ on the faults. Principal axes of strain rates (area averages) have been normalized by the maximum value of the principal axis strain rate within each grid area (bold = compressional, white = extensional). Color background is the log of the second invariant of strain rate (area averages).

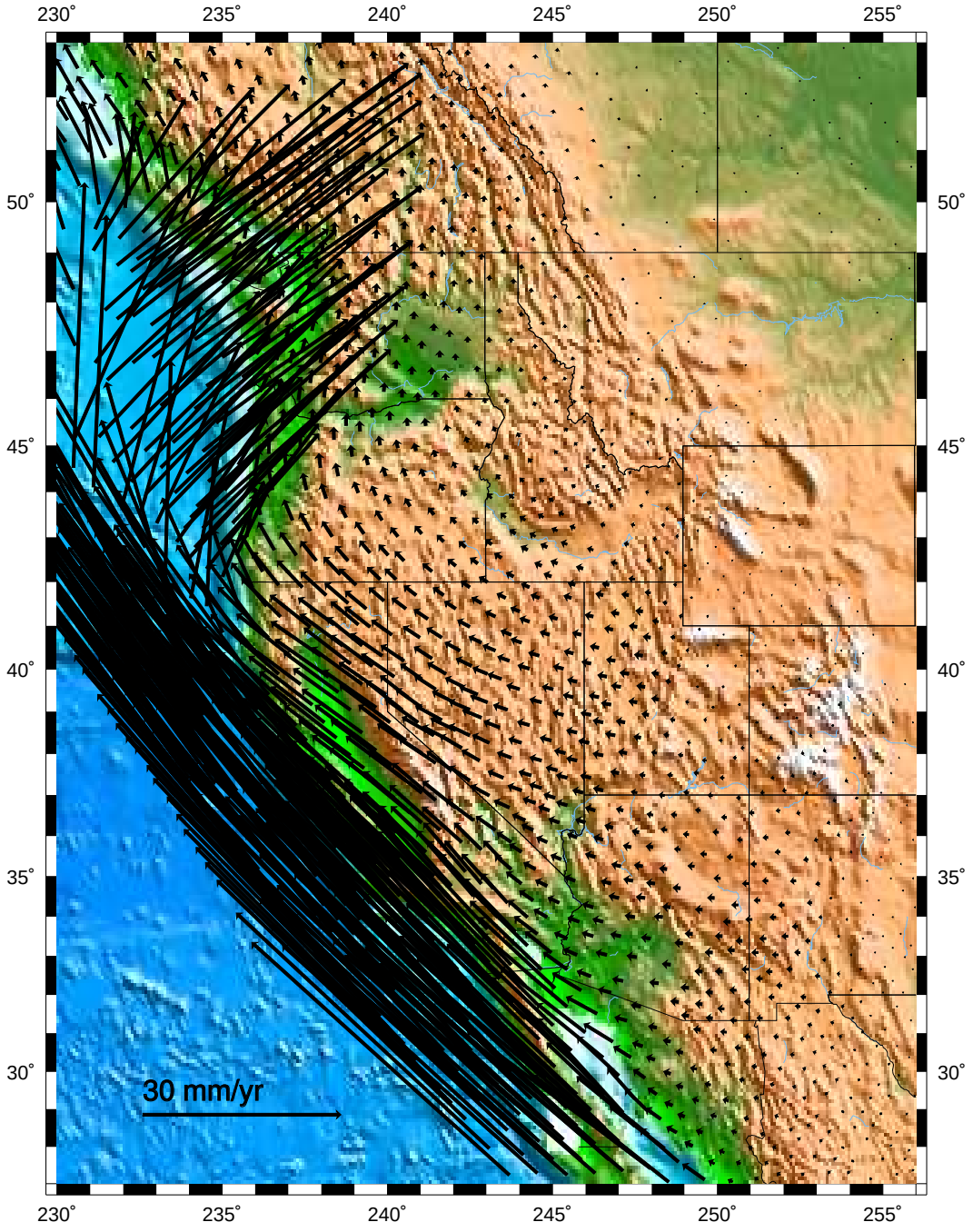

Figure 3.18: The forward dynamic velocity field for the case of a seismogenic crust defined with $\mu = 0.30$ on the faults.

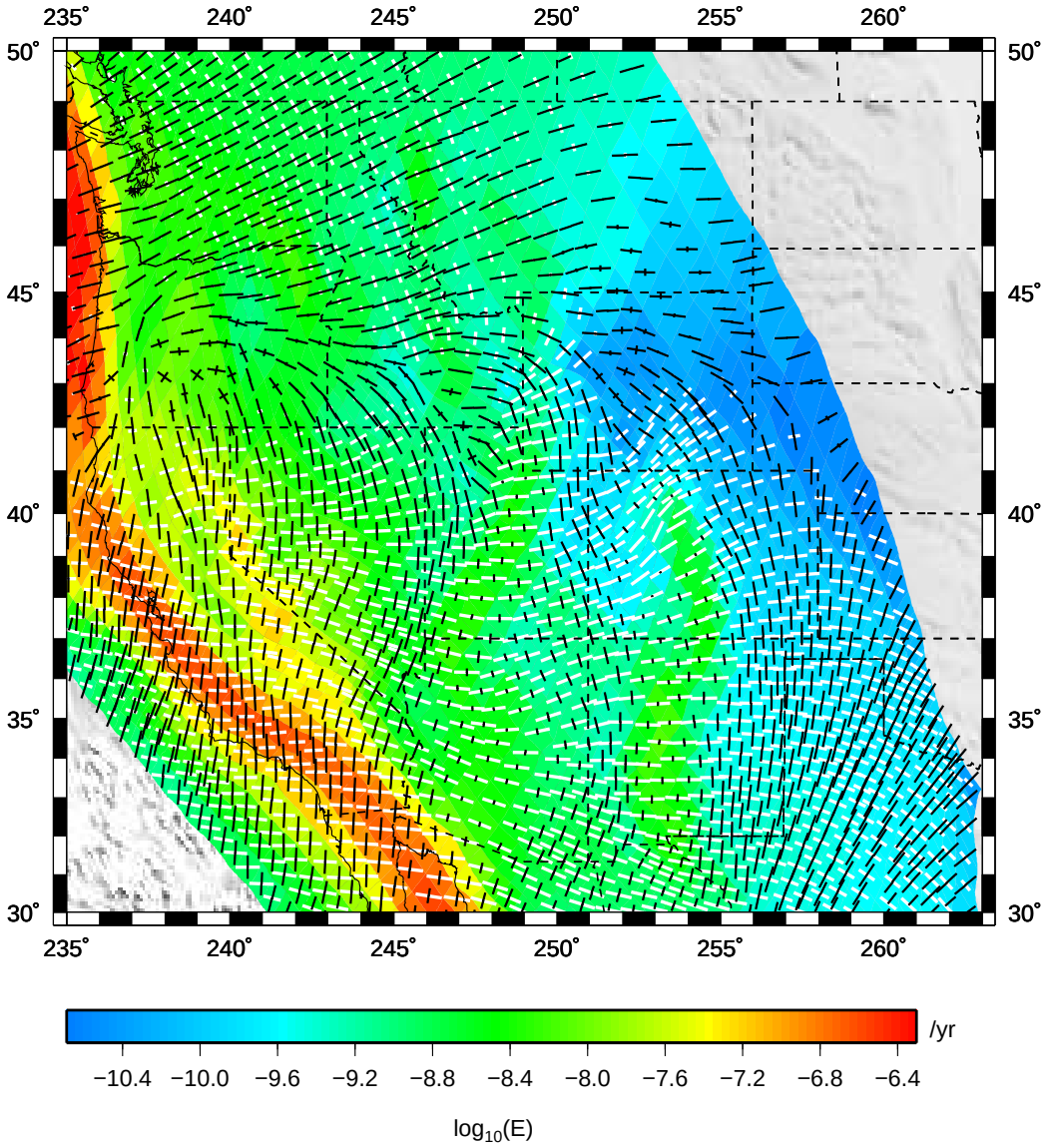

Figure 3.19: The forward dynamic strain rate tensor field for the case of a seismogenic crust defined with $\mu = 0.70$ on the faults. Principal axes of strain rates (area averages) have been normalized by the maximum value of the principal axis strain rate within each grid area (bold = compressional, white = extensional). Color background is the log of the second invariant of strain rate (area averages).

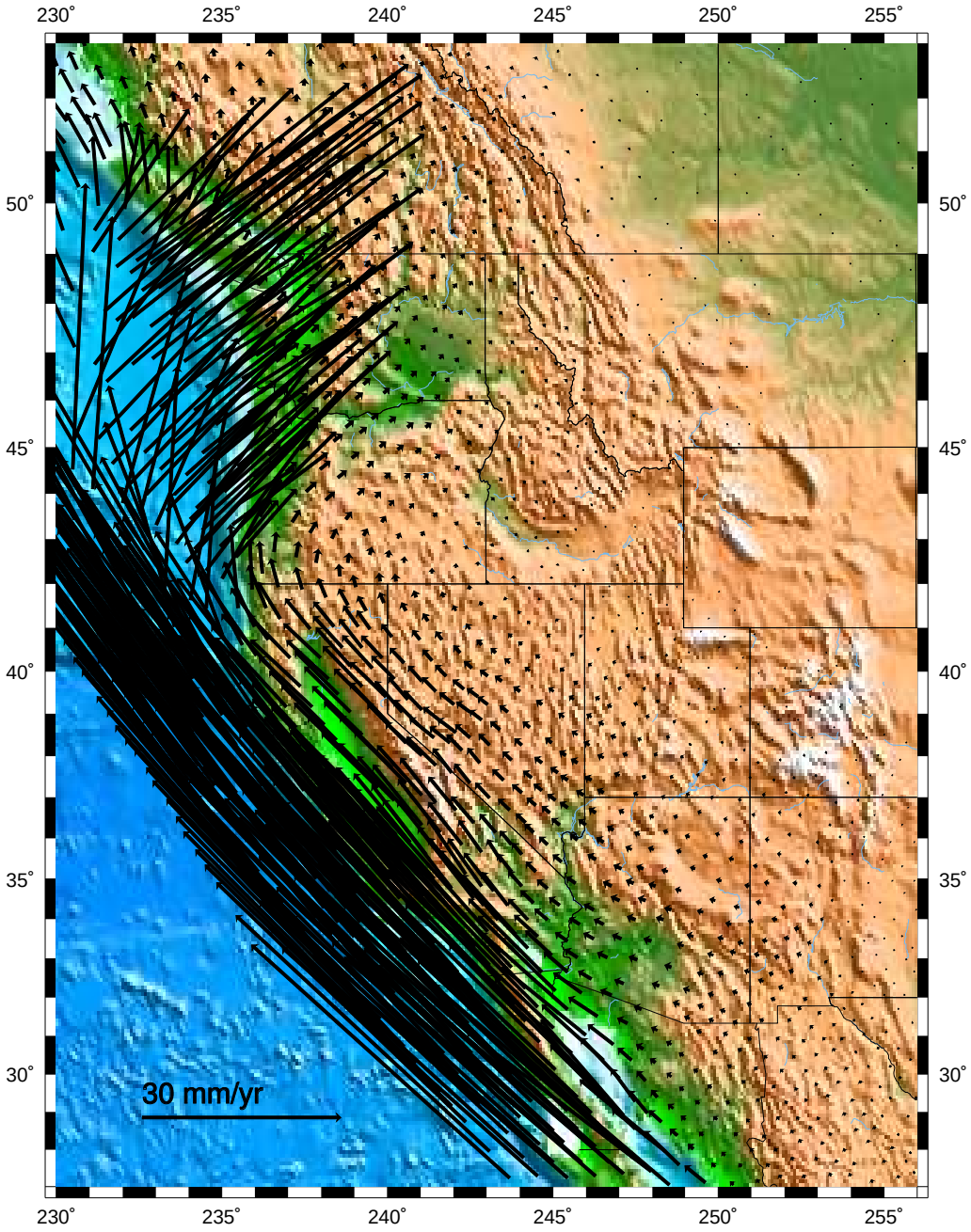

Figure 3.20: The forward dynamic velocity field for the case of a seismogenic crust defined with $\mu = 0.70$ on the faults. The dynamic velocities obtained with this fault friction model achieve a poor minimum reduced chi-square misfit with the long-term kinematic velocities shown in Figure 3.4.

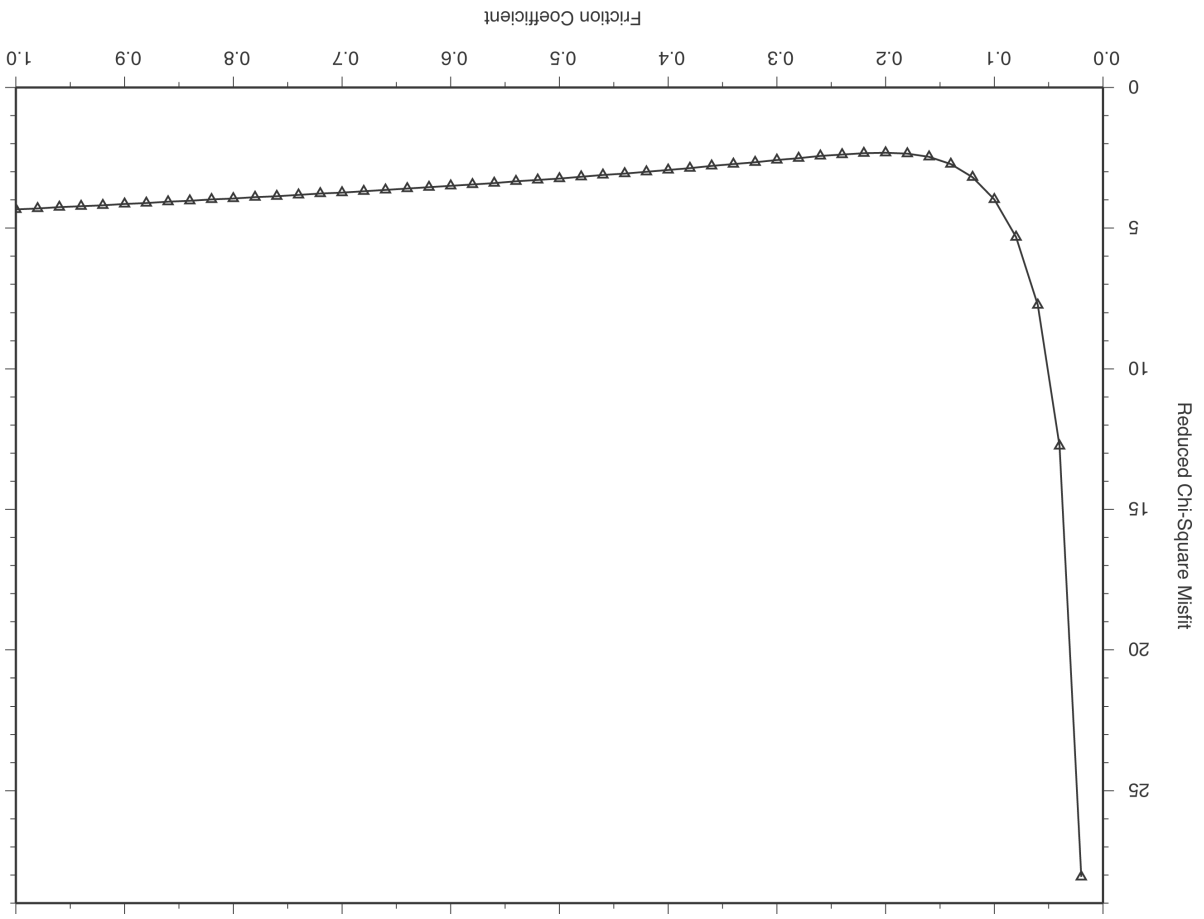

Figure 3.21: Reduced chi-square misfit for 1517 points in model region (see Figure 3.22) between long-term velocity field and that predicted by dynamic model with given friction coefficient on dense network of faults. Minimum reduced chi-square misfit occurs with low long-term fault friction coefficients.

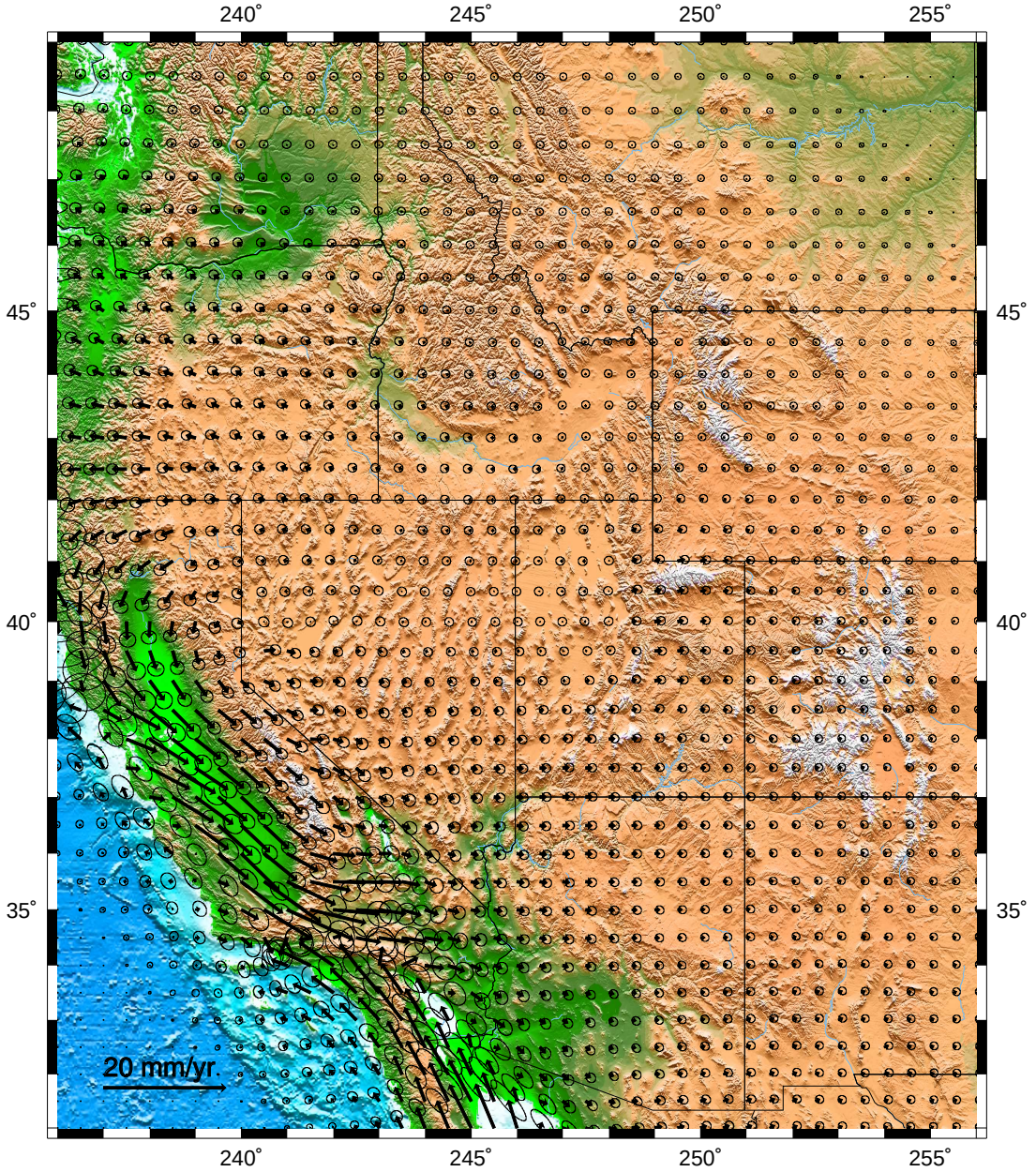

Figure 3.22: The velocity difference field between the minimum reduced chi-square misfit forward dynamic and the long-term kinematic velocity models. The minimum reduced chi-square misfit is obtained with a uniform value of $\mu = 0.20$ on faults of the seismogenic crust.

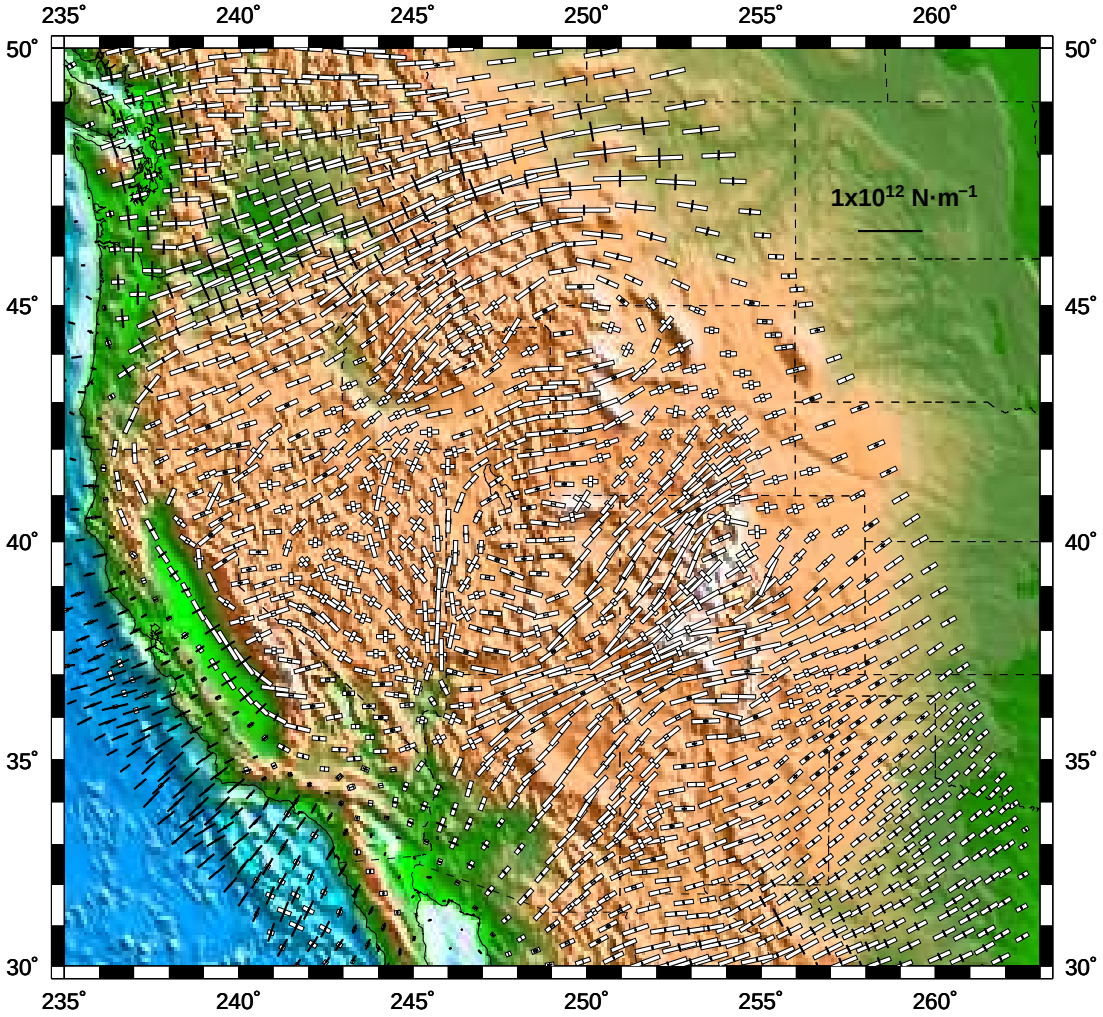

Figure 3.23: The depth-integrated deviatoric stress field associated with gravitational potential energy differences (GPE) for the weak fault friction model ($\mu = 0.10$). White vectors represent tensional principal axes of deviatoric stress. Bold vectors represent compressional principal axes of compressional stress.

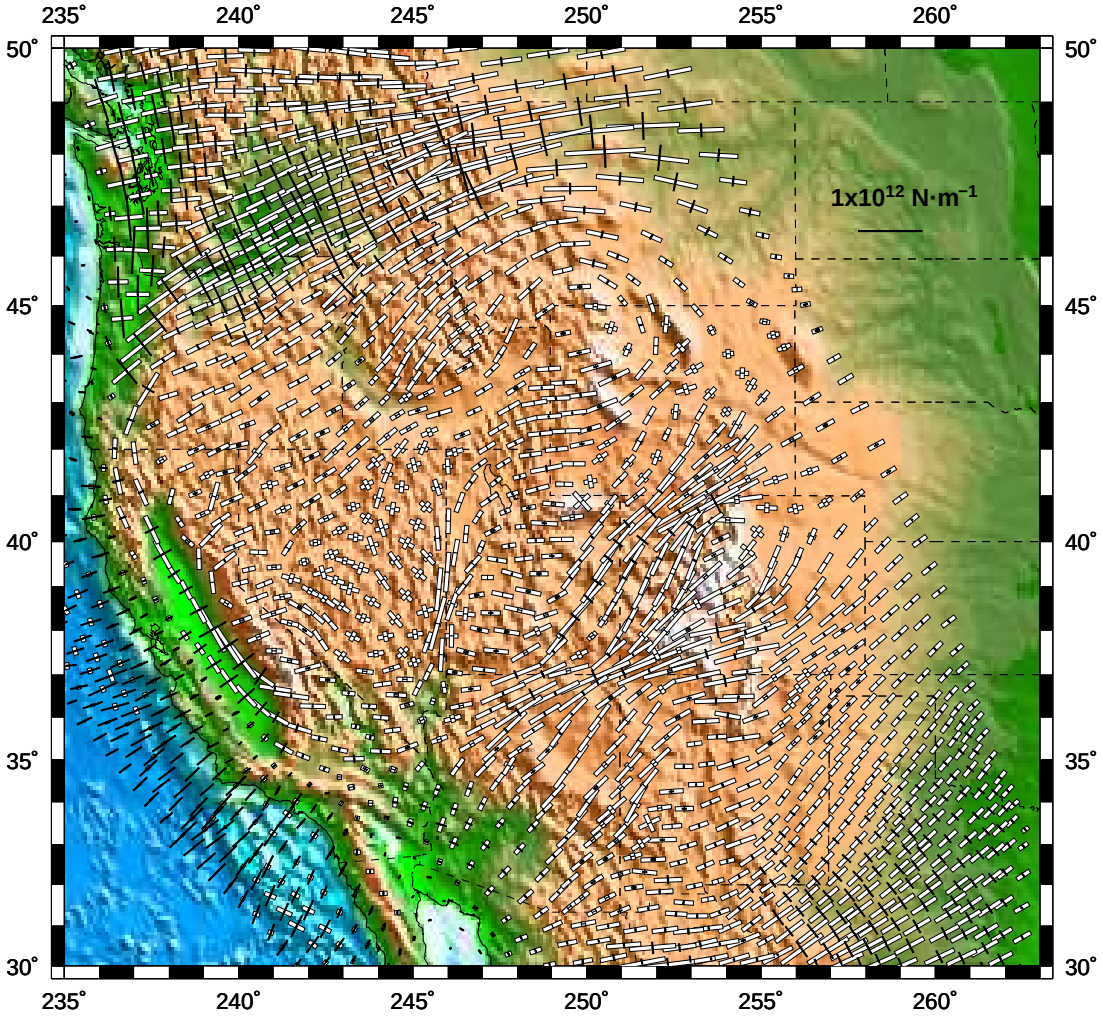

Figure 3.24: The depth-integrated deviatoric stress field associated with gravitational potential energy differences (GPE) for the strong fault friction model ($\mu = 0.70$). White vectors represent tensional principal axes of deviatoric stress. Bold vectors represent compressional principal axes of compressional stress.

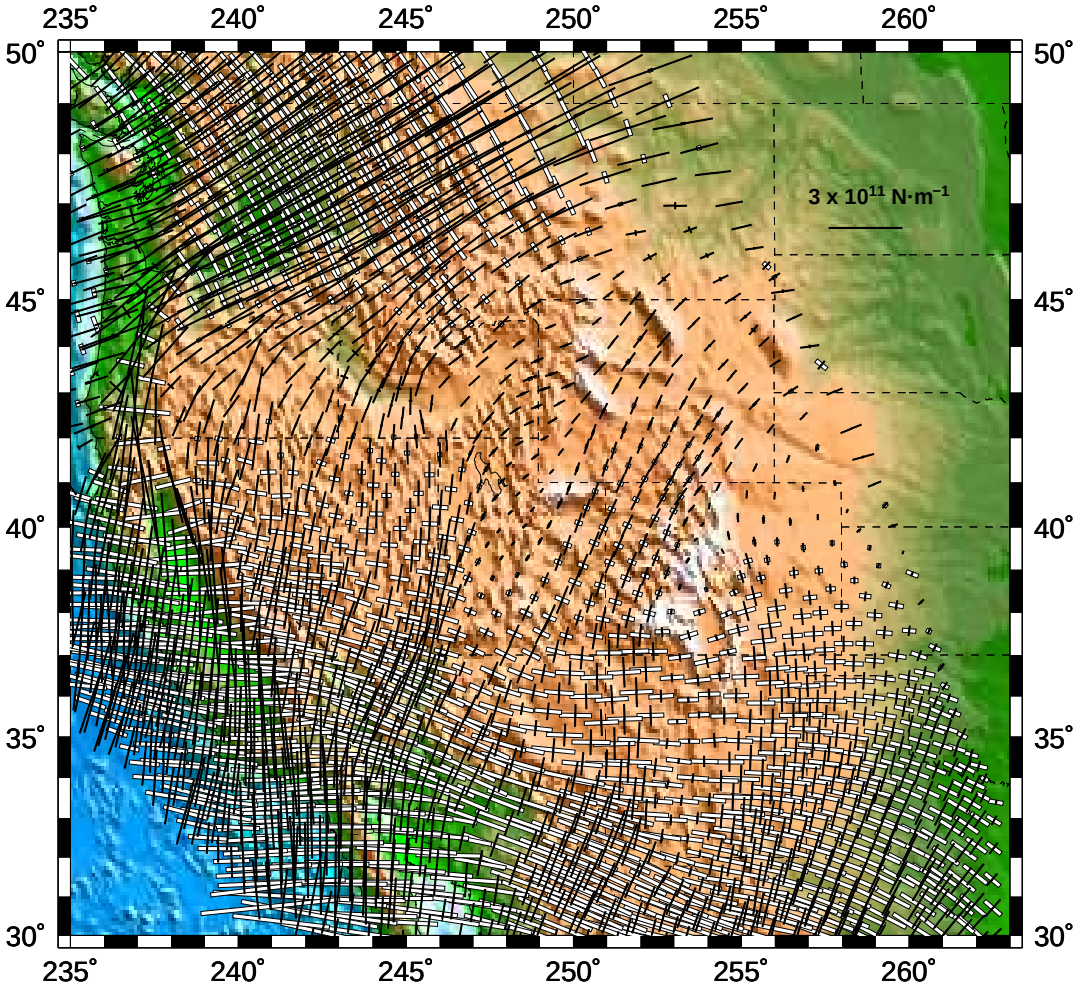

Figure 3.25: The forward dynamic depth-integrated deviatoric stress field associated with velocity boundary conditions for the weak fault friction model ($\mu = 0.10$). White vectors represent tensional principal axes of deviatoric stress. Bold vectors represent compressional principal axes of compressional stress.

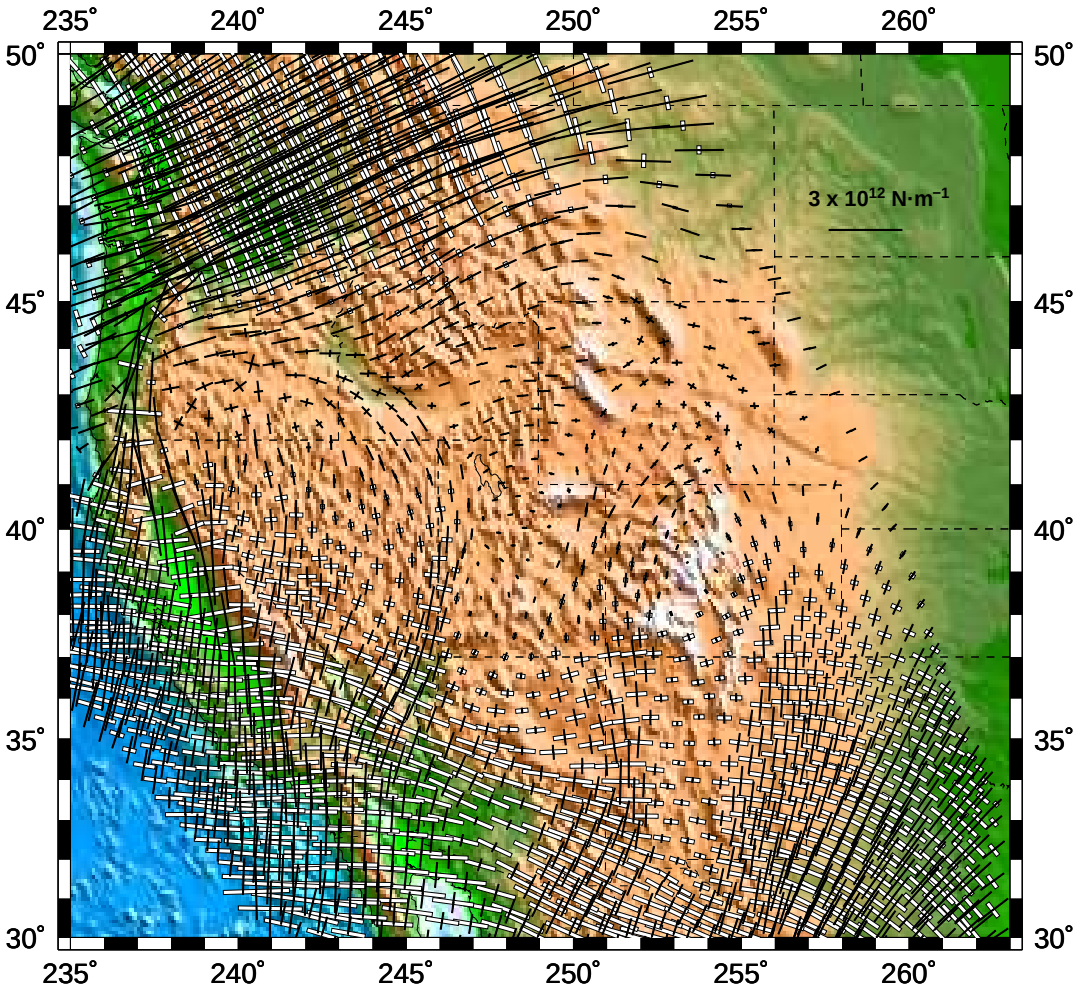

Figure 3.26: The forward dynamic depth-integrated deviatoric stress field associated with velocity boundary conditions for strong fault friction model ($\mu = 0.70$). White vectors represent tensional principal axes of deviatoric stress. Bold vectors represent compressional principal axes of compressional stress.

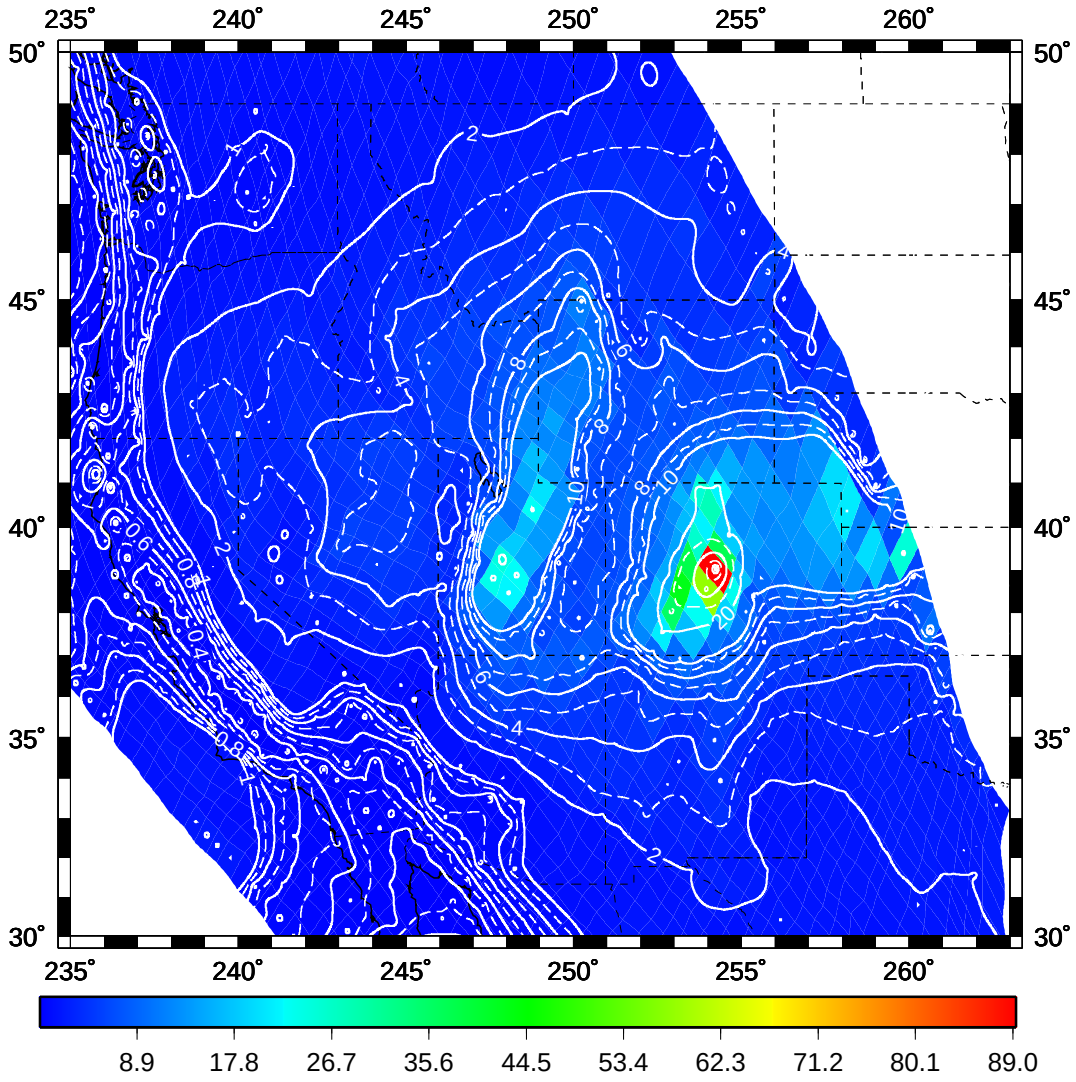

Figure 3.27: The Argand number distribution associated with the weak fault model ($\mu = 0.10$) that achieves a best-fit to the long-term deformation indicators (see text for description and Figures 3.10 and 3.9a).

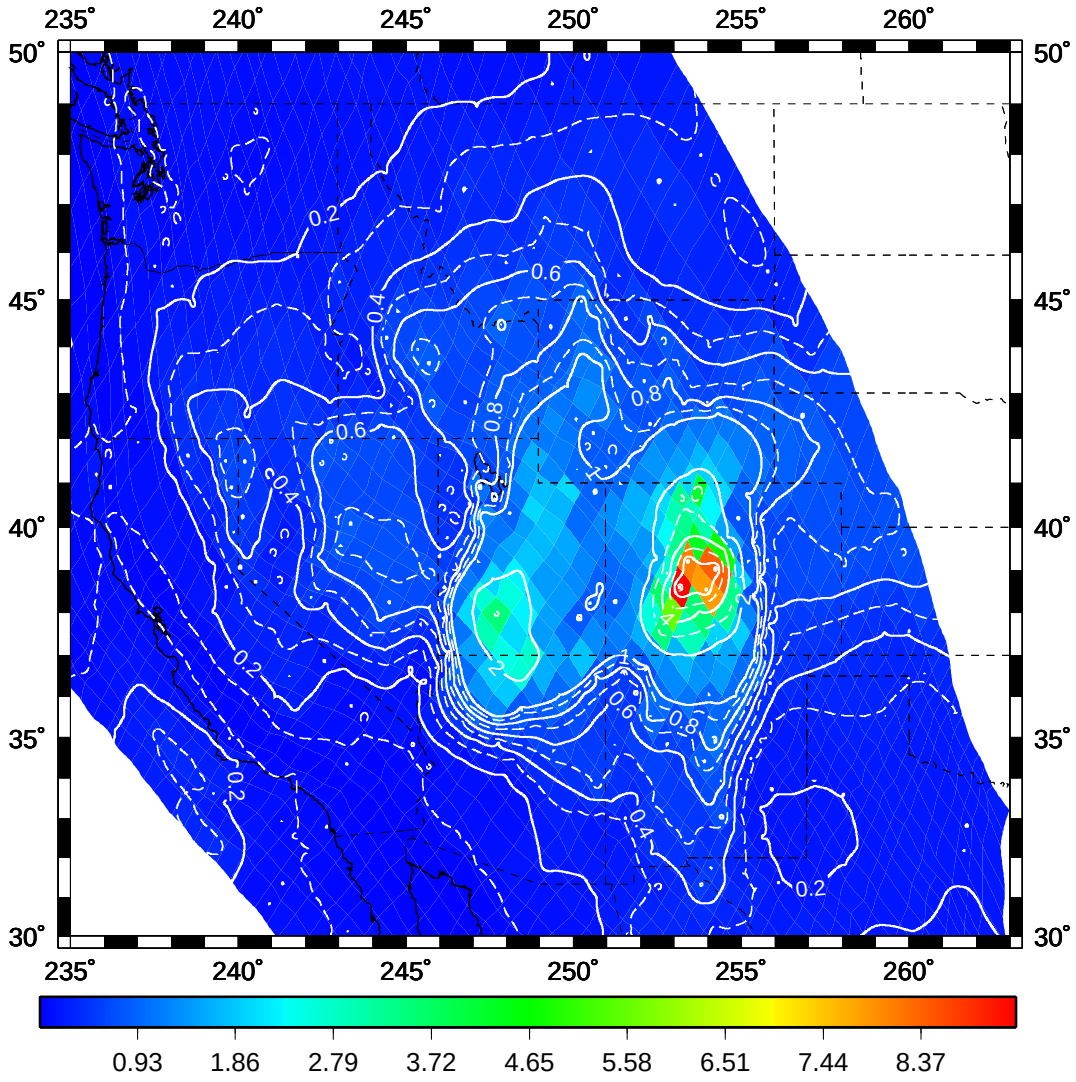

Figure 3.28: The Argand number distribution associated with the strong fault model($\mu = 0.70$) that achieves a poor fit to long-term deformation indicators (see text for description and Figures 3.10 and 3.9c).

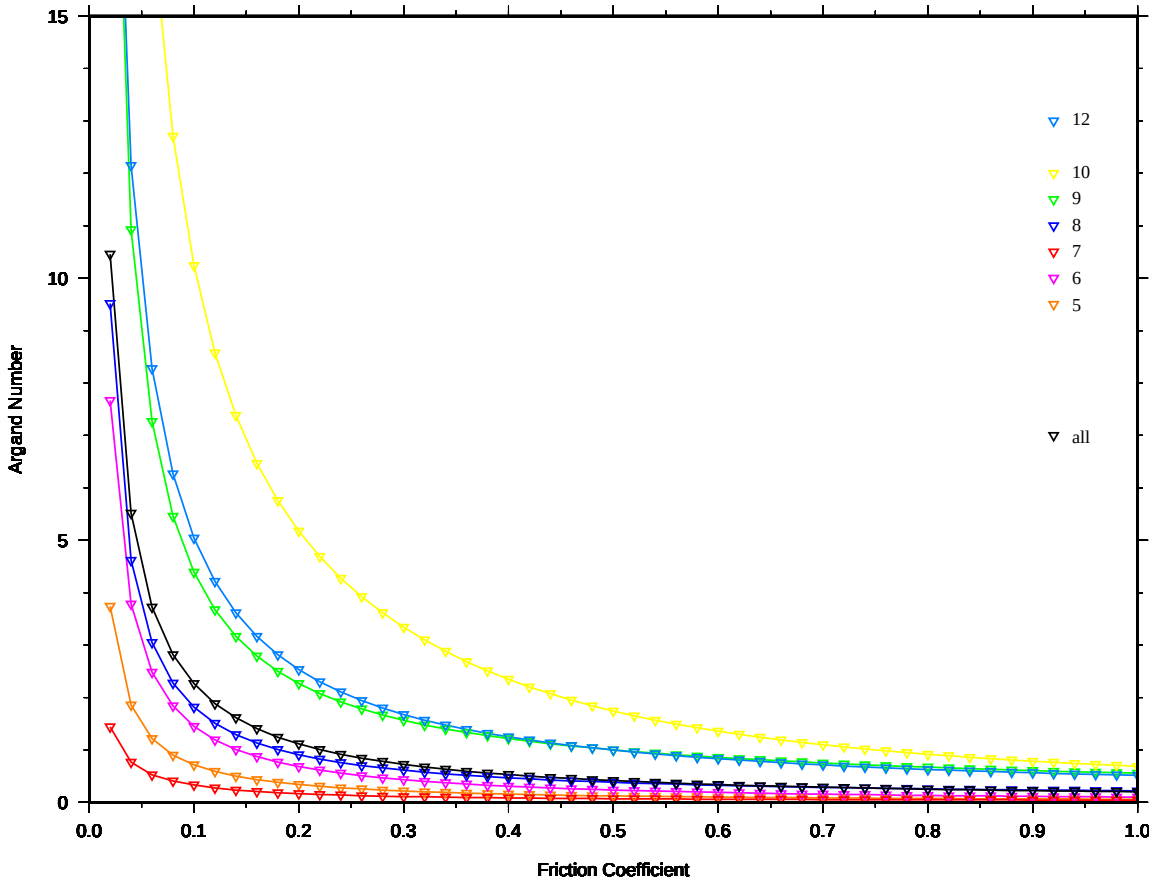

Figure 3.29: Argand number as a function of long-term friction coefficient used in the forward dynamic models for all grid elements (numbered regions correspond to asterisked entries in the legend of Figure 3.1).

Chapter 4

Crustal dynamics within Western North America: Is it block-like or more evenly distributed?

Crustal dynamics within Western North America:

Is it block-like or more evenly distributed?

Elliot C. Klein, Lucy M. Flesch, William E. Holt, and A. John Haines

(In preparation for submission to *Earth and Planetary Science Letters*)

Abstract We investigate the dynamics that result from specific block-like geometries for the crust of western North America. The block model geometries contain block-bounding shear zones with low fault friction and block interiors with high crustal friction. The forward dynamic models we build and test incorporate internal body force distributions, the effects of plate interaction through imposed velocity boundary conditions, and lateral viscosity variations defined by block model geometries. We score our self-consistent dynamic model output with detailed kinematic output to explore the controversy of whether block-like behavior, or a more distributed fabric of faults, is consistent with the observed patterns of finite strain within the diffuse plate boundary zone. Observations from Quaternary fault networks provide a set of unparalleled constraints with which to test and evaluate our forward dynamic block models. Block model geometries yield depth-integrated deviatoric stresses associated with velocity boundary conditions (accommodation of plate motions) that dominate over the deviatoric stresses associated with GPE differences. Dynamic solutions generated with block model geometries do not match the long-term patterns of finite strain everywhere in western North America. Argand number distributions associated with block model geometries are much lower than those produced with a best-fit, low uniform fault friction model defined with a more evenly distributed fault fabric.

4.1 Introduction

Diverse models of continental deformation in western North America impart fundamental insight into the physics of diffuse plate boundary deformation. One end-member model of continental deformation convincingly argues for block-like behavior to explain the interseismic deformation field in western North America [*Meade and Hager*, 2005; *McCaffrey*, 2005; *McCaffrey et al.*, 2007; *Hammond and Thatcher*, 2004, 2005, 2007]. The block models successfully describe the fundamental observation from GPS that deformation appears to be concentrated within relatively narrow shear zones. The other end-member model of the continental deformation argues for more distributed deformation in western North America [*Sonder and Jones*, 1999; *Shen-Tu et al.*, 1999; *Flesch et al.*, 2000; *Liu and Bird*, 2002; *Flesch et al.*, 2007; *Humphreys and Coblentz*, 2007; *Liu et al.*, 2007]. The advantage of the continuum dynamics approach is that the forces responsible for deformation can be explicitly dealt with. However, such continuum models require lateral variations in effective rheology in order to reproduce the deformation gradients. Block models may successfully match the kinematics, but what are the set of forces that move the blocks? Because block model methods are purely kinematic, the forces remain unknown and as such, these models cannot define the underlying dynamics of crustal motions. Furthermore, a purely kinematic treatment makes it difficult to predict or understand deformation within low strain rate regions (block interiors), such as the February 21, 2008, 6.0 Mw, Wells, Nevada earthquake. This places fundamental limitations on our ability to interpret crustal motions in light of fault behavior, the role of crustal rheological variations, the role of internal crustal buoyancies, large-scale mantle circulation and coupling, and plate motion accommodation.

Flesch et al. [2007] and *Humphreys and Coblentz* [2007] have quantified the relative role of GPE differences, plate motion accommodation, and mantle convection-related

basal tractions, but these studies have not addressed how the relative forcings act on crustal block geometries, or existing fault compliance, to yield the long-term, and even interseismic deformation fields. We present a forward dynamic modeling approach to investigate the fundamental long-term behavior of the seismogenic crust in western North America. We investigate specific block models. For these dynamic models the long-term friction of the blocks, as well as the faults that bound the blocks, are defined, a priori. The forward models contain internal body force distributions, the effects of plate interaction through imposed velocity boundary conditions, and lateral viscosity variations that approximate fault-like and block-like distributions. Our analysis of the dynamics is firmly linked with quantitative comparisons of model predictions with surface observations possessing unprecedented detail.

4.2 Defining Block Geometries

In this study of the diffuse plate boundary zone of western North America, we quantify the dynamics associated with two different block model geometries. In one model geometry, called block model 1, block boundaries are defined by a set of Quaternary fault observations since 15,000 years and in the second model geometry, called block model 2, the block boundaries are defined by *McCaffrey* [2005]; *McCaffrey et al.* [2007]. The block model 1 geometry combines faults defined in the long-term kinematic models of *Flesch et al.* [2007] and *Klein et al.* [2008] with Quaternary fault slip rate estimates culled from the U.S. Geological Survey, 2006, Quaternary fault and fold database for the United States (accessed March 23, 2006, from USGS web site: http://earthquake.usgs.gov/regional/qfaults). We select from the Quaternary fault and fold database for the United States only those faults with established slip-sense and slip rate since 15 ka for block model 1. We do not incorporate additional faults or shear zones into block model 2 geometry defined by *McCaffrey* [2005]; *Mc-*

Caffrey et al. [2007]. For both block models, grid areas that do not contain faults are defined as block interiors and have assigned strong crustal friction coefficients. In addition, grid areas that contain faults are treated as block-bounding shear zones, defined with weak fault friction coefficients.

We utilize the long-term horizontal deformation field in western North America defined with Quaternary fault observations (see Figure 4.1) to provide the basis for evaluating the forward dynamic solutions associated with each of the block model geometries. As in Chapter 3, we follow the forward model methodology of *Flesch et al.* [2001] to define the internal body force distributions, known far-field velocity boundary conditions, and lateral variations in effective viscosity for the upper crust. However, lateral variations are controlled by the inferred friction of rock material, as well as the expected strain rate magnitude [*Klein et al.*, 2008]. Solutions to force-balance equations define self-consistent velocity, strain rate tensor, and stress tensor fields.

Flesch et al. [2001] show that a solution to the depth-integrated three-dimensional force balance equations is arrived at through the minimization of the functional

$$\Theta(v) = \int\int_s [D - v_\alpha f_\alpha]\, dxdy, \tag{4.1}$$

where f_α is the body force term associated with gradients in gravitational potential energy per unit area (GPE), v_α is the velocity, and D is the dissipation potential. The dissipation potential is expressed as

$$D = \frac{n}{n+1} B(\dot{\epsilon}_{\alpha\beta}\dot{\epsilon}_{\alpha\beta} + \dot{\epsilon}_{\gamma\gamma}\dot{\epsilon}_{\gamma\gamma})^{\frac{n+1}{2n}}), \tag{4.2}$$

depends on the components of strain rate, where $\dot{\epsilon}_{\gamma\gamma} = (\dot{\epsilon}_{xx} + \dot{\epsilon}_{yy}) = -\dot{\epsilon}_{zz}$, the value of B [*England and McKenzie*, 1982; *Sonder and England*, 1986], and the power law exponent n.

Optimization of equation 4.1 requires calculation of the optimal strain rate distribution (continuous velocity field) embedded in the dissipation potential, D, where the known velocity boundary conditions of PA-NA, JF-NA, CO-NA, and RV-NA are imposed in the dynamic modeling (see section 3.2 in Chapter 3). Also pre-defined are the internal body forces, defined by gradients in vertically integrated vertical stresses (GPE), and the B-value distribution [*Flesch et al.*, 2001]. The GPE distribution is the same as that defined by *Klein et al.* [2008].

In generating the forward model solutions of Chapter 3, we defined B-values dependent on uniform long-term friction on the faults, as well as the expected strain rates for the volumes containing the faults. In this study, the inferred B-value distribution is sensitive to the spatial distribution of the frictionally weak shear zones and the frictionally strong block interiors.

The depth-integrated B-value for the upper crust, [*England and McKenzie*, 1982; *Sonder and England*, 1986; *Klein et al.*, 2008] for a given grid element is

$$B = \frac{\int_{-h}^{L} (\sigma_1 - \sigma_3) dz}{\sqrt{2}\dot{E}^{\frac{1}{n}}}, \tag{4.3}$$

where $\dot{E}$ is the second invariant of strain rate, and n is the power law exponent. The numerator is the depth-integrated strength for the upper crust. For the faults resisting long-term frictional sliding within the block-bounding shear zones, σ_1 are the maximum, and σ_3 are the minimum principal total stresses at frictional failure. For the long-term strong crust associated with the block interiors, σ_1 are the maximum, and σ_3 are the minimum principal total stresses necessary to fracture intact country rock. Equation 4.3 can be written as

$$B = \frac{\int_{-h}^{L} \left[\frac{-2\mu\sigma_{zz}(1-\lambda)}{\sqrt{\mu^2+1}+c\mu} \right] dz}{\sqrt{2}\dot{E}^{\frac{1}{n}}}, \tag{4.4}$$

where μ is either the coefficient of fault friction in shear zones or the coefficient of friction for intact rock in block interiors, σ_{zz} is the vertical stress or lithostatic stress, λ is the ratio of pore pressure to lithostatic stress [*Klein et al.*, 2008], and c is a constant that is 1 for normal faulting, -1 for thrust faulting, and 0 for strike-slip faulting domains. These relations apply to pure end-member fault cases. To build a B-value distribution, we identify the expected pure fault style from our long term kinematic strain rate tensor solution (see Figure 3.4, Chapter 3) for the upper crust of western North America.

Our estimate of effective viscosity, B, for the block model geometries involves assignment of weak long-term fault friction coefficients of $\mu = 0.10$ to grid elements containing faults and strong long-term rock friction coefficients of $\mu = 0.70$ to grid elements containing block interiors. There are therefore six possible values of depth-integrated strength for the upper crust of western North America associated with each block model: three for shear zones and three for block interiors (see Figures 4.2 and 4.3). Depth-integrated strength is divided by $\sqrt{2}$ to determine the expected depth-integrated second invariant of deviatoric stress, T, at failure. Grid locations that plot in red or orange delineate the block-bounding, weak shear zones in Figures 4.2 and 4.3. The block model constrained with fault distributions since 15 ka (block model 1) results in wide block-bounding shear zones in the Basin and Range. In contrast, the block boundaries in model 2 result in narrow block-bounding shear zones within the Basin and Range and wide block-bounding shear zones in the Pacific Northwest.

The remaining step is defining the effective viscosity distribution, B, by division of $\dot{E}^{\frac{1}{n}}$. Within shear zones we use the strain rates from the long-term kinematic solution. Within block interiors, we use a low nominal value $0.1\ x\ 10^{-9} \cdot \mathrm{yr}^{-1}$. The power law exponent, n is set equal to 1 in generation of all our dynamic models. The very low long-term strain rates located in the interior of blocks exhibit the highest effective viscosities in each of the block models (Figures 4.4 and 4.5). Such regions show little

lateral variation in stiffness. The lowest values of effective viscosity are associated with block-bounding shear zones located in regions of high to very high strain rate found in much of California and coastal Washington and Oregon (see Figures 4.4 and 4.5). The lowest B-value is 1.20 x 10^{25} N/m $\cdot$ s for the block geometries of block model 2 and the minimum B-value is 2.89 x 10^{25} N/m $\cdot$ s for block model 2. Both block model geometries have maximum B-values of 1.97 x 10^{30} N/m $\cdot$ s.

4.3 Dynamic Modeling Results

The dynamic horizontal strain rate solution from model 1 defines a mix of principal extensional and compressional strain rate axes that dominate most regions of western North America (Figure 4.6). The bulk of the deformation is accommodated by the strike-slip style strain rates along the Pacific-North America portion of the plate boundary zone. The forward dynamic horizontal strain rate solution in Figure 4.6 is inconsistent with deformation indictors associated with Quaternary fault observations. The strain rate solution for block model 2 defines compressional strain rates for many areas of the northern Basin and Range, Oregon, central Washington, southern Idaho and Montana, and the Yellowstone region, as well as dominant strike-slip style deformation for most other regions of western North America. The forward dynamic horizontal strain rate solution shown in Figure 4.7 is also inconsistent with deformation indictors associated with Quaternary fault observations. In particular, this solution produces no normal fault styles of deformation in the Great Basin or larger Basin and Range regions. Both block models are dominated by strike-slip mechanisms to the south of 40°N with moderate-to-low strain rates within block interiors and moderate to high strain rates concentrated in the block-bounding shear zones. Each of these block models predict strain rate axes that are inconsistent with the recent 6.0 Mw, Wells, Nevada, normal fault earthquake (41.153°N, 114.867°W).

Block model 1 yields strike-slip mechanisms for the Wells, Nevada region, whereas block model 2 yields pure compression mechanisms. In contrast, the dynamic strain rate solution defined with a more evenly distributed, uniform fault friction coefficient of 0.10-0.20 (see Figure 3.15 of Chapter 3) yields strain rate styles in northeastern Nevada that are consistent with the Wells, Nevada, normal fault earthquake event.

We investigate a distributed fault model defined that combines the best of models from Chapter 3. That is, a model with uniform friction of 0.10 matched the Quaternary faults in Oregon and Washington; a model with uniform friction of 0.20 misfit fault styles in Oregon and Washington but provided a best-fit to long-term velocities across the Great Basin. This model, denoted model 3, is defined with long-term fault friction coefficients of $\mu = 0.10$ for the faults north of 40°N and with long-term fault friction coefficients of $\mu = 0.20$ for the faults south of 40°N. The effective viscosity distribution for model 3 is more evenly distributed than the B-value distributions associated with either block model 1 or 2 (Figure 4.8). The highest values of effective viscosity for model 3 are generally found to the east of the Rio Grande Rift, where B-values are as high as $1.27\ x\ 10^{29}$ N/m $\cdot$ s. In addition, B-values in the diffuse plate boundary zone are in general two orders of magnitude lower than this. B-values for model 3 are as low as $1.20\ x\ 10^{25}$ N/m $\cdot$ s along the coast of Oregon and Washington State.

The forward dynamic strain rate solution associated with model 3 produces E-W compression in the trench and N-S oriented compressive deviatoric stress in Oregon and Washington state (Figure 4.9). These results are in accord with *Wang and He* [1999] and are consistent with Quaternary fault observations. Model 3 produces strike-slip faulting within the Eastern California Shear Zone and mixed strike-slip and normal within the Walker Lane region. Model 3 also produces pure normal faulting east and northeast of Walker Lane. The strain rate styles and orientations found near Wells, Nevada are consistent with the inferred sense of slip associated with the

recent 6.0 Mw, normal fault earthquake there. The lowest strain rates associated with model 3 are found neighboring the Rio Grande Rift rift and the Colorado Rocky mountains. Low strain rates are also found to the east of Yellowstone, and within northern Idaho and northeastern Oregon. Moderate to high strain rates are located within the Eastern California Shear Zone and the Walker Lane regions, as well as along the San Andreas system. The highest strain rates are off the coast of Oregon and Washington State in the Juan de Fuca trench.

We assess the misfit of the forward dynamic strain rate tensor field for all models with the Quaternary strain rate observations shown in Figure 4.1 using

$$M = \frac{1}{2}\left(1 - \frac{e^{obs} \cdot e^{dyn}}{E^{obs} E^{dyn}}\right), \tag{4.5}$$

where the second invariant of strain rate, E^{obs} and E^{dyn} are computed from Quaternary strain rate observations and forward dynamic strain rate solutions respectively and

$$\begin{aligned} e^{obs} \cdot e^{dyn} &= \dot{\epsilon}_{xx}^{obs}\dot{\epsilon}_{xx}^{dyn} + \dot{\epsilon}_{yy}^{obs}\dot{\epsilon}_{yy}^{dyn} + \dot{\epsilon}_{zz}^{obs}\dot{\epsilon}_{zz}^{dyn} + \dot{\epsilon}_{xy}^{obs}\dot{\epsilon}_{xy}^{dyn} + \dot{\epsilon}_{yx}^{obs}\dot{\epsilon}_{yx}^{dyn} \\ &= 2\dot{\epsilon}_{xx}^{obs}\dot{\epsilon}_{xx}^{dyn} + \dot{\epsilon}_{xx}^{obs}\dot{\epsilon}_{yy}^{dyn} + \dot{\epsilon}_{yy}^{obs}\dot{\epsilon}_{xx}^{dyn} + 2\dot{\epsilon}_{yy}^{obs}\dot{\epsilon}_{yy}^{dyn} + 2\dot{\epsilon}_{xy}^{obs}\dot{\epsilon}_{xy}^{dyn}. \end{aligned}$$

.

We present the spatial distribution of our model misfit values for each model geometry. Block model 1 fits deformation indicators extremely well ($M < 0.10$) in the northern portion of the Wasatch mountain range, along the Idaho and Wyoming state border, and along sections of the San Andreas system. Block model 1 also matches deformation indicators well ($M < 0.30$) in eastern Oregon and in southern California, but misfits the deformation indicators ($0.30 < M < 0.70$) in central Oregon, and in regions surrounding the Rio Grande Rift (Figure 4.10). Portions of northwestern Nevada fail to adequately match ($M > 0.70$) Quaternary deformation indicators.

Block model 2 only matches deformation indicators along the San Andreas system and in some portions of the Eastern California Shear Zone ($0.10 < M < 0.30$) (Figure 4.11). Elsewhere, block model 2 provides a poor fit to deformation indicators. Model 3 matches deformation indicators throughout the Eastern California Shear Zone, the Basin and Range, and the Rio Grande rift (Figure 4.12). Model 3 also matches the N-S compression orientations in Washington State, but misfits deformation indicators within parts of coastal Pacific Northwest where Quaternary fault and fold database for the United States shows normal faulting.

We plot the long-term dynamic velocity fields associated with each block model 1 and 2 with respect to a North America frame of reference (Figure 4.13 and 4.14). The velocity fields for both block models 1 and 2 fail to adequately match the long-term velocity model (see Figure 3.4 in Chapter 3). Ironically, the block models 1 and 2 fail to localize strain rate entirely within the weak shear zones. Some distributed deformation occurs also within the high strength block interiors. The dynamic velocity field associated with model 3 does localize strain rates in the correct places while adequately matching the long-term velocity model (Figure 4.15).

4.4 Depth-integrated Deviatoric Stress Fields Associated With Crustal Block Geometry Models

Both block model solutions appear to be dominated by the accommodation of velocity boundary conditions, with GPE differences playing a secondary very minor role. We next evaluate the GPE related stresses and the boundary condition related stresses separately in order to quantify their relative contribution throughout the plate boundary zone for block models 1 and 2. To calculate GPE related stresses,

we use the method of *Flesch et al.* [2001], outlined in Chaper 2, but with a laterally variable viscosity, rather than a constant viscosity. To evaluate the boundary condition stresses, we run the forward model in the absence of internal body forces (GPE differences).

Block model 1 geometry produces relatively low depth-integrated deviatoric stresses associated with GPE differences within broad regions of the Basin and Range and the Rio Grande Rift (Figure 4.16). This result is consistent with the wide, diffuse block-bounding shear zones, which define the block boundary geometries of block model 1 (see Figures 4.2 and 4.4). Block model 2 produces relatively high depth-integrated deviatoric stresses associated with GPE differences throughout much of the Basin and Range (Figure 4.17). However, tight bands of relatively low depth-integrated deviatoric stresses associated with GPE differences are also located in this region. The principal axes of deviatoric stress are also predominately tensional for the diffuse plate boundary zone. The differences of solutions in Figure 4.16 and Figure 4.17, as well as differences with the GPE solution in Chapter 3, highlight the dependence of GPE related stresses on the relative viscosity distribution. Overall, however, the range of depth-integrated magnitudes of deviatoric stress associated with GPE differences are limited in the range of $0.1 - 2\ x\ 10^{12}\ \mathrm{N} \cdot \mathrm{m}^{-1}$ for block models 1 and 2.

We evaluate the block model responses to the accommodation of velocity boundary conditions by running dynamic forward models in the absence of internal body forces (no GPE differences). Block model 1 geometry produces relatively low depth-integrated deviatoric stresses within broad regions of the Basin and Range and the Rio Grande Rift. However, rigid regions act as stress guides, transmitting large stress magnitudes (Figure 4.18). Likewise block model 2 produces large depth-integrated deviatoric stresses associated with velocity boundary conditions within high strength regions (Figure 4.19). There are bands of relatively low depth-integrated deviatoric stresses associated with velocity boundary conditions that are co-located with the

narrow block boundaries defined in block model 2 (see Figures 4.3 and 4.5). The principal axes of deviatoric stress are also predominately a mix of compressional and tensional for the diffuse plate boundary zone. The forward dynamic depth-integrated deviatoric stress magnitudes associated with velocity boundary conditions are often in excess of one order of magnitude larger than the depth-integrated deviatoric stress magnitudes associated with GPE differences for both block model geometries. For both solutions, the block-like regions act as tremendous stress guides for the high values of depth-integrated stress, transmitting the influence of plate motions and minimizing the influence of internal buoyancies.

In Chapter 3, we show that the Ar number can be redefined as the expected ratio of the 2nd invariant of stress associated with GPE differences to the 2nd invariant of stress associated with the accommodation of velocity boundary conditions. The Argand number distribution for block model 1 highlights the strong influence of the velocity boundary condition stresses throughout diffuse plate boundary zone and the Pacific Northwest (Figure 4.20). Argand numbers are ubiquitously far less than 1.0 throughout western North America. Argand numbers are also less than 0.50 throughout western North America for block model 2 (Figure 4.21). These Argand number distributions imply that deviatoric stresses arising from GPE differences would not drive long-term deformation within western North America for such block models. Instead the plate boundary zone deformation would be driven mainly by accommodation of the Pacific and Juan de Fuca plates. The Argand number distribution defined by model 3 is similar to Argand number distributions defined with low, uniform long-term fault friction models in Chapter 3. Argand numbers associated with model 3 are less than 1.0 in northern Texas, northern Mexico, southern California, southwestern Arizona, west of the Sierra Nevada mountains, along the Oregon coast, and within Washington State (Figure 4.22). In the western portion of the Basin and Range and in the interior Pacific Northwest, GPE differences are roughly equal to

velocity boundary conditions; however, stresses associated with GPE differences are the dominant drivers of deformation (Ar = 2–5) in the eastern Basin and Range. For the Colorado Rocky mountain ranges, the stresses associated with GPE differences completely dominate over contribution from velocity boundary conditions ($Ar > 10$).

4.5 Conclusions

The Quaternary fault observations allow us to test and evaluate our set of forward dynamic models in unparalleled detail. Our block model geometries have weak fault friction (μ=0.1) in regions with block-bounding shear zones and much higher crustal friction within block interiors (μ=0.7). Such models fail to produce the required lateral variations in effective viscosity needed to define a dynamic strain rate tensor field that achieves a best-fit with Quaternary deformation indicators. The block model geometries also define deviatoric stresses arising from GPE differences that contribute little to driving the long-term deformation of the Basin and Range. These models instead result in diffuse plate boundary deformation driven mainly by accommodation of the Pacific and Juan de Fuca plates (i.e., $Ar < 1.0$), in which the deformation field is dominated by strike-slip strain rates south of 40°N, or the influence of Pacific-North America motion. In contrast to these results, we have shown in Chapter 3, that a more distributed fault fabric, with uniform low fault friction, yields a far better fit to the long-term deformation indicators. Similarly, model 3 yields a close match to long-term deformation indicators throughout the diffuse plate boundary zone. Surprisingly, such models with relatively uniform long-term friction yield the primary and important zones of relatively concentrated shear (San Andreas System, Juan de Fuca trench, Eastern California Shear Zone and Walker Lane, and Wasatch), whereas block model 1 and 2 are prone to placing distributed shear within improper zones. Furthermore, model 3 yields the proper balance of internal buoyancies relative

to plate motion accommodation mechanisms.

The level of the long-term friction on the faults, along with the distribution of the fault fabric, controls the relative influence that internal buoyancies and plate boundary forces have on the deformation field. Our dynamic models strongly suggest that stress and strain rate tensor fields and velocity fields are exceedingly sensitive to the intrinsic mechanical properties of the faults, and to the density of available fault fabric. Based on our scoring of self-consistent dynamic model output with detailed kinematic output, we argue that a more distributed fault fabric than that provided by block model geometries is required to explain the patterns of finite strain observed within the diffuse plate boundary zone of western North America. Moreover, we suggest that ironically one needs a weak (in terms of long-term friction) broader Basin and Range region in order to focus strain rates within the San Andreas and Eastern California Shear Zone and Walker Lane Systems.

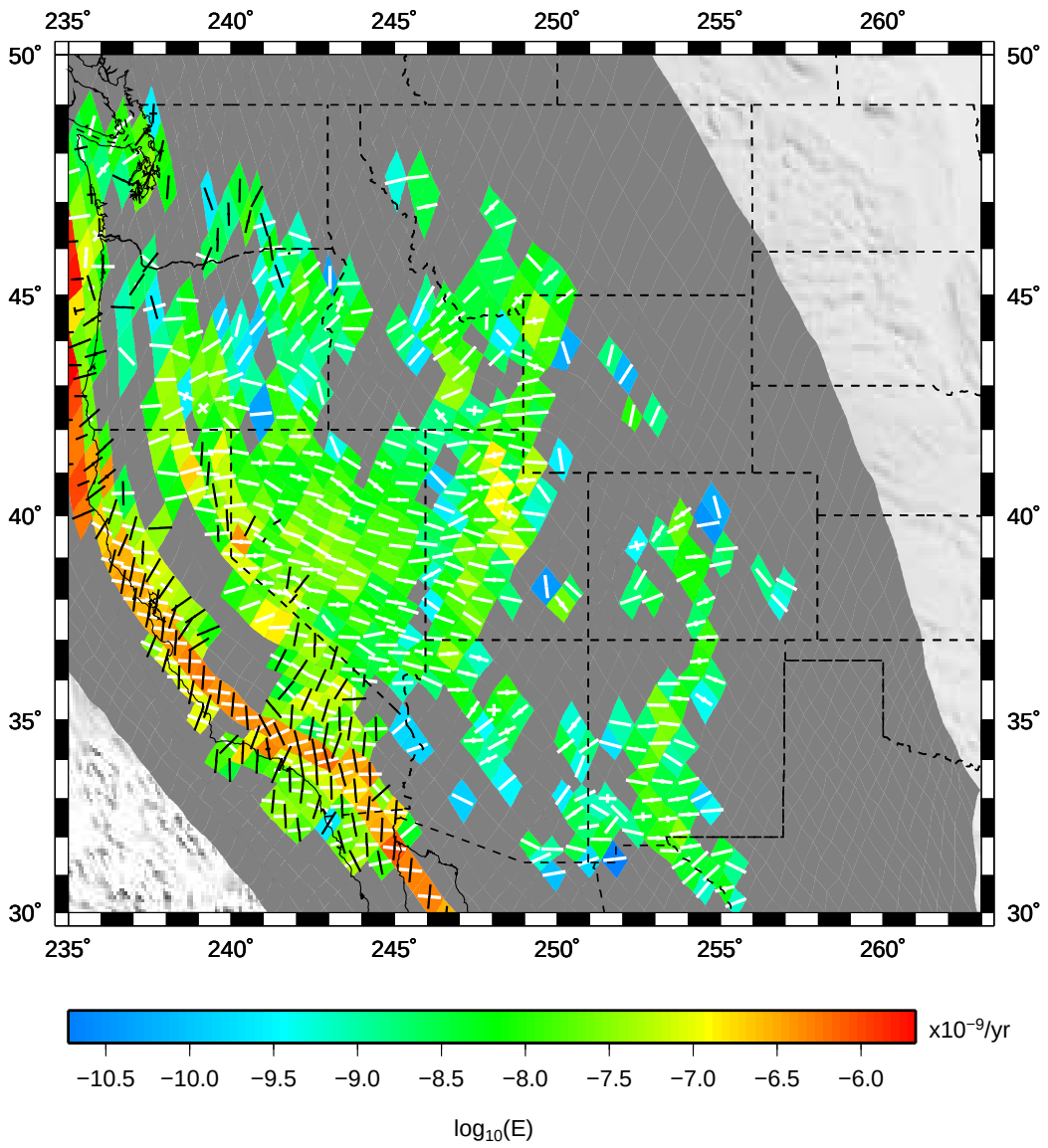

Figure 4.1: The long-term estimate of the horizontal strain rate tensor field inferred from Kostrov summation of faults for grid areas containing geologic rate data. Principal axes of strain rates (area averages) have been normalized by the maximum value of the principal axis strain rate within each grid area (bold = compressional, white = extensional). Color background is the second invariant of strain rate (area averages). Grid areas without data plot in gray.

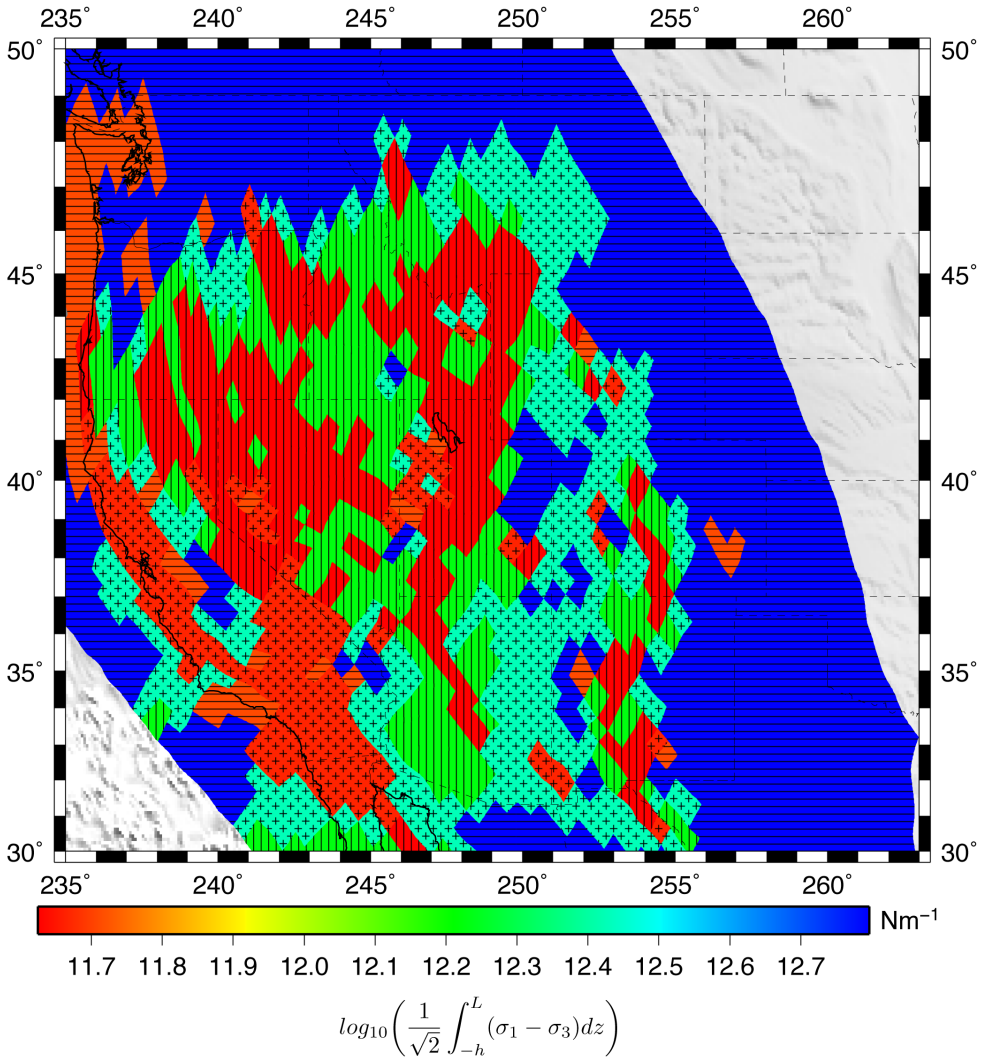

Figure 4.2: Block model 1: The distribution of the log of depth-integrated strength for the crust of western North America scaled by $1/\sqrt{2}$. We assign weak fault friction ($\mu = 0.10$) to grid elements containing faults that have ruptured since 15k ago and strong crustal friction ($\mu = 0.70$) to all other grid elements. The depth integral of strength depends on fault style. All fault styles are grouped into one of three pure tectonic regimes defined by the long-term kinematic strain rate tensor field solution shown in Figure 3.4 of Chapter 3. Vertical rule indicates normal faulting style, horizontal is thrust, and cross is strike-slip (used to define the depth integral of strength). The fault observations are located within the grid elements that plot in red or orange. All faults associated with the Quaternary fault and fold database for the United States are reported to have slipped no later than 15 ka.

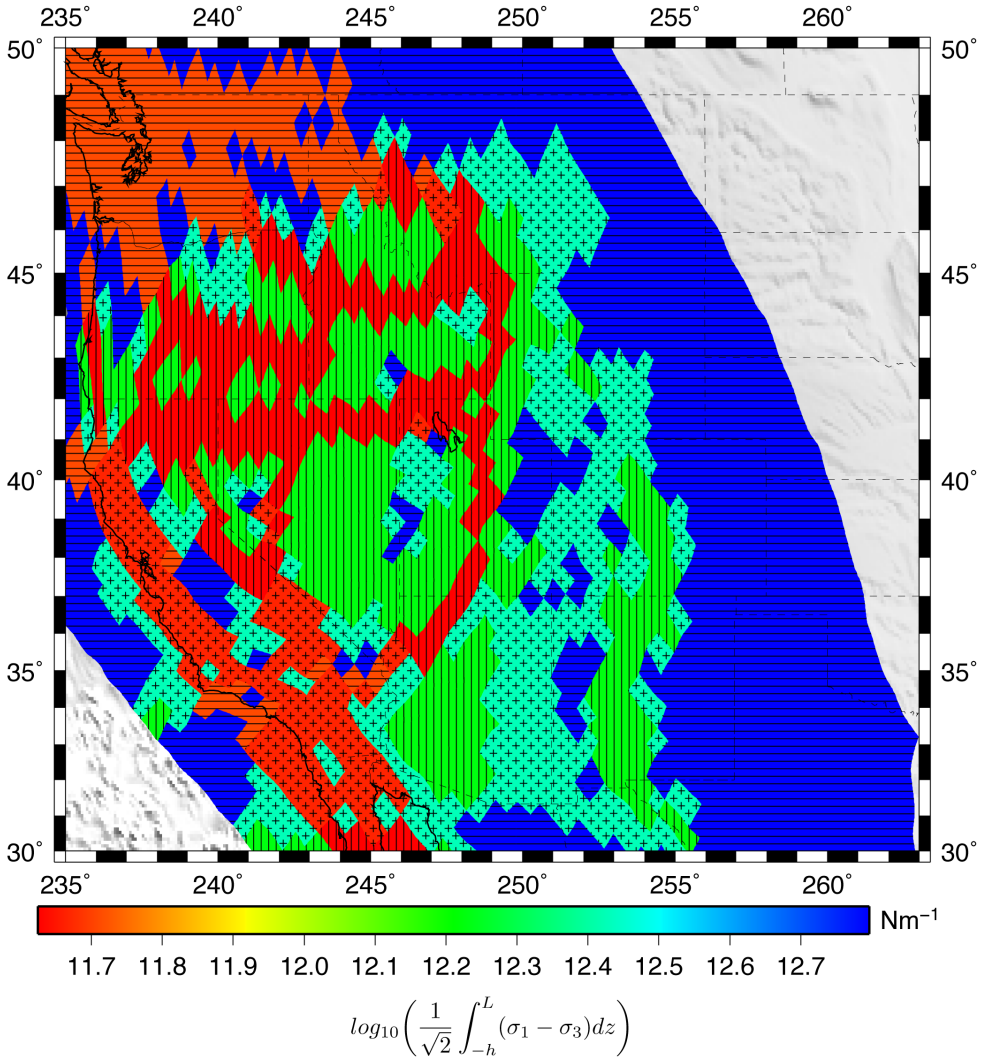

Figure 4.3: Block model 2: The distribution of the log of depth-integrated strength for the crust of western North America scaled by $1/\sqrt{2}$. We assign weak fault friction ($\mu = 0.10$) to grid elements associated with the block boundaries of *McCaffrey* [2005]; *McCaffrey et al.* [2007] and strong crustal friction ($\mu = 0.70$) to all other grid elements. The depth integral of strength depends on fault style. All fault styles are grouped into one of three pure tectonic regimes defined by the long-term kinematic strain rate tensor field solution shown in Figure 3.4 of Chapter 3. Vertical rule indicates normal faulting style, horizontal is thrust, and cross is strike-slip (used to define the depth integral of strength). The block boundaries are those grid elements that plot in red or orange.

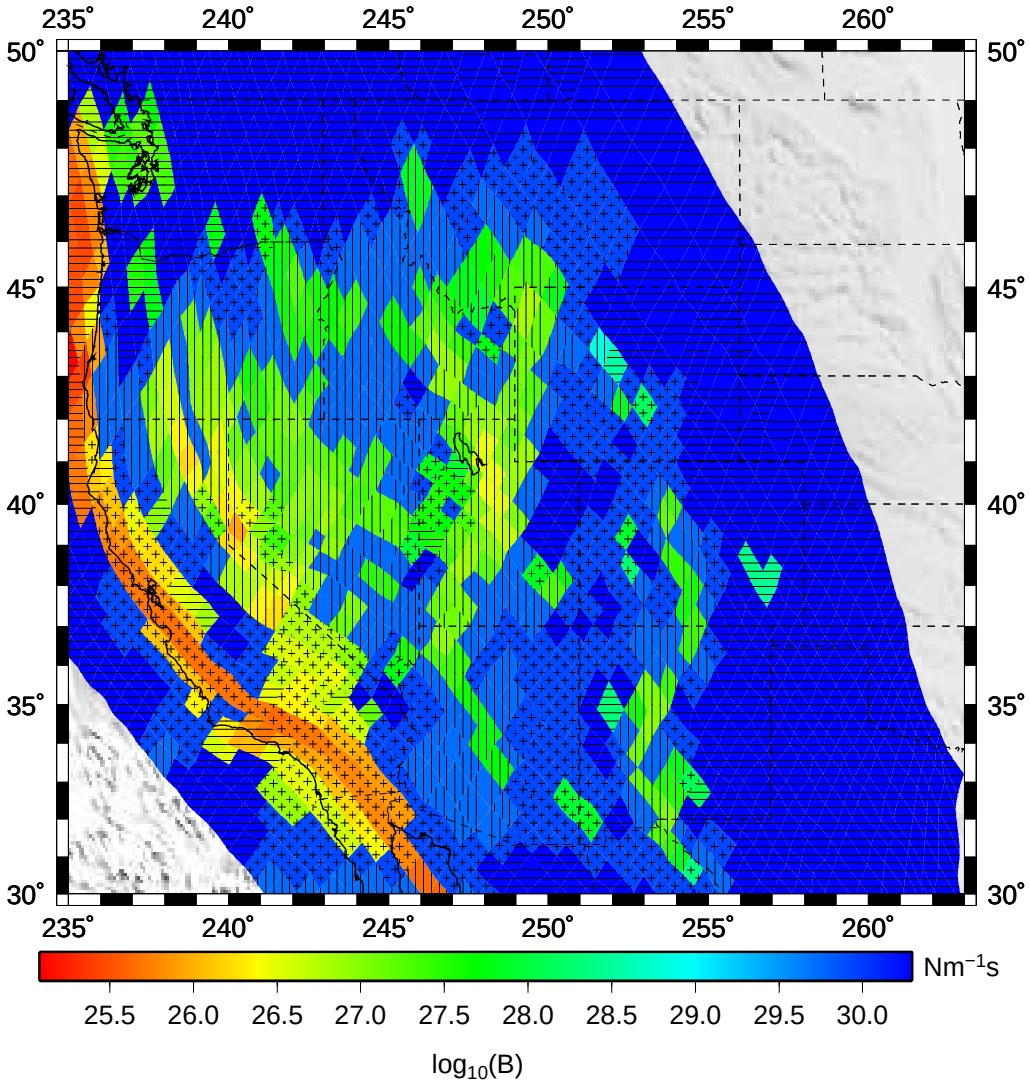

Figure 4.4: Block model 1: The log of the B-value distribution for the crust of western North America assuming the distribution associated with the fault observations shown in Figure 4.2, a power law exponent of $n = 1$ strain rates from our long-term model strain rate tensor field for the shear zones and a value of 0.1 x 10^{-9} $\cdot$ yr^{-1} for the block interiors. Vertical rule indicates normal faulting style, horizontal is thrust, and cross is strike-slip, used to define the depth integral of strength.

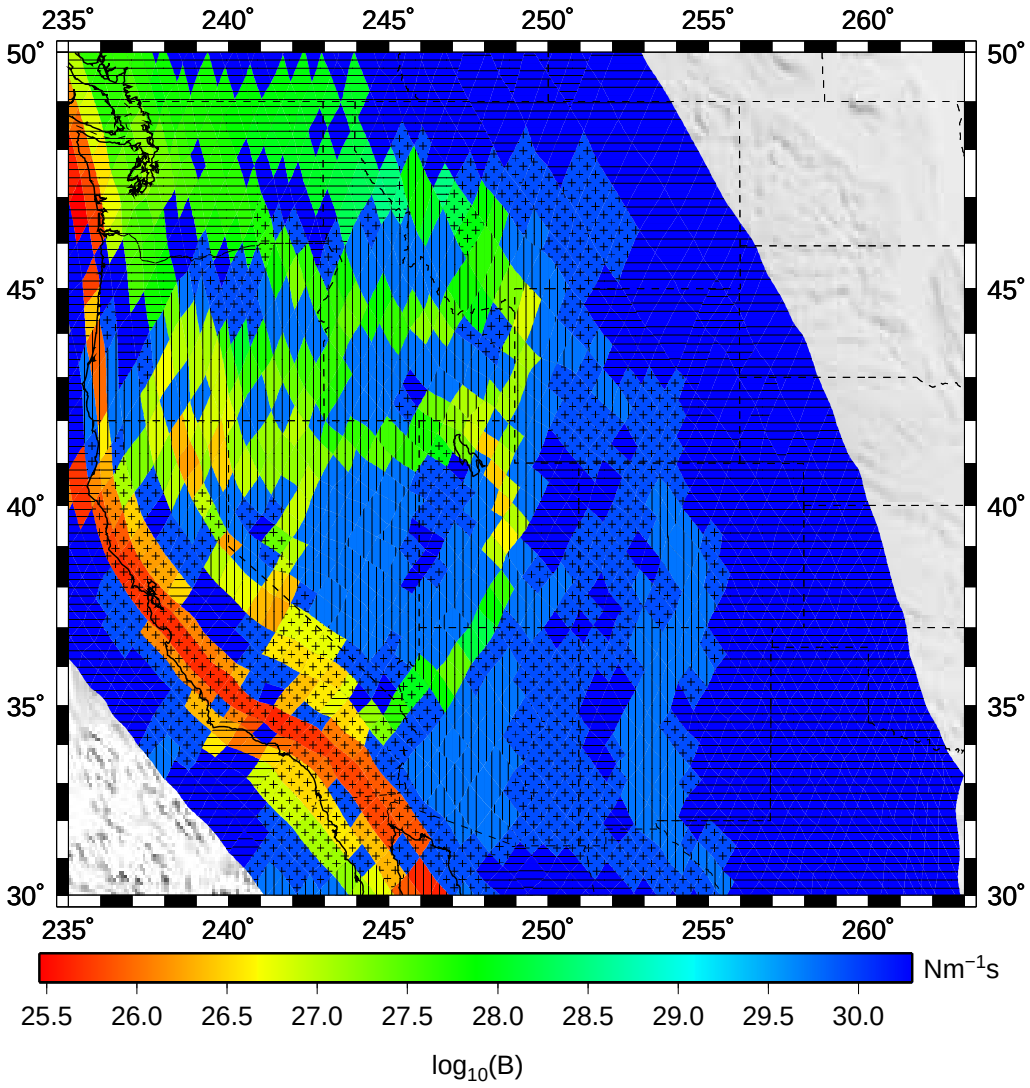

Figure 4.5: Block model 2: The log of the B-value distribution for the crust of western North America assuming the distribution associated with the block boundaries of *McCaffrey* [2005]; *McCaffrey et al.* [2007] shown in Figure 4.3, a power law exponent of $n = 1$ and strain rates from our long-term model strain rate tensor field for the shear zones and a value of 0.1 x 10^{-9} $\cdot$ yr^{-1} for the block interiors. Vertical rule indicates normal faulting style, horizontal is thrust, and cross is strike-slip, used to define the depth integral of strength.

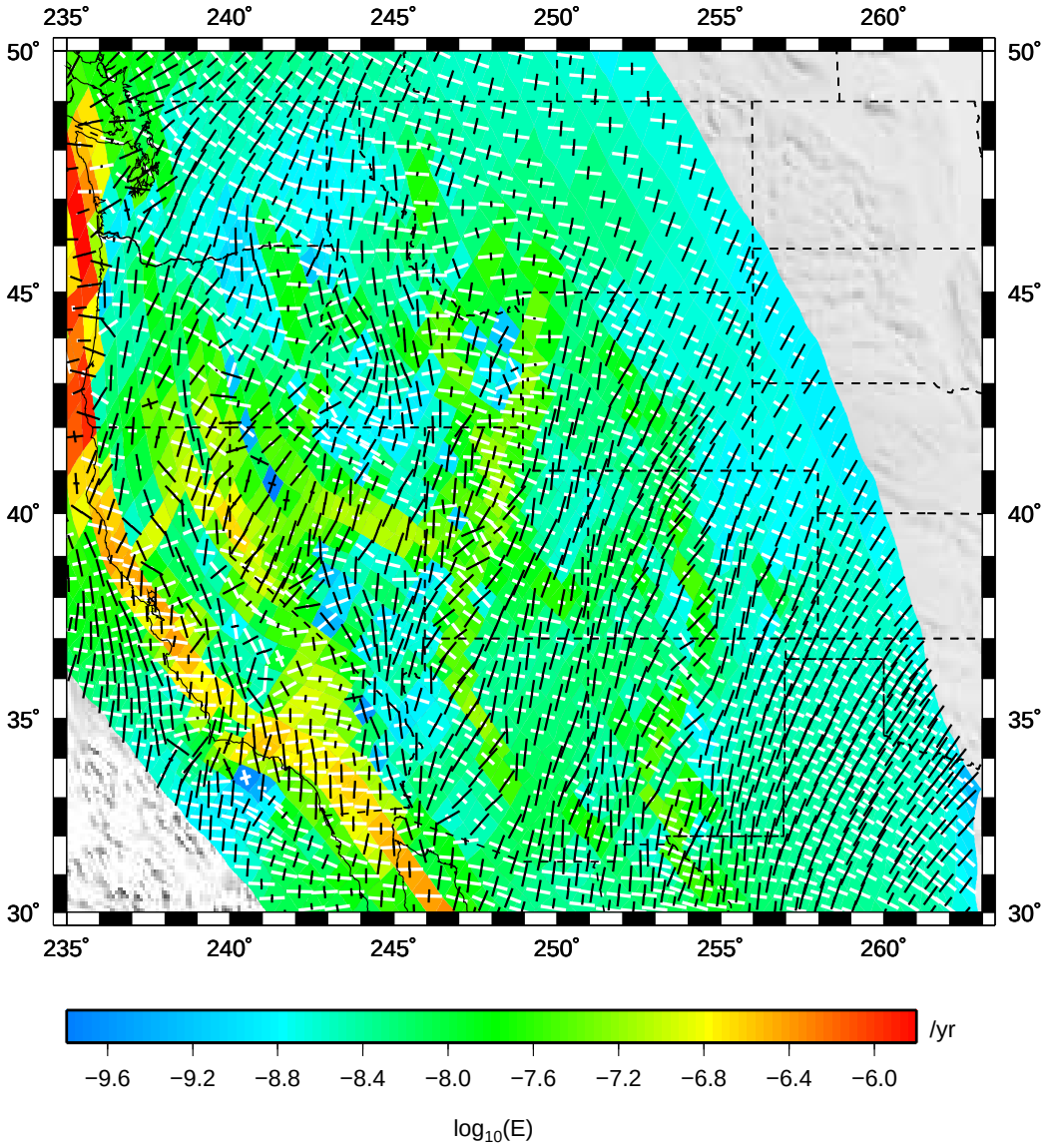

Figure 4.6: The forward dynamic strain rate tensor field defined with the B value distribution shown in Figure 4.4 (block model 1). Principal axes of strain rates (area averages) have been normalized by the maximum value of the principal axis strain rate within each grid area (bold = compressional, white = extensional). Color background is the log of the second invariant of strain rate (area averages).

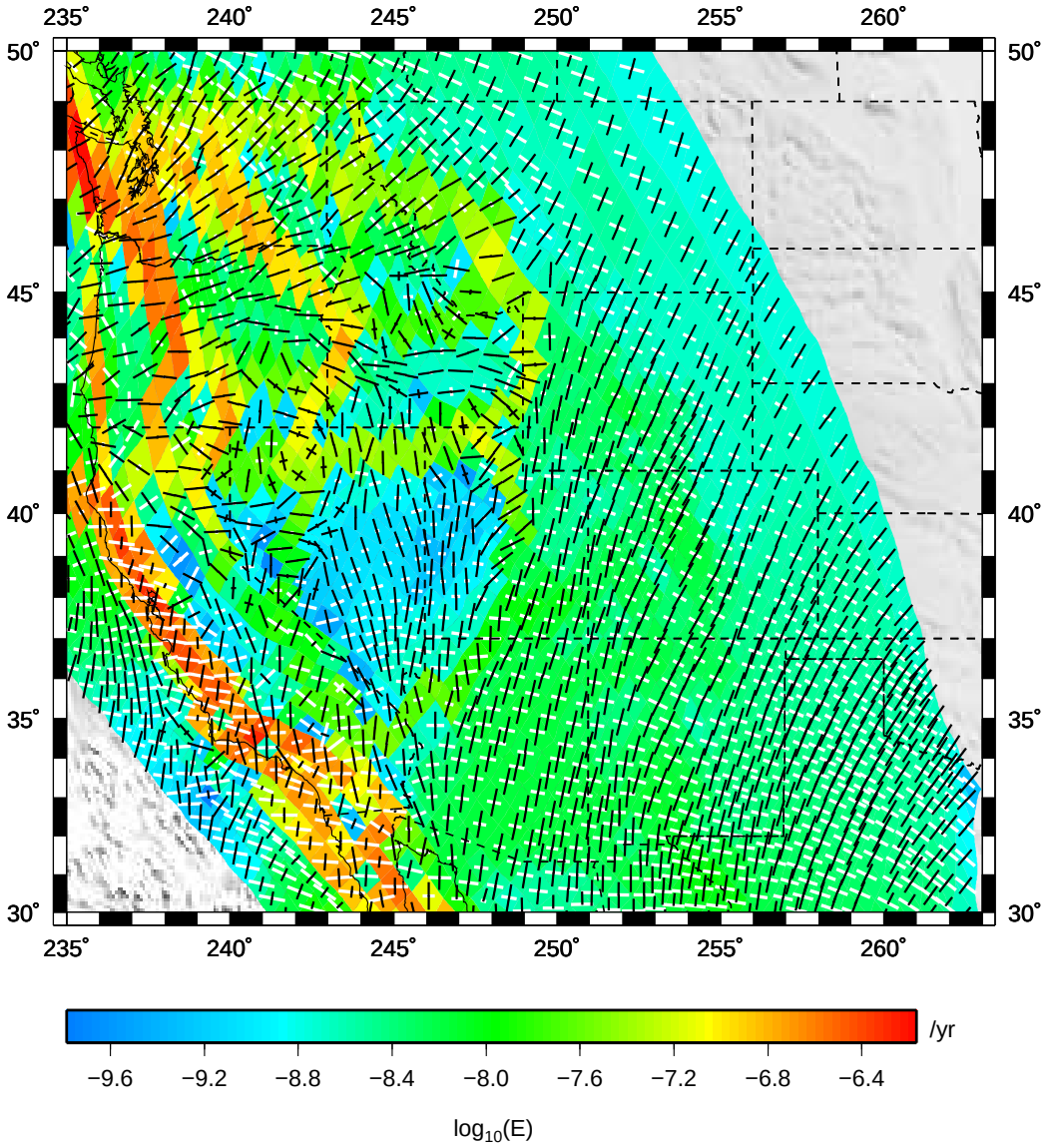

Figure 4.7: The forward dynamic strain rate tensor field defined with the B value distribution shown in Figure 4.5 (block model 2). Principal axes of strain rates (area averages) have been normalized by the maximum value of the principal axis strain rate within each grid area (bold = compressional, white=extensional). Color background is the log of the second invariant of strain rate (area averages).

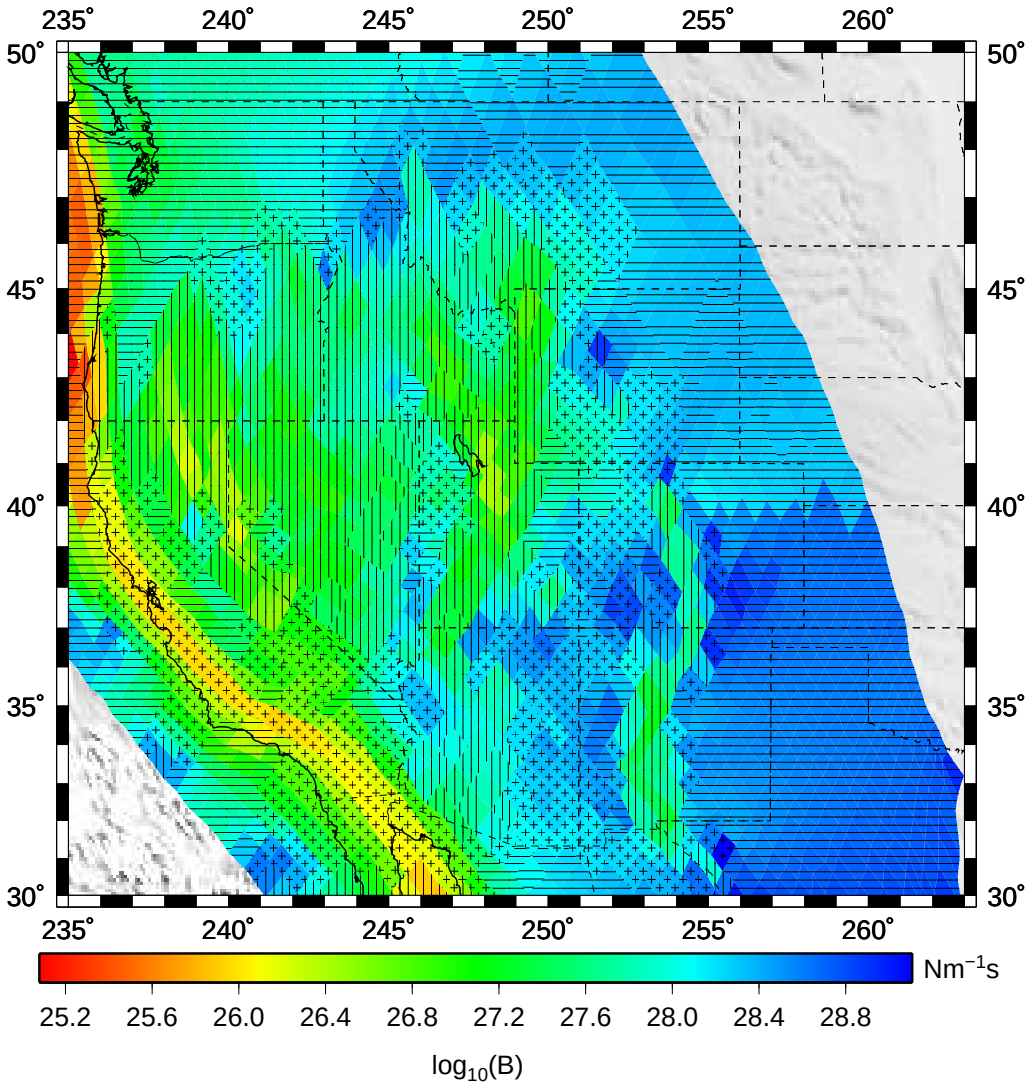

Figure 4.8: Model 3: The log of the B-value distribution for the crust of western North America associated with assignment of relatively low values of friction (0.1 – 0.2) in all areas (e.g., no high friction blocks). The long-term depth-integrated strength in this distribution is defined by assigning fault friction coefficients of $\mu = 0.10$ to all areas north of 40°N and by assigning friction coefficients of $\mu = 0.20$ to all areas south of 40°N. We scale these expected depth integrals of strength by $1/\sqrt{2}$. To define the B-values we assume a power-law exponent of $n = 1$ and strain rates from our long-term model strain rate tensor field. Vertical rule indicates normal faulting style, horizontal is thrust, and cross is strike-slip, used to define the depth integral of strength.

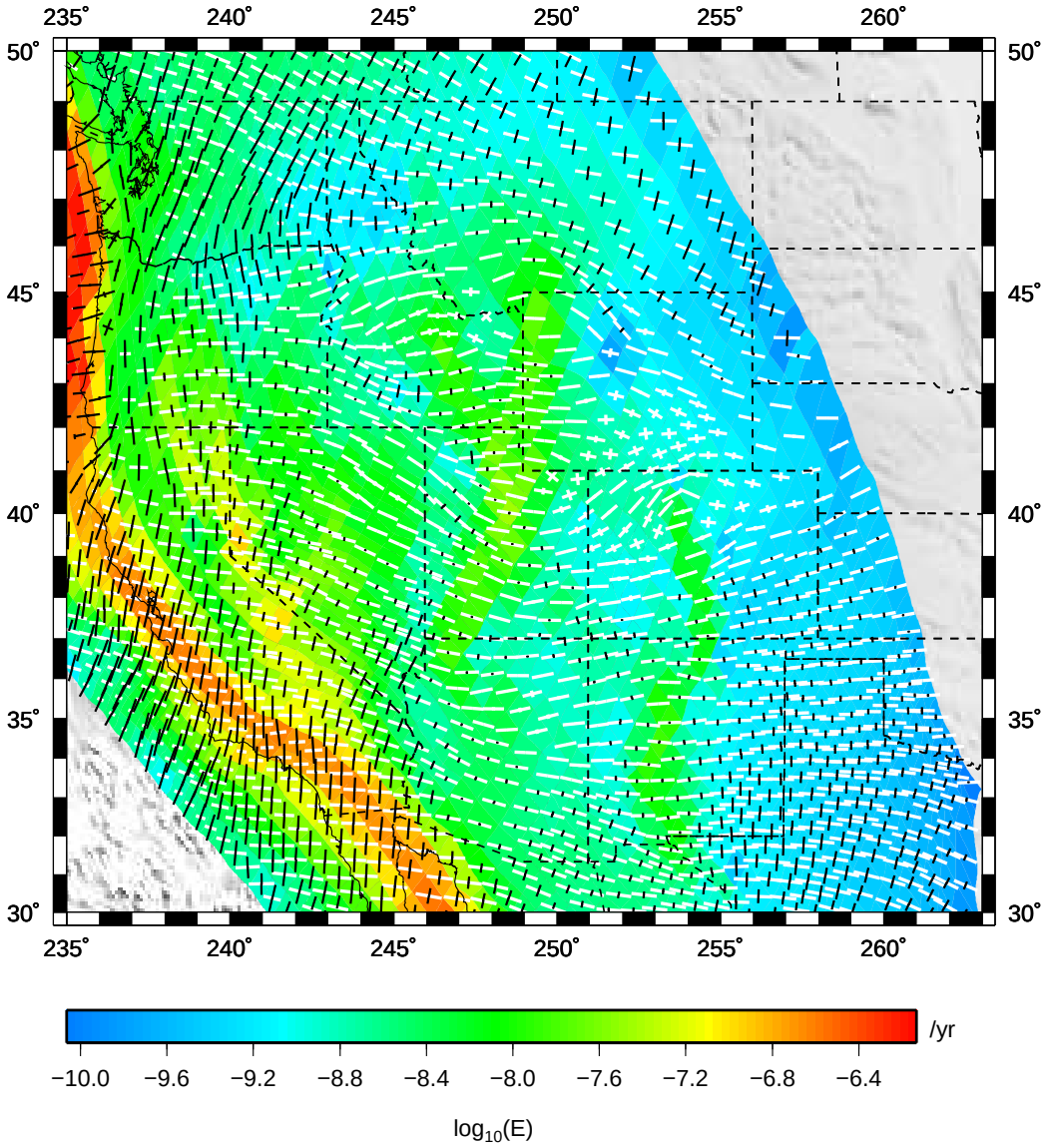

Figure 4.9: The forward dynamic strain rate tensor field defined with the B value distribution shown in Figure 4.8 (model 3). Principal axes of strain rates (area averages) have been normalized by the maximum value of the principal axis strain rate within each grid area (bold = compressional, white=extensional). Color background is the log of the second invariant of strain rate (area averages).

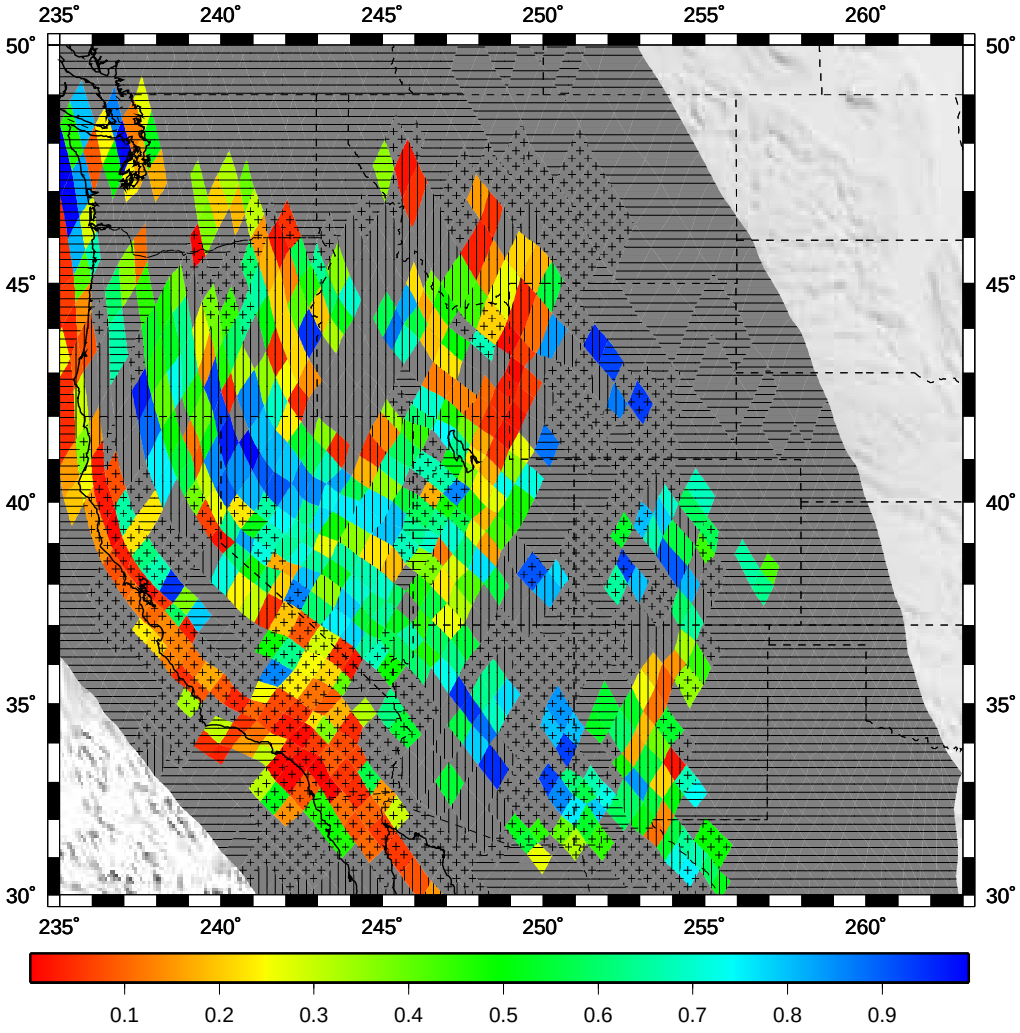

Figure 4.10: The distribution of misfit (defined in equation 4.5) for block model 1. The misfit function quantifies the agreement between the unit tensors from the forward dynamic strain rate tensor field (see Figure 4.6) with the long-term strain rate field inferred from Kostrov summation of faults shown in Figure 4.1. Vertical rule indicates normal faulting style, horizontal is thrust, and cross is strike-slip from the long-term kinematic solution.

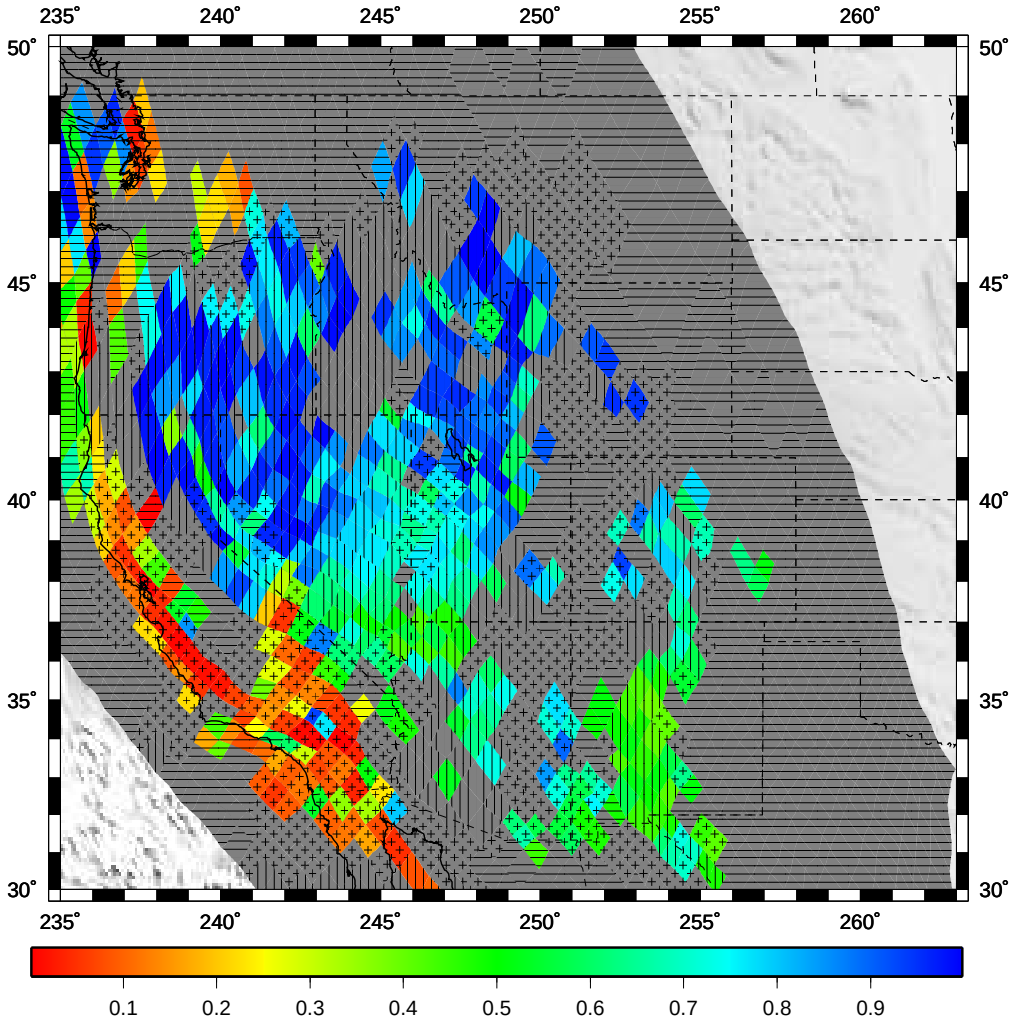

Figure 4.11: The distribution of misfit (defined in equation 4.5) for block model 2. The misfit function quantifies the agreement between the unit tensors from the forward dynamic strain rate tensor field (see Figure 4.7) with the long-term strain rate field inferred from Kostrov summation of faults shown in Figure 4.1. Vertical rule indicates normal faulting style, horizontal is thrust, and cross is strike-slip from the long-term kinematic solution.

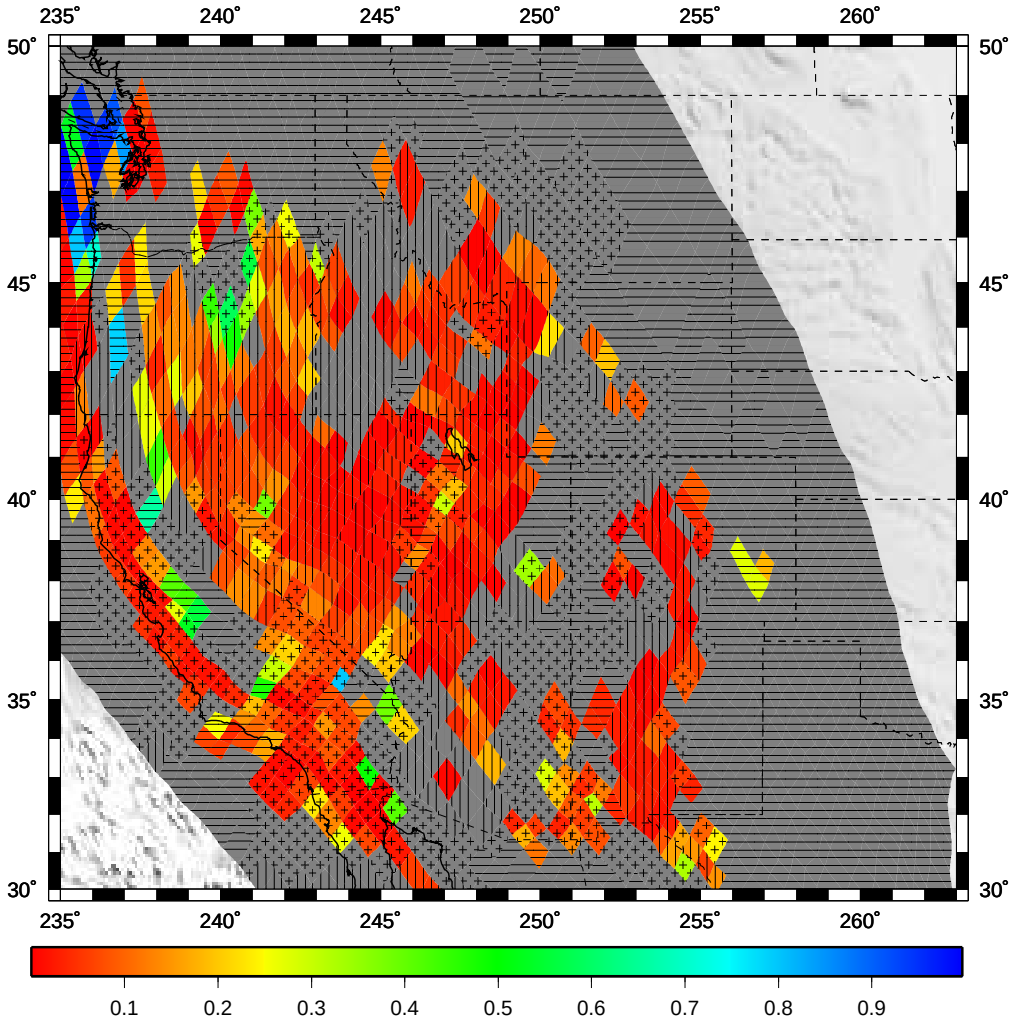

Figure 4.12: The distribution of misfit (defined in equation 4.5) for model 3. The misfit function quantifies the agreement between the unit tensors from the forward dynamic strain rate tensor field (see Figure 4.9) with the long-term strain rate field inferred from Kostrov summation of faults shown in Figure 4.1. Vertical rule indicates normal faulting style, horizontal is thrust, and cross is strike-slip from the long-term kinematic solution.

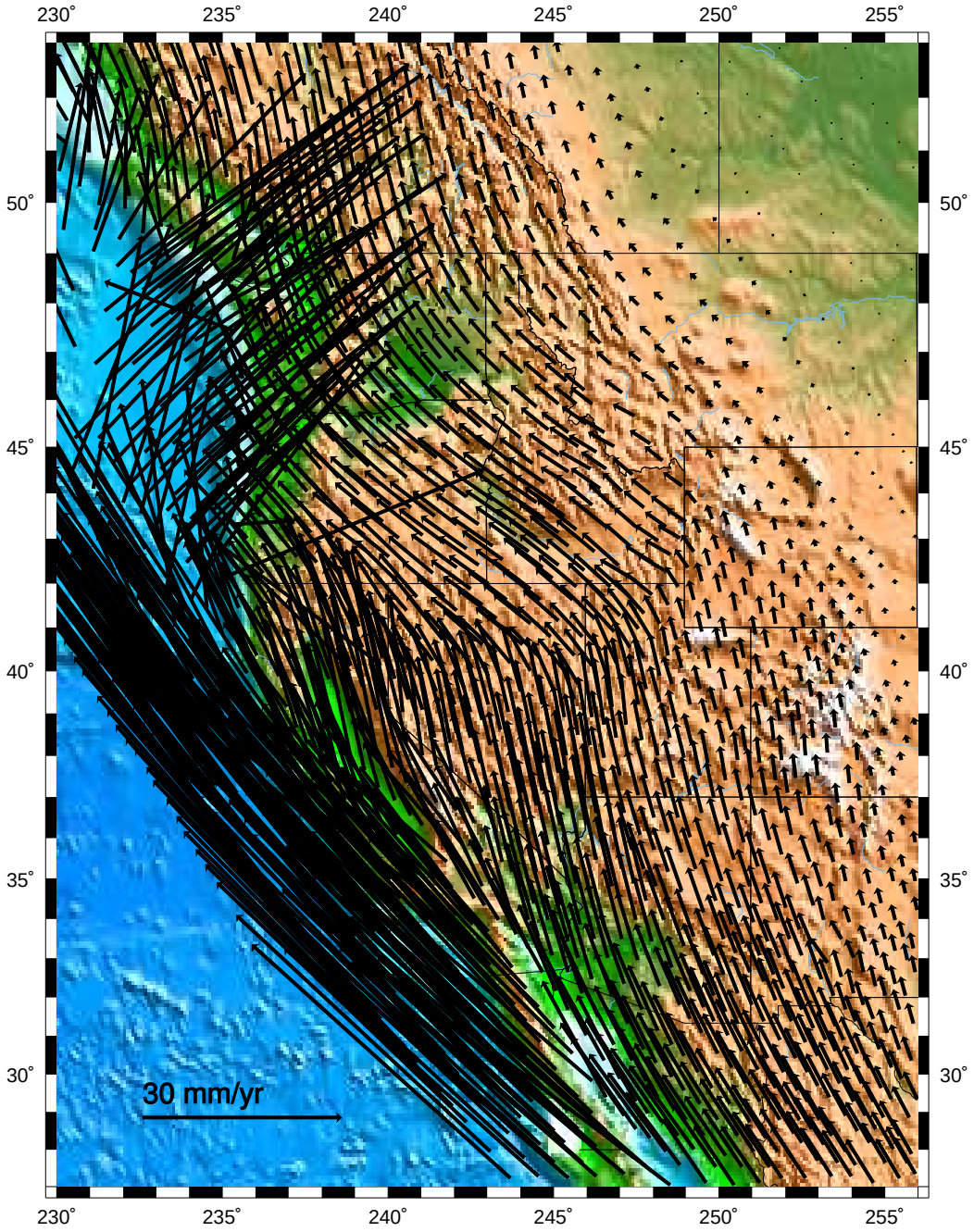

Figure 4.13: The forward dynamic model velocity field for the upper crust defined from block model 1.

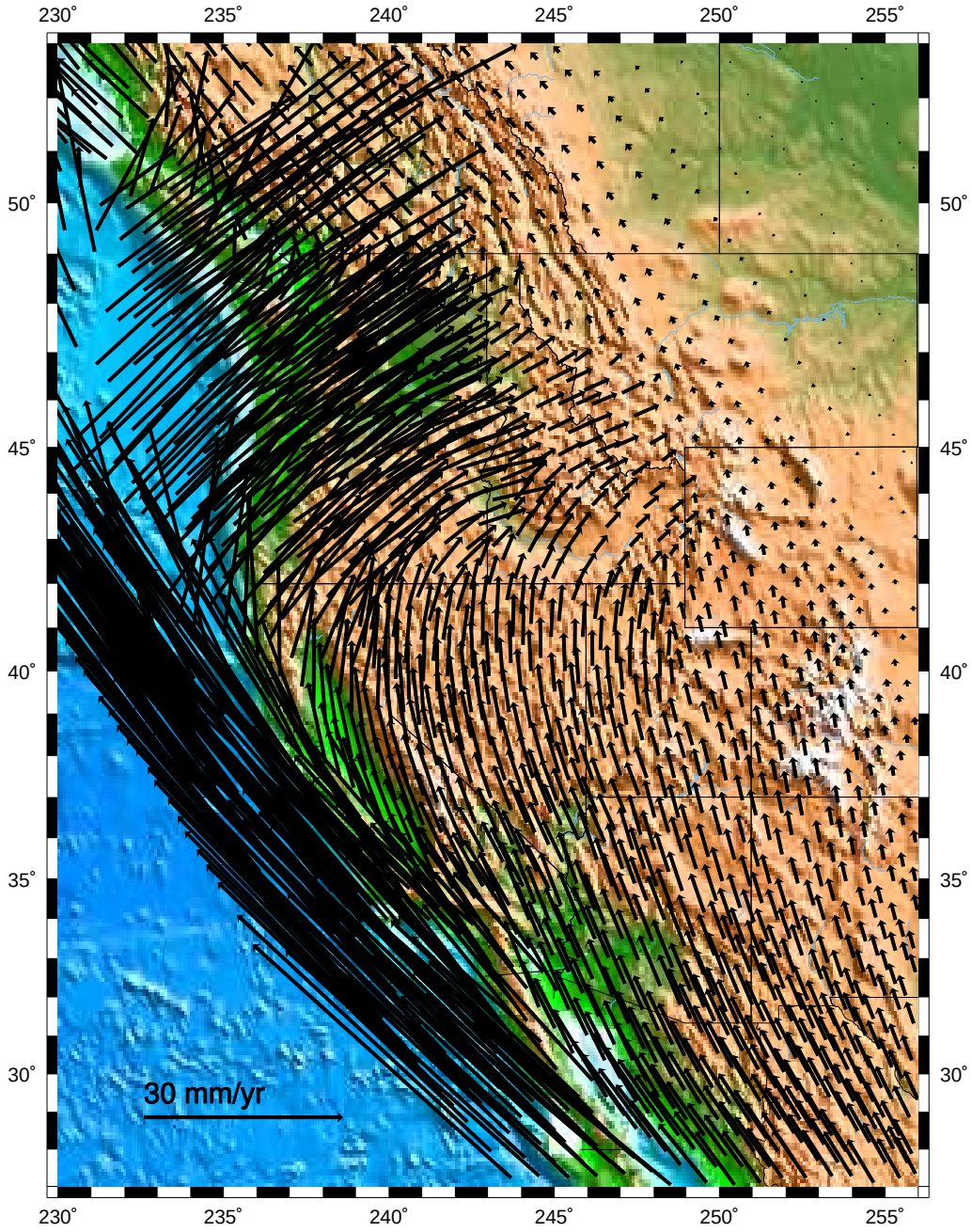

Figure 4.14: The forward dynamic model velocity field for the upper crust defined from block model 2.

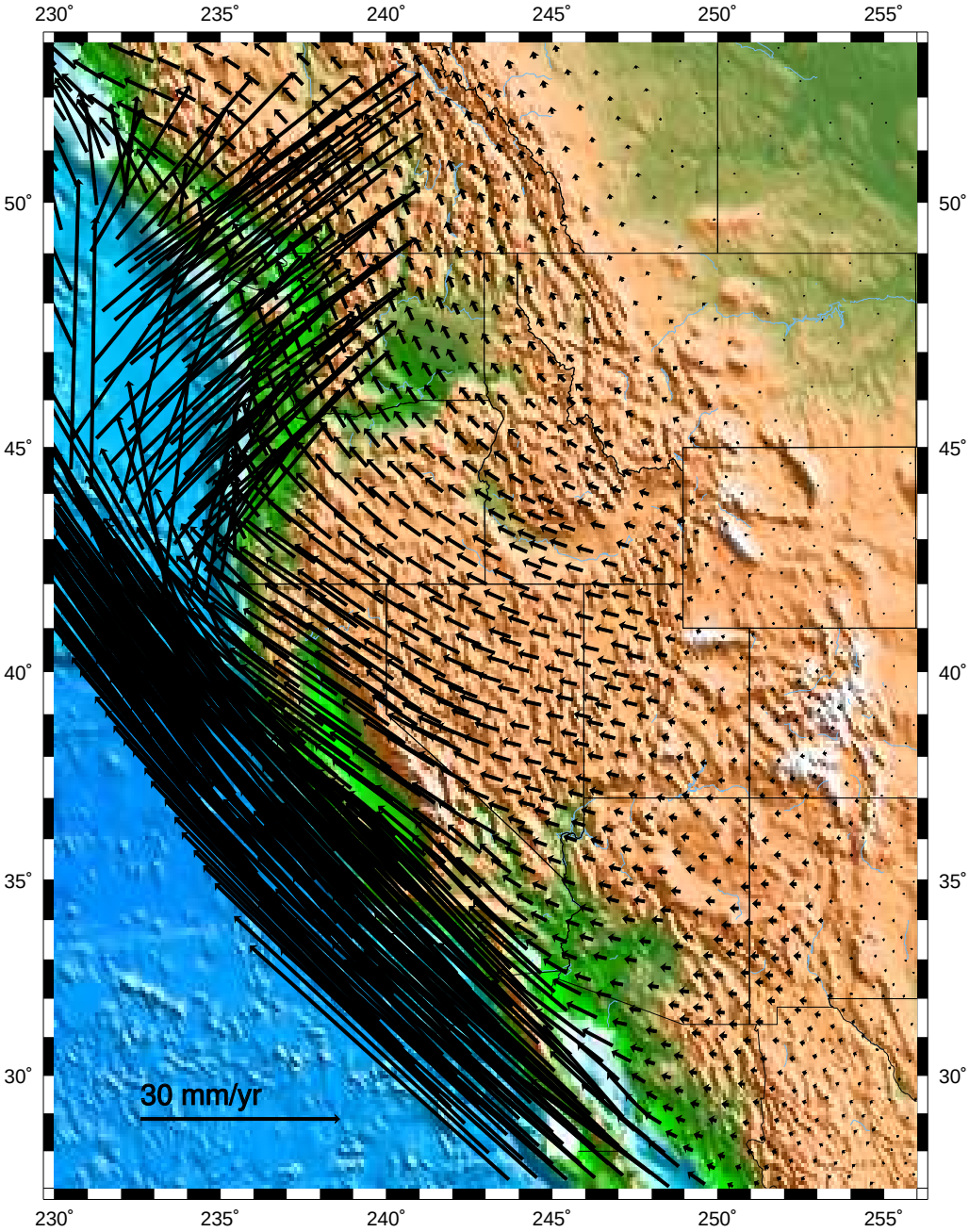

Figure 4.15: The forward dynamic model velocity field associated with model 3.

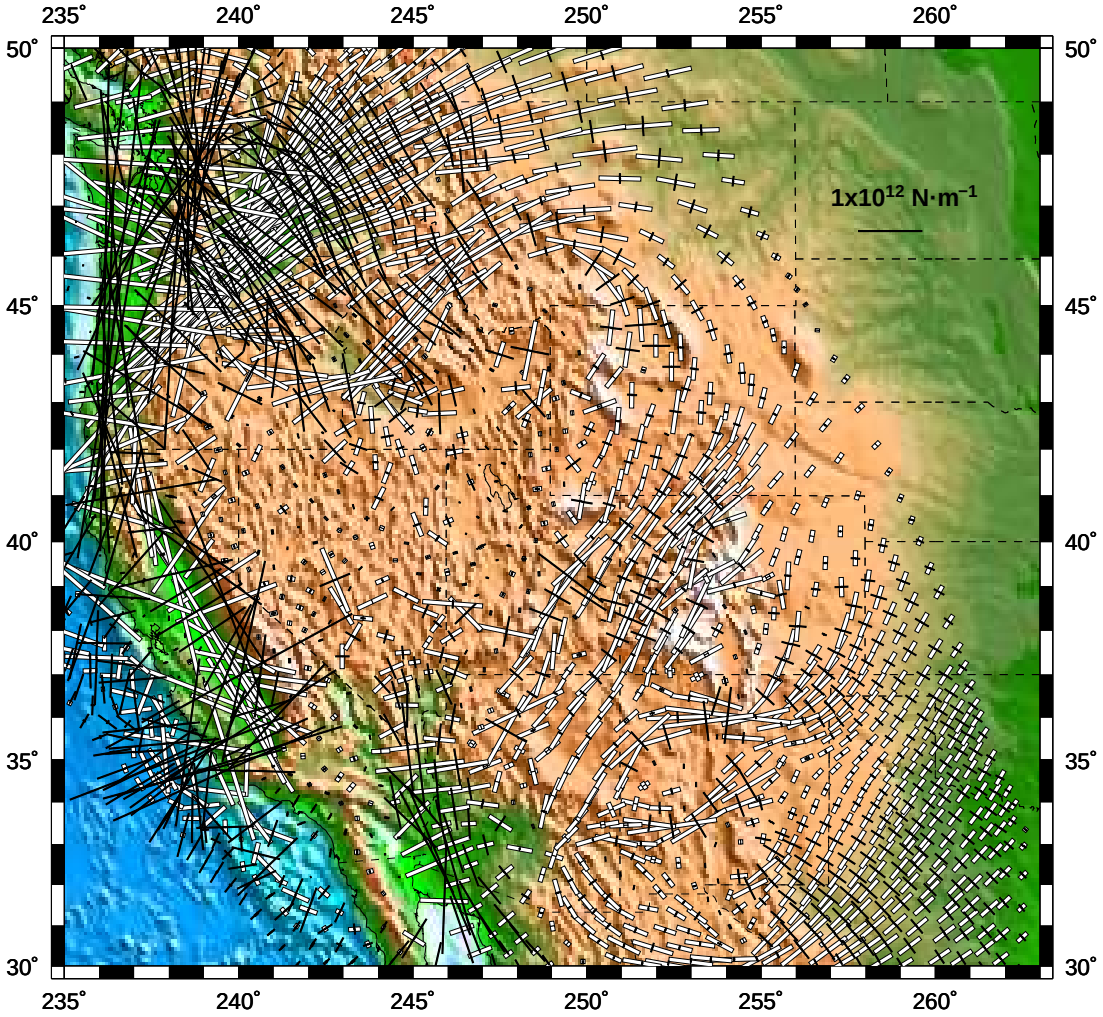

Figure 4.16: The depth-integrated deviatoric stress field associated with gravitational potential energy differences (GPE) for the crust with B-values defined by block model 1. White vectors represent tensional principal axes of deviatoric stress. Bold vectors represent compressional principal axes of compressional stress.

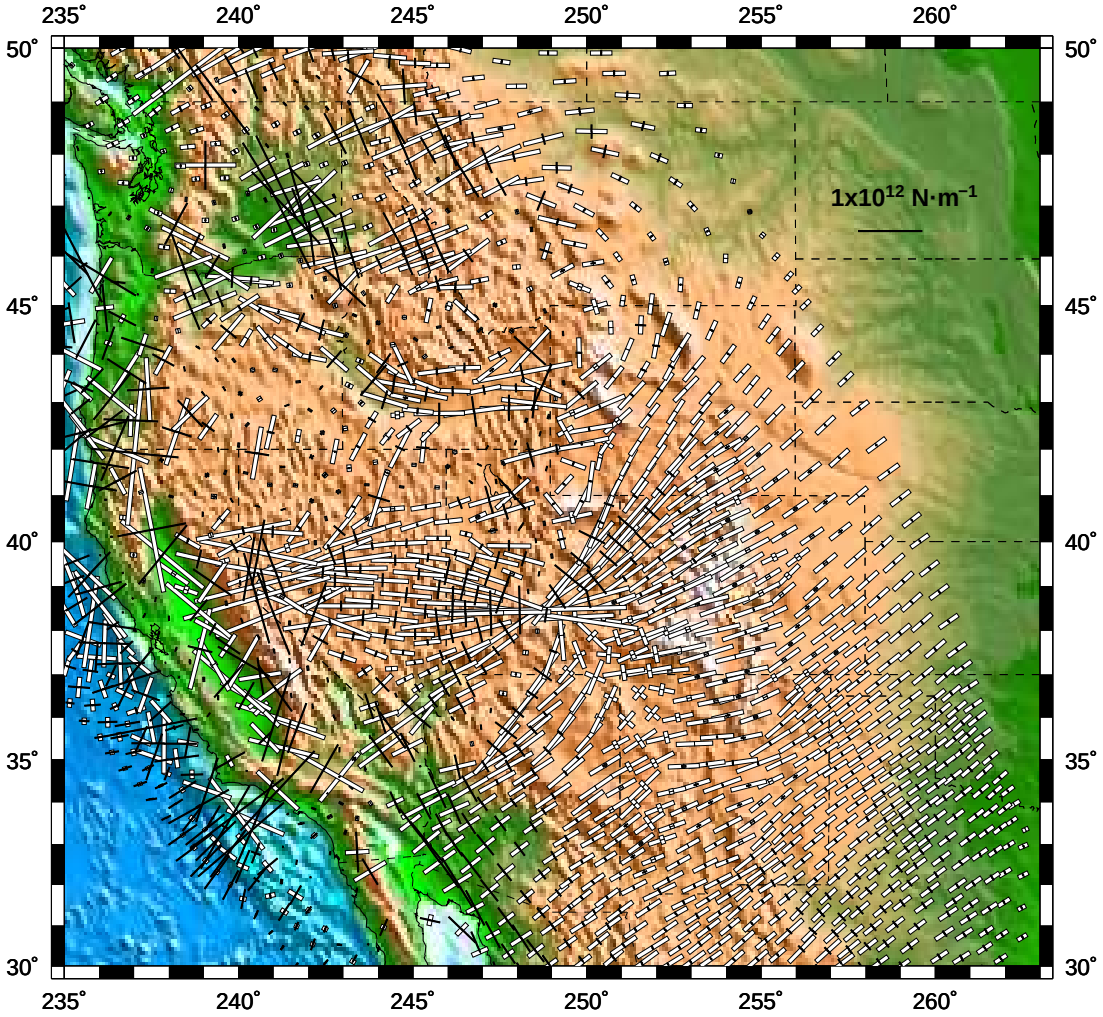

Figure 4.17: The depth-integrated deviatoric stress field obtained associated with gravitational potential energy differences (GPE) for the crust with B-values defined by block model 2. White vectors represent tensional principal axes of deviatoric stress. Bold vectors represent compressional principal axes of compressional stress.

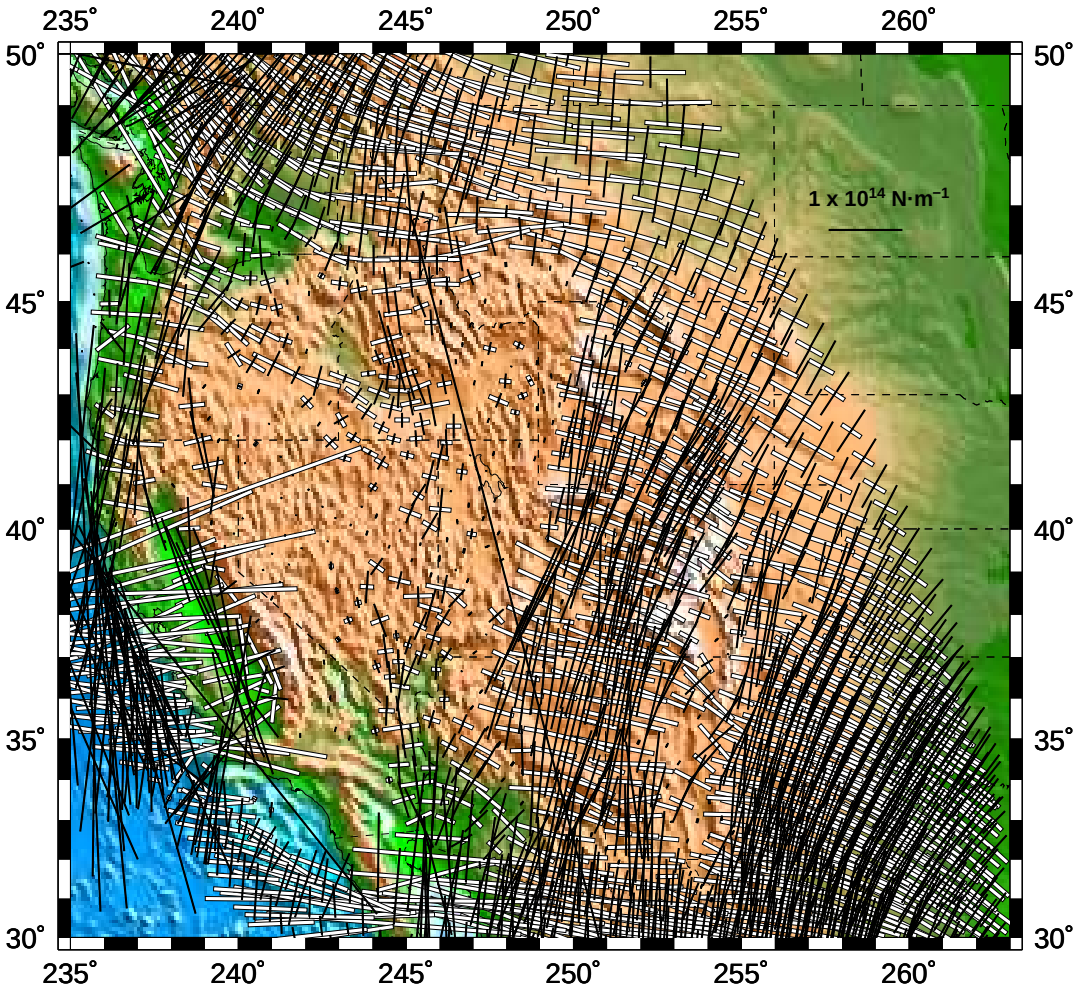

Figure 4.18: The forward dynamic depth-integrated deviatoric stress field associated with velocity boundary conditions for a flat sheet (no internal buoyancies) defined with B-values from block model 1. White vectors represent tensional principal axes of deviatoric stress. Bold vectors represent compressional principal axes of compressional stress.

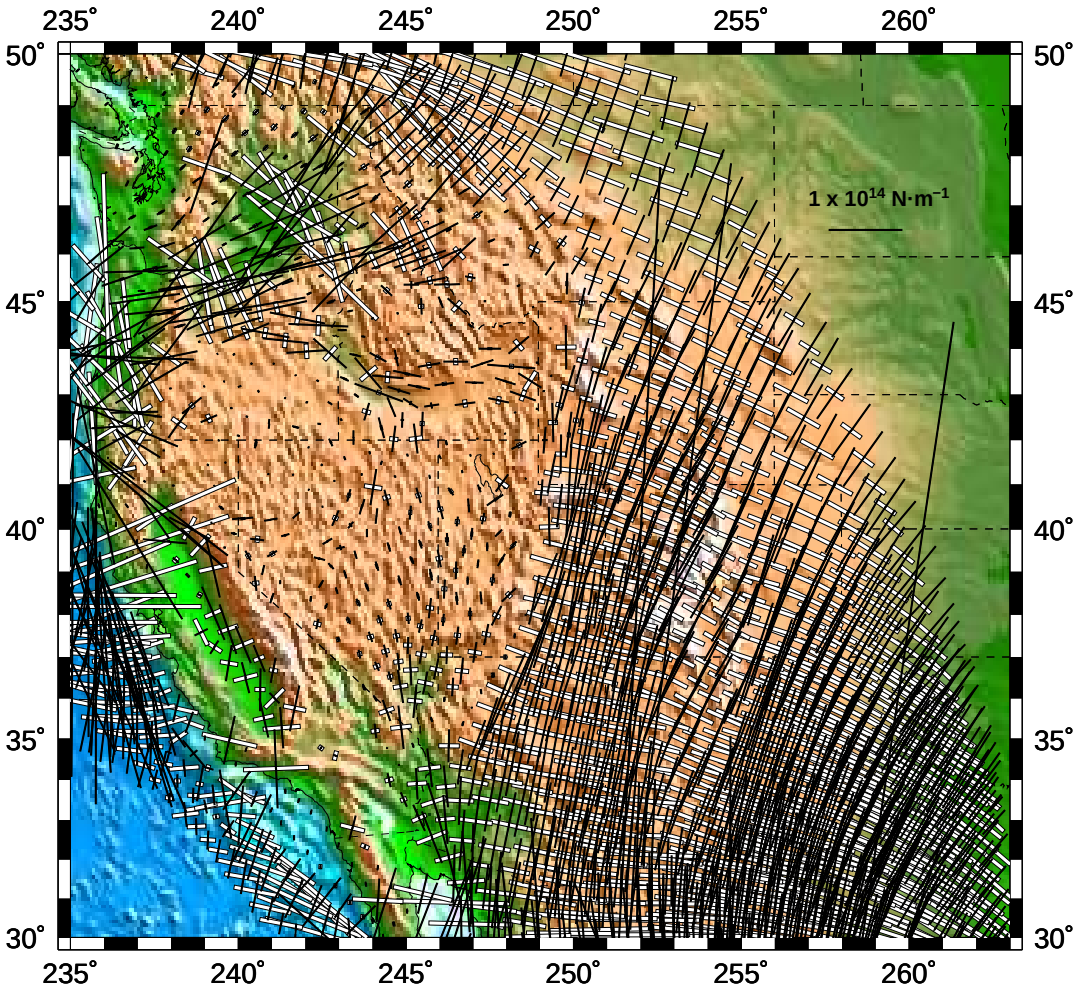

Figure 4.19: The forward dynamic depth-integrated deviatoric stress field associated with velocity boundary conditions for a flat sheet (no GPE differences) defined with B-values from block model 2. White vectors represent tensional principal axes of deviatoric stress. Bold vectors represent compressional principal axes of compressional stress.

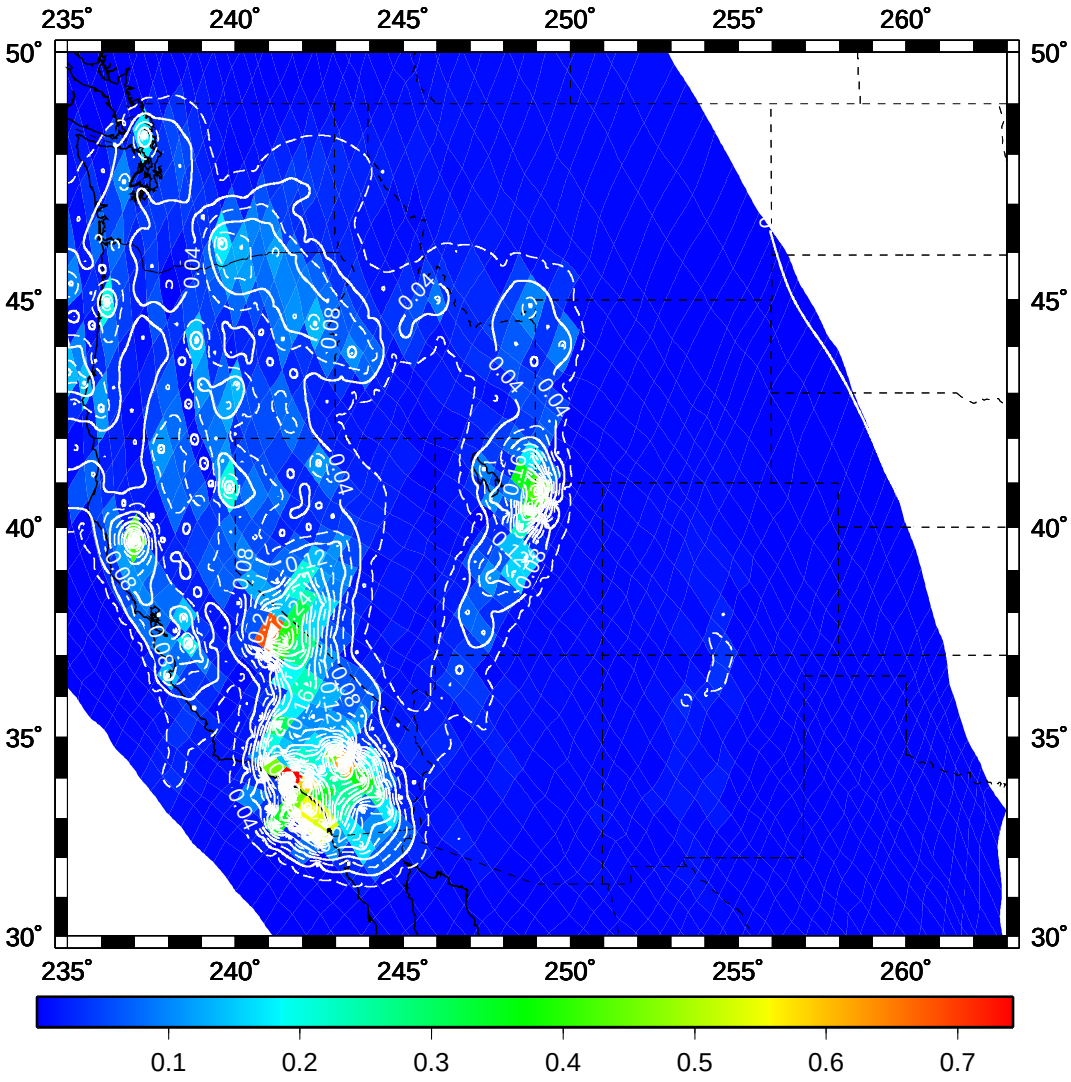

Figure 4.20: The Argand number distribution defined by block model 1. This model achieves a poor fit to long-term deformation indicators shown in Figure 4.10.

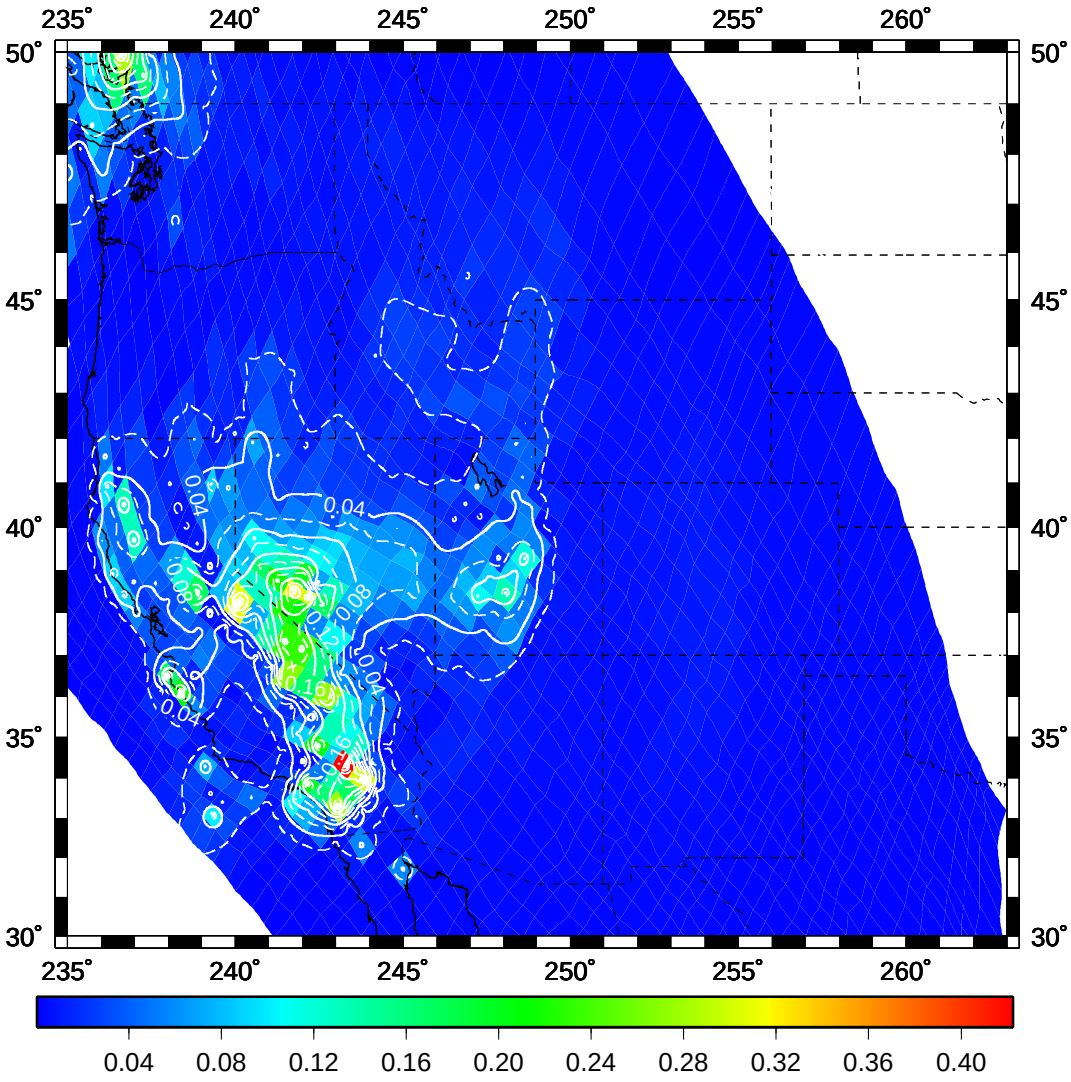

Figure 4.21: The Argand number distribution defined by block model 2. This model achieves a poor fit to long-term deformation indicators shown in Figure 4.11.

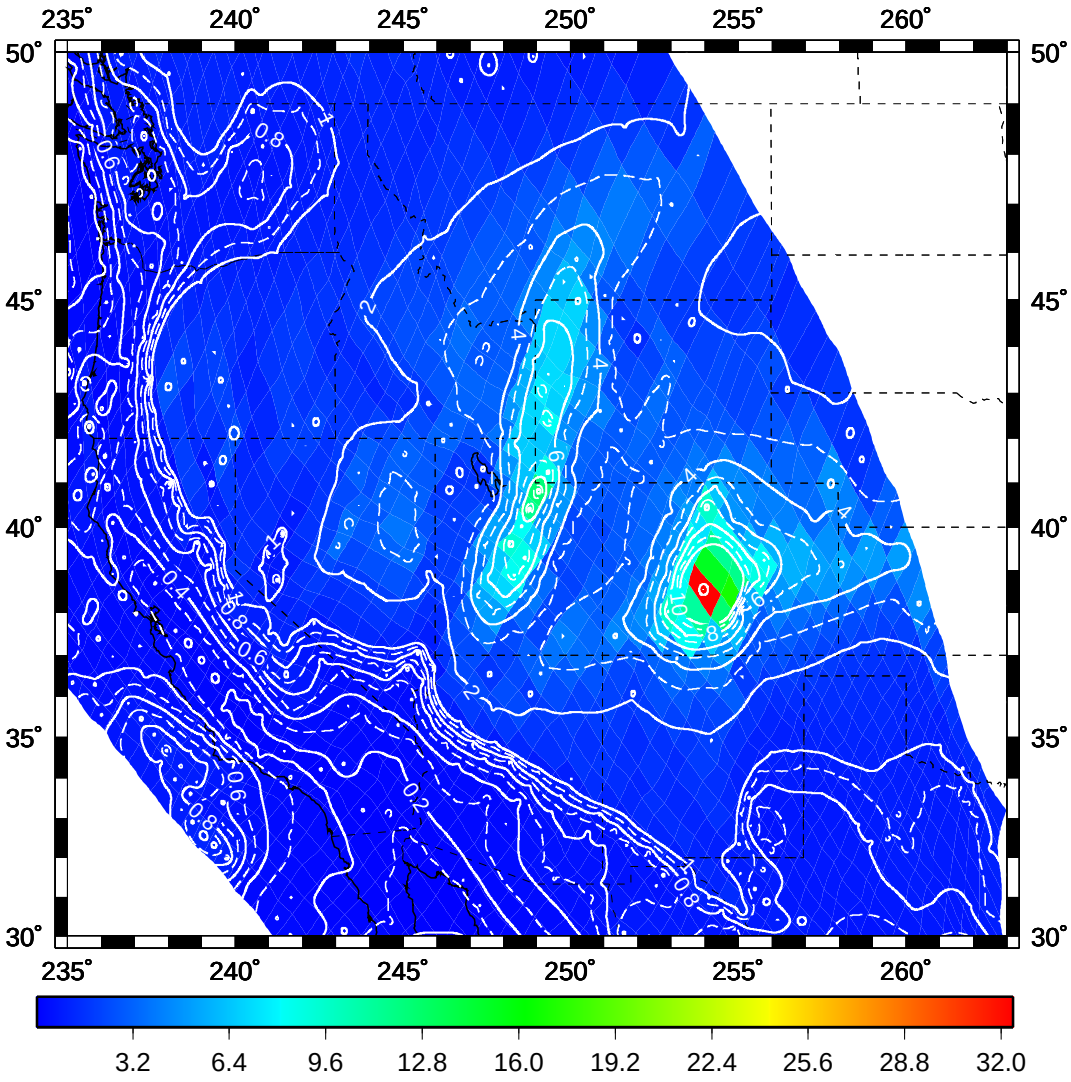

Figure 4.22: The Argand number distribution associated with model 3. This model matches the long-term deformation indicators shown in Figure 4.12.

Chapter 5

Conclusions

Conclusions

In this dissertation I addressed the long-term frictional strength of the faults within the seismogenic crust through investigation of the dynamics of the upper crust. I limited the integration depth to include only the layer of thickness from the topographic surface down to the depth of the 20 km below sea level when generating forward and inverse dynamic models. I used seismic velocity data to define the densities that define the gravitational potential energy per unit area (GPE) within the upper crust. I then solved for the depth-integrated deviatoric stress field that balances the lateral differences in GPE within the upper crustal layer. For the inverse modeling case, the deviatoric stress field associated with lateral differences in GPE calibrates the magnitude of total deviatoric stress available within the upper crust. I then solved for boundary condition stresses associated with stress field contributions from sources outside the modeled region. The boundary condition stress field, when added to the solution from GPE differences, provides a best match to deformation indicators within western North America.

The inverse models of upper crust show that stresses due to GPE variations are similar in magnitude to boundary condition stresses in western North America. The magnitudes of total deviatoric stress in the long-term seismogenic crust from the surface to 20 km below the sea level range between 0.05 – 0.75 x 10^{12} N $\cdot$ m^{-1}. From the best-fit total deviatoric stress field model, I obtain depth-integrated total stress differences and used these as a proxy for depth integrals of fault strength in moderate-to-high strain rate regions. The depth-integrated stress differences define long-term fault friction coefficients, under hydrostatic pore pressure conditions, that are considerably lower ($\overline{\mu}$ = 0.02 – 0.20) than the Byerlee-like friction coefficients obtained in laboratory studies on typical crustal rocks. I explored the sensitivity of these results by testing a range of maximum depths of integration. For depth integrals taken in excess of 20 km below sea level, there is diminishing contribution to

the depth-integrated stress differences, and by proxy depth-integrated fault strength. Sensitivity test results indicate that a seismogenic layer thickness of approximately 20 km is consistent with the depth to the expected long-term brittle-ductile transition for the diffuse plate boundary zone.

I used the recently updated United States Geologic Survey Quaternary fault and fold data base of the United States (QFBD) to build a suite of kinematic models that placed primary constraints on forward models of the upper crust for western North America. In the forward dynamic modeling approach, the dynamics of the upper crust are defined by the known internal buoyancy distributions, inferred lateral variations in effective viscosity, and imposed far-field velocity boundary conditions. Input uniform fault friction coefficients and pure fault styles inferred from our long-term kinematic strain rate model, along with the strain rates themselves, defined lateral variation in effective viscosity. Body forces are generated from differences in GPE. The velocity boundary conditions are defined using PA-NA, CO-NA, RI-NA, and JF-NA plate motion estimates. Solutions to the force-balance equations in the forward modeling method define self-consistent dynamic stress tensor, velocity, and strain rate tensor fields for the model crust. I tested and evaluated the model solutions to determine a best-fit match with long-term stress field indicators within western North America

Crustal models are defined from the surface to 20 km below sea level using a range of uniform long-term fault friction coefficients from ($\mu = 0.02$–1.0) under hydrostatic pore pressure conditions. I found that the forward dynamic solutions are sensitive to the level of friction on the faults and the distribution of the fault fabric. These two factors primarily control the relative influence that internal crustal buoyancies and plate boundary forces have on the deformation field. Evaluation of fitness of the dynamic solutions to deformation indicators is achieved using two different measures. In one fitness measure, the forward dynamic strain rate tensor styles are scored by misfit to the kinematic strain rate tensor styles inferred from Kostrov summation

of Quaternary fault observations. The uniform long-term fault friction coefficient of $\mu = 0.10$ achieved the best-fit with tensor styles of strain rate defined by Quaternary fault observations. In a second fitness measure, the dynamic model velocity fields are scored via reduced chi-square misfit with the long-term kinematic model velocity field defined by Quaternary fault observations. A uniform long-term fault friction coefficient of $\mu = 0.20$, achieved the lowest reduced chi-square misfit with the long-term kinematic model velocity field.

Forward dynamic solutions required at least an equal or greater contribution of stresses from differences in GPE than stresses arising from velocity boundary conditions in order to provide a close match to deformation indicators and patterns of finite strain in western North America. I quantifed the ratio of stress related to GPE to stress related to velocity boundary conditions, or Argand Number (Ar), for the first time for western North America. For the case with uniform long-term fault friction coefficients of $\mu = 0.10$, stresses associated with velocity boundary conditions made the primary contribution to long-term deformation along the San Andreas fault system ($Ar < 1$) only. Within the Basin and Range, however, stresses associated with GPE differences are the dominant drivers of deformation (Ar = 2–6). For the Wasatch and Colorado Rocky mountain ranges, the stresses associated with GPE differences completely dominate over contribution from velocity boundary conditions ($Ar > 10$). The lateral viscosity variations have a strong influence on the expected distribution of the Ar number, particularly within the easternmost portion of the plate boundary zone.

The strain rate tensor styles inferred from Kostrov summation of Quaternary fault observations have allowed for evaluation of forward dynamic models in great detail. I generate self-consistent dynamic stress tensor, velocity, and strain rate tensor field solutions associated with specific block model geometries for the crust and compare output from such models with observations of long-term patterns of finite strain

in the western North America. The block model geometries are defined with low fault friction ($\mu = 0.10$) in the narrow regions co-located with block bounding shear zones. Strong crustal friction ($\mu = 0.70$) is assigned to block interiors. Block model geometries yield dynamic strain rate tensor styles that are at odds with the kinematic strain rate tensor styles associated with Quaternary deformation indicators within many regions of the plate boundary zone. Overall, these models do a relatively poor job in fitting deformation styles throughout the diffuse plate boundary zone. The block model geometries produce deviatoric stresses arising from GPE differences that have little influence in driving long-term deformation within the Basin and Range. The models instead predict that the diffuse plate boundary deforms primarily through accommodation of the Pacific and Juan de Fuca plates (i.e., $Ar < 1$). The models transfer large deviatoric stresses into the plate boundary zone interior. A surprising result is that these block models, possessing large strength contrasts between shear zones and block interiors, generate a more distributed deformation than do models with uniform fault strength. Based on scoring of self-consistent dynamic model output with detailed kinematic output, I argue that a more distributed fault fabric than provided by block model geometries is required to explain the patterns of finite strain observed within the diffuse plate boundary zone of western North America. Moreover, the forward model results indicate that the level of long-term friction on the faults, along with the distribution of the fault fabric, dictate the degree to which internal buoyancies and plate boundary forces influence the deformation field. The dynamic stress and strain rate tensor fields and the dynamic velocity field each are acutely sensitive to the intrinsic mechanical properties of the faults, and to the density of available fault fabric. The deformation field in western North America therefore suggests and supports the premise of a sufficiently dense fabric of faults (e.g., like the QFBD) that possess low long-term friction coefficients of 0.10–0.20.

Bibliography

Anderson, E. M., *The Dynamics of Faulting and Dike Formation With Application to Britain*, 2^{nd} ed., Oliver and Boyd, White Plains, NY, 1951.

Antonelis, K., D. J. Johnson, M. M. Miller, and R. Palmer, GPS determination of current Pacific-North American plate motion, *Geology*, *27*, 299–302, 1999.

Bawden, G. W., W. Thatcher, R. S. Stein, K. W. Hudnut, and G. Peltzer, Tectonic contraction across Los Angeles after removal of groundwater pumping effects, *Nature*, *412*, 812–815, 2001.

Beavan, J., and J. Haines, Contemporary horizontal velocity and strain rate fields of the Pacific-Australian plate boundary zone through New Zealand, *J. Geophys. Res.*, *106*, 741–770, 2001.

Becker, T. W., and R. J. O'Connell, Predicting plate velocities with mantle circulation models, *Geochem. Geophys. Geosyst.*, *2*, 10.1029/2001GC000,171, 2001.

Becker, T. W., J. L. Hardebeck, and G. Anderson, Constraints on fault slip rates of the southern California plate boundary from GPS velocity and stress inversions, *Geophys. J. Int.*, *160*, 634–650, 2005.

Bennett, R. A., J. L. Davis, and B. P. Wernicke, Present-day pattern of cordilleran deformation in the western United States, *Geology*, *27*, 371–374, 1999.

Bennett, R. A., J. L. Davis, J. E. Normandeau, and B. P. Wernicke, Space geodetic measurements of plate boundary deformation in the western U.S. Cordillera, in *Plate Boundary Zones*, edited by S. Stein and J. T. Freymueller, vol. 30 of *Geodyn. Ser.*, pp. 27–55, AGU, Washington, D.C., 2002.

Bennett, R. A., B. P. Wernicke, N. A. Niemi, A. M. Friedrich, and J. L. Davis, Contemporary strain rates in the northern Basin and Range Province from GPS data, *Tectonics*, *22*, 1008, 2003.

Bird, P., Initiation of intracontinental subduction in Himalaya, *J. Geophys. Res.*, *83*, 4975–4987, 1978.

Bird, P., Computer simulations of Alaskan neotectonics, *Tectonics*, *15*, 225–236, 1996.

Bird, P., and X. Kong, Computer simulations of California tectonics confirm very low strength of major faults, *Geol. Soc. Am. Bull.*, *106*, 159–174, 1994.

Bird, P., and K. Piper, Plane-stress finite-element models of tectonic flow in southern California, *Phys. Earth Planet. Inter.*, *21*, 158–175, 1980.

Blanpied, M. L., D. A. Lockner, and J. D. Byerlee, An earthquake mechanism based on rapid sealing of faults, *Nature*, *358*, 574–576, 1992.

Bonner, J. L., D. D. Blackwell, and E. T. Herrin, Thermal constraints on earthquake depths in California, *Bull. Seismol. Soc. Am.*, *93*, 2333–2354, 2003.

Bos, B., and C. J. Spiers, Experimental investigation into the microstructural and mechanical evolution of phyllosilicate-bearing fault rock under conditions favouring pressure solution, *J. Struct. Geol.*, *23*, 1187–1202, 2001.

Bos, B., and C. J. Spiers, Frictional-viscous flow of phyllosilicate-bearing fault rock; microphysical model and implications for crustal strength profiles, *J. Geophys. Res.*, *107*, 2028, 2002.

Brace, W., and D. Kohlstedt, Limits on lithospheric stress imposed by laboratory experiments, *J. Geophys. Res.*, *85*, 6248–6252, 1980.

Brace, W. F., and J. D. Byerlee, Stick-slip as a mechanism for earthquakes, *Science*, *153*, 990–992, 1966.

Brocher, T. M., Empirical relations between elastic wavespeeds and density in the earth's crust, *Bull. Seismol. Soc. Am.*, *95*, 2081–2092, 2005.

Brodsky, E. E., and H. Kanamori, Elastohydrodynamic lubrication of faults, *J. Geophys. Res.*, *106*, 16,357–16,374, 2001.

Brodsky, E. E., and S. G. Prejean, New constraints on mechanisms of remotely triggered seismicity at Long Valley Caldera, *J. Geophys. Res.*, *110*, B04,302, 2005.

Brodsky, E. E., V. Karakostas, and H. Kanamori, A new observation of dynamically triggered regional seismicity; earthquakes in Greece following the August, 1999 Izmit, Turkey earthquake, *Geophys. Res. Lett.*, *27*, 2741–2744, 2000.

Brodsky, E. E., E. Roeloffs, D. Woodcock, I. Gall, and M. Manga, A mechanism for sustained groundwater pressure changes induced by distant earthquakes, *J. Geophys. Res.*, *108*, 2390, 2003.

Brudy, M., M. D. Zoback, K. Fuchs, F. Rummel, and J. Baumgaertner, The KTB deep drill hole, *J. Geophys. Res.*, *102*, 18,453–18,475, 1997.

Brune, J. N., T. L. Henyey, and R. F. Roy, Heat flow, stress, and rate of slip along the San Andreas fault, California, *J. Geophys. Res.*, *74*, 3821–3827, 1969.

Bürgmann, R., and G. Dresen, Rheology of the lower crust and upper mantle: Evidence from rock mechanics, geodesy, and field observations, *Annu. Rev. Earth Planet. Sci.*, *36*, 531–567, 2008.

Burov, E., and A. Watts, The long-term strength of continental lithosphere: "jelly sandwich" or "creme brulee"?, *GSA Today*, *16*, 4–10, 2006.

Byerlee, J., Model for episodic flow of high-pressure water in fault zones before earthquakes, *Geology*, *21*, 303–306, 1993.

Byerlee, J. D., Brittle-ductile transition in rocks, *J. Geophys. Res.*, *73*, 4741–4750, 1968.

Byerlee, J. D., Rock friction and earthquake prediction, *Pure Appl. Geophys.*, *116*, 615–626, 1978.

Byerlee, J. D., Friction, overpressure and fault normal compression, *Geophys. Res. Lett.*, *17*, 2109–2112, 1990.

Carter, N. L., and M. C. Tsenn, Flow properties of continental lithosphere, *Tectonophysics*, *136*, 27–63, 1987.

Chen, W.-P., and P. Molnar, Focal depths of intracontinental and intraplate earthquakes and their implications for the thermal and mechanical properties of the lithosphere, *J. Geophys. Res.*, *88*, 4183–4214, 1983.

Chéry, J., M. D. Zoback, and R. Hassani, An integrated mechanical model of the San Andreas fault in central and northern California, *J. Geophys. Res.*, *106*, 22,051–22,066, 2001.

Chéry, J., M. Zoback, and S. Hickman, A mechanical model of the San Andreas fault and SAFOD Pilot Hole stress measurements, *Geophys. Res. Lett.*, *31*, L15S13, 2004.

Chester, F. M., J. P. Evans, and R. L. Biegel, Internal structure and weakening mechanisms of the San-Andreas fault, *J. Geophys. Res.*, *98*, 771–786, 1993.

Chulick, G. S., and W. D. Mooney, Seismic structure of the crust and uppermost mantle of North America and adjacent oceanic basins; a synthesis, *Bull. Seismol. Soc. Am.*, *92*, 2478–2492, 2002.

Connolly, J. A. D., and Y. Y. Podladchikov, Fluid flow in compressive tectonic settings: Implications for midcrustal seismic reflectors and downward fluid migration, *J. Geophys. Res.*, *109*, B04,201, 2004.

Cox, S. F., Fluid flow in mid- to deep crustal shear systems: Experimental constraints, observations on exhumed high fluid flux shear systems, and implications for seismogenic processes, *Earth Planets Space*, *54*, 1121–1125, 2002.

d'Alessio, M. A., C. F. Williams, and R. Bürgmann, Frictional strength heterogeneity and surface heat flow: Implications for the strength of the creeping San Andreas fault, *J. Geophys. Res.*, *111*, B05,410, 2006.

DeMets, C., A reappraisal of seafloor spreading lineations in the Gulf of California; implications for the transfer of Baja California to the Pacific plate and estimates of Pacific-North America motion, *Geophys. Res. Lett.*, *22*, 3545–3548, 1995.

DeMets, C., and T. H. Dixon, New kinematic models for Pacific-North America motion from 3 Ma to present; I, Evidence for steady motion and biases in the NUVEL-1A model, *Geophys. Res. Lett.*, *26*, 1921–1924, 1999.

DeMets, C., and S. Stein, Present-day kinematics of the Rivera Plate and implications for tectonics in southwestern Mexico, *J. Geophys. Res.*, *95*, 21,931–21,948, 1990.

DeMets, C., and D. Wilson, Relative motions of the Pacific, Rivera, North American, and Cocos plates since 0.78 Ma, *J. Geophys. Res.*, *102(B2)*, 2789–2806, 1997.

DeMets, C., R. G. Gordon, D. F. Argus, and S. Stein, Effect of recent revisions to the

geomagnetic reversal time scale on estimates of current plate motions, *Geophys. Res. Lett.*, *21*, 2191–2194, 1994.

Di Toro, G., D. L. Goldsby, and T. E. Tullis, Friction falls towards zero in quartz rock as slip velocity approaches seismic rates, *Nature*, *427*, 436–439, 2004.

Dixon, T. H., M. Miller, F. Farina, H. Wang, and D. Johnson, Present-day motion of the Sierra Nevada block and some tectonic implications for the Basin and Range Province, North American Cordillera, *Tectonics*, *19*, 1–24, 2000.

Dixon, T. H., E. Norabuena, and L. Hotaling, Paleoseismology and Global Positioning System: Earthquake-cycle effects and geodetic versus geologic fault slip rates in the Eastern California shear zone, *Geology*, *31*, 55–58, 2003.

Edwards, M., and L. Ratschbacher, Seismic and aseismic weakening effects in transtension: Field and microstructural observations on the mechanics and architecture of a large fault zone in southeastern Tibet, in *High-Strain Zones: Structure and Physical Properties*, edited by D. Bruhn and L. Burlini, vol. 245 of *Geol. Soc. Spec. Publ.*, pp. 109–141, 2005.

England, P., and D. McKenzie, A thin viscous sheet model for continental deformation, *Geophys. J. R. Astron. Soc.*, *70*, 295–321, 1982.

Faulkner, D. R., and E. H. Rutter, Can the maintenance of overpressured fluids in large strike-slip fault zones explain their apparent weakness?, *Geology*, *29*, 503–506, 2001.

Fay, N., and E. Humphreys, Dynamics of the Salton Block: Absolute fault strength and crust-mantle coupling in Southern California, *Geology*, *34*, 261–264, 2006.

Fialko, Y., L. Rivera, and H. Kanamori, Estimate of differential stress in the up-

per crust from variations in topography and strike along the San Andreas fault, *Geophys. J. Int.*, *160*, 527–527, 2005.

Fitzenz, D. D., and S. A. Miller, Fault compaction and overpressured faults: Results from a 3-d model of a ductile fault zone, *Geophys. J. Int.*, *155*, 111–125, 2003.

Flesch, L. M., W. E. Holt, A. J. Haines, and B. M. Shen-Tu, Dynamics of the Pacific-North American plate boundary in the western United States, *Science*, *287*, 834–836, 2000.

Flesch, L. M., A. J. Haines, and W. E. Holt, Dynamics of the India-Eurasia collision zone, *J. Geophys. Res.*, *106*, 16,435–16,460, 2001.

Flesch, L. M., W. E. Holt, A. J. Haines, L. Wen, and B. Shen-Tu, The dynamics of western North America: Stress magnitudes and the relative role of gravitational potential energy, plate interaction at the boundary, and basal tractions, *Geophys. J. Int.*, *169*, 866–896, 2007.

Freed, A. M., S. T. Ali, and R. Burgmann, Evolution of stress in Southern California for the past 200 years from coseismic, postseismic and interseismic stress changes, *Geophys. J. Int.*, *169*, 1164–1179, 2007.

Freymueller, J. T., M. H. Murray, S. Paul, and C. David, Kinematics of the Pacific-North America plate boundary zone, northern California, *J. Geophys. Res.*, *104*, 7419–7441, 1999.

Gan, W., J. L. Svarc, J. C. Savage, and W. H. Prescott, Strain accumulation across the eastern California shear zone at latitude 36 degrees 30° N, *J. Geophys. Res.*, *105*, 16,229–16,236, 2000.

Geist, E. L., and D. J. Andrews, Slip rates on San Francisco Bay area faults from

anelastic deformation of the continental lithosphere, *J. Geophys. Res.*, *105*, 25,543–25,552, 2000.

Ghosh, A., W. E. Holt, L. M. Flesch, and L. Dimitrova, Contribution of gravitational potential energy differences to the global stress field (submitted), *J. Geophys. Res.*, 2008a.

Ghosh, A., W. E. Holt, L. Wen, L. M. Flesch, and A. J. Haines, Joint modeling of lithosphere and mantle dynamics elucidating lithosphere-mantle coupling, *Geophys. Res. Lett.*, *xxx*, xxx, 2008b.

Ghosh, A., W. E. Holt, L. Wen, L. M. Flesch, and A. J. Haines, Predicting the lithospheric stress field and plate motions by joint modeling of lithosphere and mantle dynamics (submitted), *J. Geophys. Res.*, 2008c.

Gomberg, J., P. Bodin, K. Larson, and H. Dragert, Earthquake nucleation by transient deformations caused by the M=7.9 Denali, Alaska, earthquake, *Nature*, *427*, 621–624, 2004.

Haines, A. J., and W. E. Holt, A procedure for obtaining the complete horizontal motions within zones of distributed deformation from the inversion of strain-rate data, *J. Geophys. Res.*, *98*, 12,057–12,082, 1993.

Hammond, W. C., and W. Thatcher, Contemporary tectonic deformation of the basin and range province, western united states: 10 years of observation with the global positioning system, *J. Geophys. Res.*, *109*, B08,403, 2004.

Hammond, W. C., and W. Thatcher, Northwest Basin and Range tectonic deformation observed with the Global Positioning System, 1999-2003, *J. Geophys. Res.*, *110*, B10,405, 2005.

Hammond, W. C., and W. Thatcher, Crustal deformation across the Sierra Nevada, northern Walker lane, Basin and Range transition, western United States measured with GPS, 2000-2004, *J. Geophys. Res.*, *112*, B05,411, 2007.

Han, R., T. Shimamoto, T. Hirose, J.-H. Ree, and J.-i. Ando, Ultralow Friction of Carbonate Faults Caused by Thermal Decomposition, *Science*, *316*, 878–881, 2007.

Handy, M. R., and J.-P. Brun, Seismicity, structure and strength of the continental lithosphere, *Earth Planetary Sci. Lett.*, *223*, 427–441, 2004.

Hetland, E. A., and B. H. Hager, Relationship of geodetic velocities to velocities in the mantle, *Geophysical Research Letters*, *31*, L17,604, 2004.

Hetland, E. A., and B. H. Hager, Interseismic strain accumulation: Spin-up, cycle invariance, and irregular rupture sequences, *Geochem. Geophys. Geosyst.*, *7*, Q05,004, 2006.

Hickman, S., and M. Zoback, Stress orientations and magnitudes in the SAFOD pilot hole, *Geophys. Res. Lett.*, *31*, L15S12, 2004.

Hill, D. P., et al., Seismicity remotely triggered by the magnitude 7.3 Landers, California, earthquake, *Science*, *260*, 1617–1623, 1993.

Holdsworth, R., Weak faults; rotten cores, *Science*, *303*, 181–182, 2004.

Holdsworth, R. E., M. Stewart, J. Imber, and R. A. Strachan, The structure and rheological evolution of reactivated continental fault zones; a review and case study, in *Continental Reactivation and Reworking*, edited by J. A. Miller, R. E. Holdsworth, I. S. Buick, and M. Hand, vol. 184 of *Geol. Soc. Spec. Publ.*, pp. 115–137, 2001.

Holt, W. E., B. Shen-Tu, J. Haines, and J. Jackson, On the determination of self-consistent strain rate fields within zones of distribution continental deformation,

in *The History and Dynamics of Global Plate Motions*, edited by M. A. Richards, R. G. Gordon, and R. D. Van der Hilst, vol. 121 of *Geophys. Monogr. Ser.*, pp. 113–141, AGU, Washington, D.C., 2000.

Horsman, E., and B. Tikoff, Quantifying simultaneous discrete and distributed deformation, *J. Struct. Geol.*, *27*, 1168–1189, 2005.

Hubbert, M. K., and W. W. Rubey, Mechanics of fluid-filled porous solids and its application to overthrust faulting, part 1 of role of fluid pressure in mechanics of overthrust faulting, *Geol. Soc. Am. Bull.*, *70*, 115–166, 1959.

Humphreys, E., and D. D. Coblentz, North American dynamics and western U.S. tectonics,, *Rev. Geophys.*, *45*, RG3001, 2007.

Hyndman, R. D., and K. Wang, Thermal constraints on the zone of major thrust earthquake failure: The Cascadia Subduction Zone, *J. Geophys. Res.*, *98*, 2039—2060, 1993.

Imber, J., R. E. Holdsworth, C. A. Butler, and R. A. Strachan, A reappraisal of the Sibson-Scholz fault zone model; the nature of the frictional to viscous ("brittle-ductile") transition along a long-lived, crustal-scale fault, Outer Hebrides, Scotland, *Tectonics*, *20*, 601–624, 2001.

Jackson, J., Strength of the continental lithosphere; time to abandon the jelly sandwich?, *GSA Today*, *12*, 4–10, 2002.

Jackson, J. A., and N. J. White, Normal faulting in the upper continental crust: observations from regions of active extension, *J. Struct. Geol.*, *11*, 15–36, 1989.

Jaeger, J. C., and N. G. W. Cook, *Fundamentals of Rock Mechanics*, 2^{nd} ed., Chapman and Hall Ltd., London, 1976.

Janecke, S. U., and J. P. Evans, Feldspar-influenced rock rheologies, *Geology*, *16*, 1064–1067, 1988.

Jefferies, S., R. Holdsworth, C. Wibberley, T. Shimamoto, C. Spiers, A. Niemeijer, and G. Lloyd, The nature and importance of phyllonite development in crustal-scale fault cores: An example from the Median Tectonic Line, Japan, *J. Struct. Geol.*, *28*, 220–235, 2006.

Jennings, C., Fault activity map of California and adjacent areas, *Tech. rep.*, California Department of Conservation, Division of Mines and Geology, Sacramento, 1994.

Johnson, P. A., and X. Jia, Nonlinear dynamics, granular media and dynamic earthquake triggering, *Nature*, *437*, 871–874, 2005.

Kaban, M. K., and W. D. Mooney, Density structure of the lithosphere in the southwestern United States and its tectonic significance, *J. Geophys. Res.*, *106*, 721–739, 2001.

Kennedy, B. M., Y. K. Kharaka, W. C. Evans, A. Ellwood, D. J. DePaolo, J. Thordsen, G. Ambats, and R. H. Mariner, Mantle fluids in the San Andreas fault system, California, *Science*, *278*, 1278–1281, 1997.

Khazaradze, G., A. Qamar, and H. Dragert, Tectonic deformation in western Washington from continuous GPS measurements, *Geophys. Res. Lett.*, *26*, 3153–3156, 1999.

Klein, E. C., L. M. Flesch, W. E. Holt, and A. J. Haines, Evidence of long-term weakness on seismogenic faults in western North America from dynamic modeling, *J. Geophy. Res.*, *under review.*, 2008.

Kohlstedt, D. L., B. Evans, and S. J. Mackwell, Strength of the lithosphere; constraints imposed by laboratory experiments, *J. Geophys. Res.*, *100*, 17,587–17,602, 1995.

Kostrov, V. V., Seismic moment, energy of earthquakes, and the seismic flow of rock, *Izv. Acad. Sci. USSR Phys. Solid Earth, Engl. Transl.*, *10*, 23–44, 1974.

Kreemer, C., W. E. Holt, and A. J. Haines, An integrated global model of present-day plate motions and plate boundary deformation, *Geophys. J. Int.*, *154*, 8–34, 2003.

Lachenbruch, A. H., and J. H. Sass, Heat-flow from Cajon Pass, fault strength, and tectonic implications, *J. Geophys. Res.*, *97*, 4995–5015, 1992.

Lavallee, D., et al., GPSVEL Project: Towards a dense global GPS velocity field, in *Proceedings of the International Association of Geodesy Scientific Assembly, Budapest, 2-7*, 2001.

Lithgow-Bertelloni, C., and J. H. Guynn, Origin of the lithospheric stress field, *J. Geophys. Res.*, *109*, B01,408, 2004.

Liu, M., Y. Q. Yang, Q. S. Li, and H. Zhang, Parallel computing of multi-scale continental deformation in the Western United States: Preliminary results, *Phys. Earth Planet Int.*, *163*, 35–51, 2007.

Liu, Z., and P. Bird, North america plate is driven westward by lower mantle flow, *Geophys. Res. Lett.*, *29*, 2164, 2002.

Lowry, A. R., and R. B. Smith, Strength and rheology of the western U.S. Cordillera, *J. Geophys. Res.*, *100*, 17,947–17,963, 1995.

Lowry, A. R., N. M. Ribe, and R. B. Smith, Dynamic elevation of the Cordillera, western United States, *J. Geophys. Res.*, *105*, 23,371–23,390, 2000.

Ludwig, W. J., J. E. Nafe, and C. L. Drake, Seismic refraction, in *The Sea*, edited by A. E. Maxwell, vol. 4, pp. 53–84, Wiley-Interscience, New York, 1970.

Ma, C., and J. Ryan, NASA Space Geodesy Program - GSFC data analysis-1998, VLBI geodetic results 1979-1998, *Tech. rep.*, NASA, 1998.

Ma, K. F., E. E. Brodsky, J. Mori, C. Ji, T. R. A. Song, and H. Kanamori, Evidence for fault lubrication during the 1999 Chi-Chi, Taiwan, earthquake (Mw7.6), *Geophys. Res. Lett.*, *30*, 1244, 2003.

Macelwane, J. B., Problems and progress on the geologico-seismological frontier, *Science*, *83*, 193–198, 1936.

Maggi, A., J. A. Jackson, D. McKenzie, and K. Priestley, Earthquake focal depths, effective elastic thickness, and the strength of the continental lithosphere, *Geology*, *28*, 495–498, 2000.

McCaffrey, R., Block kinematics of the Pacific–North america plate boundary in the southwestern United States from inversion of GPS, seismological, and geologic data, *J. Geophys. Res.*, *110*, B07,401, 2005.

McCaffrey, R., M. D. Long, C. Goldfinger, P. C. Zwick, J. L. Nabelek, C. K. Johnson, and C. Smith, Rotation and plate locking at the southern Cascadia subduction zone, *Geophys. Res. Lett.*, *27*, 3117–3120, 2000.

McCaffrey, R., A. I. Qamar, R. W. King, R. Wells, G. Khazaradze, C. A. Williams, C. W. Stevens, J. J. Vollick, and P. C. Zwick, An update of quaternary faults of central and eastern oregon, *Geophys. J. Int.*, *169*, 1315–1340, 2007.

McCaig, A. M., Deep fluid circulation in fault zones, *Geology*, *16*, 867–870, 1988.

McClusky, S. C., S. C. Bjornstad, B. H. Hager, R. W. King, B. J. Meade, M. M. Miller, F. C. Monastero, and B. J. Souter, Present day kinematics of the eastern

California shear zone from a geodetically constrained block model, *Geophys. Res. Lett.*, *28*, 3369–3372, 2001.

McGarr, A., Some constraints on levels of shear stress in the crust from observations and theory, *J. Geophys. Res.*, *85*, 6231–6238, 1980.

Meade, B. J., and B. H. Hager, Block models of crustal motion in southern California constrained by GPS measurements, *J. Geophys. Res.*, *110*, B03,403, 2005.

Melosh, H. J., Acoustic fluidization; a new geologic process?, *J. Geophys. Res.*, *84*, 7513–7520, 1979.

Melosh, H. J., Dynamical weakening of faults by acoustic fluidization, *Nature*, *379*, 601–606, 1996.

Miller, M. M., D. J. Johnson, T. H. Dixon, and R. K. Dokka, Refined kinematics of the eastern California shear zone from GPS observations, 1993-1998, *J. Geophys. Res.*, *106*, 2245–2263, 2001a.

Miller, M. M., J. Johnson, Daniel, C. M. Rubin, H. Dragert, K. Wang, A. Qamar, and C. Goldfinger, GPS-determination of along-strike variation in Cascadia margin kinematics; implications for relative plate motion, subduction zone coupling, and permanent deformation, *Tectonics*, *20*, 161–176, 2001b.

Miller, S. A., Inferring fault strength from earthquake rupture properties and the tectonic implications of high pore pressure faulting, *Earth Planets Space*, *54*, 1173–1179, 2002.

Miller, S. A., and A. Nur, Permeability as a toggle switch in fluid-controlled crustal processes, *Earth Planetary Sci. Lett.*, *183*, 133–146, 2000.

Miller, S. A., A. Nur, and D. L. Olgaard, Earthquakes as a coupled shear stress-high pore pressure dynamical system, *Geophys. Res. Lett.*, *23*, 197–200, 1996.

Miller, S. A., C. Collettini, L. Chiaraluce, M. Cocco, M. Barchi, and B. J. P. Kaus, Aftershocks driven by a high-pressure CO_2 source at depth, *Nature*, *427*, 724–727, 2004.

Moore, D. E., and D. A. Lockner, Crystallographic controls on the frictional behavior of dry and water-saturated sheet structure minerals, *J. Geophys. Res.*, *109*, B03,401, 2004.

Morrow, C., B. Radney, and J. D. Byerlee, Frictional strength and the effective pressure law of montmorillonite and illite clays, in *Fault mechanics and Transport Properties of Rocks; A Festschrift in Honor of W. F. Brace*, edited by B. Evans and T.-F. Wong, pp. 69–88, Academic Press, London, 1992.

Morrow, C., J. Solum, S. Tembe, D. Lockner, and T. Wong, Using drill cutting separates to estimate the strength of narrow shear zones at SAFOD, *Geophys. Res. Lett.*, *34*, L11,301, 2007.

Mount, V. S., and J. Suppe, State of stress near the San Andreas fault; implications for wrench tectonics, *Geology*, *15*, 1143–1146, 1987.

Niemeijer, A., and C. Spiers, Influence of phyllosilicates on fault strength in the brittle-ductile transition: Insights from rock analogue experiments, in *High-Strain Zones: Structure and Physical Properties*, edited by D. Bruhn and L. Burlini, vol. 245 of *Geol. Soc. Spec. Publ.*, pp. 303–327, 2005.

Numelin, T., C. Marone, and E. Kirby, Frictional properties of natural fault gouge from a low-angle normal fault, Panamint Valley, California, *Tectonics*, *26*, TC2004, 2007.

Oldow, J. S., Active transtensional boundary zone between the western Great Basin and Sierra Nevada block, western U.S. Cordillera, *Geology*, *31*, 1033–1036, 2003.

Oskin, M., L. Perg, D. Blumentritt, S. Mukhopadhyay, and A. Iriondo, Slip rate of the Calico fault: Implications for geologic versus geodetic rate discrepancy in the Eastern California Shear Zone, *J. Geophys. Res.*, *112*, B03,402, 2007.

Parsons, T., Nearly frictionless faulting by unclamping in long-term interaction models, *Geology*, *30*, 1063–1066, 2002.

Paterson, M. S., Relating experimental and geological rheology, *Int. J. Earth Sci.*, *90*, 157–167, 2001.

Petersen, M. D., and S. G. Wesnousky, Fault slip rates and earthquake histories for active faults in southern California, *Bull. Seismol. Soc. Am.*, *84*, 1608–1649, 1994.

Plafker, G., and H. C. Berg, The Geology of Alaska, in *The geology of North America*, edited by G. Plafker and H. C. Berg, vol. G-1, chap. Overview of the geology and tectonic evolution of Alaska, pp. 989–1021, Geol. Soc. of Am., 1994.

Pollitz, F. F., The relationship between the instantaneous velocity field and the rate of moment release in the lithosphere, *Geophys. J. Int.*, *153*, 595–608, 2003.

Pollitz, F. F., and M. Vergnolle, Mechanical deformation model of the western united states instantaneous strain-rate field, *Geophys. J. Int.*, *167*, 421–444, 2006.

Pollitz, F. F., P. McCrory, J. Svarc, and J. Murray, Dislocation models of interseismic deformation in the western United States, *J. Geophys. Res.*, *113*, B04,413, 2008.

Prescott, W. H., J. C. Savage, J. L. Svarc, and D. Manaker, Deformation across the Pacific-North America Plate boundary near San Francisco, California, *J. Geophys. Res.*, *106*, 6673–6682, 2001.

Provost, A.-S., and H. Houston, Orientation of the stress field surrounding the creeping section of the San Andreas Fault: Evidence for a narrow mechanically weak fault zone, *J. Geophys. Res.*, *106*, 11,373–11,386, 2001.

Puskas, C. M., R. B. Smith, C. M. Meertens, and W. L. Chang, Crustal deformation of the Yellowstone-Snake River Plain volcano-tectonic system: Campaign and continuous GPS observations, 1987-2004, *J. Geophys. Res.*, *112*, B03,401, 2007.

Raleigh, C. B., J. H. Healy, and J. D. Bredehoeft, Experiment in earthquake control at Rangely, Colorado, *Science*, *191*, 1230–1237, 1976.

Ranalli, G., and D. C. Murphy, Rheological stratification of the lithosphere, *Tectonophysics*, *132*, 281–295, 1987.

Reasenberg, P. A., and R. W. Simpson, Response of regional seismicity to the static stress change produced by the Loma Prieta earthquake, *Science*, *255*, 1687–1690, 1992.

Regenauer-Lieb, K., R. F. Weinberg, and G. Rosenbaum, The effect of energy feedbacks on continental strength, *Nature*, *442*, 67–70, 2006.

Rice, J., Fault stress states, pore pressure distributions, and the weakness of the San Andreas fault, in *Fault mechanics and Transport Properties of Rocks; A Festschrift in Honor of W. F. Brace*, edited by B. Evans and T.-F. Wong, pp. 69–88, Academic Press, 1992.

Ruff, L. J., Limits of the seismogenic zone, in *MARGINS Theoretical and Experimental Earth Science Series*, edited by G. D. Karner, B. Taylor, N. W. Driscoll, and D. L. Kohlstedt, pp. 261–283, Columbia Univ. Press, New York, 2004.

Saffer, D. M., B. A. Bekins, and S. Hickman, Topographically driven groundwater flow and the San Andreas heat flow paradox revisited, *J. Geophys. Res.*, *108*, 2274, 2003.

Sauber, J., S. McClusky, and R. King, Relation of ongoing deformation rates to the

subduction zone process in southern Alaska, *Geophys. Res. Lett.*, *24*, 2853–2856, 1997.

Savage, J. C., W. Gan, W. H. Prescott, and J. L. Svarc, Strain accumulation across the Coast Ranges at the latitude of San Francisco, 1994-2000, *J. Geophys. Res.*, *109*, B03,413, 2004.

Scholz, C., The brittle-plastic transition and the depth of seismic faulting, *Geol. Rundsch.*, *77*, 319–328, 1988.

Scholz, C. H., Earthquakes and friction laws, *Nature*, *391*, 37–42, 1998.

Scholz, C. H., Evidence for a strong San Andreas fault, *Geology*, *28*, 163–166, 2000.

Scholz, C. H., and T. C. Hanks, The strength of the San Andreas fault: A discussion, in *MARGINS Theoretical and Experimental Earth Science Series*, edited by G. D. Karner, B. Taylor, N. W. Driscoll, and D. L. Kohlstedt, pp. 261–283, Columbia Univ. Press, New York, 2004.

Shea, W. T., and A. K. Kronenberg, Rheology and deformation mechanisms of an isotropic mica schist, *J. Geophys. Res.*, *97*, 15,201–15,237, 1992.

Shen-Tu, B., W. E. Holt, and A. J. Haines, Deformation kinematics in the western United States determined from Quaternary fault slip rates and recent geodetic data, *J. Geophys. Res.*, *104*, 28,927–28,956, 1999.

Sibson, R. H., Frictional constraints on thrust, wrench and normal faults, *Nature*, *249*, 542–544, 1974.

Sibson, R. H., Fault zone models, heat flow, and the depth distribution of earthquakes in the continental crust of the United States, *Bull. Seismol. Soc. Am.*, *72*, 151–163, 1982.

Sibson, R. H., Continental fault structure and the shallow earthquake source, *J. Geol. Soc. London*, *140*, 741–767, 1983.

Sibson, R. H., Roughness at the base of the seismogenic zone; contributing factors, *J. Geophys. Res.*, *89*, 5791–5799, 1984.

Sibson, R. H., A note on fault reactivation, *J. Struct. Geol.*, *7*, 751–754, 1985.

Sibson, R. H., Conditions for fault-valve behaviour, in *Deformation mechanisms, rheology and tectonics*, edited by R. J. Knipe and E. H. Rutter, vol. 54 of *Geo. Soc. Spec. Publ.*, pp. 15–28, 1990a.

Sibson, R. H., Rupture nucleation on unfavorably oriented faults, *Bull. Seismol. Soc. Am.*, *80*, 1580–1604, 1990b.

Sibson, R. H., An assessment of field evidence for Byerlee friction, *Pure Appl. Geophys.*, *142*, 645–662, 1994.

Sleep, N. H., and M. L. Blanpied, Creep, compaction and the weak rheology of major faults, *Nature*, *359*, 687–692, 1992.

Sleep, N. H., and M. L. Blanpied, Ductile creep and compaction: A mechanism for transiently increasing fluid pressure in mostly sealed fault zones, *Pure Appl. Geophys.*, *143*, 9–40, 1994.

Smith, B. R., and D. T. Sandwell, A model of the earthquake cycle along the San Andreas Fault System for the past 1000 years, *J. Geophys. Res.*, *111*, B01,405, 2006.

Sonder, L. J., and P. England, Vertical averages of rheology of the continental lithosphere - relation to thin sheet parameters, *Earth Planetary Sci. Lett.*, *77*, 81–90, 1986.

Sonder, L. J., and C. H. Jones, Western United States extension: How the west was widened, *Annu. Rev. Earth Planet. Sci.*, *27*, 417–462, 1999.

Sornette, D., and A. Sornette, Acoustic fluidization for earthquakes?, *Bull. Seismol. Soc. Am.*, *90*, 781–785, 2000.

Spray, J. G., Evidence for melt lubrication during large earthquakes, *Geophys. Res. Lett.*, *32*, L07,301, 2005.

Steinberger, B., H. Schmeling, and G. Marquart, Large-scale lithospheric stress field and topography induced by global mantle circulation, *Earth Planetary Sci. Lett.*, *186*, 75–91, 2001.

Stewart, M., R. E. Holdsworth, and R. A. Strachan, Deformation processes and weakening mechanisms within the frictional-viscous transition zone of major crustal-scale faults; insights from the Great Glen fault zone, Scotland, *J. Struct. Geol.*, *22*, 543–560, 2000.

Streit, J. E., Low frictional strength of upper crustal faults; a model, *J. Geophys. Res.*, *102*, 24,619–24,626, 1997.

Svarc, J. L., J. C. Savage, W. H. Prescott, and M. H. Murray, Strain accumulation and rotation in western Oregon and southwestern Washington, *J. Geophys. Res.*, *107*, Art. No. 2087, 2002a.

Svarc, J. L., J. C. Savage, W. H. Prescott, and A. R. Ramelli, Strain accumulation and rotation in western Nevada, 1993-2000, *J. Geophys. Res.*, *107*, Art. No. 2090, 2002b.

Tembe, S., D. A. Lockner, J. G. Solum, C. A. Morrow, T. Wong, and D. E. Moore, Frictional strength of cuttings and core from SAFOD drillhole phases 1 and 2, *Geophys. Res. Lett.*, *33*, L23,307, 2006.

Thatcher, W., Microplate versus continuum descriptions of active tectonic deformation, *J. Geophys. Res.*, *100*, 3885–3894, 1995.

Thatcher, W., GPS constraints on the kinematics of continental deformation, *Int. Geol. Rev.*, *45*, 191–212, 2003.

Thatcher, W., G. R. Foulger, B. R. Julian, J. Svarc, E. Quilty, and G. W. Bawden, Present-day deformation across the Basin and Range Province, western United States, *Science*, *283*, 1714–1718, 1999.

Townend, J., and M. Zoback, Regional tectonic stress near the San Andreas fault in central and southern California, *Geophys. Res. Lett.*, *31*, L15S11, 2004.

Townend, J., and M. D. Zoback, How faulting keeps the crust strong, *Geology*, *28*, 399–402, 2000.

Wallace, R. E., Patterns and timing of late quaternary faulting in the Great Basin province and relation to some regional tectonic features, *J. Geophys. Res.*, *89(B7)*, 5763–5769, 1984.

Wang, K. L., and J. H. He, Mechanics of low-stress forearcs: Nankai and Cascadia, *J. Geophys. Res.*, *104*, 15,191–15,205, 1999.

Watson, K. M., Y. Bock, and D. T. Sandwell, Satellite interferometric observations of displacements associated with seasonal groundwater in the Los Angeles basin, *J. Geophys. Res.*, *107*, 2074, 2002.

West, M., J. J. Sanchez, and S. R. McNutt, Periodically triggered seismicity at Mount Wrangell, Alaska, after the Sumatra earthquake, *Science*, *308*, 1144–1146, 2005.

Wilson, B., T. Dewers, Z. Reches, and J. Brune, Particle size and energetics of gouge from earthquake rupture zones, *Nature*, *434*, 749–752, 2005.

Wilson, D. S., Confidence intervals for motion and deformation of the Juan de Fuca Plate, *J. Geophys. Res.*, *98*, 16,053–16,071, 1993.

Wintsch, R. P., R. Christoffersen, and A. K. Kronenberg, Fluid-rock reaction weakening of fault zones, *J. Geophys. Res.*, *100*, 13,021–13,032, 1995.

Wong, I. G., and D. S. Chapman, Deep intraplate earthquakes in the western United States and their relationship to lithospheric temperatures, *Bull. Seismol. Soc. Am.*, *80*, 589–599, 1990.

Zoback, M., and J. Townend, Implications of hydrostatic pore pressures and high crustal strength for the deformation of intraplate lithosphere, *Tectonophysics*, *336*, 19–30, 2001.

Zoback, M. D., and G. C. Beroza, Evidence for near-frictionless faulting in the 1989 (M 6.9) Loma Prieta, California, earthquake and its aftershocks, *Geology*, *21*, 181–185, 1993.

Zoback, M. D., and J. H. Healy, In situ stress measurements to 3.5 km depth in the Cajon Pass scientific research borehole; implications for the mechanics of crustal faulting, *J. Geophys. Res.*, *97*, 5039–5057, 1992.

Zoback, M. D., et al., New evidence on the state of stress of the San Andreas fault system, *Science*, *238*, 1105–1111, 1987.